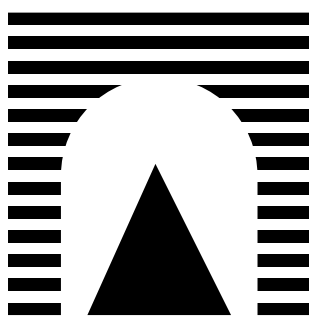


UNIVERSITÀ DEGLI STUDI “ROMA TRE”

Facoltà di Scienze Matematiche Fisiche e Naturali

Dottorato in Matematica XXI ciclo



Quantum lattice Boltzmann methods  
for the linear and nonlinear Schrödinger  
equation in several dimensions

*Relatori*

Prof. Renato Spigler

Prof. Sauro Succi

*Candidata*

Silvia Palpacelli

---

# Contents

<b>Introduction</b>	<b>1</b>
<b>1 A lattice kinetic approach to quantum mechanics</b>	<b>7</b>
1.1 The non-relativistic Schrödinger equation . . . . .	10
1.2 The Dirac equation . . . . .	11
1.2.1 Inclusion of an electromagnetic potential . . . . .	13
1.2.2 Fluid formulation of the Dirac equation . . . . .	14
1.3 The hydrodynamic lattice Boltzmann equation . . . . .	14
1.3.1 The adiabatic assumption . . . . .	17
1.4 Formal parallel between LBE and Dirac equation . . . . .	18
1.5 Quantum lattice Boltzmann equation . . . . .	21
1.6 One-dimensional quantum lattice Boltzmann model . . . . .	24
1.6.1 Adding a potential to the qLB model . . . . .	28
1.7 Numerical results for the one-dimensional qLB scheme . . . . .	30
1.7.1 Free particle propagation . . . . .	30
1.7.2 Harmonic oscillator . . . . .	31
1.7.3 Scattering from a rectangular barrier . . . . .	33
<b>2 The multi-dimensional quantum lattice Boltzmann model</b>	<b>37</b>
2.1 Extension to two and three dimensions: a survey . . . . .	38
2.2 Two-dimensional model . . . . .	40
2.2.1 Inclusion of a potential interaction . . . . .	43
2.3 Free propagation of a quantum wave packet . . . . .	44
2.3.1 Comparison with the analytical solution and convergence test	46
2.3.2 Mean position and mean spreads . . . . .	50
2.4 Two-dimensional harmonic oscillator . . . . .	51
2.5 Two-dimensional rotated, non-isotropic oscillator . . . . .	56
2.6 Three-dimensional model . . . . .	59
2.6.1 Three-dimensional harmonic oscillator . . . . .	62
<b>3 Ground state computation of Bose–Einstein condensates</b>	<b>65</b>
3.1 The time-dependent Gross–Pitaevskii equation . . . . .	65
3.2 The ground state solution of the GPE . . . . .	68
3.3 The imaginary-time quantum lattice Boltzmann model . . . . .	69

3.3.1	Imaginary-time qLB in one dimension . . . . .	69
3.3.2	Adding a potential to the imaginary-time qLB . . . . .	71
3.4	Extension to two spatial dimensions . . . . .	72
3.5	Dispersion relation for the equation governing $\phi^-$ . . . . .	75
3.6	Crank-Nicolson and Backward Euler Finite Difference schemes . .	76
3.6.1	One dimensional CN and BEFD schemes . . . . .	77
3.6.2	Two dimensional CN and BEFD schemes . . . . .	78
3.7	Thomas-Fermi approximation . . . . .	78
3.7.1	Thomas-Fermi chemical potential in one dimension . . . . .	79
3.7.2	Thomas-Fermi chemical potential in two dimensions . . . . .	80
3.8	Numerical results . . . . .	80
3.8.1	Numerical results in one dimension . . . . .	81
3.8.2	Numerical results in two dimensions . . . . .	86
3.9	Computation of the first excited state . . . . .	94
3.9.1	Computation of the first excited state in one dimension . .	94
3.9.2	Computation of the first excited state in two dimensions . .	95
3.10	Halving the discretization step . . . . .	102
3.11	From qLB to physical units . . . . .	104
<b>4</b>	<b>Quantum LB simulation of expanding BECs in random potentials</b>	<b>107</b>
4.1	Review of the quantum Lattice Boltzmann model . . . . .	108
4.1.1	The real-time qLB model . . . . .	109
4.2	The Gross-Pitaevskii equation . . . . .	110
4.2.1	qLB scaling . . . . .	111
4.3	Numerical construction of the random speckle potential . . . . .	112
4.4	Anderson localization of expanding BEC in speckle potential . . .	113
4.5	Numerical results . . . . .	118
4.6	Long-time depletion . . . . .	122
<b>5</b>	<b>Ground state computation of the GPE-Newton equations</b>	<b>127</b>
5.1	Quantum state reduction as a gravitational effect . . . . .	129
5.2	The Schrödinger-Newton model . . . . .	130
5.3	The attractive Bose-Einstein condensate . . . . .	132
5.4	Adding a “gravitational” term to the attractive BEC . . . . .	137
<b>6</b>	<b>Future research</b>	<b>147</b>
6.1	Complex geometries . . . . .	148
6.2	Parallel computing . . . . .	149
6.3	Application of the qLB scheme to the Khon-Sham equations . . . .	151
	<b>Conclusions</b>	<b>153</b>



# Introduction

In the last decade the lattice kinetic approach to fluid dynamics, and notably the Lattice Boltzmann (LB) method, has consolidated into a powerful alternative to the discretization of the Navier-Stokes equations for the numerical simulation of a wide range of complex fluid flows [97, 67, 18, 139]. To date, the overwhelming majority of LB work has been directed to the investigation of classical (non quantum) fluids. Nonetheless a small group of authors have also investigated lattice kinetic formulations of quantum mechanics [24, 22, 19, 98, 99] which led to the definition of the so-called *quantum lattice* gas methods for solving linear and non-linear Schrödinger equations.

Due to its central role in quantum mechanics, many numerical studies have been devoted to the solution of the time-dependent (nonlinear) Schrödinger equation and of the time-independent Gross-Pitaevskii equation (GPE), which is a special Schrödinger equation with a cubic nonlinearity describing the behavior of Bose-Einstein condensates. In particular, to solve the time-dependent Schrödinger equation, Chiofalo et al. proposed a particle-inspired scheme [33, 34], finite difference methods have been proposed by Ruprecht et al. [120], Ensher et al. [54] and Wang [144], and a time-splitting spectral (TSSP) method was developed by Bao and coworkers initially for the Schrödinger equation in the semi-classical regime [15, 16] and then extended to the GPE [14, 11]. In particular, the TSSP method shows good properties of accuracy and efficiency.

To compute stationary solutions of the GPE, several approaches have been also proposed: Runge-Kutta methods [53, 1], explicit imaginary-time algorithms [33, 35, 10, 13] and direct minimization of the energy functional [12]. It is remarkable that by far the most numerical works for these methods have appeared in the physical literature.

The earliest LB model for quantum motion was proposed by Succi and Benzi in 1993 and it built upon a formal analogy between the Dirac equations and a Boltzmann equation satisfied by a complex distribution function [138, 133]. It was then shown that the non-relativistic Schrödinger equation derives from the

complex Boltzmann equation under the same adiabatic assumptions (in imaginary time), which takes the Boltzmann equation for classical molecules into the Navier-Stokes equations of continuum fluid mechanics. Based on this formal analogy, a quantum lattice Boltzmann scheme was formulated, in which the discrete speeds are identified with the four-spinor components of the Dirac's wave function. For 1+1-dimensional problems (evolutionary problems in one space dimension) this identification is fairly natural, since the spin can always be aligned with momentum (unit helicity). In higher dimensions, however, such helicity=1 representation is no longer viable because the spin does not transform as ordinary vectors and consequently the Dirac propagation matrices cannot be diagonalized simultaneously. To cope with this problem, the classical stream-collide structure of the Boltzmann equation was augmented with a 'rotation' step, designed in such a way as to secure alignment between momentum and spin degrees of freedom along each direction of propagation (operator splitting).

However, such a multi-dimensional version of the quantum lattice Boltzmann (qLB) method was not numerically validated in Refs. [138, 133]. Indeed, the first result of this thesis is the effective numerical extension and validation of the multi-dimensional qLB scheme.

In particular, in Ref. [105], we present a numerical study of the two- and three-dimensional qLB model, based on an operator splitting approach. Our results show a satisfactory agreement with the analytical solutions, thereby demonstrating the validity of the three-step stream-collide-rotate theoretical structure of the multi-dimensional qLB scheme.

Moreover, in Ref. [108], we extend the qLB model by developing an imaginary-time version of the scheme in order to compute the ground state solution of the Gross-Pitaevskii equation (GPE). The GPE is commonly used to describe the dynamics of zero-temperature Bose-Einstein condensates (BEC) and it is a nonlinear Schrödinger equation with a cubic nonlinearity. The ground state solution of the GPE is the eigenstate which corresponds to the minimum energy level. Typically, this minimizer is found by applying to the GPE a transformation, known as Wick rotation, which consists on "rotating" the time axis on the complex plane so that time becomes purely imaginary [2, 33, 35, 100]. With this rotation of the time axis, the GPE becomes a diffusion equation with an absorption/emission term given by the nonlinear potential.

Thus, the basic idea behind the imaginary-time qLB model is to apply the Wick rotation to the real-time qLB scheme. The imaginary-time qLB scheme proposed in Ref. [108] is also extended to multi-dimensions by using the same splitting operator approach already applied to the real-time qLB model [105, 107].

In addition, we apply the qLB scheme to the study of the dynamics of a BEC in a random potential [106], which is a very active topic in present time research on condensed matter and atomic physics research. In particular, based on Ref. [124], we investigate the conditions under which an expanding BEC in a random speckle potential can exhibit Anderson localization.

Recently, a large number of experimental and numerical studies have been devoted to the localization properties of Bose gases [123, 93, 36, 56, 37, 101, 3, 130, 94]. Indeed, it is well known that disorder can profoundly affect the behavior of quantum systems, Anderson localization being one of the most fascinating phenomena in point [8]. Back in 1958, Anderson showed that the eigenstates of single quantum particles in a weak random potential can become localized, which means that the corresponding wave functions exhibit an exponential decay at large distances [123].

In Ref. [106], we explore the use of qLB for the case of nonlinear interactions with random potentials and, in particular, we investigate the mechanism by which the localized state of the BEC is modified by the residual self-interaction in the (very) long-time term evolution of the condensate.

These studies have demonstrated the viability of the qLB model as numerical algorithm for solving linear and nonlinear Schrödinger equations for both the time-dependent and ground state solutions, even in external random potentials.

The qLB method is also very promising as a suitable algorithm for prospective quantum computers. Indeed, as it was first suggested by Feynman [55], the most natural application of quantum computers would be solving problems from quantum mechanics [50]. The lattice kinetic approach is particularly well suited for quantum computing since, as observed in [91], the stream-and-collide structure of the quantum lattice Boltzmann equation maps naturally onto the structure of quantum networks, i. e., quantum computing devices consisting of quantum logic gates, whose computational operation proceeds synchronously in time. The outputs of some gates are wire-connected to the input of some others (streaming step), and locally processed by unitary operations (the collision step). Moreover, it was shown that the so-called quantum lattice gas cellular automata [98], which bears many similarities with the qLB model, can be used to simulate systems of nonrelativistic quantum particles with exponential speedup in the number of particles [24].

Besides this attractive but still hypothetical future application to quantum computing, such lattice kinetic methods for quantum mechanics represent interesting numerical schemes, which can be easily implemented on classical computers, retaining the usual attractive features of LB methods: simplicity, computational

speed, straightforward parallel implementation.

Indeed, as an explicit numerical method, qLB offers an appealing set of properties, norm preserving (unitary) and amenability to parallel processing. Moreover, being based on a first-order, relativistic formulation, the qLB method offers stability provided that  $\Delta z = c\Delta t$  for any value of  $\Delta t$ . This contrasts with standard explicit schemes, whose numerical stability is constrained by the Courant-Friedrichs-Lewy (CFL) conditions of the form  $\Delta t < \frac{2m}{\hbar} \Delta z^2$ .

This dissertation is organized as follows.

- In Chapter 1, we introduce the qLB model as first presented by Succi and Benzi [138]. In particular, we review the derivation of the Schrödinger equation in the adiabatic limit for the one dimensional model and discuss the theoretical procedure for the extension to multi-dimensions. Moreover, we include some one dimensional numerical results taken from Ref. [133] in order to validate the one dimensional qLB model.
- In Chapter 2, we discuss in detail the extension to multi-dimensions presenting numerical results in both, two and three space dimensions. However, most of the simulations and comparisons against analytical results are performed for the two-dimensional case. This is due to the fact that the scheme requires a large amount of memory (the distribution fields are complex), thus allowing only for small lattices in three dimensions. This difficulty could be overcome implementing the algorithm in parallel, which task is being considered at the present time.
- In Chapter 3, we extend the qLB model to the computation of the ground state of the nonlinear Schrödinger equation. In particular, the imaginary-time qLB model is defined and numerical results are compared with Crank-Nicolson results and theoretical approximations of the solutions such as the Thomas-Fermi ground state solutions.
- In Chapter 4, we present the application of the qLB scheme to the study of the dynamics of a BEC in a random potential. Our results are compared with classical Crank-Nicolson scheme for validation.
- In Chapter 5, we study a particular nonlinear equation, namely the GPE with attractive interactions coupled with a Newton-like potential. This last work was inspired by a paper by Moroz, Penrose and Tod [102], where they consider a particular nonlinear quantum wave equation, namely the so-called



Schrödinger-Newton equation (SNE) proposed by Penrose [115] within a theory which explains the quantum state reduction as a gravitational effect.

Due to the similar mathematical structure of the GPE with attractive interactions and the SNE, we applied the approach presented in Ref. [102] to the GPE equation in order to compare the eigenstates of these two systems and we then coupled the GPE with the Newtonian potential.

This part of the work deviates from the rest of the thesis because we decided to not use the quantum lattice Boltzmann scheme. This choice was induced by several considerations which are summarized in the introduction of Chapter 5.

- In Chapter 6, we briefly discuss future perspectives of this work, such as the extension to complex geometries and the development of a parallel implementation in order to fully appreciate the computational efficiency of the qLB model for large, three-dimensional problems. Finally, we suggest to use such a parallel version of the scheme to compute the solution of a set of coupled eigenvalues equations known as Khon-Sham equations.



# Chapter 1

## A lattice kinetic approach to quantum mechanics

Quantum wave equations, in particular the non-relativistic Schrödinger equation, play a central role in both theoretical and experimental physics (see e. g. [126, 146]). The fundamental idea that matter, similarly to electromagnetic radiation, has a dual character behaving sometimes like corpuscular particles and, some other times, like a wave, was first suggested by Louis de Broglie in 1923 [40]. However, in the development of quantum mechanics a different approach was proposed in the years 1925-1926 by Werner Heisenberg, Max Born, Pascual Jordan and Wolfgang Pauli, the so-called matrix formulation [66, 26, 44, 110] and the wave mechanics was then temporarily abandoned.

In 1926, Erwin Schrödinger showed how the wave mechanics formalism could be used in order to reproduce the results obtained with the matrix formulation. In a famous series of papers [128, 127, 129], Schrödinger first suggested the familiar non-relativistic equation which is now named after him and then presented a relativistic extension of this equation. The relativistic Schrödinger equation was independently derived also by Oskar Klein [81] and Walter Gordon [61] and nowadays it is known as the Klein-Gordon equation.

However, the Klein-Gordon equation (or relativistic Schrödinger) presents an unphysical behavior, it can lead to negative probabilities. In order to solve this problem, in 1928, Paul Dirac [45, 46] formulated the first relativistic theory which takes into account the electron's spin from the beginning [146]. This theory leads to the famous relativistic Dirac equation (which can also be thought of as the relativistic limit of the non-relativistic Schrödinger equation) for particle with spin-1/2 which, in particular, is a relativistic formalism with positive probabilities.

Even though, the Dirac equation is an answer to the negative probability problem, it gave rise to a much more troublesome question: negative energies. In fact, given

a momentum  $\mathbf{p}$ , there are four independent solutions of the Dirac equation in the form of plane waves and two of them are associated to a positive energy, but the remaining two have a negative energy. Dirac proposed many interpretations of this effect [47] and finally he “predicted” the existence of a new kind of positively charged particle of the same mass of an electron [48]. This particle was effectively discovered by Carl D. Anderson [6, 7] in 1932 and it is now known as positron.

In this work, we propose a method to numerically integrate the quantum wave equations, such as the linear and nonlinear Schrödinger equation, by means of a lattice kinetic approach. In particular, we inspect and extend the quantum lattice Boltzmann (qLB) model originally proposed in 1993 [138].

As we shall see in detail, the qLB model is based on a formal analogy between the Dirac equation and the kinetic lattice Boltzmann equation (LBE), so that the Dirac equation can be written as a kinetic quantum lattice Boltzmann equation (qLBE) and it can be shown that the non-relativistic Schrödinger equation ensues from this complex qLBE under the same adiabatic assumption which takes the LBE for classical molecules into the Navier-Stokes equations of continuum fluid mechanics.

The basic idea is to associate the wave functions composing the Dirac quadrispinor with the discrete distribution functions of the LBE. In one spatial dimension, this analogy is natural and the quadrispinor components can be assimilated to quantum particles of different types propagating with velocities  $\pm c$  and colliding when they meet at the same space-time location.

However, in multi-dimensional formulation, the analogy is no longer straightforward. This is mainly due to the fact that the Dirac streaming operator is not diagonal along all the spatial directions (i. e. Dirac matrices can not be simultaneously diagonalized). We could roughly say that, unlike classical particles, quantum particles of different types mix up while propagating (“spinning particles”). To cope with this problem, a new step has to be included besides the classical collision and streaming steps: a so-called “rotation” step. A detailed discussion on the extension of the qLB model to multi-dimensions is presented in Chapter 2.

The qLB scheme is one of the first attempts to export the basic concepts of lattice Boltzmann (LB) models [97, 67, 68, 18, 89] to quantum mechanics.

Indeed, LB models have been initially proposed as a numerical tool for simulating fluid flows and, nowadays, they have consolidated into a powerful alternative to more classical computational fluid dynamics models based on the discretization of the Navier-Stokes equations of continuum mechanics.

The LB models were historically derived from lattice gas cellular automata (LGCA)

(for a review see e. g. [148]).

The basic idea of LGCA is to simulate the macroscopic behavior of a fluid flow by implementing an extremely simplified model of the microscopic interactions between particles. The LB schemes were developed, starting from LGCA, in the attempt to overcome their major drawbacks: statistical noise, increasing complexity of the collision operator (especially for three dimensional problems) and high viscosity (due to small number of collisions) [97, 67, 68].

However, LB models and, in general, the lattice kinetic approach, have been mainly used with classical (non quantum) fluid.

The intriguing and well known analogies between quantum mechanics and fluid mechanics, which were pointed out since the early days of the formulation of quantum theory [95], suggested to extend the lattice kinetic approach also to quantum mechanics.

Furthermore, with the increasing interest on quantum computing, the qLB scheme and, more generally, the so-called quantum lattice gas (QLG) models have been studied with particular attention since they seem to be good candidates for perspective quantum computers [24, 22, 23, 19, 98, 99, 151, 143, 152].

In particular, in Ref. [24], Boghosian and Taylor demonstrate how the QLG could be used to solve the many-particle Schrödinger equation with exponential speed up in the number of particles if it was possible to implement the model on a quantum computer.

Besides its hypothetical and future application to quantum computing, the qLB model for quantum wave equations is an interesting numerical scheme which can be implemented on a classical computer retaining the usual attractive features of LB schemes: simplicity, computational speed and straightforward parallel implementation. Moreover, it is norm-preserving and stable for any value of the time step provided that the light-cone rule is fulfilled (i. e.  $\Delta t = c\Delta z$ ), and these are remarkable properties for an explicit numerical scheme.

In this chapter, we revise the theoretical derivation of the qLB model and describe its one-dimensional implementation. Numerical results presented in Ref. [133] are revised in order to validate the one-dimensional model, moreover the operator splitting approach proposed in Ref. [138] to extend the scheme to two and three spatial dimensions is also outlined. In order to maintain the discussion self-consistent as much as possible, we briefly introduce the Schrödinger and Dirac equations which are central elements of the qLBE theory.

## 1.1 The non-relativistic Schrödinger equation

As previously mentioned, the non-relativistic Schrödinger equation was formulated in the attempt to obtain a quantitative description of the non-relativistic motion of a particle. To derive this partial differential equation many assumptions need to be done, but the starting idea is to suppose that the wave-particle duality, characteristic of photons, holds also for all other particles such as electrons or protons.

Let  $\psi(\mathbf{x}, t)$  be the wave function representing the quantum state of a particle, the Schrödinger equation describing the dynamics of this particle of mass  $m$  in an external potential  $V(\mathbf{x}, t)$  reads as follows:

$$i\hbar\partial_t\psi(\mathbf{x}, t) = -\frac{\hbar^2}{2m}\Delta\psi(\mathbf{x}, t) + V(\mathbf{x}, t)\psi(\mathbf{x}, t). \quad (1.1)$$

The wave function density

$$|\psi(\mathbf{x}, t)|^2 = \psi(\mathbf{x}, t)\psi^*(\mathbf{x}, t)$$

(where  $\psi^*$  denotes the complex conjugate of  $\psi$ ), represents the position probability density. This means that  $|\psi(\mathbf{x}, t)|^2 d\mathbf{x}$  is the probability of finding a particle in the volume element  $d\mathbf{x}$  about position  $\mathbf{x}$  at time  $t$ .

The interpretation of  $|\psi(\mathbf{x}, t)|^2$  as a probability density implies the following normalization constraint on  $\psi$ :

$$\int |\psi(\mathbf{x}, t)|^2 d\mathbf{x} = 1.$$

Simple algebra shows that Eq. (1.1) can be written in fluid form thus revealing an interesting analogy between quantum mechanics and fluid mechanics.

In particular, multiplying Eq. (1.1) by  $\psi^*$  on the left and the conjugate of Eq. (1.1) by  $\psi$  on the right and then subtracting the resulting equations, we obtain

$$i\hbar\partial_t|\psi(\mathbf{x}, t)|^2 = -\frac{\hbar^2}{2m}[\psi^*(\mathbf{x}, t)\Delta(\psi(\mathbf{x}, t)) - \Delta(\psi^*(\mathbf{x}, t))\psi(\mathbf{x}, t)], \quad (1.2)$$

and, observing that

$$\nabla \cdot [\psi^*\nabla\psi - (\nabla\psi^*)\psi] = \psi^*\Delta\psi - (\Delta\psi^*)\psi,$$

Eq. (1.2) becomes

$$\partial_t|\psi|^2 + \frac{\hbar}{2im}\nabla \cdot [\psi^*\nabla\psi - (\nabla\psi^*)\psi] = 0. \quad (1.3)$$

Eq. (1.3) is a familiar continuity equation for a quantum fluid of density  $\rho = |\psi|^2$  and current density  $\mathbf{J}$ , where

$$\mathbf{J} = \frac{\hbar}{2im}[\psi^*\nabla\psi - (\nabla\psi^*)\psi]. \quad (1.4)$$

This analogy becomes even more revealing if we use the eikonal formalism [87]:

$$\psi(\mathbf{x}, t) = \rho(\mathbf{x}, t)^{1/2} \exp(i\theta(\mathbf{x}, t)), \quad (1.5)$$

so that  $|\psi|^2 = \rho$  and, upon inserting Eq. (1.5) into Eq. (1.4), we obtain

$$\mathbf{J} = \frac{\hbar}{m} \rho \nabla \theta \equiv \rho \mathbf{u}.$$

Hence, in this representation,  $\rho$  is the density of the quantum fluid and  $(\hbar/m)\nabla\theta$  represents its velocity.

The fluid formulation of the Schrödinger equation can be obtained by simply inserting Eq. (1.5) into Eq. (1.1) and taking the imaginary and the real part, respectively. In particular, by computing the imaginary part we obtain the analogue of Eq. (1.3):

$$\partial_t \rho(\mathbf{x}, t) + \frac{\hbar}{m} \nabla \cdot (\rho(\mathbf{x}, t) \nabla \theta(\mathbf{x}, t)) = 0,$$

while, taking the real part, we derive the following dynamic equation for  $\theta$

$$\begin{aligned} \hbar \rho(\mathbf{x}, t) \partial_t \theta(\mathbf{x}, t) &= \frac{\hbar^2}{2m} \rho(\mathbf{x}, t) \left[ \rho^{-1/2}(\mathbf{x}, t) \Delta \rho^{1/2}(\mathbf{x}, t) - (\nabla \theta(\mathbf{x}, t))^2 \right] \\ &\quad - V(\mathbf{x}, t) \rho(\mathbf{x}, t). \end{aligned}$$

In conclusion, the Schrödinger equation can be written in fluid form and, as we shall illustrate in the following, there is a strong similarity between the relativistic associate to the Schrödinger equation, namely the Dirac equation, and the kinetic lattice Boltzmann equation (LBE).

For all their intellectual charm, it is now commonly accepted that this similarities are only formal. However they can be extremely useful for modeling purposes to formulate non-relativistic quantum mechanics in terms of first-order (relativistic) numerical schemes.

Roughly speaking, the idea is that the Schrödinger equation can be obtained in the non-relativistic limit from the Dirac equation under an adiabatic assumption that is formally similar to the one which takes the LBE to the Navier-Stokes equations of fluid mechanics in the macroscopic limit.

## 1.2 The Dirac equation

As previously mentioned, the Dirac equation was formulated in 1928 by Paul Dirac in the attempt to provide a description of elementary spin-1/2 particles, such as electrons, consistent with both the principle of quantum mechanics and the theory of special relativity. In particular, this equation is derived by formally

requiring Lorence invariance on quantum mechanics which implies a symmetric balance between space and time derivatives. This balance is evidently broken by the non-relativistic Schrödinger equation where the time derivative is only first order whereas the space derivative is second order.

This situation is once again similar to the fluid dynamics case, indeed, in the LBE time and space derivatives are in balance (both first order), while in the Navier-Stokes equations they shows the same asymmetry than in the Schrödinger equation.

For a free particle of mass  $m$ , the Dirac equation reads as follows:

$$\partial_t \psi + c \boldsymbol{\alpha} \cdot \nabla \psi = -i \frac{mc^2}{\hbar} \beta \psi, \quad (1.6)$$

where  $\psi = (\psi_1, \psi_2, \psi_3, \psi_4)^T$  is a complex quadrispinor,  $\boldsymbol{\alpha} = (\alpha^x, \alpha^y, \alpha^z)$  and  $\beta$  are  $4 \times 4$  matrices and, in the standard form, they are defined as follows

$$\begin{aligned} \alpha^x &= \begin{pmatrix} 0 & 0 & 0 & 1 \\ 0 & 0 & 1 & 0 \\ 0 & 1 & 0 & 0 \\ 1 & 0 & 0 & 0 \end{pmatrix}, & \alpha^y &= \begin{pmatrix} 0 & 0 & 0 & -i \\ 0 & 0 & i & 0 \\ 0 & -i & 0 & 0 \\ i & 0 & 0 & 0 \end{pmatrix}, \\ \alpha^z &= \begin{pmatrix} 0 & 0 & 1 & 0 \\ 0 & 0 & 0 & -1 \\ 1 & 0 & 0 & 0 \\ 0 & -1 & 0 & 0 \end{pmatrix}, & \beta &= \begin{pmatrix} 1 & 0 & 0 & 0 \\ 0 & 1 & 0 & 0 \\ 0 & 0 & -1 & 0 \\ 0 & 0 & 0 & -1 \end{pmatrix}. \end{aligned} \quad (1.7)$$

It is known that the choice of the Dirac matrices is not unique, indeed all possible choices are related by similarity transformations by means of a unitary matrix.

For the following, it will be very useful to recast Eq. (1.6) into a form where all streaming matrices are real-valued. This is the so-called Majorana form [87] and it can be simply accomplished by applying to the standard Dirac matrices and to the quadrispinor  $\psi$  of Eq. (1.6) the unitary transformation

$$S = \frac{1}{\sqrt{2}}(\alpha^y + \beta) = \frac{1}{\sqrt{2}} \begin{pmatrix} 1 & 0 & 0 & -i \\ 0 & 1 & i & 0 \\ 0 & -i & -1 & 0 \\ i & 0 & 0 & -1 \end{pmatrix},$$



which yields the following transformed matrices

$$\begin{aligned}\alpha_S^x &\equiv \begin{pmatrix} 0 & 0 & 0 & -1 \\ 0 & 0 & -1 & 0 \\ 0 & -1 & 0 & 0 \\ -1 & 0 & 0 & 0 \end{pmatrix} = -\alpha^x, & \alpha_S^y &\equiv \begin{pmatrix} 1 & 0 & 0 & 0 \\ 0 & 1 & 0 & 0 \\ 0 & 0 & -1 & 0 \\ 0 & 0 & 0 & -1 \end{pmatrix} = \beta, \\ \alpha_S^z &\equiv \begin{pmatrix} 0 & 0 & -1 & 0 \\ 0 & 0 & 0 & 1 \\ -1 & 0 & 0 & 0 \\ 0 & 1 & 0 & 0 \end{pmatrix} = -\alpha^z, & \beta_S &\equiv \begin{pmatrix} 0 & 0 & 0 & -i \\ 0 & 0 & i & 0 \\ 0 & -i & 0 & 0 \\ i & 0 & 0 & 0 \end{pmatrix} = \alpha^y.\end{aligned}$$

Hence, Eq. (1.6) can be equivalently written as

$$\partial_t \psi + c(-\alpha^x \partial_x + \beta \partial_y - \alpha^z \partial_z) \psi = -i \frac{mc^2}{\hbar} \alpha^y \psi \equiv -i \omega_c \alpha^y \psi, \quad (1.8)$$

where  $\omega_c = mc^2/\hbar$  is the Compton frequency and the Dirac quadrispinor is also transformed by applying  $S$ .

### 1.2.1 Inclusion of an electromagnetic potential

Up to this point, we have considered the Dirac equation for a free particle, however the inclusion of an external electromagnetic potential is straightforward. In fact, terms that involve electromagnetic potentials can be added to Eq. (1.6) in a relativistic way by making the following usual replacement of the operators [87]:

$$\begin{aligned}i\hbar \partial_t &\longrightarrow i\hbar \partial_t + qV, \\ -i\hbar \nabla &\longrightarrow -i\hbar \nabla + \frac{q}{c} \mathbf{A},\end{aligned} \quad (1.9)$$

where  $qV + \frac{q}{c} \mathbf{A}$  is the interaction of the elementary charge  $q$  with an external electromagnetic field described by the 4-component potential  $(V, \mathbf{A})$ .

Upon replacing the operators of Eq. (1.6) as prescribed by Eq. (1.9), the Dirac equation transforms into

$$\partial_t \psi + c \boldsymbol{\alpha} \cdot \nabla \psi = -i \omega_c \beta \psi + i \frac{q}{\hbar} V \psi - i \frac{q}{\hbar} (\mathbf{A} \cdot \boldsymbol{\alpha}) \psi \equiv i M \psi, \quad (1.10)$$

where

$$M = -\omega_c + \frac{q}{\hbar} V - \frac{q}{\hbar} (\mathbf{A} \cdot \boldsymbol{\alpha}), \quad (1.11)$$

thus, the external interaction is easily accommodated into a formal redefinition of the mass matrix  $M$ .

### 1.2.2 Fluid formulation of the Dirac equation

As the Schrödinger equation, also the Dirac equation can be written in fluid form by multiplying Eq. (1.10) on the left by  $\psi^\dagger$  and the hermitian adjoint equation

$$\partial_t \psi^\dagger + c(\nabla \psi^\dagger) \cdot \boldsymbol{\alpha} = -i\psi^\dagger M,$$

on the right by  $\psi$  and then summing the resulting equations [49]. This yields

$$\partial_t(\psi^\dagger \psi) + c\nabla \cdot (\psi^\dagger \boldsymbol{\alpha} \psi) = 0,$$

and, by defining

$$\rho = \psi^\dagger \psi, \quad \mathbf{J} = c\psi^\dagger \boldsymbol{\alpha} \psi,$$

we obtain

$$\partial_t \rho + \nabla \cdot \mathbf{J} = 0. \tag{1.12}$$

Note that  $\rho = \psi^\dagger \psi$  is always positive so that it can be interpreted as a position probability density, while  $c\boldsymbol{\alpha}$  is a sort of fluid velocity.

Since  $\psi$  is a quadrispinor, the quantum fluid can be seen as a four-component fluid mixture.

The fluid interpretation of the Dirac equation and, in particular, the analogy with the LBE is transparent: the quadrispinor components can be assimilated to quantum particles of different types propagating in space with velocities  $\pm c$  and colliding via the “scattering” matrix  $M$  when they meet at the same space-time location. However, unlike classical particles, quantum particles of different type mix up while propagating (“spinning particles”), this is due to the fact that the Dirac streaming operator is not diagonal along all the three spatial directions.

As we shall see in the following of this chapter, this is the major problem to overcome to obtain a full correspondence between the LBE and the Dirac equation.

In the following section we introduce the LBE and we briefly sketch the adiabatic procedure which takes us from the LBE to the Navier-Stokes equations of fluid dynamics in order to substantiate the analogy

$$\text{Dirac Eq.} \longrightarrow \text{Schrödinger Eq.}$$

$$\text{Lattice Boltzmann Eq.} \longrightarrow \text{Navier-Stokes Eqs.}$$

## 1.3 The hydrodynamic lattice Boltzmann equation

In this section, since many indices are involved in some computations, in order to maintain a compact notation, vector components are indicated by italic subscript, i. e.  $v_l$  is an equivalent substitute of  $\mathbf{v}$ . Moreover, the Einstein notation is

adopted, this means that sum on repeated indices is implicitly assumed, so that the scalar product  $\mathbf{v} \cdot \mathbf{w}$  is equivalently written as  $v_l w_l$ .

The hydrodynamic lattice Boltzmann equation is a fully discrete kinetic equation of the form

$$f_i(\mathbf{x} + \mathbf{c}_i \Delta t, t + \Delta t) - f_i(\mathbf{x}, t) = \sum_{j=1}^b A_{ij} (f_j - f_j^{eq}), \quad i = 1, \dots, b, \quad (1.13)$$

where  $f_i$  are the discrete distribution functions propagating along directions  $\mathbf{c}_i$ ,  $A_{ij}$  is the scattering matrix mediating collisions between the  $i$ -th and  $j$ -th distributions and  $b$  is the number of discrete speeds connecting each site to its nearest neighbors. Here,  $f_i^{eq}$  represent the equilibrium distribution functions expanded up to second order terms in the flow field in order to retain convective effects. Formally, one has

$$f_i^{eq} = \frac{\rho}{b} \left( 1 + \frac{c_{il} u_l}{c_s^2} + \frac{Q_{ilm} u_l u_m}{2c_s^4} \right),$$

where  $c_s^2 = c^2/D$  with  $c = |\mathbf{c}_i|$  (not to be confused with the light speed),  $Q_{ilm} = c_{il} c_{im} - c_s^2 \delta_{lm}$  and  $D$  is the dimension of the space. The hydrodynamical quantities  $\rho$  and  $u_l$  are defined as follows

$$\rho = \sum_{i=1}^b f_i, \quad u_l = \frac{1}{\rho} \sum_{i=1}^b c_{il} f_i.$$

In order for Eq. (1.13) to reproduce the Navier-Stokes equations in the continuum limit, the following sum-rules have to be fulfilled by the collision matrix:

$$\begin{aligned} \sum_{i=1}^b A_{ij} &= 0, \quad \text{for all } j = 1, \dots, b, \\ \sum_{i=1}^b c_{il} A_{ij} &= 0, \quad \text{for all } j = 1, \dots, b; \quad l = 1, \dots, D, \end{aligned}$$

which correspond to mass and momentum conservation, respectively. In addition, fourth order tensors of the form  $T_{lmno} = \sum_{i=1}^b c_{il} c_{im} Q_{ino}$  must be isotropic to ensure rotational invariance at the macroscopic level [18].

These conditions are fulfilled only by a restricted class of lattices, the most popular being the hexagonal lattice proposed by Frish, Hasslacher and Pomeau in two dimensions and the face-centered-hypercube in four dimensions [57].

The discrete LBE of Eq. (1.13) can be thought of as a discretization of the following set of partial differential equations:

$$\partial_t f_i + c_{ia} \partial_a f_i = \sum_{j=1}^b A_{ij} (f_j - f_j^{eq}), \quad i = 1, \dots, b. \quad (1.14)$$

It can be shown that Eq. (1.14) is the first-order equation resulting from the multiscale expansion procedure commonly adopted to study the macro-dynamics of LBE [18].

By projecting Eq. (1.14) upon the eigenvectors of the scattering matrix  $A_{ij}$ , a set of hyperbolic equations for the hydrodynamic fields  $\rho$ ,  $\rho u_l \equiv J_l$  and  $S_{lm} = \sum_i Q_{ilm} f_i$  are derived [134]. In particular, restricting to the hydrodynamic sector, we obtain

$$\partial_t \rho + \partial_l J_l = 0, \quad (1.15)$$

$$\partial_t J_l + \partial_m P_{lm} = 0, \quad l = 1, \dots, D, \quad (1.16)$$

$$\partial_t S_{lm} + \partial_n R_{lmn} = \lambda(S_{lm} - S_{lm}^{eq}), \quad l, m = 1, \dots, D, \quad (1.17)$$

where

$$P_{lm} = \sum_{i=1}^b c_{il} c_{im} f_i = S_{lm} + P \delta_{lm}, \quad \text{with } P = \rho c_s^2,$$

and the tensor  $R_{lmn}$  is defined as

$$R_{lmn} = \sum_{i=1}^b f_i Q_{ilm} c_{in}. \quad (1.18)$$

Eqs. (1.15)-(1.17) does not exhaust all the equations which are obtained by projecting upon the eigenvectors of  $A_{ij}$ . In fact, Eq. (1.15) and Eq. (1.16) (which is a group of  $D$  equations) are related to the eigenvectors corresponding to the zero eigenvalues, whereas Eq. (1.17) (which is composed by  $D(D+1)/2 - 1$  independent equations) is associated to the leading non-zero eigenvalue of  $A_{ij}$ ,  $\lambda$ . There are still other eigenvectors of  $A_{ij}$  associated to non-zero eigenvalues.

Projecting upon those eigenvectors yields equations similar to those in Eqs. (1.15)-(1.17) but related to fields which have no physical meaning and do not emerge from the microscopic to the macroscopic level, these are called *ghost* fields. Even though they do not add physical information, they cannot be erased from the dynamics in order to preserve essential symmetries [134].

As macroscopic fields  $\rho$ ,  $J_l$ ,  $S_{lm}$  can be expressed as linear combination of the distribution functions  $f_i$ , it is possible to write  $f_i$  as a linear combination of the macroscopic fields. Considering only the hydrodynamic components, we obtain

$$f_i^H = \frac{\rho}{b} \left[ 1 + \frac{c_{il} u_l}{c_s^2} + \frac{Q_{ilm} S_{lm}}{2c_s^4} \right]. \quad (1.19)$$

By directly inserting this expression into the definition of the tensor  $R_{lmn}$  given by Eq. (1.18) and using the property of isotropy of the lattice, we obtain that the divergence of the hydrodynamic part of  $R_{lmn}$  corresponds to the Navier-Stokes

stress tensor [134]:

$$H_{lm} \equiv \partial_n R_{lmn}^H = c_s^2 \frac{D}{D+2} \left[ \partial_l J_m + \partial_m J_l - \frac{2}{D} (\partial_n J_n) \delta_{lm} \right]. \quad (1.20)$$

### 1.3.1 The adiabatic assumption

The system of Eqs. (1.15)-(1.17), with the additional equations for the ghost fields, contains exactly the same amount of information of the LBE just projected on a different base set. This system is an hyperbolic super-set of the Navier-Stokes equations, note, indeed, that it contains some redundancy with respect to Navier-Stokes equations because of the ghost fields which are inactive on a macroscopic scale but crucial to maintain the correct symmetries of the macroscopic dynamics. To recover the Navier-Stokes equations, we need to break the hyperbolic nature of this system and write it in a dissipative form, where spatial and temporal derivatives are no more in balance.

The key idea is adiabatic assumption on the “slow”, non-conserved modes, in this case the shear stress tensor  $S_{lm}$ . With adiabatic assumption, in this contest, we mean that we assume that  $S_{lm}$  relaxes to its local equilibrium on a time-scale which is much smaller of any typical hydrodynamic scale.

Mathematically, this is equivalent to neglect the time derivative on the evolution-equation of the shear tensor (see Eq. (1.17))

$$|\partial_t S_{lm}| \ll \lambda |S_{lm} - S_{lm}^{eq}|.$$

Assuming that the ghost fields are negligible ( $\partial_n R_{lmn} \sim H_{lm}$ ), from Eq. (1.17), we obtain

$$H_{lm} \sim \lambda (S_{lm} - S_{lm}^{eq}),$$

and this yields

$$S_{lm} \sim S_{lm}^{eq} + \frac{H_{lm}}{\lambda}. \quad (1.21)$$

Inserting Eq. (1.21) into Eq. (1.16), we obtain

$$\partial_t J_l + \partial_m \left( S_{lm}^{eq} + \frac{H_{lm}}{\lambda} + P \delta_{lm} \right) = 0.$$

For a proper choice of the equilibrium functions,  $S_{lm}^{eq} = \rho u_l u_m$ , and this finally yields

$$\partial_t J_l + \partial_m (\rho u_l u_m + P \delta_{lm}) = -c_s^2 \frac{D}{D+2} \frac{1}{\lambda} \partial_m \left[ \partial_l J_m + \partial_m J_l - \frac{2}{D} (\partial_n J_n) \delta_{lm} \right],$$

where Eq. (1.20) has been used.

This is the Navier-Stokes equation with kinematic viscosity  $\nu \sim 1/\lambda$ . Clearly,

this is a very cheap approach to the hydrodynamic limit, in this treatment all the details of the multiscale Chapman-Enskog procedure [148] have been hidden. From LGCA theory, it is known that neglecting some details of the multiscale expansion does not change the qualitative structure of the macroscopic equations, but it does introduce quantitative errors on the transport coefficients [134]. In particular, it can be shown that the correct expression for the viscosity is

$$\nu = -c_s^2 \frac{D}{D+2} \left( \frac{1}{\lambda} + \frac{1}{2} \right).$$

In conclusion, the Navier-Stokes equations are obtained as the large-scale limit of the kinetic LBE.

In particular, the adiabatic assumption is valid in the low Knudsen limit, where the Knudsen number,  $K_n$ , is the ratio between the particle mean free path length  $l_\mu$  (i. e. the mean distance covered by a particle between two subsequent collisions), and a typical macroscopic length scale  $l_M$ .

As we shall see in the next section, the Schrödinger equation ensues from the Dirac equation in a formally equivalent adiabatic assumption valid in the non-relativistic limit  $\beta = v/c \rightarrow 0$ , where  $c$  denotes the light speed. Hence, the formal parallel emerging from this analogy is

$$K_n = \frac{l_\mu}{l_M} \sim \beta = \frac{v}{c},$$

so that as the LBE tends to the Navier-Stokes equations for  $K_n \rightarrow 0$ , similarly the Dirac equation tends to the Schrödinger equation for  $\beta \rightarrow 0$  under a formally equivalent adiabatic assumption.

## 1.4 Formal parallel between LBE and Dirac equation

In this section, we substantiate the formal parallel between the LBE and the Dirac equation by deriving the Schrödinger equation from the Dirac equation under an adiabatic assumption which is valid in the non-relativistic limit  $\beta = v/c \ll 1$ .

Here, for the sake of simplicity, we consider only the one-dimensional version of Eq. (1.6) and, consequently, we derive the one-dimensional Schrödinger equation. The details of the extension to two and three spatial dimensions of this procedure are discussed in the next chapter where we introduce the multi-dimensional formulation of the qLB model. However, this one-dimensional version is sufficient to show the basic ideas underlying the adiabatic approximation procedure leading to the Schrödinger equation.

The following discussion is based on the original work by Succi and Benzi [138]

and on a recent review article by Palpacelli and Succi [107].

Let us consider, the one dimensional version of Eq. (1.6) written in the Majorana form [87], where all the streaming matrices are real valued, this reads:

$$\begin{aligned}\partial_t u_{1,2} + c \partial_z u_{1,2} &= \omega_c d_{2,1}, \\ \partial_t d_{1,2} - c \partial_z d_{1,2} &= -\omega_c u_{2,1}.\end{aligned}\tag{1.22}$$

Here, we denote the quadrispinor components as  $\boldsymbol{\psi} = (u_1, u_2, d_1, d_2)$  to recall that the  $u_{1,2}$  components are moving “up” (i. e. with speed  $c$ ), while the  $d_{1,2}$  components are moving “down” (i. e. with speed  $-c$ ).

Let us define the symmetric/antisymmetric modes according to the unitary transformation

$$\phi_{1,2}^{\pm} = \frac{1}{\sqrt{2}}(u_{1,2} \pm i d_{2,1}).\tag{1.23}$$

Starting from Eq. (1.22), it is easy to check that  $\phi_{1,2}^{\pm}$  fulfill the following equations:

$$\begin{aligned}\partial_t \phi_{1,2}^+ + c \partial_z \phi_{1,2}^- &= -i \omega_c \phi_{1,2}^+, \\ \partial_t \phi_{1,2}^- + c \partial_z \phi_{1,2}^+ &= i \omega_c \phi_{1,2}^-.\end{aligned}\tag{1.24}$$

Up to now, the system is still symmetric and time and space derivatives are in balance (both first order). As in kinetic theory, we need to break the symmetry of this hyperbolic system and write it in a dissipative form, where spatial and time derivative are no more in balance. The symmetry is broken by choosing a specific time direction via the energy phase-shift [136]

$$\phi_{1,2}^{\pm} \longrightarrow \phi_{1,2}^{\pm} \exp(i \omega_c t).$$

With this definition of  $\phi_{1,2}^{\pm}$ , Eq. (1.24) transforms into:

$$\partial_t \phi_{1,2}^+ + c \partial_z \phi_{1,2}^- = 0,\tag{1.25}$$

$$\partial_t \phi_{1,2}^- + c \partial_z \phi_{1,2}^+ = 2i \omega_c \phi_{1,2}^-.\tag{1.26}$$

In the non-relativistic limit,  $\beta = v/c \ll 1$ , the following adiabatic assumption holds:

$$|\partial_t \phi_{1,2}^-| \ll 2\omega_c |\phi_{1,2}^-|.$$

From Eq. (1.26), by neglecting the time derivative, we obtain

$$\phi_{1,2}^- \sim \frac{c}{2i\omega_c} \partial_z \phi_{1,2}^-.\tag{1.27}$$

Inserting Eq. (1.27) into Eq. (1.25), we finally obtain the Schrödinger equation for a free particle of mass  $m$ ,

$$i\hbar \partial_t \phi_{1,2}^+ = -\frac{\hbar^2}{2m} \partial_z^2 \phi_{1,2}^+.$$

The antisymmetric modes  $\phi_{1,2}^-$  can be assimilated to the ghost fields of the LBE, in the sense that they are needed to preserve the correct symmetries, although they do not “emerge” at the macroscopic scale.

Indeed, relativistic motion implies that any particle of momentum  $\mathbf{p}$  is invariably associated to an antiparticle with opposite momentum  $-\mathbf{p}$ . The symmetric combination of these two give rise to a smooth, emergent field, whereas the antisymmetric combination defines a low amplitude, high frequency mode which decouples from the system dynamics in the limit  $\beta \rightarrow 0$ .

To better illustrate this point, we inspect the behavior of  $\phi_{1,2}^-$  with respect to  $\phi_{1,2}^+$  by rewriting Eq. (1.24) in terms of the energy and momentum operators of quantum mechanics

$$\begin{aligned} i\hbar\partial_t &\longrightarrow E, \\ -i\hbar\partial_z &\longrightarrow p_z. \end{aligned}$$

By inserting these expressions into Eq. (1.24), we obtain

$$\begin{aligned} E\phi_{1,2}^+ - cp_z\phi_{1,2}^- &= mc^2\phi_{1,2}^+, \\ E\phi_{1,2}^- - cp_z\phi_{1,2}^+ &= -mc^2\phi_{1,2}^-. \end{aligned} \tag{1.28}$$

In order to take the non-relativistic limit, we make the usual replacement [126]

$$E \longrightarrow E' + mc^2, \quad \text{with } E' \ll mc^2 \quad \text{for } \beta \rightarrow 0.$$

This corresponds to the energy shift and the adiabatic assumption performed above to transform Eq. (1.24) into Eqs. (1.25) and (1.26). Hence, Eq. (1.28) becomes

$$E'\phi_{1,2}^+ - cp_z\phi_{1,2}^- = 0, \tag{1.29}$$

$$(E' + 2mc^2)\phi_{1,2}^- - cp_z\phi_{1,2}^+ \sim 2mc^2\phi_{1,2}^- - cp_z\phi_{1,2}^+ = 0. \tag{1.30}$$

From Eq. (1.30), we obtain

$$\frac{|\phi_{1,2}^-|}{|\phi_{1,2}^+|} = \frac{1}{2} \frac{v}{c} = \frac{\beta}{2}.$$

From a standard Fourier analysis of Eqs. (1.25) and (1.26), we can study the relation between the frequencies of  $\phi^+$  and  $\phi^-$ . In particular, let us assume

$$\begin{aligned} \phi^+ &= \rho^+ \exp[i(kz - \omega^+ t)], \\ \phi^- &= \rho^- \exp[i(kz - \omega^- t)], \end{aligned} \tag{1.31}$$

substituting Eq. (1.31) into Eqs. (1.25) and (1.26), it can be checked that

$$\frac{\omega^-}{\omega^+} \sim \frac{1}{\beta^2}.$$



Summarizing, the amplitude of  $\phi^-/\phi^+$  scales like  $\beta$ , whereas the frequency ratio  $\omega^-/\omega^+$  goes like  $1/\beta^2$ . This means that, as  $\beta$  goes to zero, the antisymmetric modes become smaller and smaller in amplitude and faster and faster in frequency so that they finally become unobservable on scales longer than  $1/\omega^-$ .

This picture recalls closely the adiabatic elimination of the slow modes in kinetic theory, however there is a fundamental difference. Kinetic theory describes dissipative phenomena in which transient modes tend to die out in a short time due to the real-valued relaxation coefficient. Quantum mechanics is time-reversible, and fast modes never die out (their relaxation coefficient is purely imaginary), they just oscillate so fast that any observation on time-scales longer than their period of oscillation overlooks them [134].

Note that it is the fast mode, not the antiparticle mode, that fades away, the particle-antiparticle twin-link does not dissolve even in the low energy limit.

Another interesting remark concerns the symmetry breaking induced by a non-zero mass. If the particle mass is taken to be null, then the “up” and “down” components move with velocity  $\pm c$ , respectively with no interaction, they do not even “see” each other, the result being the wave equation for photons. Evidently, this is a singular limit which cannot be described by the Schrödinger equation. Any non-zero mass causes “collisions” which slow down the wave packets and confer on them a subluminal speed  $v < c$ .

## 1.5 Quantum lattice Boltzmann equation

In the previous section, we finally showed the intriguing analogy between the Dirac equation and the LBE: the Schrödinger equation can be obtained from the Dirac equation in the same way as the Navier-Stokes equations are derived from the LBE. This invites a quantitative correspondence between LBE and Dirac equation. To this end, let us rewrite the three-dimensional Dirac equation in Majorana form, this reads

$$\partial_t \psi + c(-\alpha^x \partial_x + \beta \partial_y - \alpha^z \partial_z) \psi = -i\omega_c \alpha^y \psi. \quad (1.32)$$

The formal parallel between Eq. (1.32) and Eq. (1.14) is based on the identification of the wave functions composing the Dirac quadrispinor  $\psi = (\psi_1, \psi_2, \psi_3, \psi_4)^T$  with the discrete distribution functions  $f_i$  of the LBE.

In one spatial dimension, this analogy is natural and the quadrispinor components can be assimilated to quantum particles of different types propagating with velocities  $\pm c$ .

In this more general, three-dimensional, situation the proposed identification is as follows:

- the discrete distribution functions  $f_i$  are the analogue of the Dirac quadrispinor

components  $\psi_j$ ;

- the discrete speeds  $\mathbf{c}_i$  are the analogue of the streaming matrices  $\mathbf{L} \equiv c(-\alpha^x, \beta, -\alpha^z)$ ;
- the scattering matrix  $A$  is the analogue of the mass matrix  $-i\omega_c\alpha^y$ , or, more generally, of the mass matrix  $M$  defined in Eq. (1.11).

Let us examine these positions in detail taking into account the distinct physical nature of LBE and Dirac equation, there are indeed some fundamental differences:

1. the discrete distribution functions  $f_i$  are  $b$  real-valued variables, with  $b$  being a sensitive function of dimensionality, whereas  $\psi_j$  are always four complex-valued wave functions in any spatial dimension;
2. the scattering matrix  $A_{ij}$  is symmetric whereas  $M_{ij}$  is skew-symmetric;
3. the LBE streaming operators is diagonal along all the spatial directions, while the Dirac streaming operator is not, because it is not possible to simultaneously diagonalize the three matrices  $\mathbf{L} = c(-\alpha^x, \beta, -\alpha^z)$ .

From point (1) above, the quantity  $\rho_j = (\psi_j^*)\psi_j$  (instead of  $\psi_j$ ) represents the probability density of finding a particle along link  $j$ -th. In this respect, point (2) is the necessary condition in order for the probability density  $\rho = \sum_j \rho_j$  to be locally conserved. Moreover, point (1) clearly requires an extension of LBE to complex-valued distribution functions. However, the major drawback coming from point (1) is the dimensionality mismatch between LBE and Dirac equation. Indeed, the Dirac quadrispinor has always four components, in any spatial dimension, whereas the array of the discrete distribution functions is composed of  $b$  elements with  $b$  being a parameter whose actual value is a function of the spatial dimension.

Point (3) above represents the main problem of this proposed identification, there is a structural mismatch between LBE and Dirac equation conceiving the streaming operator. While the streaming operator of LBE is always diagonal there is no way the three Dirac matrices can be simultaneously diagonalized. Both the dimensionality and structural mismatch are basically due to the quantum nature of the spin variable. In quantum mechanics, spin has dimensions of angular momentum ( $\mathbf{r} \times \mathbf{p}$ ) and the spin quantization is a true physical effect due to the impossibility of measuring the speed and position at a time. In particular, only one component of the spin is measurable and, once it is fixed, it takes only two values  $\pm 1$  (here we restrict to particle with spin  $1/2$ ).

To achieve a full correspondence between LBE and Dirac equation, one should be able to [138]:

1. simultaneously diagonalize the three matrices  $\mathbf{L} = (-\alpha^x, \beta, -\alpha^z)$ ;
2. fix  $b$  to the value of 4;

in order to solve the structural and dimensionality mismatches.

As previously mentioned, point (1) is forbidden, it would be equivalent to state that the spin is a common three-dimensional vector. Point (2) seems also hard to be accomplished, because it is incompatible with the interpretation of  $\psi_j$  as complex particle distributions propagating along the links of a three-dimensional lattice. In fact, by symmetry, at least  $2D$  propagating directions are needed, that is two opposite directions along each coordinate axis.

In conclusion, despite the intriguing qualitative analogies between LBE and Dirac equations, a deeper analysis shows a quantitative conflict which, at a first sight, seems difficult to be overcome. However, a way out of both of these difficulties can be found and it is based on the idea that even though simultaneous diagonalization of the streaming matrices is not possible, they can be diagonalized separately in a sequence [138].

In Ref. [138], it is suggested to use an operator splitting technique and hence consider three equivalent formulations of the same equation, each having a diagonal streaming operator along  $x$ ,  $y$  and  $z$ , respectively. The key point is that we do not work with the same representation of the Dirac equations during the three separate streaming steps, instead we perform each one-dimensional partial streaming in the representation where the corresponding streaming matrix is diagonal. This is possible, because we diagonalize only one streaming matrix at a time, never all of them together.

In practice, the classical stream-collide structure of the Boltzmann equation is augmented with a “rotation” step, designed in such a way as to secure alignment between momentum and spin along each direction of propagation.

In particular, let us assume we start from the representation where the spin is aligned along  $z$ , this means we consider the one-dimensional Dirac equation under a proper unitary transformation  $Z$  such that the streaming matrix along  $z$  is diagonal. In this one-dimensional version, a full correspondence between LBE and Dirac equation is achieved, thus collision and streaming along  $z$  can be performed. Next, we need to move along  $y$ , then the system is “rotated”, i. e. a unitary transformation matrix  $Y$  is applied to the Dirac equation so that the  $y$ -streaming matrix is diagonalized and the collision and streaming steps are performed along  $y$  for the transformed quadrispinor  $\psi_y = Y\psi$ . Finally, the system is rotated again, by means of a unitary transformation matrix  $X$ , so that the  $x$ -streaming matrix is diagonal and the collision and streaming steps are performed once again. After

the three sequential applications of the one dimensional stream-collide operator, the resulting quadrispinor is transformed back in order to obtain the original wave function only displaced at  $(z + \Delta z, y + \Delta y, x + \Delta x, t + \Delta t)$ .

In Ref. [138], this procedure is outlined but it is not numerically implemented and verified, moreover the collision matrix  $Q$  of each one of the three steps is assumed to be exactly the one dimensional collision matrix (see Eq. (1.36) below). As we shall clarify in Chapter 2, which is entirely devoted to the multi-dimensional extension of the model, this is not correct and leads to a scheme that does not solve the Schrödinger equation in the adiabatic limit.

From this discussion, it is evident that the model is built upon the one-dimensional version of Eq. (1.32), hence, in the following sections, we introduce the one-dimensional qLB scheme and revise the numerical results reported in Ref. [133] in order to validate the model.

## 1.6 One-dimensional quantum lattice Boltzmann model

Let us rewrite the one-dimensional Dirac equation in Majorana form for the complex quadrispinor  $\psi = (u_1, u_2, d_1, d_2)^T$ , this reads:

$$\begin{aligned}\partial_t u_{1,2} + c\partial_z u_{1,2} &= \omega_c d_{2,1}, \\ \partial_t d_{1,2} - c\partial_z d_{1,2} &= -\omega_c u_{2,1}.\end{aligned}\tag{1.33}$$

As observed in Ref. [138], this is a Boltzmann equation for a couple of complex bispinor  $u_{1,2}$  and  $d_{1,2}$ . The propagation step consists on streaming  $u_{1,2}$  and  $d_{1,2}$  along  $z$  with speeds  $\pm c$ , respectively, while the collision is performed according to the scattering matrix of the right hand side of (1.33). The quantum lattice Boltzmann model is obtained by discretizing Eq. (1.33) and an important difference with the LBE for classical fluids is to be pointed out.

In fact, an explicit time-marching along the trajectories would deliver the exact analogue of the LBE for classical fluids [18, 89, 135]:

$$\begin{aligned}u_{1,2}(z + \Delta z, t + \Delta t) - u_{1,2}(z, t) &= \Delta t \omega_c d_{2,1}(z, t), \\ d_{1,2}(z - \Delta z, t + \Delta t) - d_{1,2}(z, t) &= -\Delta t \omega_c u_{2,1}(z, t),\end{aligned}$$

where  $\Delta z = c\Delta t$  according to the light-cone discretization rule. However, such an explicit light-cone marching is unconditionally unstable for any size of  $\Delta t$  [135] and the resulting scheme is not norm-preserving.

This is due to the fact that the collision matrix

$$S = \begin{pmatrix} 1 & 0 & 0 & \tilde{m} \\ 0 & 1 & \tilde{m} & 0 \\ 0 & -\tilde{m} & 1 & 0 \\ -\tilde{m} & 0 & 0 & 1 \end{pmatrix},$$

where  $\tilde{m} = \omega_c \Delta t$ , is not unitary. In particular, this implies that

$$\|S\|_2 = \left( \max_k |\lambda_k| \right) = [1 + (\omega_c \Delta t)^2]^{1/2} > 1,$$

where  $\lambda_k$ , for  $k = 1, \dots, 4$ , denotes the eigenvalues of the scattering matrix  $S$ . Hence the post-collision quadrispinor,  $\psi'(z, t + \Delta t)$ , which is computed as

$$\psi'(z, t + \Delta t) = S\psi(z, t),$$

satisfies  $\|\psi'\|_2 = \|S\|_2 \|\psi\|_2 > \|\psi\|_2$ , thus driving an instability into the system and also failing to satisfy local norm conservation.

A simple and effective way out is to discretize the right hand side of Eq. (1.33) computing an implicit (Crank-Nicolson) average between the term at time  $t$  and position  $z$  and the same term at time  $t + \Delta t$  and position  $z \pm \Delta z$  for  $u_{1,2}$  and  $d_{1,2}$ , respectively. The left hand side is discretized integrating along the characteristics (light-cone rule). The resulting (implicit) scheme reads as follows:

$$\begin{aligned} \hat{u}_{1,2} - u_{1,2} &= \frac{\tilde{m}}{2}(d_{2,1} + \hat{d}_{2,1}), \\ \hat{d}_{1,2} - d_{1,2} &= -\frac{\tilde{m}}{2}(u_{2,1} + \hat{u}_{2,1}), \end{aligned} \tag{1.34}$$

where  $\hat{u}_{1,2} = u_{1,2}(z + \Delta z, t + \Delta t)$ ,  $\hat{d}_{1,2} = d_{1,2}(z - \Delta z, t + \Delta t)$ ,  $u_{1,2} = u(z, t)$ ,  $d_{1,2} = d(z, t)$  and  $\tilde{m} = \omega_c \Delta t$  is the dimensionless Compton frequency.

The scheme of Eq. (1.34) is implicit, but it can be solved algebraically for  $\hat{u}_{1,2}$  and  $\hat{d}_{1,2}$  thus yielding the following explicit form

$$\begin{aligned} \hat{u}_{1,2} &= au_{1,2} + bd_{2,1}, \\ \hat{d}_{1,2} &= ad_{1,2} - bu_{2,1}, \end{aligned} \tag{1.35}$$

where

$$a = \frac{1 - \tilde{m}^2/4}{1 + \tilde{m}^2/4}, \quad b = \frac{\tilde{m}}{1 + \tilde{m}^2/4}.$$

We note that, in analogy with the classical lattice Boltzmann model for fluid dynamics, the scheme of Eq. (1.34) can be derived from Eq. (1.33) by integrating along the characteristics of  $u$  and  $d$  respectively and approximating the right hand

side by means of the trapezium rule. Moreover, since the qLB operator is linear, while the classical LB operator is not, the resulting scheme of Eq. (1.34) can be directly solved for  $\hat{u}_{1,2}$  and  $\hat{d}_{1,2}$  (as we see in Eq. (1.35)). This is in contrast with the classical case where, to avoid implicitness of the scheme, the equilibrium distribution function is introduced, which is nonlinearly related to the original one [64]. Such nonlinearity stems from the quadratic dependence of the classical local equilibrium on the fluid speed, as required to describe nonlinear hydrodynamic interactions.

The scheme of Eq. (1.35) is a lattice Boltzmann equation in matrix form [68], where the collision step is performed by applying the unitary collision matrix

$$Q = \begin{pmatrix} a & 0 & 0 & b \\ 0 & a & b & 0 \\ 0 & -b & a & 0 \\ -b & 0 & 0 & a \end{pmatrix}, \quad (1.36)$$

to the quadrispinor  $\psi = (u_1, u_2, d_1, d_2)^T$  and the streaming step consists on propagating  $u_{1,2}$  forwards and  $d_{1,2}$  backwards according to the light-cone rule,  $\Delta z = c\Delta t$ . Note that stability is secured by the unitarity of the collision matrix  $Q$  for any value of  $\Delta t$  such that  $\Delta z = c\Delta t$ . This contrasts with standard explicit schemes, whose numerical stability is constrained by CFL-like inequalities of the form  $\Delta t < \frac{2m}{\hbar} \Delta z^2$ .

In particular, the stability of the scheme can be proved by setting

$$\mathbf{v}_n := (u_1(z + n\Delta z, t + n\Delta t), u_2(z + n\Delta z, t + n\Delta t), \\ d_1(z - n\Delta z, t + n\Delta t), d_2(z - n\Delta z, t + n\Delta t))^T, \quad n = 0, 1, \dots,$$

and writing the collision matrix  $Q$  as follows

$$Q = \begin{pmatrix} \cos \vartheta & 0 & 0 & \sin \vartheta \\ 0 & \cos \vartheta & \sin \vartheta & 0 \\ 0 & -\sin \vartheta & \cos \vartheta & 0 \\ -\sin \vartheta & 0 & 0 & \cos \vartheta \end{pmatrix},$$

where

$$\cos \vartheta := \frac{1 - \tilde{m}^2/4}{1 + \tilde{m}^2/4}.$$

With these positions, the basic scheme obtained solving (hence, making explicit) the modified Crank-Nicolson scheme, reads

$$\mathbf{v}_1 = Q\mathbf{v}_0,$$

and iterating,

$$\mathbf{v}_{n+1} = Q\mathbf{v}_n = \dots = Q^{n+1}\mathbf{v}_0.$$

Therefore, a direct computation of the entries of  $\mathbf{v}_{n+1}$  is only affected by the rounding errors in evaluating the matrix-vector product  $Q^{n+1}\mathbf{v}_0$ , being

$$Q^{n+1} = \begin{pmatrix} \cos((n+1)\vartheta) & 0 & 0 & \sin((n+1)\vartheta) \\ 0 & \cos((n+1)\vartheta) & \sin((n+1)\vartheta) & 0 \\ 0 & -\sin((n+1)\vartheta) & \cos((n+1)\vartheta) & 0 \\ -\sin((n+1)\vartheta) & 0 & 0 & \cos((n+1)\vartheta) \end{pmatrix},$$

which is not worse than computing  $U\mathbf{v}_0$ . Therefore,  $\mathbf{v}_n$  is computed in a stable way, for every  $n$ .

Moreover, the unitarity of the collision matrix  $Q$  also yields another important property, namely norm-preservation. In particular, the 2-norm of  $Q$  satisfies

$$\|Q\|_2 = \left( \max_k |\lambda_k| \right) = (|a|^2 + |b|^2)^{1/2} = 1,$$

thus, the norm is preserved by the scheme on each node.

Finally, we observe that the qLB scheme produces the correct dispersion relation up to second order in the time step  $\Delta t$  [135]. Indeed, by performing a standard Fourier analysis of Eq. (1.34), we insert

$$\begin{aligned} u(z, t) &\sim U e^{i(kz - \omega t)}, \\ d(z, t) &\sim D e^{i(kz - \omega t)}, \end{aligned}$$

into Eq. (1.34), we obtain (since the dynamics of the pairs  $(u_1, d_2)$  and  $(u_2, d_1)$  is equivalent, indices are dropped for simplicity)

$$\begin{cases} U e^{i(k\Delta z - \omega\Delta t)} = U + \frac{\tilde{m}}{2} D (1 + e^{-i(k\Delta z + \omega\Delta t)}), \\ D e^{-i(k\Delta z + \omega\Delta t)} = D - \frac{\tilde{m}}{2} U (1 + e^{i(k\Delta z - \omega\Delta t)}), \end{cases}$$

this is an homogeneous system in  $U$  and  $D$ , thus admitting non-trivial solutions only when the determinant is null. By requiring that the determinant is equal to zero we derive the following dispersion relation

$$\cos(\omega\Delta t) = \left( \frac{1 - \tilde{m}^2/4}{1 + \tilde{m}^2/4} \right) \cos(k\Delta z).$$

It is readily checked that a second order expansion of the cosines of the above dispersion relation, in the limit  $\Delta t \rightarrow 0$ , yields the well known continuum dispersion relation for relativistic bosons

$$\omega^2 = k^2 c^2 + \omega_c^2,$$

up to terms of order  $\Delta t^3$ .

Large time steps,  $\tilde{m} = \omega_c \Delta t > 1$ , lead to unphysical results as is to be expected since the Compton frequency  $\omega_c$  is no longer resolved. Indeed, even though the qLB method offers stability for any value of  $\Delta t$  provided that  $\Delta z = c\Delta t$ , its accuracy is subjected to the condition

$$\omega_c \Delta t = \frac{\Delta z}{\lambda_B} \leq 1,$$

where  $\lambda_B = c/\omega_c$  is the de Broglie wavelength of the particle.

Since the time step scales linearly with the mesh spacing, the grid resolution can be increased without suffering the time step collapse typical of classical explicit schemes where the CFL stability condition holds. On the other hand, a lack of adiabaticity could occur for  $\omega_c \Delta t \ll 1$ , and this effect must be carefully watched, while decreasing the lattice spacing, in order to preserve the validity of qLB.

Summarizing, the qLB is an explicit, norm-preserving scheme which is stable for any value of  $\Delta t = \Delta z/c$ . Moreover, since most of the computational work is placed upon the collision step, which is completely local, no communication is required between neighbors during this phase, whence its outstanding amenability to parallel computing [138].

### 1.6.1 Adding a potential to the qLB model

Interactions with an external or self-consistent fields are readily included by a minor extension of the “collision operator”. In particular, we consider the one-dimensional Dirac equation with an electrostatic potential interaction, this reads

$$\begin{aligned} \partial_t u_{1,2} + c \partial_z u_{1,2} &= \omega_c d_{2,1} + i g u_{1,2}, \\ \partial_t d_{1,2} - c \partial_z d_{1,2} &= -\omega_c u_{2,1} + i g d_{1,2}, \end{aligned} \tag{1.37}$$

where  $g = qV/\hbar$  is the space dependent frequency coupling to the potential  $V$  and  $q$  is the particle electric charge. Self-consistent potentials, such as those arising in connection with the nonlinear Schrödinger equation, are easily accommodated by making  $g$  a function of the density  $|\phi^+|^2 + |\phi^-|^2$  (see Eq. (1.23)).

We note that, in the presence of an interaction potential, non-relativistic motion is still reproduced by the model in the adiabatic (low-frequency) limit

$$|\omega - \omega_c| \ll |\omega_c + g|,$$

where  $\omega$  is the typical frequency or energy of the solution,  $\psi$ , so that one can estimate  $|\partial_t \psi| \sim \omega |\psi|$ , but with the additional constraint of “small” potential



interaction

$$|g| \ll \omega_c. \quad (1.38)$$

Indeed, by defining as above the symmetric and antisymmetric modes

$$\phi_{1,2}^{\pm} = \frac{1}{\sqrt{2}} \exp(i\omega_c t) (u_{1,2} \pm i d_{2,1}),$$

from Eq. (1.37), it is easy to check that the following equations are satisfied

$$\begin{aligned} \partial_t \phi_{1,2}^+ + c \partial_z \phi_{1,2}^- &= i g \phi_{1,2}^+, \\ \partial_t \phi_{1,2}^- + c \partial_z \phi_{1,2}^+ &= 2i \omega_c \phi_{1,2}^- + i g \phi_{1,2}^-. \end{aligned} \quad (1.39)$$

From Eq. (1.39), after adiabatic elimination of the fast antisymmetric modes

$$|\partial_t \phi_{1,2}^-| \ll |2\omega_c + g| |\phi_{1,2}^-|,$$

we obtain

$$i\hbar \partial_t \phi_{1,2}^+ = -\frac{\hbar^2 c^2}{2\omega_c} \partial_z \left( \frac{2\omega_c}{2\omega_c + g} \partial_z \phi_{1,2}^+ \right) - qV \phi_{1,2}^+ \approx -\frac{\hbar^2}{2m} \partial_z^2 \phi_{1,2}^+ - qV \phi_{1,2}^+, \quad (1.40)$$

where the last approximation in Eq. (1.40) is valid in the small potential interaction limit given by Eq. (1.38).

The qLB scheme is obtained by integrating Eq. (1.37) along the characteristics of  $u_{1,2}$  and  $d_{1,2}$  respectively and approximating the right hand side integral by using the trapezoidal rule. Assuming  $\Delta z = c\Delta t$ , the following scheme is obtained

$$\begin{aligned} \hat{u}_{1,2} - u_{1,2} &= \frac{\tilde{m}}{2} (d_{2,1} + \hat{d}_{2,1}) + \frac{i\tilde{g}}{2} (u_{1,2} + \hat{u}_{1,2}), \\ \hat{d}_{1,2} - d_{1,2} &= -\frac{\tilde{m}}{2} (u_{2,1} + \hat{u}_{2,1}) + \frac{i\tilde{g}}{2} (d_{1,2} + \hat{d}_{1,2}), \end{aligned} \quad (1.41)$$

where  $\hat{u}_{1,2} = u_{1,2}(z + \Delta z, t + \Delta t)$ ,  $\hat{d}_{1,2} = d_{1,2}(z - \Delta z, t + \Delta t)$ ,  $u_{1,2} = u_{1,2}(z, t)$ ,  $d_{1,2} = d_{1,2}(z, t)$  and  $\tilde{m} = \omega_c \Delta t$ ,  $\tilde{g} = g \Delta t$ . The linear system of Eq. (1.41) is algebraically solved for  $\hat{u}_{1,2}$  and  $\hat{d}_{1,2}$  and yields the explicit scheme:

$$\begin{aligned} \hat{u}_{1,2} &= a_g u_{1,2} + b_g d_{2,1}, \\ \hat{d}_{1,2} &= a_g d_{1,2} - b_g u_{2,1}, \end{aligned} \quad (1.42)$$

where

$$a_g = \frac{1 - \Omega/4}{1 + \Omega/4 - i\tilde{g}}, \quad b_g = \frac{\tilde{m}}{1 + \Omega/4 - i\tilde{g}},$$

with  $\Omega = \tilde{m}^2 - \tilde{g}^2$ .

## 1.7 Numerical results for the one-dimensional qLB scheme

The one-dimensional qLB scheme has been numerically validated in a series of calculations for which analytical results are known [133]. In particular, in Ref. [133], the qLB has been tested by simulating

- free particle propagation;
- harmonic oscillator;
- scattering from a rectangular barrier.

Here, we briefly revise these results in order to show the viability of the scheme in its one-dimensional formulation. In this section, in order to have reasonable numerical values for the parameter of the scheme, we work in atomic units ( $c = \hbar = 1$  and  $q = -1$ ) and we normalize space time in units of lattice spacings (in particular, we set  $\Delta z = \Delta t = 1$ ). Note that, with these assumptions, the Compton frequency  $\omega_c = mc^2/\hbar$  becomes equal to  $m$ , hence the parameter  $\tilde{m} = \omega_c \Delta t$  is given by  $\tilde{m} = m \Delta t$ .

### 1.7.1 Free particle propagation

The motion of a quantum particle in the absence of any external force is characterized by the well known phenomenon of loss of coherence, i. e. the spatial extent of the wave function increases in time so that the wave packet becomes less and less localized.

This behavior can be analyzed for the so-called “minimum uncertainty wave packet” [126], since, in this case, analytical solutions are available. A minimum uncertainty wave packet is a wave packet for which minimum uncertainty in both position  $z$  and momentum  $p$  is attained. In one dimension, this reads

$$\psi_0(z) = (2\pi\Delta_0^2)^{-1/4} \exp(-imv_z z) \exp\left(-\frac{(z-z_0)^2}{4\Delta_0^2}\right). \quad (1.43)$$

This is a Gaussian wave packet centered about  $z_0$ , with initial width  $\Delta_0$  and propagating along  $z$  with speed  $v_z$ . In order to set this initial condition on the model, we set

$$\begin{aligned} u_1 &= u_2 = \frac{1}{2}\psi_0, \\ d_1 &= d_2 = -\frac{i}{2}\psi_0, \end{aligned}$$

so that  $\phi_{1,2}^+ = \psi_0/\sqrt{2}$  and  $|\psi^+|^2 = |\phi_1^+|^2 + |\phi_2^+|^2 = |\psi_0|^2$ .

With the initial condition given in Eq. (1.43), the analytical solution of the

Schrödinger equation for a freely propagating particle is given by (recall that we are using atomic units:  $c = \hbar = 1$ ):

$$\begin{aligned} \psi_{an}(z, t) = (2\pi)^{-1/4} \left( \Delta_0 + \frac{it}{2m\Delta_0} \right)^{-1/2} \exp \left( -\frac{(z - z_0 - v_z t)^2}{4\Delta_0^2 + (2it/m)} \right) \\ \times \exp(imv_z z) \exp \left( -\frac{imv_z^2 t}{2} \right). \end{aligned} \quad (1.44)$$

Based on this solution, the mean position  $Z(t)$  and the mean spread  $\Delta_z(t)$  defined as

$$\begin{aligned} Z(t) &= \int z |\psi(z, t)|^2 dz, \\ \Delta_z(t) &= \int (z - Z(t))^2 |\psi(z, t)|^2 dz, \end{aligned}$$

evolve according to the equations

$$\begin{aligned} Z(t) &= z_0 + v_z t, \\ \Delta_z(t) &= \left( \Delta_0^2 + \frac{t^2}{4m\Delta_0^2} \right)^{1/2}. \end{aligned} \quad (1.45)$$

In Fig. 1.1, we show  $Z(t) - z_0$  and  $\Delta_z(t)$  as functions of time for the following choice of parameters:  $m = 0.2$ ,  $\Delta_0 = 50$ ,  $v_z = 0.1$  and  $z_0 = 1024$  on a lattice of size  $N_z = 2048$  nodal points. In particular,  $Z(t)$  and  $\Delta_z(t)$  are computed on  $|\phi^+|^2$  and are compared with the analytical curves of (1.45).

In Fig. 1.2, we show the probability distribution function  $|\phi^+|^2$  as a function of the space for three different times. These results show a good agreement between the analytical behavior and the numerical solution, thus proving that the model correctly describes non-relativistic Schrödinger dynamics in the adiabatic limit. However, as observed in Ref. [133], the accuracy of the results is affected by the value of  $m$  (since  $\tilde{m} = m\Delta t$  must be lower than one but not too small for the adiabaticity condition to hold) and also by the choice of  $\Delta_0$ . In particular,  $\Delta_0$  must be well resolved (i. e. discretized with a large number of grid points, typically above 16 nodes) so as to prevent high wave number components of the wave packet from violating the adiabaticity condition.

### 1.7.2 Harmonic oscillator

As a second example, we consider a one-dimensional harmonic oscillator that is a quantum particle trapped within a parabolic potential centered about the midpoint of the computational domain. Hence, the external potential reads as follows:

$$V(z) = \frac{1}{2} m \omega_0^2 (z - z_0)^2. \quad (1.46)$$

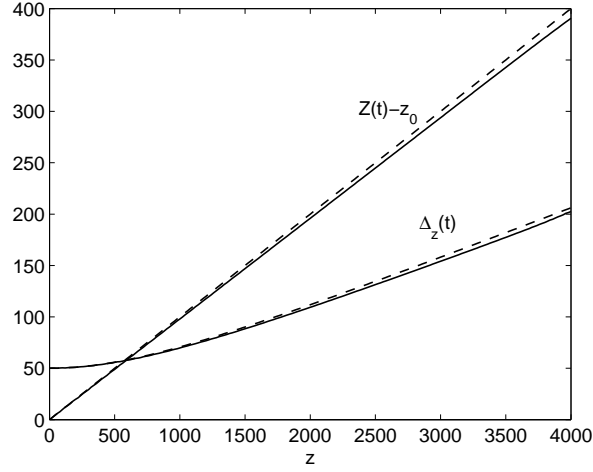


Figure 1.1: Comparison between  $Z(t)$  and  $\Delta_z(t)$  and the expected curves given by Eq. (1.45) for the following setting:  $N_z = 2048$ ,  $v_z = 0.1$ ,  $\Delta_0 = 50$ , and  $m = 0.2$ . Solid lines represent  $Z(t)$  and  $\Delta_z(t)$  given by the model while dashed lines are the expected curves. Time and space are expressed in lattice units.

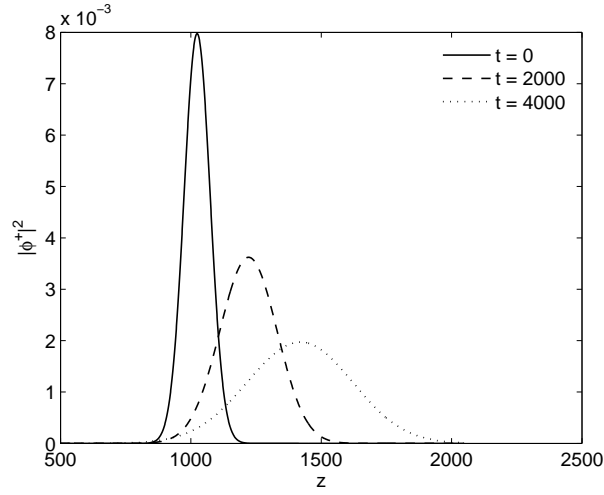


Figure 1.2: Probability distribution function  $|\phi^+|^2$  as a function of the space for three different times. Parameters are set as follows:  $N_z = 2048$ ,  $v_z = 0.1$ ,  $\Delta_0 = 50$ , and  $m = 0.2$ . Time and space are expressed in lattice units.

The initial condition is given again by the minimum uncertainty wave packet of Eq. (1.43). The analytical solution of the Schrödinger equation with the external potential given in Eq. (1.46) is known and the mean position,  $Z(t)$ , and momentum,  $P(t)$ , obey the classical equations of motion of the harmonic oscillator

$$\dot{Z}(t) = P(t)/m, \quad \ddot{Z}(t) + \omega_0^2 Z(t) = 0,$$

and this yields

$$Z(t) = z_0 + \frac{v_z}{\omega_0} \sin(\omega_0 t).$$

Moreover, by setting  $\Delta_0$  such that the relation

$$\omega_0 = \frac{1}{2m\Delta_0^2},$$

is fulfilled, then the initial wave packet spreading is preserved all along the evolution.

We want to check the ability of the model to preserve  $\Delta_0$  for different parameter settings.

In Tab. 1.1, the numerical results are reported, the spreading  $\Delta_z$  is the wave function variance averaged over ten periods,  $T = 2\pi/\omega_0$ , of the harmonic oscillator. In those simulations we set  $v_z = 0$ . From the table, we observe that good agreement

Table 1.1: Averaged variances of the packet along  $z$  for different setting of the parameters  $N_z$ ,  $m$  and  $\omega_0$ . Here  $v_z = 0$ .

$N_z$	$\omega_0$	$m$	$\Delta_z$	Expected $\Delta$
1024	$8/64^2$	$1/16$	$64.08 \pm 1.23$	64
1024	$2/32^2$	$1/4$	$32.07 \pm 0.32$	32
512	$4/32^2$	$1/8$	$32.05 \pm 0.60$	32
512	$2/32^2$	$1/4$	$31.99 \pm 0.16$	32
256	$2/16^2$	$1/4$	$16.04 \pm 0.32$	16
256	$1/16^2$	$1/2$	$15.99 \pm 0.09$	16

is obtained on smaller grids.

An example of the solution for  $v_z = 0.1$  and  $N_z = 512$ ,  $m = 1/4$ ,  $\omega_0 = 2/32^2$ ,  $\Delta_0 = 32$  at times 0,  $1/4T$  and  $3/4T$  is shown in Fig. 1.3

### 1.7.3 Scattering from a rectangular barrier

As a final test, we consider the scattering of a wave packet by a rectangular repulsive potential of the form

$$V(z) = \begin{cases} V_0 & z_1 < z < z_2, \\ 0 & \text{otherwise.} \end{cases} \quad (1.47)$$

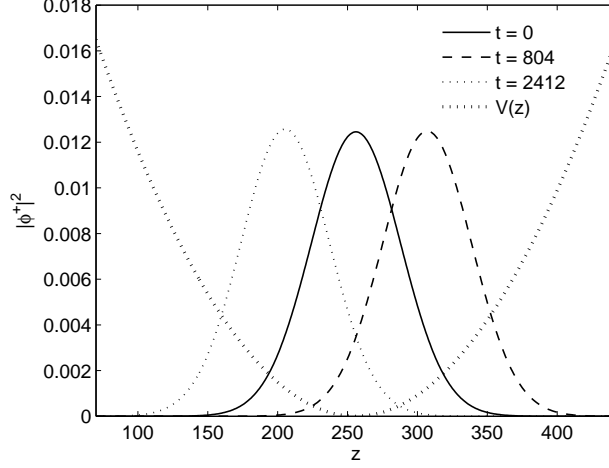


Figure 1.3: Wave function density  $|\phi^+|^2$  for the harmonic oscillator potential of Eq. (1.46) at times  $t = 0$ ,  $t = T/4$  and  $t = 3/4T$ . Parameters are set as follows:  $N_z = 512$ ,  $v_z = 0.1$ ,  $m = 1/4$ ,  $\omega_0 = 2/32^2$ ,  $\Delta_0 = 32$ . Time and space are expressed in lattice units.

A typical manifestation of quantal effects is a finite probability for the quantum particle to go through the potential barrier even if its energy  $E$  is lower than the potential energy  $V_0$  (quantum tunneling) [134].

Under tunneling conditions, an incident plane wave  $\psi_{in} = Ae^{ik_{in}z}$  at  $z = z_1$  develops transmitted and reflected components of the form

$$\psi(z) = T \exp(ik_t z) + R \exp(-ik_r z),$$

where the reflected and transmitted wave numbers are given by

$$k_t = \sqrt{2m(E - V_0)}, \quad k_r = \sqrt{2mE},$$

respectively.

Clearly, where the potential exceeds the total energy  $E$ , the wave number becomes imaginary, and the transmitted wave undergoes an exponential decay.

The presence of both oscillating and decaying behaviors is well visible from Fig. 1.4, which illustrates the dynamics of a minimum uncertainty wave packet colliding with the potential barrier. The main numerical parameters are set as in Ref. [133]:

$$N_z = 16384, \quad m = 0.2, \quad v_z = 0.1, \quad V_0 = 0.002, \quad \Delta_0 = 128.$$

From the figure, we can easily detect the bounce-back of the wave function and its

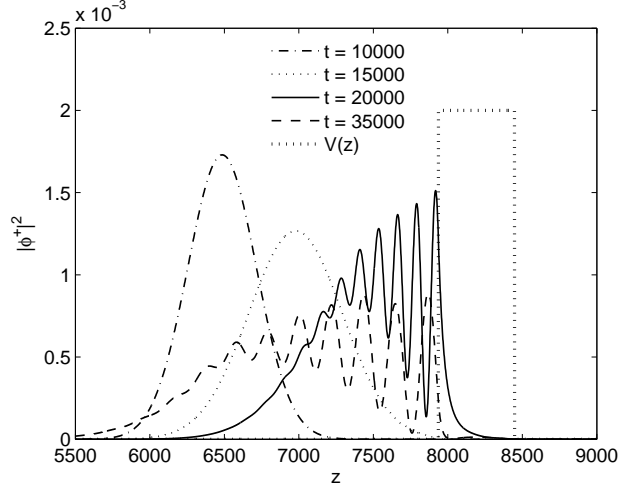


Figure 1.4: Wave function density  $|\phi^+|^2$  for scattering from a potential barrier of Eq. (1.47) at different times. Parameters are set as follows:  $N_z = 16384$ ,  $v_z = 0.1$ ,  $m = 0.2$ ,  $V_0 = 0.002$ ,  $\Delta_0 = 128$ . Time and space are expressed in lattice units.

exponential decaying penetration into the classically forbidden region  $z_1 < z < z_2$ .

These tests demonstrate the viability of the qLB in one dimension. However, the extension to multi-spatial dimensions following the idea suggested in Ref. [138] and presented in Sec. 1.5 was not validated by actual numerical simulations. This is indeed one of the major achievements of this work and it is presented in full detail in the next chapter and in Ref. [105].





## Chapter 2

# The multi-dimensional quantum lattice Boltzmann model

As discussed in the previous chapter, the earliest LB model for quantum motion built upon a formal analogy between the Dirac equation and a Boltzmann equation for a complex distribution function [138, 133, 135]. It was then shown that the non-relativistic Schrödinger equation derives from the complex Boltzmann equation under the same adiabatic assumptions (in imaginary time) which take the Boltzmann equation for classical molecules into the Navier-Stokes equations of continuum fluid mechanics. Based on this analogy, a quantum lattice Boltzmann scheme was formulated, in which the discrete speeds are identified with the four-spinor components of the Dirac's wave function. For 1+1-dimensional problems (evolutionary problems in one spatial dimension) this identification is fairly natural, since the spin can always be aligned with momentum (unit helicity). In higher dimensions, however, such helicity=1 representation is no longer viable because the spin does not transform like ordinary vectors and consequently the Dirac propagation matrices cannot be diagonalized simultaneously. To cope with this problem, the classical stream-collide structure of the Boltzmann equation was augmented with a “rotation” step, designed in such a way as to secure alignment between momentum and spin degrees of freedom along each direction of propagation (operator splitting). However, such multi-dimensional version of the quantum lattice Boltzmann (qLB) scheme was not validated by actual numerical simulations in Ref. [138].

In this chapter, which is an extended version of the paper in Ref. [105], we present the first such validation for the case of a free particle and the harmonic

oscillator in both two and three-dimensions.

Moreover, we revise the theoretical procedure proposed in Ref. [138] for the extension to the multi-dimensional case and discuss its actual implementation. In particular, we point out a difference with respect to the algorithm described in Ref. [138] which would lead to a scheme that does not solve the Schrödinger equation in the adiabatic limit.

Our numerical results show a satisfactory agreement with the analytical solutions, thereby proving the viability of the three-step, stream-collide-rotate, theoretical structure of the multi-dimensional qLB scheme. However, most of the numerical results presented here refer to the two-dimensional scheme. This is due to the fact that the qLB scheme is computationally expensive in terms of storage requirements, since the distribution functions are complex valued. As a result, in three dimensions, on a single PC, only small lattices (not larger than  $100 \times 100 \times 100$  nodal points) are allowed. A detailed analysis of the numerical results for the three-dimensional scheme could be performed by implementing a parallel version of the algorithm, a study which is indeed under development at the present time.

## 2.1 Extension to two and three dimensions: a survey

In this section, we work out the details of multidimensional qLB scheme. For the sake of simplicity, we restrict our discussion to the free particle case ( $V = 0$ ), however the inclusion of a potential is straightforward.

According to the idea presented in [138], we start from the representation of the Dirac equation in which all the spin matrices are real. For a free particle of mass  $m$  in three dimensions, this reads:

$$\partial_t \psi + c(-\alpha^x \partial_x + \beta \partial_y - \alpha^z \partial_z) \psi = -i \frac{mc^2}{\hbar} \alpha^y \psi \equiv -i\omega_c \alpha^y \psi, \quad (2.1)$$

where  $\alpha^a$  for  $a = x, y, z$  and  $\beta$  are the standard  $4 \times 4$  Dirac matrices (see Eq. (1.7)) and  $\psi$  is the Dirac quadrispinor. In [138], a formal parallel between the discrete speeds of LBE and the discrete spin states of the Dirac quadrispinor is proposed in order to solve Eq. (2.1) by means of a kinetic equation (see Sec. 1.5).

As mentioned in the previous chapter, the main problem with this idea is that, in order to achieve a full correspondence between LBE and Dirac equation, the matrices  $\mathbf{L} = (-\alpha^x, \beta, -\alpha^z)$  should be simultaneously diagonalized, which is clearly forbidden. However, even though simultaneous diagonalization of the three matrices is impossible, we can diagonalize each of them separately in a sequence. This means we need to find two  $4 \times 4$  transformation matrices  $Y$  and  $X$  such that  $\tilde{L}^y = Y^{-1} L^y Y$  and  $\tilde{L}^x = X^{-1} L^x X$  are diagonal. We have then three equivalent formulations of the same equation, each featuring a diagonal streaming operator

along  $x$ ,  $y$  and  $z$  respectively. Hence, we split the operator and use the one-dimensional LBE three times in sequence.

In practice, this means that collision and streaming are first performed along one direction, then the system is “rotated” using a transformation matrix and collision and streaming are performed again along a second direction. Finally the same procedure is applied to the third direction.

To summarize, the three-step algorithm reads as follows:

1. • Collision along  $z$ :

$$\psi'(P, t + \Delta t) = \hat{Q}\psi(P, t),$$

where  $P = (x, y, z)$  and  $\hat{Q}$  is the collision matrix (see Eq. (2.7) below for details on the definition of  $\hat{Q}$  in the two dimensional case).

- Streaming along  $z$ :

$$\psi(P_z, t + \Delta t) = S_z\psi'(P, t + \Delta t),$$

where  $P_z = P + \hat{k}\Delta z$  and  $S_z$  is the streaming operator along  $z$ .

2. • Rotation of the system:

$$\psi_y = Y\psi, \quad \hat{Q}^y = Y^{-1}\hat{Q}Y.$$

- Collision along  $y$ :

$$\psi'_y(P_z, t + \Delta t) = \hat{Q}^y\psi_y(P_z, t + \Delta t).$$

- Streaming along  $y$ :

$$\psi_y(P_{yz}, t + \Delta t) = S_y\psi'_y(P_z, t + \Delta t),$$

where  $P_{yz} = P + \hat{j}\Delta y + \hat{k}\Delta z$  and  $S_y$  is the streaming operator along  $y$ .

3. • Rotation of the system:

$$\psi_{xy} = X\psi_y, \quad \hat{Q}^{xy} = X^{-1}\hat{Q}^yX.$$

- Collision along  $x$ :

$$\psi'_{xy}(P_{yz}, t + \Delta t) = \hat{Q}^{xy}\psi_{xy}(P_{yz}, t + \Delta t).$$

- Streaming along  $x$ :

$$\psi_{xy}(P_{xyz}, t + \Delta t) = S_x\psi'_{xy}(P_{yz}, t + \Delta t),$$

where  $P_{xyz} = P + \hat{i}\Delta x + \hat{j}\Delta y + \hat{k}\Delta z$  and  $S_x$  is the streaming operator along  $x$ .

Finally the updated value is transformed back

$$\psi(P_{xyz}, t + \Delta t) = Y^{-1} X^{-1} \psi_{xy}(P_{xyz}, t + \Delta t).$$

In [138], the matrix  $\widehat{Q}$  is the one-dimensional collision matrix  $Q$  itself (see Eq. (1.36)). This is not correct (as we will clarify in the following) and leads to a scheme which does not solve the Schrödinger equation in the adiabatic limit. In the next subsection, we describe the details of the two dimensional model and we show that the evolution of the slow modes  $\phi_{1,2}^+$  is governed by the two-dimensional Schrödinger equation.

## 2.2 Two-dimensional model

Let us consider the two dimensional version of Eq. (2.1)

$$(\partial_t + c\beta\partial_y - c\alpha^z\partial_z) \psi = -i\omega_c \alpha^y \psi,$$

It is known that the choice of the Dirac matrices is not unique, in fact all possible choices are related by similarity transformations. Therefore, we apply a transformation to the matrices in order to diagonalize  $\alpha^z$ . In particular, we use the transformation matrix

$$Z = \frac{1}{\sqrt{2}} \begin{pmatrix} 0 & -1 & 0 & 1 \\ 1 & 0 & -1 & 0 \\ 0 & 1 & 0 & 1 \\ 1 & 0 & 1 & 0 \end{pmatrix}. \quad (2.2)$$

This transformation yields the following equivalent problem:

$$\begin{cases} (\partial_t + cA^z\partial_z + cA^y\partial_y) \psi = \omega_c C \psi \\ \psi(z, y, 0) = \psi_0(z, y), \end{cases} \quad (2.3)$$

where

$$\begin{aligned} A^z &= \begin{pmatrix} 1 & 0 & 0 & 0 \\ 0 & 1 & 0 & 0 \\ 0 & 0 & -1 & 0 \\ 0 & 0 & 0 & -1 \end{pmatrix}, & A^y &= \begin{pmatrix} 0 & 0 & -1 & 0 \\ 0 & 0 & 0 & -1 \\ -1 & 0 & 0 & 0 \\ 0 & -1 & 0 & 0 \end{pmatrix}, \\ C &= \begin{pmatrix} 0 & 0 & 0 & 1 \\ 0 & 0 & 1 & 0 \\ 0 & -1 & 0 & 0 \\ -1 & 0 & 0 & 0 \end{pmatrix}. \end{aligned} \quad (2.4)$$

The problem of Eq. (2.3) is solved by using the operator splitting approach. In particular, we use the *sequential splitting* in order to treat separately the two spatial dimensions.

Then, defining the splitting step  $\Delta t > 0$ , for  $(n-1)\Delta t < t \leq n\Delta t$ , we consider the sequence of initial value problems of the form

$$\begin{cases} (\partial_t + cA^z\partial_z)\psi_1^n = \frac{\omega_c}{2}C\psi_1^n, & (n-1)\Delta t < t \leq \Delta t, \\ \psi_1^n[(n-1)\Delta t] = \psi_2^{n-1}[(n-1)\Delta t], \end{cases} \quad (2.5)$$

and

$$\begin{cases} (\partial_t + cA^y\partial_y)\psi_2^n = \frac{\omega_c}{2}C\psi_2^n, & (n-1)\Delta t < t \leq \Delta t \\ \psi_2^n[(n-1)\Delta t] = \psi_1^n(n\Delta t), \end{cases} \quad (2.6)$$

for  $n = 1, 2, \dots, N$ . To start the procedure we set  $\psi_2^0(0) = \psi_0$ .

If we suppose to be able to exactly solve these two problems, then the function  $\psi_{sp}(z, y, n\Delta t) = \psi_2^n(z, y, n\Delta t)$ , defined at points  $t_n = n\Delta t$ , is called *splitting solution* of the problem and represents a first order approximation of the real solution. The two dimensional problem is now subdivided into two one dimensional problems which can be numerically solved by using the lattice Boltzmann model proposed for the one dimensional case.

However, in the two dimensional version of the model, the collision matrix  $\hat{Q}$  is slightly different from  $Q$  of Eq. (1.36) due to the factor  $1/2$  in front of matrix  $C$  in Eqs. (2.5) and (2.6). In particular, for the free particle case ( $V = 0$ ),  $\hat{Q}$  is given by:

$$\hat{Q} = \begin{pmatrix} \hat{a} & 0 & 0 & \hat{b} \\ 0 & \hat{a} & \hat{b} & 0 \\ 0 & -\hat{b} & \hat{a} & 0 \\ -\hat{b} & 0 & 0 & \hat{a} \end{pmatrix}, \quad (2.7)$$

where

$$\hat{a} = \frac{1 - \tilde{m}_2^2/4}{1 + \tilde{m}_2^2/4}, \quad \hat{b} = \frac{\tilde{m}_2}{1 + \tilde{m}_2^2/4},$$

with

$$\tilde{m}_2 = \tilde{m}/2, \quad \text{and} \quad \tilde{m} = \omega_c \Delta t.$$

Note that, in order to apply the Lattice Boltzmann model to the problem of Eq. (2.6), the equation must be transformed to diagonalize  $A_y$ . Thus, we need to find the transformation  $Y$  such that  $Y^{-1}A^yY$  is diagonal and the same transformation has to be applied to  $C$ , as well, in order to obtain an equivalent equation. One

possible choice for  $Y$  is

$$Y = \frac{1}{\sqrt{2}} \begin{pmatrix} -1 & 0 & 0 & 1 \\ 0 & -1 & 1 & 0 \\ 1 & 0 & 0 & 1 \\ 0 & 1 & 1 & 0 \end{pmatrix}. \quad (2.8)$$

As for the one-dimensional case, by defining the wave functions

$$\phi_{1,2}^{\pm} = \frac{1}{\sqrt{2}} \exp(i\omega_c t)(u_{1,2} \pm id_{2,1}),$$

it is possible to verify that if  $\psi$  is solution of Eq. (2.3), then  $\phi_{1,2}^{\pm}$  satisfy the following equations:

$$\partial_t \phi_{1,2}^+ + c \partial_z \phi_{1,2}^- - ic \partial_y \phi_{2,1}^- = 0, \quad (2.9)$$

$$\partial_t \phi_{1,2}^- + c \partial_z \phi_{1,2}^+ + ic \partial_y \phi_{2,1}^+ = 2i\omega_c \phi_{1,2}^-. \quad (2.10)$$

From Eq. (2.10), after adiabatic elimination of the “fast” antisymmetric modes

$$|\partial_t \phi_{1,2}^-| \ll 2\omega_c |\phi_{1,2}^-|,$$

we obtain

$$\phi_{1,2}^- \approx \frac{c}{2i\omega_c} \left( \partial_z \phi_{1,2}^+ + i \partial_y \phi_{2,1}^+ \right),$$

and substituting in Eq. (2.9), we have

$$i\hbar \partial_t \phi_{1,2}^+ = -\frac{\hbar^2}{2m} \left( \partial_z^2 \phi_{1,2}^+ + \partial_y^2 \phi_{1,2}^+ \right).$$

This shows that the slow symmetric modes  $\phi_{1,2}^+$  obey the Schrödinger equation for a free particle of mass  $m$ .

As previously mentioned, the procedure proposed in [138] needs a little, and yet significant, correction by a factor 2. In fact, in Ref. [138], the operator splitting is performed by taking  $\widehat{Q} = Q$ . This corresponds to solving the following sequence of problems:

$$\begin{cases} (\partial_t + cA^z \partial_z) \psi_1^n = \omega_c C \psi_1^n, & (n-1)\Delta t < t \leq \Delta t, \\ \psi_1^n[(n-1)\Delta t] = \psi_2^{n-1}[(n-1)\Delta t], \end{cases}$$

and

$$\begin{cases} (\partial_t + cA^y \partial_y) \psi_2^n = \omega_c C \psi_2^n, & (n-1)\Delta t < t \leq \Delta t \\ \psi_2^n[(n-1)\Delta t] = \psi_1^n(n\Delta t), \end{cases}$$

for  $(n-1)\Delta t < t \leq n\Delta t$ , instead of problems of Eqs. (2.5) and (2.6). Hence, we are not solving Eq. (2.3), but rather the following equation:

$$\begin{cases} (\partial_t + cA^z \partial_z + cA^y \partial_y) \psi = 2\omega_c C \psi \\ \psi(z, y, 0) = \psi_0(z, y), \end{cases}$$

Performing the same analysis as above, one sees that the wave functions  $\phi_{1,2}^\pm$  have to be defined as

$$\phi_{1,2}^\pm = \frac{1}{\sqrt{2}} \exp(i2\omega_c t)(u_{1,2} \pm id_{2,1}),$$

so that  $\phi_{1,2}^+$  are now solving

$$i2\hbar\partial_t\phi_{1,2}^+ = -\frac{\hbar}{2m} \left( \partial_z^2\phi_{1,2}^+ + \partial_y^2\phi_{1,2}^+ \right).$$

This brings up a factor, 2, only on the time derivative term, thereby delivering an incorrect factor 2 in the governing equation.

### 2.2.1 Inclusion of a potential interaction

As for the one-dimensional case, the inclusion of an external potential is straightforward. We consider the two-dimensional Dirac equation with an electrostatic potential interaction in Majorana form, this reads:

$$(\partial_t + c\beta\partial_y - c\alpha^z\partial_z)\psi = -i\omega_c\alpha^y\psi + ig\psi, \quad (2.11)$$

where  $g = qV/\hbar$  is the space dependent frequency coupling to the potential  $V$  and  $q$  is the particle electric charge. Proceeding as we did above for the case of a free particle ( $V = 0$ ), it is easy to check that in the adiabatic limit  $|\omega - \omega_c| \ll |\omega_c + g|$  and with the additional constraint of small potential interaction,  $|g| \ll \omega_c$ , the non-relativistic motion is reproduced by the symmetric modes  $\phi_{1,2}^+$ .

The qLB scheme is obtained by applying to Eq. (2.11), the operator splitting technique described above. In particular, upon transforming Eq. (2.11) by means of the unitary matrix  $Z$  of Eq. (2.2), we obtain the following equivalent problem

$$\begin{cases} (\partial_t + cA^z\partial_z + cA^y\partial_y)\psi = \omega_c C\psi + ig\psi \\ \psi(z, y, 0) = \psi_0(z, y), \end{cases} \quad (2.12)$$

where the matrices  $A^z$ ,  $A^y$  and  $C$  are the same as given in Eq. (2.4). Using the sequential splitting approach, the two spatial dimensions are treated separately by transforming Eq. (2.12) into two one-dimensional problems

$$\begin{cases} (\partial_t + cA^z\partial_z)\psi_1^n = \frac{\omega_c}{2}C\psi_1^n + i\frac{g}{2}\psi_1^n, & (n-1)\Delta t < t \leq \Delta t, \\ \psi_1^n[(n-1)\Delta t] = \psi_2^{n-1}[(n-1)\Delta t], \end{cases}$$

and

$$\begin{cases} (\partial_t + cA^y\partial_y)\psi_2^n = \frac{\omega_c}{2}C\psi_2^n + i\frac{g}{2}\psi_2^n, & (n-1)\Delta t < t \leq \Delta t \\ \psi_2^n[(n-1)\Delta t] = \psi_1^n(n\Delta t). \end{cases} \quad (2.13)$$

Each of the two problems above can be numerically solved by using the one-dimensional qLB scheme. Note that, in order to apply the one-dimensional model to Eq. (2.13), the equation must be transformed by means of a unitary matrix  $Y$  (e. g. the matrix of Eq. (2.8)), such that the scattering matrix  $A^y$  becomes diagonal.

However, as previously mentioned, the two-dimensional scattering matrix is slightly different from the one-dimensional one, this is due to the presence of the factor  $1/2$  in the collision term. This factor also multiplies the interaction term, thus yielding the following scattering matrix

$$\hat{Q}_g = \begin{pmatrix} \hat{a}_g & 0 & 0 & \hat{b}_g \\ 0 & \hat{a}_g & \hat{b}_g & 0 \\ 0 & -\hat{b}_g & \hat{a}_g & 0 \\ -\hat{b}_g & 0 & 0 & \hat{a}_g \end{pmatrix},$$

where

$$\hat{a}_g = \frac{1 - \Omega_2/4}{1 + \Omega_2/4 - i\tilde{g}_2}, \quad \hat{b}_g = \frac{\tilde{m}_2}{1 + \Omega_2/4 - i\tilde{g}_2},$$

with

$$\Omega_2 = \tilde{m}_2^2 - \tilde{g}_2^2, \quad \tilde{m}_2 = \tilde{m}/2, \quad \tilde{g}_2 = \tilde{g}/2,$$

and  $\tilde{m} = \omega_c \Delta t$ ,  $\tilde{g} = g \Delta t$ .

### 2.3 Free propagation of a quantum wave packet

In this section and in the following two, we validate the two-dimensional version of the qLB scheme by performing numerical calculations for which analytical results are known. In particular, here we consider the dynamics of a quantum particle of mass  $m$  which propagates freely.

In order to have reasonable numerical values for the parameters of the scheme, we work in atomic units ( $c = \hbar = 1$  and  $q = -1$ ) and we express space and time in lattice units. Note that, working in atomic units, the Compton frequency  $\omega_c = mc^2/\hbar$  becomes equal to  $m$ , hence the parameter  $\tilde{m} = \omega_c \Delta t$  is given by  $\tilde{m} = m \Delta t$ .

To validate the model in this regime we set, as initial condition, a minimum uncertainty wave packet

$$\begin{aligned} \psi_0(z, y) = & (2\pi\Delta_{0z}\Delta_{0y})^{-1/2} \exp\left(-\frac{(z-z_0)^2}{4\Delta_{0z}^2}\right) \\ & \times \exp\left(-\frac{(y-y_0)^2}{4\Delta_{0y}^2}\right) \exp(-im(v_z z + v_y y)). \end{aligned} \quad (2.14)$$



This is a wave packet centered about  $(z_0, y_0)$  with initial spreads  $\Delta_{0z}$ ,  $\Delta_{0y}$  along  $z$  and  $y$  respectively and propagating at speed  $(v_z, v_y)$ . To impose this initial condition on the model, as for the one-dimensional case, we set

$$\begin{aligned} u_1 &= u_2 = \frac{1}{2}\psi_0, \\ d_1 &= d_2 = -i\frac{1}{2}\psi_0. \end{aligned}$$

With the initial condition given by Eq. (2.14), the analytical solution of the Schrödinger equation for a free propagating particle is given by

$$\begin{aligned} \psi_{an}(z, y, t) &= \left[ 2\pi \left( \Delta_{0z} + \frac{it}{2m\Delta_{0z}} \right) \left( \Delta_{0y} + \frac{it}{2m\Delta_{0y}} \right) \right]^{-1/2} \\ &\times \exp \left( -\frac{(z - z_0 - v_z t)^2}{4\Delta_{0z}^2 + 2it/m} \right) \exp \left( -\frac{(y - y_0 - v_y t)^2}{4\Delta_{0y}^2 + 2it/m} \right) \\ &\times \exp(im(v_z z + v_y y)) \exp \left( -\frac{im(v_z^2 + v_y^2)t}{2} \right). \end{aligned} \quad (2.15)$$

Based on this solution, the mean position  $(Z(t), Y(t))$  and the mean spreads  $\Delta_z(t)$ ,  $\Delta_y(t)$  evolve accordingly to the equations

$$Z(t) = z_0 + v_z t, \quad Y(t) = y_0 + v_y t, \quad (2.16)$$

and

$$\Delta_z(t) = \left[ \Delta_{0z}^2 + \frac{t^2}{4m^2\Delta_{0z}^2} \right]^{1/2}, \quad \Delta_y(t) = \left[ \Delta_{0y}^2 + \frac{t^2}{4m^2\Delta_{0y}^2} \right]^{1/2}, \quad (2.17)$$

For a free particle, the mean energy  $\langle E \rangle$  is given by

$$\begin{aligned} \langle E \rangle &= i\hbar \int (\psi^* \partial_t \psi) \, dz dy \\ &= -\frac{\hbar^2}{2m} \int (\psi^* \Delta \psi) \, dz dy = \frac{\hbar^2}{2m} \int (\nabla \psi^* \nabla \psi) \, dz dy. \end{aligned}$$

Hence, for the minimum uncertainty wave packet (and recalling that we are using atomic units), we obtain

$$\langle E \rangle = \frac{1}{2m} \left( m^2(v_z^2 + v_y^2) + \frac{1}{4\Delta_{0z}^2} + \frac{1}{4\Delta_{0y}^2} \right). \quad (2.18)$$

Since our model provides both wave functions  $\phi_{1,2}^\pm$ , we can compute  $E_{1,2}^+$ ,  $E_{1,2}^-$  on  $\phi_{1,2}^+$  and  $\phi_{1,2}^-$  respectively and then define

$$E^+ = E_1^+ + E_2^+, \quad E^- = E_1^- + E_2^-, \quad E = E^+ + E^-.$$

### 2.3.1 Comparison with the analytical solution and convergence test

To study the convergence of the model, we need to fix the domain  $[z_{min}, z_{max}] \times [y_{min}, y_{max}]$  and to discretize it by using an increasing number of points  $n_z \times n_y$ . Moreover, the lattice must be uniform (i. e.  $\Delta z = \Delta y \equiv h$ ) and the relation  $h = \Delta t$  must be preserved (recall  $c = 1$  in lattice units). In general,  $h$  is given by

$$h = \frac{z_{max} - z_{min}}{n_z - 1} = \frac{y_{max} - y_{min}}{n_y - 1}.$$

This setting implies that the model parameter  $\tilde{m} = \omega_c \Delta t$  is given by  $mh$  which corresponds to an “effective” mass. For this reason, we need to take a sufficiently large domain, so that  $\tilde{m}$  is not too close to zero, indeed for  $\tilde{m} \ll 1$  a lack of adiabaticity could occur.

In this numerical test we set  $[z_{min}, z_{max}] \times [y_{min}, y_{max}] = [0, 512] \times [0, 512]$  and  $N_z = n_z - 1$  and  $N_y = n_y - 1$  take the values 128, 256, 512 and 1024. The remaining parameters are set as follows:  $\Delta_{0z} = \Delta_{0y} = 40$ ,  $v_z = 0.02$ ,  $v_y = 0.04$  and  $m = 1/8$ . The error with respect to the analytical solution, Eq. (2.15), is computed in  $L^2$  norm. In particular, we define

$$\begin{aligned} e_2(t) &= \|\psi_{an}(z, y, t) - \phi^+(z, y, t)\|_2 \\ &= \left( \int |\psi_{an}(z, y, t) - \phi^+(z, y, t)|^2 dz dy \right)^{1/2}. \end{aligned}$$

The error  $e_2$  was found to decrease from 0.08 to 0.009 as the grid resolution was increased from 128 to 1024 points in each direction, but with no clear evidence of a specific convergence rate. We tentatively interpret this as the concurrent effect of time-discretization errors, ( $\mathcal{O}(h^2)$ ), the splitting error ( $\mathcal{O}(h)$ ) and lack of adiabaticity in the limit  $mh \rightarrow 0$ . In Fig. 2.1 the function

$$e(z, y, t) = |\Re(\psi_{an}(z, y, t)) - \Re(\phi^+(z, y, t))| \quad (2.19)$$

taken at  $y = y_0$  for the different values of  $N_z$  and  $N_y$  is plotted at times 100, 300 and 500. In Fig. 2.2 the same function evaluated in  $z = z_0$  is shown.

In Tab. 2.1 we report the propagation velocity and the mean spread of the packet while increasing the number of discretization points. For the present setting the expected velocity is  $v_z = 0.02$  and  $v_y = 0.04$  and the spread at time  $t = 500$  is computed by Eq. (2.17) and is 64.03 since  $\Delta_{0z} = \Delta_{0y} = 40$ .

In the following subsection we will check the ability of the model to reproduce mean position and spread for different sets of parameters.

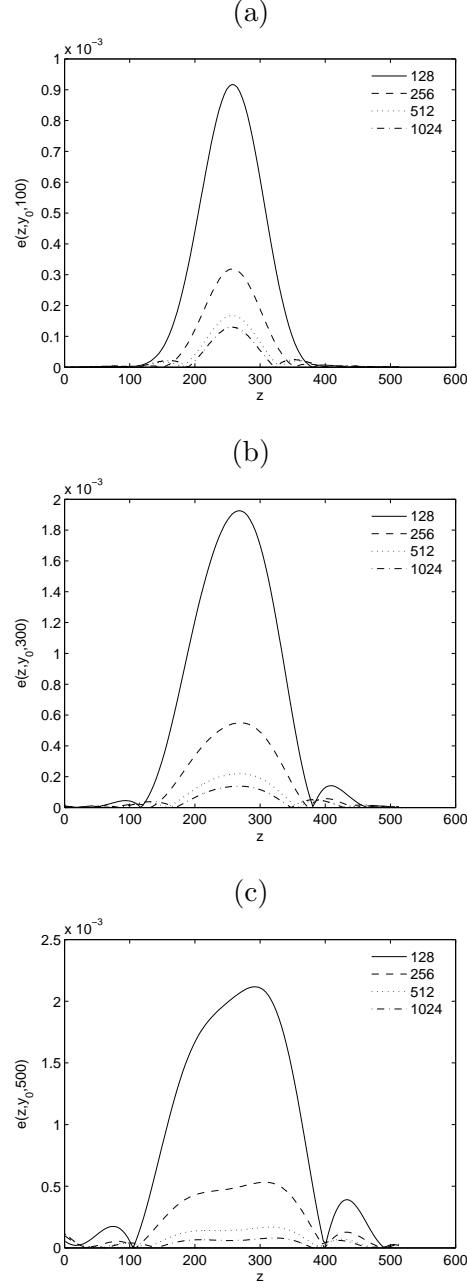


Figure 2.1: Difference between the real part of the analytical solution and the model result for  $y = y_0$  (see Eq. (2.19)) and for different values of  $N_z = N_y$  and taking  $v_z = 0.02$ ,  $v_y = 0.02$ ,  $\Delta_{0z} = \Delta_{0y} = 40$  and  $m = 1/8$ . Solid line:  $N_z = N_y = 128$ ; Dashed line:  $N_z = N_y = 256$ ; Dotted line:  $N_z = N_y = 512$ ; Dash-dotted line:  $N_z = N_y = 1024$ . (a)  $t = 100$ ; (b)  $t = 300$ ; (c)  $t = 500$ . Space and time are expressed in lattice units.

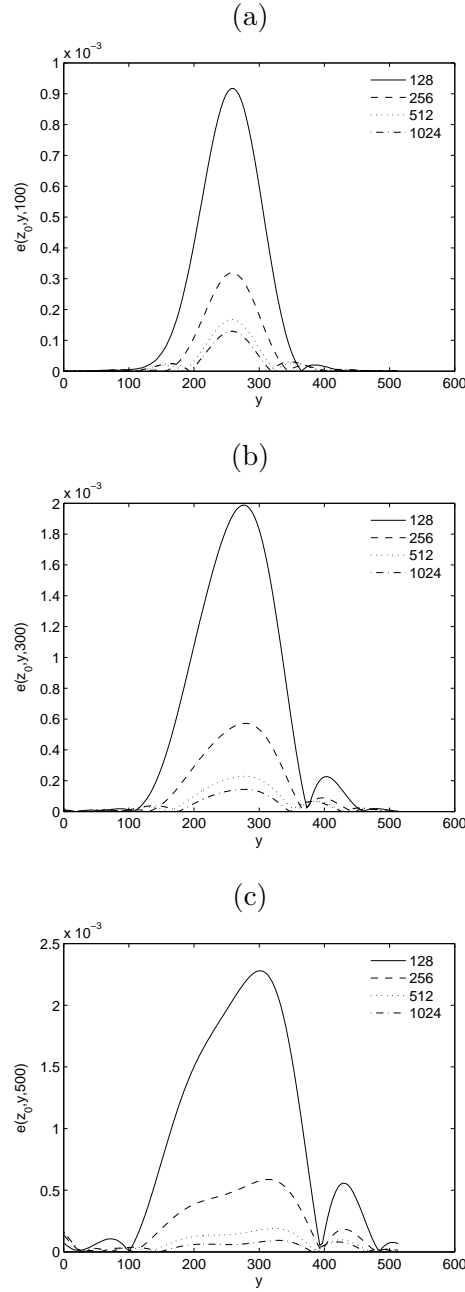


Figure 2.2: Difference between the real part of the analytical solution and the model result for  $z = z_0$  (see Eq. (2.19)) and for different values of  $N_z = N_y$  and taking  $v_z = 0.02$ ,  $v_y = 0.02$ ,  $\Delta_{0z} = \Delta_{0y} = 40$  and  $m = 1/8$ . Solid line:  $N_z = N_y = 128$ ; Dashed line:  $N_z = N_y = 256$ ; Dotted line:  $N_z = N_y = 512$ ; Dash-dotted line:  $N_z = N_y = 1024$ . (a)  $t = 100$ ; (b)  $t = 300$ ; (c)  $t = 500$ . Space and time are expressed in lattice units.

Table 2.1: Propagation velocity and spread of the packet at time  $t = 500$  for different values of  $N_z = N_y$ . The expected values are:  $v_z = 0.02$ ,  $v_y = 0.04$  and  $\Delta_z(500) = \Delta_y(500) = 64.03$ . Here  $m = 1/8$  and  $\Delta_{0z} = \Delta_{0y} = 40$ .

$N_z = N_y$	$v_z$	$v_y$	$\Delta_z(500)$	$\Delta_y(500)$
128	0.0175	0.0355	60.20	60.19
256	0.0189	0.0379	62.41	62.40
512	0.0191	0.0384	62.97	62.95
1024	0.0193	0.0386	63.11	63.09

The model is able to preserve a unit norm: quantity

$$\|\phi^+\|^2 + \|\phi^-\|^2 = \int |\phi^+(z, y, t)|^2 dz dy + \int |\phi^-(z, y, t)|^2 dz dy.$$

It follows that  $\|\phi^+\|$  cannot be preserved equal to one during the evolution. Indeed we have  $\|\phi^-\| \ll \|\phi^+\|$  and both of them are oscillating in such a way that  $\|\phi^+\|^2 + \|\phi^-\|^2 = 1$ . In Fig. 2.3  $\|\phi^+\|^2$ ,  $\|\phi^-\|^2$  and  $\|\phi^+\|^2 + \|\phi^-\|^2$  are shown, while in Fig. 2.4 only  $\|\phi^+\|^2$  is plotted, in order to have a closer appreciation of its evolution.

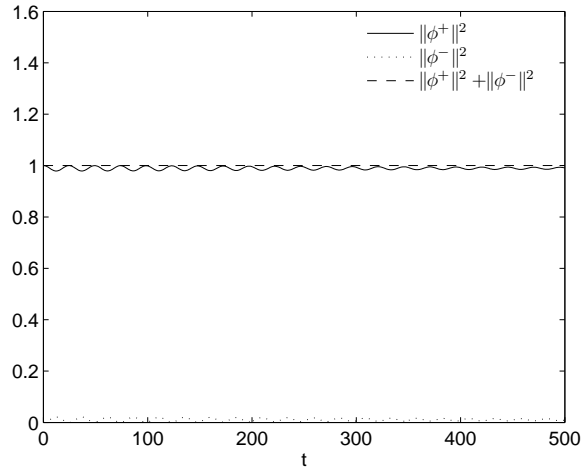


Figure 2.3:  $\|\phi^+\|^2$  (solid line),  $\|\phi^-\|^2$  (dotted line) and  $\|\phi^+\|^2 + \|\phi^-\|^2$  (dashed line) for  $N_z = N_y = 1024$  ( $\hbar = 1/2$ ),  $m = 1/8$ ,  $\Delta_{0z} = \Delta_{0y} = 40$ ,  $v_z = 0.02$  and  $v_y = 0.04$ . Time is expressed in lattice units.

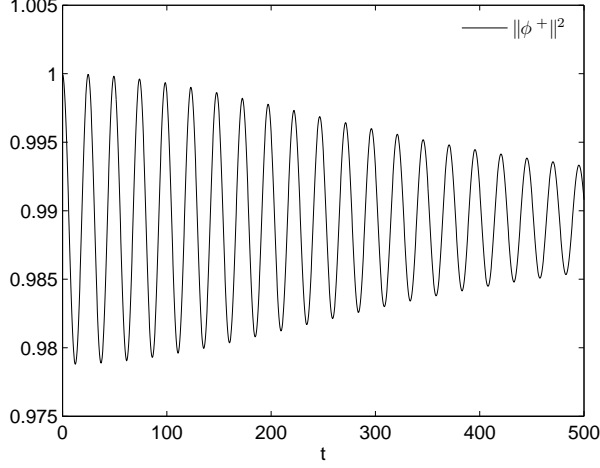


Figure 2.4:  $\|\phi^+\|^2$  for  $N_z = N_y = 1024$  ( $h = 1/2$ ),  $m = 1/8$ ,  $\Delta_{0z} = \Delta_{0y} = 40$ ,  $v_z = 0.02$  and  $v_y = 0.04$ . Time is expressed in lattice units.

A similar behavior is obtained for the energy. The model keeps constant, and very close to the expected value given by Eq. (2.18), the total kinetic energy  $E = E^+ + E^-$ , while  $E^+$  and  $E^-$  are oscillating with  $E^- \ll E^+$ . In Fig. 2.5  $E^+$ ,  $E^-$  and  $E$  are shown.

Finally, in Tab. 2.2 we report the mean values of  $\|\phi^+\|^2$ ,  $E^+$  and  $E$  while increasing the number of nodes. Note that, for the present setting, the expected value for the energy given by Eq. (2.18) is  $1.375 \times 10^{-3}$ .

Table 2.2: Mean values of  $\|\phi^+\|^2$ ,  $E^+$  and  $E$  for different values of  $N_z = N_y$ . The expected value for the energy is  $1.375 \times 10^{-3}$ . Here  $m = 1/8$ ,  $\Delta_{0z} = \Delta_{0y} = 40$ ,  $v_z = 0.02$  and  $v_y = 0.04$ .

$N_z = N_y$	$\ \phi^+\ ^2$	$E^+$	$E$
128	0.980	$1.234 \times 10^{-3}$	$1.3712 \times 10^{-3}$
256	0.985	$1.240 \times 10^{-3}$	$1.3741 \times 10^{-3}$
512	0.987	$1.293 \times 10^{-3}$	$1.3748 \times 10^{-3}$
1024	0.988	$1.320 \times 10^{-3}$	$1.3749 \times 10^{-3}$

### 2.3.2 Mean position and mean spreads

In all of the following simulations we take  $h \equiv \Delta z = \Delta y = \Delta t = 1$ , hence the computational domain is  $[0, n_z] \times [0, n_y]$  and is not fixed as in the previous section.

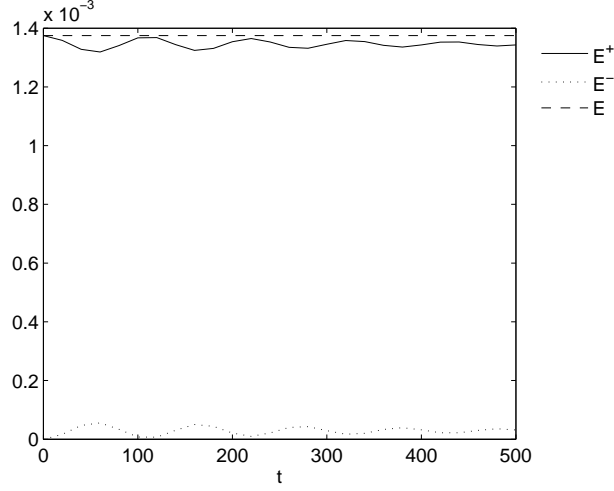


Figure 2.5:  $E^+$  (solid line),  $E^-$  (dotted line) and  $E = E^+ + E^-$  (dashed line) for  $N_z = N_y = 512$  ( $\hbar = 1$ ),  $m = 1/8$ ,  $\Delta_{0z} = \Delta_{0y} = 40$ ,  $v_z = 0.02$  and  $v_y = 0.04$ . Time is expressed in lattice units.

As we mentioned, mean position and mean spreads evolve according to Eqs. (2.16) and (2.17). We can check the ability of the model to reproduce these evolutions under a number of different conditions.

In all of the following tests, we use a grid of size  $1024 \times 1024$ . As to the position, we measure the propagation velocity of the packet for different values of the parameters  $m$  and  $\Delta_{0z} = \Delta_{0y}$ , while keeping  $v_z = 0.05$  and  $v_y = 0.025$ . In Tab. 2.3, the results of the model are reported.

To verify the asymptotic behavior of  $\Delta_z(t)$  and  $\Delta_t(t)$  we set  $v_z = v_y = 0$  so that the wave packet is not hitting the grid boundary too early. The results are reported in Tab. 2.4.

Finally, we set  $v_z \neq v_y$  and  $\Delta_{0z} \neq \Delta_{0y}$ , in particular we choose  $v_z = 0.05$ ,  $v_y = 0.02$ ,  $\Delta_{0z} = 50$ ,  $\Delta_{0y} = 32$  and  $m = 0.2$ . In Fig. 2.6, we compare  $Z(t)$  and  $\Delta_z(t)$  with the analytical curves given by Eqs. (2.16) and (2.17). A similar comparison for  $Y(t)$  and  $\Delta_y(t)$  is shown in Fig. 2.7.

## 2.4 Two-dimensional harmonic oscillator

As a second example, we consider a two dimensional harmonic oscillator. The potential is given by

$$V(z, y) = \frac{1}{2}m\omega_0^2[(z - z_0)^2 + (y - y_0)^2],$$

Table 2.3: Results on the propagation velocity for different values of  $m$  and  $\Delta_{0z} = \Delta_{0y} \equiv \Delta_0$ . With  $R_z$  and  $R_y$  are indicated the ratios between the model result and the expected value along  $z$  and  $y$  respectively. Here  $n_z = n_y = 1024$ ,  $v_z = 0.05$  and  $v_y = 0.025$ .

$\Delta_0$	$m$	$v_z$	$v_y$	$R_z$	$R_y$
50	0.1	0.048	0.024	1.038	1.040
32	0.1	0.047	0.023	1.073	1.076
32	0.2	0.048	0.024	1.034	1.035
16	0.2	0.046	0.023	1.084	1.092

Table 2.4: Asymptotic behavior of  $\Delta_z(t)$  and  $\Delta_y(t)$  for different values of  $m$  and  $\Delta_{0z} = \Delta_{0y} \equiv \Delta_0$ . With  $R_z$  and  $R_y$  are indicated the ratios between the model result and the expected value along  $z$  and  $y$  respectively. Here  $n_z = n_y = 1024$  and  $v_z = v_y = 0$ .

$\Delta_0$	$m$	$\Delta_z$	$\Delta_y$	Expected value	$R_z$	$R_y$
50	0.1	0.087	0.087	0.1	1.155	1.115
32	0.1	0.144	0.144	0.15625	1.083	1.083
32	0.2	0.0719	0.0719	0.078125	1.083	1.083
16	0.2	0.145	0.145	0.15625	1.080	1.080



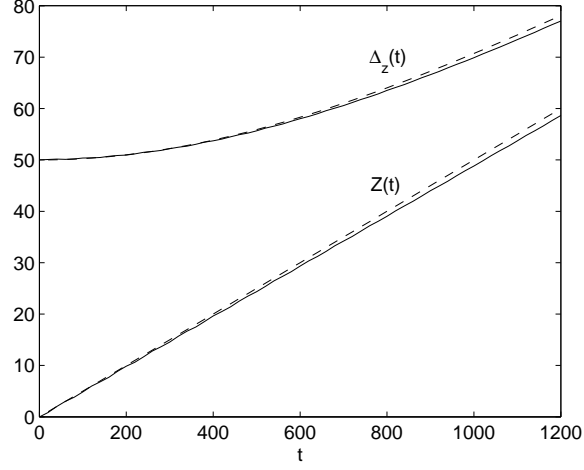


Figure 2.6: Comparison between  $Z(t)$  and  $\Delta_z(t)$  and the expected curves given by Eqs. (2.16) and (2.17) for the following setting:  $n_z = n_y = 1024$ ,  $v_z = 0.05$ ,  $v_y = 0.02$ ,  $\Delta_{0z} = 50$ ,  $\Delta_{0y} = 32$  and  $m = 0.2$ . Solid lines represent  $Z(t)$  and  $\Delta_z(t)$  given by the model; dashed lines are the expected curves. Space and time are expressed in lattice units.

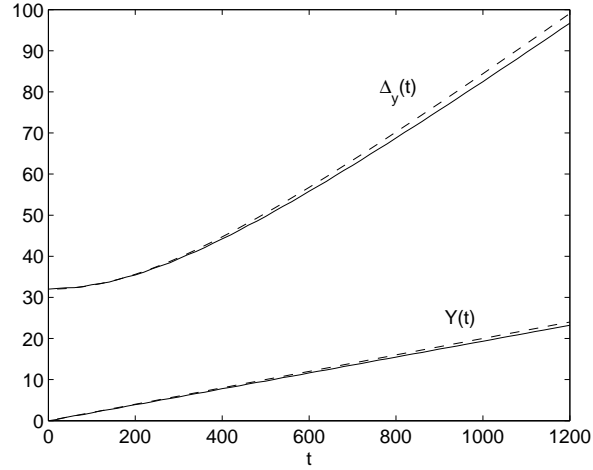


Figure 2.7: Comparison between  $Y(t)$  and  $\Delta_y(t)$  and the expected curves given by Eqs. (2.16) and (2.17) for the following setting:  $n_z = n_y = 1024$ ,  $v_z = 0.05$ ,  $v_y = 0.02$ ,  $\Delta_{0z} = 50$ ,  $\Delta_{0y} = 32$  and  $m = 0.2$ . Solid lines represent  $Y(t)$  and  $\Delta_y(t)$  given by the model; dashed lines are the expected curves. Space and time are expressed in lattice units.

where we are assuming for simplicity  $\omega_z = \omega_y = \omega_0$ . The initial condition is still given by the minimum uncertainty wave packet of Eq. (2.14).

With these assumptions, it is known that the mean quantities  $(Z(t), Y(t))$  and  $\mathbf{P}(t) = (P_z(t), P_y(t))$  obey the classical equations of motion of the harmonic oscillator

$$\begin{aligned}\dot{Z} &= P_z(t)/m, & \dot{Y} &= P_y(t)/m, \\ \ddot{Z} + \omega_0^2 Z &= 0, & \ddot{Y} + \omega_0^2 Y &= 0,\end{aligned}$$

hence,

$$\begin{aligned}Z(t) &= z_0 + \frac{v_z}{\omega_0} \sin(\omega_0 t), \\ Y(t) &= y_0 + \frac{v_y}{\omega_0} \sin(\omega_0 t).\end{aligned}\tag{2.20}$$

Moreover, by setting  $\Delta_0 \equiv \Delta_{0z} = \Delta_{0y}$  so that

$$\omega_0 = \frac{1}{2m\Delta_0^2},$$

the initial spreading is preserved all along the evolution. We want to check the ability of the model to preserve  $\Delta_0$  for different parameter settings. In Tab. 2.5, the results are shown, here  $\Delta_z$  and  $\Delta_y$  are the packet spreads averaged over two periods. In all of the simulations we set  $v_z = 0.02$  and  $v_y = 0.04$ . In Fig. 2.8,  $Z(t)$

Table 2.5: Averaged variances of the packet along  $z$  and  $y$  for different setting of the parameters  $N_z = N_y$ ,  $\tilde{m}$  and  $\omega_0$ . Here  $v_z = 0.02$  and  $v_y = 0.04$ .

$N_z = N_y$	$\omega_0$	$\tilde{m}$	$\Delta_z$	$\Delta_y$	Expected $\Delta$
1024	$8/64^2$	$1/16$	$64.35 \pm 1.33$	$64.35 \pm 1.33$	64
1024	$2/32^2$	$1/4$	$32.25 \pm 0.70$	$32.27 \pm 0.75$	32
512	$4/32^2$	$1/8$	$32.16 \pm 0.70$	$32.17 \pm 0.69$	32
512	$2/32^2$	$1/4$	$31.87 \pm 0.27$	$31.87 \pm 0.29$	32
512	$1/16^2$	$1/2$	$16.01 \pm 0.69$	$16.02 \pm 0.70$	16
256	$2/16^2$	$1/4$	$16.05 \pm 0.37$	$16.05 \pm 0.38$	16
256	$1/16^2$	$1/2$	$15.74 \pm 0.32$	$15.74 \pm 0.32$	16

and  $\Delta_z(t)$  are shown for  $N_z = N_y = 512$ ,  $\omega_0 = 2/32^2$ ,  $m = 1/4$ , in Fig. 2.9,  $Y(t)$  and  $\Delta_y(t)$  are reported for the same set of parameters.

When an external potential  $V$  is acting on the particle, as in this case, the total energy of a wave function  $\psi$  satisfying the Schrödinger equation is given by:

$$\begin{aligned}\langle E \rangle &= i\hbar \int (\psi^* \partial_t \psi) \, dzdy = \\ &= \frac{\hbar^2}{2m} \int (\nabla \psi^* \nabla \psi) \, dzdy + \int (\psi^* V \psi) \, dzdy.\end{aligned}$$

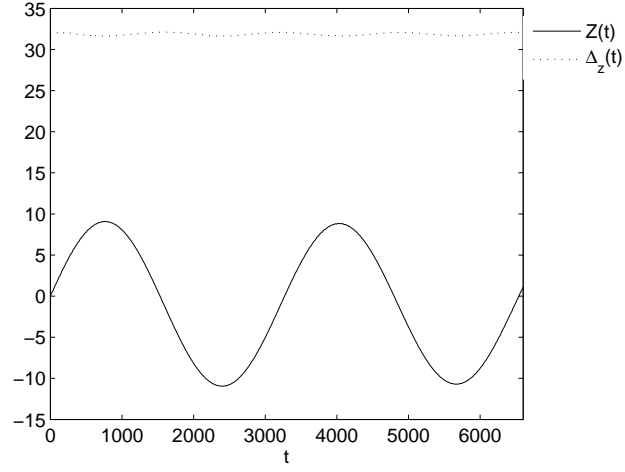


Figure 2.8:  $Z(t)$  and  $\Delta_z(t)$  for the harmonic oscillator with parameters  $N_z = N_y = 512$ ,  $\omega_0 = 2/32^2$ ,  $m = 1/4$ ,  $v_z = 0.02$  and  $v_y = 0.04$ . The solid line is  $Z(t)$ , while the dotted one is  $\Delta_z(t)$ . Space and time are expressed in lattice units.

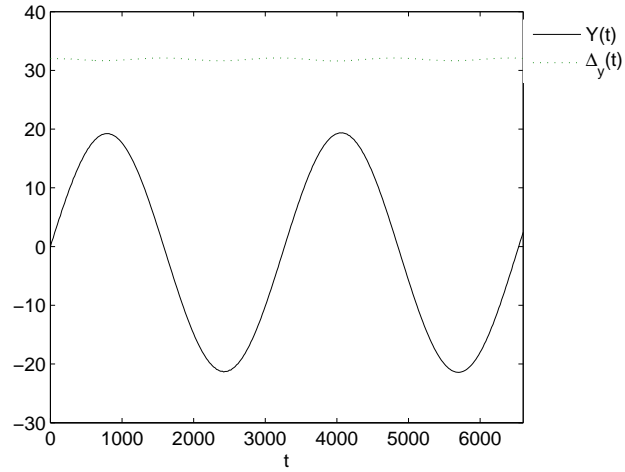


Figure 2.9:  $Y(t)$  and  $\Delta_y(t)$  for the harmonic oscillator with parameters  $N_z = N_y = 512$ ,  $\omega_0 = 2/32^2$ ,  $m = 1/4$ ,  $v_z = 0.02$  and  $v_y = 0.04$ . The solid line is  $Y(t)$ , while the dotted one is  $\Delta_y(t)$ . Space and time are expressed in lattice units.

In analogy with classical mechanics,  $\langle E \rangle$  satisfies the relation

$$\langle E \rangle = \frac{1}{2m} \langle \mathbf{P}^2 \rangle + \langle V \rangle.$$

In Fig. 2.10 kinetic and potential energy and their sum are plotted for the harmonic oscillator defined by the parameters:  $N_z = N_y = 512$ ,  $\omega_0 = 2/32^2$ ,  $m = 1/4$ . In particular, the energies are computed on  $\phi_{1,2}^+$ , so  $E_{kin}^+$ ,  $E_{pot}^+$  and  $E^+ = E_{kin}^+ + E_{pot}^+$  are shown. From this figure, a satisfactory energy conservation is observed.

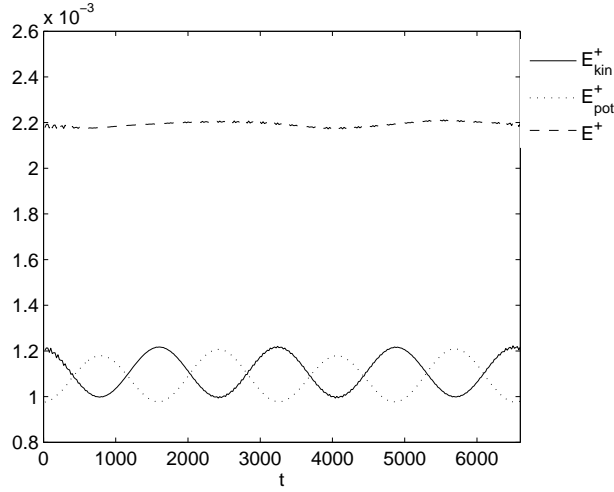


Figure 2.10: Plots of  $E_{kin}^+$ ,  $E_{pot}^+$  and  $E^+ = E_{kin}^+ + E_{pot}^+$  for the harmonic oscillator with parameters  $N_z = N_y = 512$ ,  $\omega_0 = 2/32^2$ ,  $m = 1/4$ ,  $v_z = 0.02$  and  $v_y = 0.04$ . Solid line:  $E_{kin}^+$ ; dotted line:  $E_{pot}^+$ ; dashed line:  $E^+ = E_{kin}^+ + E_{pot}^+$ . Time and energy are expressed in lattice units.

Finally, in order to verify the isotropy of the model we plot the isolines taken at some values of  $\rho = |\psi(z, y)|^2$ . This test is performed for the following set of parameters:  $N_z = N_y = 256$ ,  $\omega_0 = 1/128$ ,  $m = 1/4$ . The contour plot obtained after two periods is shown in Fig. 2.11. In particular, the isolines taken at  $\rho = 1 \times 10^{-4}$ ,  $2 \times 10^{-4}$ ,  $3 \times 10^{-4}$ ,  $4 \times 10^{-4}$ ,  $5 \times 10^{-4}$  and  $6 \times 10^{-4}$  are plotted.

## 2.5 Two-dimensional rotated, non-isotropic oscillator

As a third test we model a non-isotropic oscillator by using the following potential

$$V(z, y) = \frac{1}{2} m \omega_0^2 \left[ \frac{(z - z_0)^2}{a^2} + \frac{(y - y_0)^2}{b^2} \right],$$

then the characteristic frequencies along  $z$  and  $y$  are given by

$$\omega_{0z} = \frac{\omega_0}{a}, \quad \omega_{0y} = \frac{\omega_0}{b}.$$

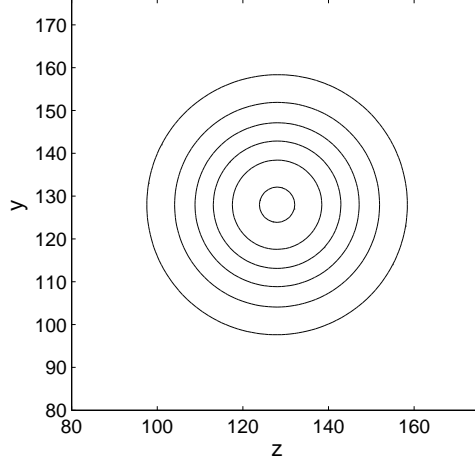


Figure 2.11: Contour plot for  $\rho = |\psi(z, y)|^2$  for the harmonic oscillator with parameters  $N_z = N_y = 256$ ,  $\omega_0 = 1/128$ ,  $m = 1/4$ ,  $v_z = v_y = 0.0$  and  $\Delta_0 = 16$ . The isolines correspond to the following values of  $\rho$ :  $1 \times 10^{-4}$ ,  $2 \times 10^{-4}$ ,  $3 \times 10^{-4}$ ,  $4 \times 10^{-4}$ ,  $5 \times 10^{-4}$  and  $6 \times 10^{-4}$  going from the outside toward the inside. Space is expressed in lattice units.

The evolution of  $Z(t)$  and  $Y(t)$  is thus described by

$$\begin{aligned} Z(t) &= z_0 + \frac{v_z}{\omega_{0z}} \sin(\omega_{0z}t), \\ Y(t) &= y_0 + \frac{v_y}{\omega_{0y}} \sin(\omega_{0y}t), \end{aligned}$$

and choosing  $\Delta_{0z}$  and  $\Delta_{0y}$  such that

$$\omega_{0z} = \frac{1}{2m\Delta_{0z}^2}, \quad \omega_{0y} = \frac{1}{2m\Delta_{0y}^2}, \quad (2.21)$$

the initial spreadings are preserved all along the evolution.

Consider, now, a rotated coordinate system

$$\begin{cases} z' = z \cos(\alpha) - y \sin(\alpha), \\ y' = z \sin(\alpha) + y \cos(\alpha). \end{cases} \quad (2.22)$$

The mean position in the rotated system  $(Z'(t), Y'(t))$ , is still following the laws

$$\begin{aligned} Z'(t) &= \frac{v_{z'}}{\omega_{0z}} \sin(\omega_{0z}t), \\ Y'(t) &= \frac{v_{y'}}{\omega_{0y}} \sin(\omega_{0y}t), \end{aligned} \quad (2.23)$$

and, from Eq. (2.22), we have that  $(Z(t), Y(t))$  must satisfy

$$\begin{aligned} Z(t) &= Z'(t) \cos(\alpha) + Y'(t) \sin(\alpha), \\ Y(t) &= -Z'(t) \sin(\alpha) + Y'(t) \cos(\alpha). \end{aligned} \quad (2.24)$$

We next check the ability of the model to reproduce these evolutions for  $Z(t)$  and  $Y(t)$  for this elliptic-rotated oscillator.

As a first example, we set the parameters as follows:  $N_z = N_y = 1024$ ,  $a^2 = 2$ ,  $b^2 = 4$ ,  $m = 1/8$ ,  $\omega_0 = 1/512$ ,  $v_{z'} = 0.05$ ,  $v_{y'} = 0$  and  $\alpha = \pi/4$ . With this setting we have:

$$\omega_{0z} = \frac{1}{\sqrt{2}} \frac{1}{512} \quad \omega_{0y} = \frac{1}{1024},$$

and, from Eq. (2.21), we obtain

$$\Delta_{0z} = 53.817, \quad \Delta_{0y} = 64.$$

Moreover, since  $v_{y'=0}$ , from Eqs. (2.23) and (2.24), we expect the following evolution for  $Z(t)$  and  $Y(t)$

$$\begin{aligned} Z(t) &= \frac{v_{z'}}{\omega_{0z}} \sin(\omega_{0z}t) \cos(\alpha) = \frac{v_{z'}}{\omega_{0z}} \sin(\omega_{0z}t) \frac{\sqrt{2}}{2}, \\ Y(t) &= -\frac{v_{z'}}{\omega_{0z}} \sin(\omega_{0z}t) \sin(\alpha) = -\frac{v_{z'}}{\omega_{0z}} \sin(\omega_{0z}t) \frac{\sqrt{2}}{2}. \end{aligned}$$

In Fig. 2.12,  $Z(t)$  and  $Y(t)$  are plotted. We also observe that

$$\frac{v_{z'}}{\omega_{0z}} \frac{\sqrt{2}}{2} = 25.6,$$

in close agreement with the maximum absolute value reached by  $Z(t)$  and  $Y(t)$ , which is 25.47.

As a second example we set  $N_z = N_y = 1024$ ,  $a^2 = 1$ ,  $b^2 = 2$ ,  $m = 1/4$ ,  $\omega_0 = 1/1024$ ,  $v_{z'} = 0.05$ ,  $v_{y'} = 0.0$  and  $\alpha = \pi/6$ . With this parameters we obtain:

$$\omega_{0z} = \frac{1}{1024} \quad \omega_{0y} = \frac{1}{\sqrt{2}} \frac{1}{1024},$$

and, from Eq. (2.21)

$$\Delta_{0z} = 45.255, \quad \Delta_{0y} = 53.817.$$

As in the previous example, since  $v_{y'=0}$ , from Eqs. (2.23) and (2.24), we expect the following evolution for  $Z(t)$  and  $Y(t)$

$$\begin{aligned} Z(t) &= \frac{v_{z'}}{\omega_{0z}} \sin(\omega_{0z}t) \cos(\alpha) = \frac{v_{z'}}{\omega_{0z}} \sin(\omega_{0z}t) \frac{\sqrt{3}}{2}, \\ Y(t) &= -\frac{v_{z'}}{\omega_{0z}} \sin(\omega_{0z}t) \sin(\alpha) = -\frac{v_{z'}}{\omega_{0z}} \sin(\omega_{0z}t) \frac{1}{2}. \end{aligned}$$

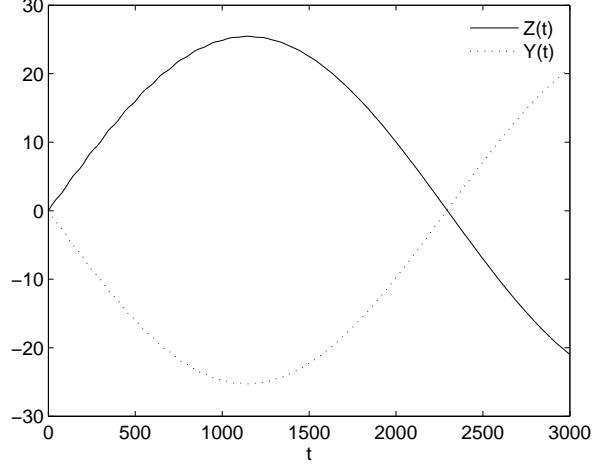


Figure 2.12:  $Z(t)$  and  $Y(t)$  for the rotated elliptic oscillator of the first test. The solid line is  $Z(t)$ , while the dotted one is  $Y(t)$ . In this first test, the parameters are as follows:  $N_z = N_y = 1024$ ,  $a^2 = 2$ ,  $b^2 = 4$ ,  $m = 1/8$ ,  $\omega_0 = 1/512$ ,  $v_{z'} = 0.05$ ,  $v_{y'} = 0$  and  $\alpha = \pi/4$ . Space and time are expressed in lattice units.

In Fig. 2.13,  $Z(t)$  and  $Y(t)$  are plotted. We also observe that

$$\frac{v_{z'}}{\omega_{0z}} \frac{\sqrt{3}}{2} = 44.34, \quad \frac{v_{z'}}{\omega_{0z}} \frac{1}{2} = 25.6,$$

again in close agreement with the maximum absolute values reached by  $Z(t)$  and  $Y(t)$ , namely 43.90 and 25.27, respectively.

## 2.6 Three-dimensional model

The two dimensional model just described can be easily extended to three dimensions. In this case, as a result of the application of transformation  $Z$  (see Eq. (2.2)), the Dirac equation given in Eq. (2.1) takes the form

$$\begin{cases} (\partial_t + cA^x\partial_x + cA^y\partial_y + cA^z\partial_z) \psi = \omega_c C\psi + ig\psi \\ \psi(x, y, z, 0) = \psi_0(x, y, z), \end{cases} \quad (2.25)$$

where  $A^y$ ,  $A^z$  and  $C$  are the same as in Eq. (2.4) and

$$A^x = \begin{pmatrix} 0 & 0 & 0 & -1 \\ 0 & 0 & 1 & 0 \\ 0 & 1 & 0 & 0 \\ -1 & 0 & 0 & 0 \end{pmatrix}.$$

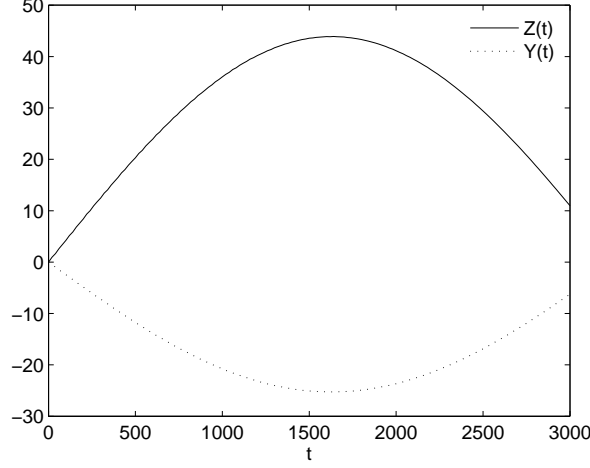


Figure 2.13:  $Z(t)$  and  $Y(t)$  for the rotated elliptic oscillator of the second test. The solid line is  $Z(t)$ , while the dotted one is  $Y(t)$ . In this second test, the parameters are as follows:  $N_z = N_y = 1024$ ,  $a^2 = 1$ ,  $b^2 = 2$ ,  $m = 1/4$ ,  $\omega_0 = 1/1024$ ,  $v_{z'} = 0.05$ ,  $v_{y'} = 0.0$  and  $\alpha = \pi/6$ . Space and time are expressed in lattice units.

By using the sequential splitting method, we consider the sequence of three initial value problems for  $(n-1)\Delta t < t \leq n\Delta t$

$$\begin{cases} \partial_t \psi_1^n + cA^x \partial_x \psi_1^n = \frac{\omega_c}{3} C \psi_1^n + i \frac{g}{3} \psi_1^n, \\ \psi_1^n[(n-1)\Delta t] = \psi_3^{n-1}[(n-1)\Delta t], \end{cases} \quad (2.26)$$

$$\begin{cases} \partial_t \psi_2^n + cA^y \partial_y \psi_2^n = \frac{\omega_c}{3} C \psi_2^n + i \frac{g}{3} \psi_2^n, \\ \psi_2^n[(n-1)\Delta t] = \psi_1^n(n\Delta t), \end{cases}$$

and

$$\begin{cases} \partial_t \psi_3^n + cA^z \partial_z \psi_3^n = \frac{\omega_c}{3} C \psi_3^n + i \frac{g}{3} \psi_3^n, \\ \psi_3^n[(n-1)\Delta t] = \psi_2^n(n\Delta t). \end{cases}$$

To start the procedure, we set  $\psi_3^0(0) = \psi_0$  and  $\psi_{sp}(x, y, z, n\Delta t) = \psi_3^n(x, y, z, n\Delta t)$  is the splitting solution of the problem.

The three-dimensional problem is now subdivided into three one-dimensional problems which can be numerically solved by using the lattice Boltzmann model proposed for the one-dimensional case.

The collision matrix  $\hat{Q}_g$  is different from  $Q$  of Eq. (1.36) due to the factor  $1/3$  in



front of the scattering matrix  $C$ , in particular, it reads

$$\hat{Q}_g = \begin{pmatrix} \hat{a}_g & 0 & 0 & \hat{b}_g \\ 0 & \hat{a}_g & \hat{b}_g & 0 \\ 0 & -\hat{b}_g & \hat{a}_g & 0 \\ -\hat{b}_g & 0 & 0 & \hat{a}_g \end{pmatrix},$$

where

$$\hat{a}_g = \frac{1 - \Omega_3/4}{1 + \Omega_2/4 - i\tilde{g}_3}, \quad \hat{b}_g = \frac{\tilde{m}_3}{1 + \Omega_3/4 - i\tilde{g}_3},$$

with

$$\Omega_3 = \tilde{m}_3^2 - \tilde{g}_3^2, \quad \tilde{m}_3 = \tilde{m}/3, \quad \tilde{g}_3 = \tilde{g}/3,$$

and  $\tilde{m} = \omega_c \Delta t$ ,  $\tilde{g} = g \Delta t$ .

Note that, in order to solve Eq. (2.26) with the one-dimensional qLB scheme,  $A^x$  needs to be diagonalized. A possible choice for the transformation matrix is given by

$$X = \frac{1}{\sqrt{2}} \begin{pmatrix} 1 & 0 & -1 & 0 \\ 0 & -1 & 0 & 1 \\ 1 & 0 & 1 & 0 \\ 0 & 1 & 0 & 1 \end{pmatrix}.$$

For the free particle case ( $V = 0$ ), by defining the wave functions

$$\phi_{1,2}^\pm = \frac{1}{\sqrt{2}} \exp(i\omega_c t)(u_{1,2} \pm id_{2,1}),$$

it is possible to verify that, since  $\psi$  is solution of Eq. (2.25), then the symmetric and antisymmetric modes  $\phi_{1,2}^\pm$  satisfy the following equations:

$$\partial_t \phi_1^+ + c \partial_z \phi_1^- - ic \partial_y \phi_2^- - ic \partial_x \phi_1^- = 0, \quad (2.27)$$

$$\partial_t \phi_2^+ + c \partial_z \phi_2^- - ic \partial_y \phi_1^- + ic \partial_x \phi_2^- = 0, \quad (2.28)$$

and

$$\partial_t \phi_1^- + c \partial_z \phi_1^+ + ic \partial_y \phi_2^+ + ic \partial_x \phi_1^+ = 2i\omega_c \phi_1^-, \quad (2.29)$$

$$\partial_t \phi_2^- + c \partial_z \phi_2^+ + ic \partial_y \phi_1^+ - ic \partial_x \phi_2^+ = 2i\omega_c \phi_2^-. \quad (2.30)$$

From Eqs. (2.29) and (2.30), after adiabatic elimination of the fast antisymmetric modes  $|\partial_t \phi_{1,2}^-| \ll 2\omega_c |\phi_{1,2}^-|$ , we obtain

$$\phi_1^- \approx \frac{c}{2i\omega_c} (\partial_z \phi_1^+ + i\partial_y \phi_2^+ + i\partial_x \phi_1^+),$$

$$\phi_2^- \approx \frac{c}{2i\omega_c} (\partial_z \phi_2^+ + i\partial_y \phi_1^+ - i\partial_x \phi_2^+),$$

and substituting into Eqs. (2.27) and (2.28), we obtain the three-dimensional Schrödinger equation for a free particle of mass  $m$ :

$$i\hbar \partial_t \phi_{1,2}^+ = -\frac{\hbar^2}{2m} (\partial_x^2 + \partial_y^2 + \partial_z^2) \phi_{1,2}^+.$$

### 2.6.1 Three-dimensional harmonic oscillator

In order to test the isotropy of the three dimensional model, we simulate a three dimensional harmonic oscillator potential:

$$V(x, y, z) = \frac{1}{2}m\omega_0^2[(x - x_0)^2 + (y - y_0)^2 + (z - z_0)^2],$$

and we show that by fixing  $\Delta_{0x} = \Delta_{0y} = \Delta_{0z} \equiv \Delta_0$  such that

$$\omega_0 = \frac{1}{2m\Delta_0^2}, \quad (2.31)$$

the packet spreading is kept constant all along the evolution.

For this test we set  $N_x = N_y = N_z = 100$ ,  $\Delta_0 = 14$ ,  $m = 0.1$ ,  $v_x = v_y = v_z = 0$ , the initial condition is given by the three-dimensional minimum uncertainty wave packet and periodic boundary conditions are imposed. With this setting, from Eq. (2.31), we obtain  $\omega_0 = 0.02551$ . The numerical values given by the model for  $\Delta_x$ ,  $\Delta_y$  and  $\Delta_z$  averaged over a quarter of a period are

$$\Delta_x = 15.35 \pm 1.38, \quad \Delta_y = 14.40 \pm 0.88, \quad \Delta_z = 15.47 \pm 1.50.$$

Let us consider the radius  $r$  defined as  $r^2 = (x - x_0)^2 + (y - y_0)^2 + (z - z_0)^2$ , where the point  $(x_0, y_0, z_0)$  is the center of the initial Gaussian packet and, for this test, corresponds to the center of the computational domain  $(N_x/2, N_y/2, N_z/2)$ . In Fig. 2.14, a scatter plot of  $|\phi^+(x, y, z)|^2$  against  $r^2$  at time  $t = T/4$  (where  $T$  is the harmonic oscillator period,  $T = 2\pi/\omega_0 \approx 250$  lattice units) is reported in order to show the degree of isotropy of the model. In the figure, results are shown for  $r^2 < (3\Delta_0)^2$ , because for larger values of  $r^2$ ,  $|\phi^+|^2$  takes such small values that a statistical behavior is no more observable. To be noted that due to the exponential dependence of  $|\phi^+|^2$  on the radius ( $|\phi^+|^2 \sim e^{-r^2/(2\Delta_0^2)}$ ), even mild lack of isotropy results in large (exponential) fluctuations in the large-radius region of the scatter plot representation. This is well shown in Fig. 2.14. In particular, for  $r^2 < \Delta_0^2$ , the linear dependence of  $\log(|\phi^+|^2)$  from  $r^2$  is clearly visible and a minimum scatter is shown. For increasing values of  $r^2$ , however, the scatter also increases. Finally, for  $r^2$  close to  $(3\Delta_0)^2$  the boundary conditions effects start to show up. In fact, we note that the solution is not affected by periodic boundary conditions as long as the wave function remains negligible at the boundary. Going much further on time with this setting is not possible since the effect due to the boundary conditions will propagate into the domain compromising the solution even for smaller values of  $r^2$ . To overcome this limitation, a much larger domain should be used or different boundary conditions should be imposed.

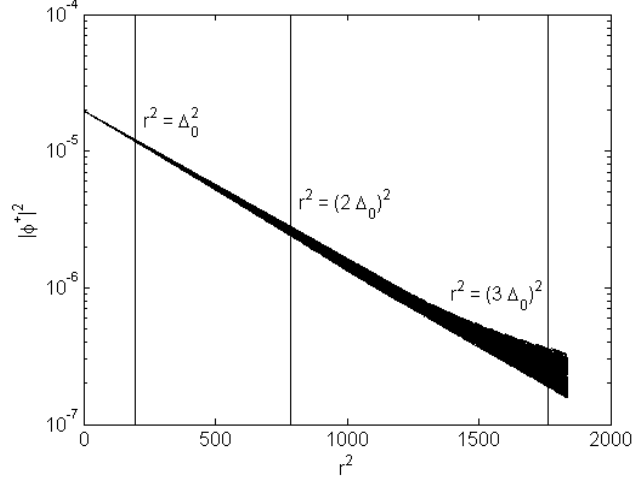


Figure 2.14: Scatter plot of  $|\phi^+(x, y, z)|^2$  against  $r^2$  for a three dimensional harmonic oscillator with parameters:  $N_x = N_y = N_z = 100$ ,  $m = 0.1$ ,  $v_x = v_y = v_z = 0$ ,  $\Delta_0 = 14$  and  $\omega_0 = 0.02551$  at time  $t = T/4$ .  $|\phi^+(x, y, z)|^2$  is represented on a logarithmic scale in order to show its linear dependence from  $r^2$ . Here, coordinates  $x$ ,  $y$  and  $z$  are expressed in lattice units.

In conclusion, the above results explicitly demonstrates the viability of the quantum lattice Boltzmann (qLB) scheme for the numerical solution of the time-dependent Schrödinger equation in *multiple* spatial dimensions. Being based on a unitary, first-order, relativistic formulation, at variance with most explicit schemes for non-relativistic quantum wave equations, the qLB method offers unconditioned stability with the size of the time-step/mesh-size provided that  $\Delta z = c\Delta t$ . However, as previously mentioned, its accuracy is subject to the condition  $\omega_c\Delta t = \Delta z/\lambda_B \leq 1$ ,  $\lambda_B = c/\omega_c$  being the De Broglie wavelength of the particle. Since the time-step scales linearly with the mesh-spacing (a result of the relativistic formulation), qLB can be taken down to very refined grids without suffering the time-step collapse typical of non-relativistic Courant-Friedrichs-Lewy stability conditions,  $\Delta t < \frac{2m}{\hbar} \Delta z^2$ , thus compensating for its low-order accuracy. However, care must be taken to ensure that errors due to lack of adiabaticity remain under control when  $\omega_c\Delta t$  is sent to zero.



## Chapter 3

# Ground state computation of Bose–Einstein condensates

The staggering achievements in Bose-Einstein condensation [38, 90] over the last decade are fueling an increasing demand of efficient and accurate computational schemes for the numerical solution of nonlinear quantum wave equations, most notably, the Gross-Pitaevskii equation (GPE) describing zero-temperature Bose-Einstein condensates (BEC) [63, 117]. In particular, the time-independent GPE has been numerically solved by using several approaches: Runge-Kutta methods [53, 1], explicit imaginary-time algorithms [33, 35, 10, 13] and direct minimization of the energy functional [12]. In Ref. [108], we propose an imaginary-time quantum lattice Boltzmann (qLB) model obtained by performing a so-called Wick rotation of the original, real-time qLB scheme.

In this chapter, which is an extended version of the paper in Ref. [108], the nonlinear qLB is defined and applied to the numerical computation of the ground-state of the GPE in one and two spatial dimensions, and its viability demonstrated through systematic comparison with numerical solutions obtained via standard implicit methods, as well as with analytical results based on the Thomas-Fermi approximation. For completeness, in Sec. 3.1 and Sec. 3.2, we briefly introduce the time-dependent and time-independent GPE, respectively.

### 3.1 The time-dependent Gross–Pitaevskii equation

At zero temperature, the dynamics of a trapped Bose–Einstein condensates (BEC) is described by the time-dependent Gross–Pitaevskii equation (GPE). The GPE

for a quantum wave function  $\psi(\mathbf{r}, t)$  with  $\mathbf{r} = (x, y, z)^T \in \mathbb{R}^3$  reads as:

$$i\hbar \frac{\partial \psi(\mathbf{r}, t)}{\partial t} = \left( -\frac{\hbar^2}{2m} \Delta_{\mathbf{r}} + V_{ext}(\mathbf{r}) + NU_0 |\psi(\mathbf{r}, t)|^2 \right) \psi(\mathbf{r}, t), \quad (3.1)$$

where  $m$  is the atomic mass,  $U_0 = 4\pi\hbar^2 a/m$  is the coupling strength,  $a$  is the scattering length and  $N$  is the number of particles in the condensate,  $V_{ext}(\mathbf{r})$  is the external trapping potential. Furthermore, the wave function  $\psi(\mathbf{r}, t)$  satisfies the normalization condition

$$\int_{\mathbb{R}^3} |\psi(\mathbf{r}, t)|^2 d\mathbf{r} = 1.$$

Typically, the external potential is taken in the form of an harmonic trap:

$$V_{ext}(x, y, z) = \frac{1}{2}m(\omega_x^2(x - x_0)^2 + \omega_y^2(y - y_0)^2 + \omega_z^2(z - z_0)^2).$$

The three dimensional GPE can be reduced to two dimensions or even one dimension for two particular choices of the harmonic trap [72, 88, 12, 1]. We briefly revisit this reduction procedure following [12].

- Disk-shaped condensation:

$$\omega_z \approx \omega_y, \quad \omega_x \gg \omega_z.$$

The three dimensional GPE of Eq. (3.1) can be reduced to a two dimensional GPE by assuming that the time evolution does not affect the wave function along the  $x$ -axis. Thus, one assumes that the wave function along  $x$  is always well described by the ground state wave function  $\phi_g(x, y, z)$ :

$$\psi(x, y, z, t) = \psi_{zy}(z, y, t)\psi_x(x) \quad \text{with} \quad \psi_x(x) = \left( \int_{\mathbb{R}^2} |\phi_g(x, y, z)|^2 dz dy \right)^{1/2}.$$

By means of this assumption the GPE of Eq. (3.1) is reduced to a two dimensional GPE for  $\mathbf{r} = (z, y)^T$  of the same form of Eq. (3.1), where the coupling strength is now given by

$$\tilde{U}_0 = U_0 \int_{\mathbb{R}} \psi_x^4(x) dx.$$

- Cigar-shaped condensation:

$$\omega_x \gg \omega_z, \quad \omega_y \gg \omega_z.$$

In this case, the three dimensional GPE can be reduced to a one dimensional GPE for  $\mathbf{r} = z$ . As in the previous case, one assumes that the wave function along  $x$  and  $y$  is always well described by the ground state  $\phi_g(x, y, z)$ :

$$\psi(x, y, z, t) = \psi_z(z, t)\psi_{xy}(x, y) \quad \text{with} \quad \psi_{xy}(x, y) = \left( \int_{\mathbb{R}} |\phi_g(x, y, z)|^2 dz \right)^{1/2}.$$

The GPE of Eq. (3.1) is then reduced to a one dimensional GPE of the same form, where the coupling strength is given by

$$\tilde{U}_0 = U_0 \int_{\mathbb{R}^2} \psi_{xy}^4(x, y) dx dy.$$

In the following we will consider the GPE in the following form

$$i\hbar \frac{\partial \psi(\mathbf{r}, t)}{\partial t} = \left( -\frac{\hbar^2}{2m} \Delta_{\mathbf{r}} + V_{ext}(\mathbf{r}) + NU_d |\psi(\mathbf{r}, t)|^2 \right) \psi(\mathbf{r}, t), \quad (3.2)$$

for  $\mathbf{r} \in \mathbb{R}^d$  with  $d = 1, 2, 3$  and

$$U_d = \begin{cases} U_0 \int_{\mathbb{R}^2} \psi_{xy}^4 dx dy, & d = 1 \\ U_0 \int_{\mathbb{R}} \psi_x^4 dx, & d = 2 \\ U_0, & d = 3 \end{cases}. \quad (3.3)$$

Furthermore, we require

$$\int_{\mathbb{R}^d} |\psi(\mathbf{r})|^2 d\mathbf{r} = 1.$$

However, in this work, we solve Eq. (3.2) in one and two dimensions using  $NU_d$  as a coupling parameter. In particular, we do not compute  $U_d$  from Eq. (3.3), we simply consider the value of  $NU_d \equiv V_{nl}$  as a measure of the interaction strength. Moreover, we do not use the classical scaling usually applied to make the GPE dimensionless, but a qLB scaling (see Sec. 3.11 for details) which transforms Eq. (3.1) into

$$i \frac{\partial \psi(\mathbf{r}, t)}{\partial t} = \left( -\frac{1}{2\tilde{m}} \Delta_{\mathbf{r}} + V_{ext}(\mathbf{r}) + V_{nl} |\psi(\mathbf{r}, t)|^2 \right) \psi(\mathbf{r}, t), \quad (3.4)$$

where all quantities are expressed in lattice units and  $\tilde{m} = \omega_c \Delta t$ . Unless differently stated, in our numerical examples  $V_{ext}(\mathbf{r})$  is an harmonic potential in one and two dimensions and is given by:

$$V_{ext}(z) = \frac{1}{2} \tilde{m} \omega_z^2 (z - z_0)^2, \quad d = 1, \quad (3.5)$$

$$V_{ext}(z, y) = \frac{1}{2} \tilde{m} (\omega_z^2 (z - z_0)^2 + \omega_y^2 (y - y_0)^2), \quad d = 2, \quad (3.6)$$

where again lattice units are used.

### 3.2 The ground state solution of the GPE

Following [10, 13], we derive the nonlinear eigenvalue problem from which one can compute the ground state solution of the GPE of Eq. (3.2).

In order to find a stationary solution of Eq. (3.2), we set

$$\psi(\mathbf{r}, t) = e^{-i\mu t/\hbar} \phi(\mathbf{r}), \quad (3.7)$$

where  $\mu$  is the chemical potential of the condensate and  $\phi(\mathbf{r})$  is a real-valued function independent of time. Inserting Eq. (3.7) into Eq. (3.2), we find the following equation for  $\phi(\mathbf{r})$ :

$$\mu \phi(\mathbf{r}) = \left( -\frac{\hbar^2}{2m} \Delta \mathbf{r} + V_{ext}(\mathbf{r}) + NU_d |\phi(\mathbf{r})|^2 \right) \phi(\mathbf{r}), \quad (3.8)$$

with the normalization condition

$$\int_{\mathbb{R}^d} |\phi(\mathbf{r})|^2 d\mathbf{r} = 1. \quad (3.9)$$

This is a nonlinear eigenvalue problem under a constraint and any eigenvalue  $\mu$  can be computed from its corresponding eigenfunction  $\phi$ . In particular, multiplying Eq. (3.7) by  $\phi(\mathbf{r})$  and integrating we obtain

$$\mu = \int_{\mathbb{R}^d} \left( -\frac{\hbar^2}{2m} (\Delta \mathbf{r} \phi(\mathbf{r})) \phi(\mathbf{r}) + V_{ext}(\mathbf{r}) |\phi(\mathbf{r})|^2 + NU_d |\phi(\mathbf{r})|^4 \right) d\mathbf{r}.$$

Thus, integrating by parts the first term of the right hand side, we have

$$\mu = \int_{\mathbb{R}^d} \left( \frac{\hbar^2}{2m} |\nabla \mathbf{r} \phi(\mathbf{r})|^2 + V_{ext}(\mathbf{r}) |\phi(\mathbf{r})|^2 + NU_d |\phi(\mathbf{r})|^4 \right) d\mathbf{r}. \quad (3.10)$$

The ground state solution of the Bose–Einstein condensate,  $\phi_g(\mathbf{r})$ , is a real-valued function which can be found by minimizing Eq. (3.10) under the constraint of Eq. (3.9). Typically, this minimizer is found by applying to Eq. (3.2) a transformation, known as Wick rotation, which consists on “rotating” the time axis on the complex plane so that time becomes purely imaginary [2, 33, 35, 100]. With this rotation of the time axis, the GPE of Eq. (3.2) becomes a diffusion equation with an absorption/emission term given by the potential.

Wick rotation consists of introducing an imaginary variable  $\tau$  which is related to the time  $t$  by the relation  $t = -i\tau$ . Applying this transformation to Eq. (3.2), we have

$$\hbar \frac{\partial \psi(\mathbf{r}, \tau)}{\partial \tau} = \left( \frac{\hbar^2}{2m} \Delta \mathbf{r} - V_{ext}(\mathbf{r}) - NU_d |\psi(\mathbf{r}, \tau)|^2 \right) \psi(\mathbf{r}, \tau). \quad (3.11)$$

Finally, our problem is to solve Eq. (3.11) under the constraint

$$\int_{\mathbb{R}^d} |\psi(\mathbf{r}, t)|^2 d\mathbf{r} = 1. \quad (3.12)$$



Applying the qLB scaling (see Sec. 3.11) to Eq. (3.11) and hence expressing all quantities in lattice units, Eq. (3.11) becomes

$$\frac{\partial \psi(\mathbf{r}, \tau)}{\partial \tau} = \left( \frac{1}{2\tilde{m}} \Delta_{\mathbf{r}} - V_{ext}(\mathbf{r}) - V_{nl} |\psi(\mathbf{r}, \tau)|^2 \right) \psi(\mathbf{r}, \tau), \quad (3.13)$$

where  $\tilde{m} = \omega_c \Delta t$  and  $V_{ext}(\mathbf{r})$  is given by Eqs. (3.5) and (3.6).

### 3.3 The imaginary-time quantum lattice Boltzmann model

The model we propose is obtained by applying the Wick rotation to the quantum lattice Boltzmann model [138, 133, 105]. We recall that the qLB is based on a formal analogy between the Dirac quadrispinor  $\boldsymbol{\psi} = (u_1, u_2, d_1, d_2)^T$  and the discrete distribution functions of the lattice Boltzmann equation [138]. As shown in the previous chapter, by using an operator splitting approach, the model can be easily extended to two and three dimensions [138, 105].

In this section, we show that, by applying the Wick rotation to the qLB model, we obtain a scheme for the computation of the ground state solution for the GPE. For the sake of simplicity, we first describe the scheme in one and two dimensions for the free-particle case ( $V_{ext} = 0$  and  $V_{nl} = 0$ ), and subsequently discuss how to include interactions in the model.

#### 3.3.1 Imaginary-time qLB in one dimension

Consider the Dirac equation in one dimension. Using the Majorana representation [87], and projecting upon chiral eigenstates, the Dirac equation reads

$$\begin{aligned} \partial_t u_{1,2} + c \partial_z u_{1,2} &= \omega_c d_{2,1} \\ \partial_t d_{1,2} - c \partial_z d_{1,2} &= -\omega_c u_{2,1}, \end{aligned} \quad (3.14)$$

where  $\omega_c = mc^2/\hbar$  is the Compton frequency.

We introduce the imaginary variable  $\tau = it$  and write Eq. (3.14) in terms of  $\tau$ :

$$\begin{aligned} \partial_\tau u_{1,2} - ic \partial_z u_{1,2} &= -i\omega_c d_{2,1} \\ \partial_\tau d_{1,2} + ic \partial_z d_{1,2} &= i\omega_c u_{2,1}. \end{aligned} \quad (3.15)$$

Let  $\Delta\tau = i\Delta t$  be the time discretization step (note that  $\Delta\tau$  is a purely imaginary number) and  $\Delta z = -ic\Delta\tau$  the spatial discretization step. Integrating Eq. (3.15) between  $\tau$  and  $\tau + \Delta\tau$  and approximating the right hand side integral by

$$\begin{aligned} \int_\tau^{\tau+\Delta\tau} d_{2,1}(z, \tau) d\tau &\sim \frac{1}{2} \Delta t (d_{2,1}(z - \Delta z, \tau + \Delta\tau) + d_{2,1}(z, \tau)), \\ \int_\tau^{\tau+\Delta\tau} u_{2,1}(z, \tau) d\tau &\sim \frac{1}{2} \Delta t (u_{2,1}(z + \Delta z, \tau + \Delta\tau) + u_{2,1}(z, \tau)), \end{aligned}$$

we obtain

$$\begin{aligned}
u_{1,2}(z + \Delta z, \tau + \Delta \tau) - u_{1,2}(z, \tau) &= \\
&- i \frac{\omega_c}{2} (d_{2,1}(z - \Delta z, \tau + \Delta \tau) + d_{2,1}(z, \tau)) \Delta t, \\
d_{1,2}(z - \Delta z, \tau + \Delta \tau) - d_{1,2}(z, \tau) &= \\
&i \frac{\omega_c}{2} (u_{2,1}(z + \Delta z, \tau + \Delta \tau) + u_{2,1}(z, \tau)) \Delta t.
\end{aligned} \tag{3.16}$$

By defining

$$\omega_c \Delta t \equiv \tilde{m},$$

we obtain

$$\begin{aligned}
\hat{u}_{1,2} - u_{1,2} &= -i\tilde{m} \left( \frac{\hat{d}_{2,1} + d_{2,1}}{2} \right), \\
\hat{d}_{1,2} - d_{1,2} &= i\tilde{m} \left( \frac{\hat{u}_{2,1} + u_{2,1}}{2} \right),
\end{aligned} \tag{3.17}$$

where  $\hat{u}_{1,2} = u_{1,2}(z + \Delta z, \tau + \Delta \tau)$ ,  $\hat{d}_{1,2} = d_{1,2}(z - \Delta z, \tau + \Delta \tau)$ ,  $u_{1,2} = u_{1,2}(z, \tau)$  and  $d_{1,2} = d_{1,2}(z, \tau)$ .

The system of Eq. (3.17) can be algebraically solved for  $\hat{u}_{1,2}$  and  $\hat{d}_{1,2}$  and yields the imaginary-time qLB model in explicit form:

$$\begin{aligned}
\hat{u}_{1,2} &= au_{1,2} - bd_{2,1}, \\
\hat{d}_{1,2} &= ad_{1,2} + bu_{2,1},
\end{aligned} \tag{3.18}$$

where

$$a = \frac{1 + \tilde{m}^2/4}{1 - \tilde{m}^2/4}, \quad b = \frac{i\tilde{m}}{1 - \tilde{m}^2/4}. \tag{3.19}$$

Note that  $|a|^2 + |b|^2 \neq 1$ , hence the collision matrix is not unitary. This implies that the model does not verify the normalization condition, as it happens for the real-time version of the scheme. This is usual for models which compute the ground state solution by solving dynamic equations in fictitious time, such as Eq. (3.11). Hence, the normalization condition of Eq. (3.12) must be imposed at each time step by directly normalizing the wave function [35, 10, 13].

In analogy with the real-time qLB, we define the wave functions

$$\phi_{1,2}^\pm = \frac{1}{\sqrt{2}} e^{\omega_c \tau} (u_{1,2} \pm i d_{2,1}). \tag{3.20}$$

Since  $u_{1,2}$  and  $d_{1,2}$  fulfill Eq. (3.15),  $\phi_{1,2}^\pm$  satisfy the following equations

$$\partial_\tau \phi_{1,2}^+ - ic \partial_z \phi_{1,2}^- = 0, \tag{3.21}$$

$$\partial_\tau \phi_{1,2}^- - ic \partial_z \phi_{1,2}^+ = 2\omega_c \phi_{1,2}^-. \tag{3.22}$$

By taking the  $z$  derivative of Eq. (3.21), multiplying Eq. (3.22) by  $i$  and deriving it with respect to  $\tau$  and then subtracting the resulting equations, we obtain the following equation for  $\phi_{1,2}^-$

$$\hbar \partial_\tau \phi_{1,2}^- = \frac{\hbar^2}{2m} \partial_z^2 \phi_{1,2}^- + \frac{\hbar^2}{2\omega_c} \partial_\tau^2 \phi_{1,2}^- \quad (3.23)$$

The second order time derivative term drives an instability which tends to amplify  $\phi_{1,2}^-$  while preserving its spatial profile. However, the normalization step tames the effect of this term. We will clarify this point in the following, through the analysis of the dispersion relation of the governing equation for  $\phi_{1,2}^-$  when a potential is switched on (see Sec. 3.5). Here, we just observe that, for the free-particle case ( $V_{ext} = 0$  and  $V_{nl} = 0$ ),  $\phi_{1,2}^-$  obey a diffusion equation with the correct diffusion coefficient (see Eq. (3.13)).

The wave functions  $\phi_{1,2}^-$  are the ones whose dynamics tends to the ground state solution of the GPE, while the wave functions  $\phi_{1,2}^+$  are “ghost” variables, which are initialized at zero and remain negligible all along the simulation, as compared to  $\phi_{1,2}^-$ .

When a potential is included, the analysis of the governing equation for  $\phi_{1,2}^-$  is not as simple as in the free-particle case. Hence, in the following subsection, we show how to include the potential effect in the model, while in Sec. 3.5 we discuss in a more detail the equation satisfied by  $\phi_{1,2}^-$  in the interacting case.

### 3.3.2 Adding a potential to the imaginary-time qLB

As we mentioned above, the wave functions  $\phi_{1,2}^-$  tends to the ground state solution, hence, in the imaginary-time qLB, the total potential of the GPE of Eq. (3.2) in one spatial dimension is defined as follows:

$$V(x, \tau) = V_{ext}(x) + V_{nl} |\phi^-|^2, \quad (3.24)$$

where  $|\phi^-|^2 \equiv |\phi_1^-|^2 + |\phi_2^-|^2$ . To include the effect of this potential into the model, we consider the Dirac equation with a potential and apply to this equation the Wick rotation. This yields

$$\begin{aligned} \partial_\tau u_{1,2} - ic \partial_z u_{1,2} &= -i\omega_c d_{2,1} + g u_{1,2} \\ \partial_\tau d_{1,2} + ic \partial_z d_{1,2} &= i\omega_c u_{2,1} + g d_{1,2}, \end{aligned} \quad (3.25)$$

where  $g = qV/\hbar$  and  $q$  is the particle electric charge.

Applying to Eqs. (3.25) the same discretization already described for the free particle case, we obtain the following scheme

$$\begin{aligned} \hat{u}_{1,2} &= a_g u_{1,2} - b_g d_{2,1}, \\ \hat{d}_{1,2} &= a_g d_{1,2} + b_g u_{2,1}, \end{aligned} \quad (3.26)$$

where

$$a_g = \frac{(1 - \tilde{g}/2)(1 + \tilde{g}/2) + \tilde{m}^2/4}{(1 - \tilde{g}/2)^2 - \tilde{m}^2/4}, \quad b_g = \frac{i\tilde{m}}{(1 - \tilde{g}/2)^2 - \tilde{m}^2/4}, \quad (3.27)$$

and  $\tilde{m} = \omega_c \Delta t$ ,  $\tilde{g} = g \Delta t$ ,  $\hat{u}_{1,2} = u_{1,2}(z + \Delta z, \tau + \Delta \tau)$ ,  $\hat{d}_{1,2} = d_{1,2}(z - \Delta z, \tau + \Delta \tau)$ ,  $u_{1,2} = u_{1,2}(z, \tau)$  and  $d_{1,2} = d_{1,2}(z, \tau)$ . Note that  $g$  is evaluated at time  $\tau$ , i. e. there is no iteration over the nonlinearity. For real-time computations this might hamper norm-conservation, but in the case of the present ground-state computations this is not an issue because the norm is not conserved in time due to the potential interactions.

### 3.4 Extension to two spatial dimensions

As for the real-time qLB, we describe how to extend the model to two spatial dimensions (extension to three dimensions is a straightforward generalization of this procedure) in the absence of a potential. The inclusion of a potential is completely analogous to the one dimensional case.

The extension to higher dimensions is based on an operator splitting approach and follows the strategy already used to extend the real-time qLB model to the two and three-dimensional case [138, 105] (see Chapter 2).

Let us consider the two dimensional Dirac equation in Majorana form [87], so that all spin matrices have real coefficients. Furthermore, we apply to the equation a transformation in order to diagonalize the matrix of the  $\partial_z \psi$  term. With these assumptions, the equation reads

$$[\partial_t + cA^z \partial_z + cA^y \partial_y] \psi(z, y, t) = \omega_c C \psi(z, y, t), \quad (3.28)$$

where

$$A^z = \begin{pmatrix} 1 & 0 & 0 & 0 \\ 0 & 1 & 0 & 0 \\ 0 & 0 & -1 & 0 \\ 0 & 0 & 0 & -1 \end{pmatrix} \quad A^y = \begin{pmatrix} 0 & 0 & -1 & 0 \\ 0 & 0 & 0 & -1 \\ -1 & 0 & 0 & 0 \\ 0 & -1 & 0 & 0 \end{pmatrix} \quad C = \begin{pmatrix} 0 & 0 & 0 & 1 \\ 0 & 0 & 1 & 0 \\ 0 & -1 & 0 & 0 \\ -1 & 0 & 0 & 0 \end{pmatrix}.$$

Applying to Eq. (3.28) the Wick rotation, we obtain

$$[\partial_\tau + c\tilde{A}^z \partial_z + c\tilde{A}^y \partial_y] \psi(z, y, \tau) = \omega_c \tilde{C} \psi(z, y, \tau), \quad (3.29)$$

where

$$\tilde{A}^z = \begin{pmatrix} -i & 0 & 0 & 0 \\ 0 & -i & 0 & 0 \\ 0 & 0 & i & 0 \\ 0 & 0 & 0 & i \end{pmatrix} \quad \tilde{A}^y = \begin{pmatrix} 0 & 0 & i & 0 \\ 0 & 0 & 0 & i \\ i & 0 & 0 & 0 \\ 0 & i & 0 & 0 \end{pmatrix} \quad \tilde{C} = \begin{pmatrix} 0 & 0 & 0 & -i \\ 0 & 0 & -i & 0 \\ 0 & i & 0 & 0 \\ i & 0 & 0 & 0 \end{pmatrix}.$$

To solve Eq. (3.29) we use the same sequential splitting technique already introduced for the real-time qLB [105]. In particular, in the interval  $[(n-1)\Delta\tau, n\Delta\tau]$ , we consider the sequence of the two problems:

$$\begin{cases} (\partial_\tau + c\tilde{A}^z\partial_z)\psi_1^n = \frac{\omega_c}{2}\tilde{C}\psi_1^n \\ \psi_1^n[(n-1)\Delta\tau] = \psi_2^{n-1}[(n-1)\Delta\tau], \end{cases} \quad (3.30)$$

and

$$\begin{cases} (\partial_\tau + c\tilde{A}^y\partial_y)\psi_2^n = \frac{\omega_c}{2}\tilde{C}\psi_2^n \\ \psi_2^n[(n-1)\Delta\tau] = \psi_1^n(n\Delta\tau), \end{cases} \quad (3.31)$$

for  $n = 1, 2, \dots$ .

To start the procedure we set  $\psi_2^0(0) = \psi_0$  and, at time  $n\Delta\tau$ , the approximated solution is given by  $\psi_2^n(x, y, n\Delta\tau)$ .

After this splitting, the two dimensional problem of Eq. (3.29) is transformed into a sequence of two one-dimensional problems. In particular, problem of Eq. (3.30) is analogous to the system of Eq. (3.15), with the only difference being a factor  $1/2$  in front of matrix  $\tilde{C}$ . Hence, to solve Eq. (3.30), the scheme of Eq. (3.18) (or scheme of Eq. (3.26) if the potential is switched on) is used, where  $a$  and  $b$  (or  $a_g$  and  $b_g$ ) are slightly changed due to the factor  $1/2$ . In particular,  $a$  and  $b$  are turned into

$$\hat{a} = \frac{1 + \tilde{m}_2^2/4}{1 - \tilde{m}_2^2/4}, \quad \hat{b} = \frac{i\tilde{m}_2}{1 - \tilde{m}_2^2/4}, \quad (3.32)$$

while  $a_g$  and  $b_g$  become

$$\hat{a}_g = \frac{(1 - \tilde{g}_2/2)(1 + \tilde{g}_2/2) + \tilde{m}_2^2/4}{(1 - \tilde{g}_2/2)^2 - \tilde{m}_2^2/4}, \quad \hat{b}_g = \frac{i\tilde{m}_2}{(1 - \tilde{g}_2/2)^2 - \tilde{m}_2^2/4}, \quad (3.33)$$

with  $\tilde{m}_2 = \tilde{m}/2$  and  $\tilde{g}_2 = \tilde{g}/2$ .

In order to solve problem of Eq. (3.31) by means of a qLB scheme, the equation must be transformed into an equivalent one where matrix  $\tilde{A}^y$  is diagonal. In practice, we apply to  $\tilde{A}^y$ ,  $\tilde{C}$  and  $\psi$  the transformation  $Y$ :

$$Y = \frac{1}{\sqrt{2}} \begin{pmatrix} -1 & 0 & 0 & 1 \\ 0 & -1 & 1 & 0 \\ 1 & 0 & 0 & 1 \\ 0 & 1 & 1 & 0 \end{pmatrix}.$$

After this transformation, writing explicitly Eq. (3.31), we obtain

$$\begin{aligned} \partial_\tau u_{1,2}^y - ic\partial_y u_{1,2}^y &= i\frac{\omega_c}{2}d_{1,2} \\ \partial_\tau d_{1,2}^y + ic\partial_y d_{1,2}^y &= -i\frac{\omega_c}{2}u_{1,2}, \end{aligned} \quad (3.34)$$

where we indicate with  $u_{1,2}^y$  and  $d_{1,2}^y$  the components of the transformed quadrispinor  $\psi^y = Y\psi$ .

Form Eq. (3.34), using the same discretization scheme already described in the one dimensional case, we obtain

$$\begin{aligned}\hat{u}_{1,2}^y &= \hat{a}u_{1,2}^y + \hat{b}d_{1,2}^y \\ \hat{d}_{1,2}^y &= \hat{a}d_{1,2}^y - \hat{b}u_{1,2}^y,\end{aligned}$$

with  $\hat{a}$  and  $\hat{b}$  as in Eq. (3.32) (or as in Eq. (3.33) if we include the potential). Finally, we return to the original wave function via the inverse transformation  $\psi = Y^{-1}\psi^y$ .

As in one dimension, we define the wave functions  $\phi_{1,2}^\pm$

$$\phi_{1,2}^\pm = \frac{1}{\sqrt{2}}e^{\omega_c\tau}(u_{1,2} \pm id_{2,1}).$$

Since  $u_{1,2}$  and  $d_{1,2}$  fulfill Eq. (3.29), we have

$$\partial_\tau\phi_1^+ - ic\partial_z\phi_1^- - c\partial_y\phi_2^- = 0, \quad (3.35)$$

$$\partial_\tau\phi_2^+ - ic\partial_z\phi_2^- - c\partial_y\phi_1^- = 0, \quad (3.36)$$

and

$$\partial_\tau\phi_1^- - ic\partial_z\phi_1^+ + c\partial_y\phi_2^+ = 2\omega_c\phi_1^-, \quad (3.37)$$

$$\partial_\tau\phi_2^- - ic\partial_x\phi_2^+ + c\partial_y\phi_1^+ = 2\omega_c\phi_2^-. \quad (3.38)$$

By deriving Eq. (3.35) with respect to  $z$ , multiplying Eq. (3.36) by  $i$  and deriving it with respect to  $y$ , multiplying Eq. (3.37) by  $-i$  and deriving it with respect to  $\tau$  and finally summing up the resulting equations, we obtain

$$\hbar\partial_\tau\phi_1^- = \frac{\hbar^2}{2m}(\partial_z^2\phi_1^- + \partial_y^2\phi_1^-) + \frac{\hbar^2}{2\omega_c}\partial_\tau^2\phi_1^-.$$

Similarly, multiplying Eq. (3.35) by  $i$  and deriving it with respect to  $y$ , deriving Eq. (3.36) with respect to  $z$ , multiplying Eq. (3.38) by  $-i$  and deriving it with respect to  $\tau$  and finally summing up the resulting equations, we obtain

$$\hbar\partial_\tau\phi_2^- = \frac{\hbar^2}{2m}(\partial_z^2\phi_2^- + \partial_y^2\phi_2^-) + \frac{\hbar^2}{2\omega_c}\partial_\tau^2\phi_2^-.$$

In conclusion, we obtain in two dimensions the same result we have derived in one dimension (see Eq. (3.23)). The second order time derivative term represents once again an instability which is kept under control by the normalization step. The inclusion of the potential yields an equation for  $\phi_{1,2}^-$ , whose interpretation requires a more systematic analysis. To this purpose, we shall inspect the dispersion relation in order to verify that the model is solving the correct equation (see Sec. 3.5).

### 3.5 Dispersion relation for the equation governing $\phi^-$

In this section, we derive the equation satisfied by  $\phi_{1,2}^-$  and we analyze it by computing its dispersion relation. We will perform this computation only in one dimension, the two dimensional generalization is, however, straightforward. In the following the indices 1, 2 on  $\phi_{1,2}^-$  shall be dropped because the dynamics of the two wave functions is exactly the same.

In order to check that  $\phi^-$  has a correct asymptotic behavior, we derive the dispersion relation of the equation we intend to be solved by  $\phi^-$ . Hence, suppose that  $\phi^-$  is a solution of the imaginary-time GPE of Eq. (3.11). Let us rewrite Eq. (3.11) as

$$\hbar\partial_\tau\phi^- = \frac{\hbar^2}{2m}\partial_z^2\phi^- - V\phi^-, \quad (3.39)$$

where

$$V(z, \tau) = \frac{1}{2m}\omega_z^2 z^2 + V_{nl}|\phi^-|^2. \quad (3.40)$$

Note that the computation of the dispersion relation is not a rigorous procedure in this case because  $V$  is space and time dependent. However, this analysis can be useful in the limit where the potential does not change in time (because a stationary solution is reached) and is changing very slowly in space (at least in the region where  $\phi^- \neq 0$ ). Hence, locally, we can think of  $V$  as of a constant and compute the dispersion relation in the “WKB” spirit.

Assuming  $\phi^- \sim e^{i(kz - \omega\tau)/\hbar}$  and inserting this into Eq. (3.39), we obtain

$$\omega = -i \left( \frac{k^2}{2m} + V \right). \quad (3.41)$$

This is the “correct” dispersion relation we will refer to.

However,  $\phi^-$  is not solving exactly Eq. (3.39). To derive the governing equation for  $\phi^-$  we need to start from the Dirac equation given in Eq. (3.25) fulfilled by  $u_{1,2}$  and  $d_{1,2}$ . Dropping indices, Eq. (3.25) reads

$$\begin{aligned} \partial_\tau u - ic\partial_z u &= -i\omega_c d - (V/\hbar)u \\ \partial_\tau d + ic\partial_z d &= i\omega_c u - (V/\hbar)d, \end{aligned}$$

where  $V$  is defined as in Eq. (3.40).

From  $u$  and  $d$  we define  $\phi^\pm = \exp(\omega_c \tau)(u \pm id)/\sqrt{2}$  and one can easily show that for  $\phi^\pm$  the following equations yield:

$$\partial_\tau \phi^+ - ic\partial_z \phi^+ = -(V/\hbar)\phi^+, \quad (3.42)$$

$$\partial_\tau \phi^- - ic\partial_z \phi^- = 2\omega_c \phi^- - (V/\hbar)\phi^-, \quad (3.43)$$

On the assumption  $V \sim \text{constant}$ , we derive Eq. (3.42) with respect to  $z$  and Eq. (3.43) with respect to  $\tau$ . We then multiply Eq. (3.42) by  $c$  and Eq. (3.43) by  $i$  and subtract the resulting equations, to finally obtain:

$$\partial_\tau \phi^- = \frac{\hbar}{2m} \partial_z^2 \phi^- + \frac{1}{2\omega_c} \partial_\tau^2 \phi^- + \frac{V}{2mc^2} (\partial_\tau \phi^- + ic \partial_z \phi^+). \quad (3.44)$$

From Eq. (3.43), we have

$$\partial_\tau \phi^- + ic \partial_z \phi^+ = 2\partial_\tau \phi^- - 2\omega_c \phi^- + V \phi^-, \quad (3.45)$$

and inserting Eq. (3.45) into Eq. (3.44) we obtain the governing equation for  $\phi^-$ :

$$\hbar \partial_\tau \phi^- = \frac{\hbar^2}{2m} \partial_z^2 \phi^- - V \phi^- + \frac{\hbar}{2\omega_c} \left( \partial_\tau^2 \phi^- + 2 \frac{V}{\hbar} \partial_\tau \phi^- + \frac{V^2}{\hbar^2} \phi^- \right). \quad (3.46)$$

Assuming  $\phi^- \sim e^{i(kz - \omega\tau)/\hbar}$  and inserting this into Eq. (3.46), we obtain

$$\omega^2 - 2i\omega(mc^2 - V) + k^2 c^2 + 2mc^2 V - V^2 = 0. \quad (3.47)$$

Solving Eq. (3.47), we obtain

$$\omega_\pm = i(mc^2 - V) \pm i\sqrt{k^2 c^2 + m^2 c^4}.$$

Hence, for small values of  $k$ , we obtain

$$\omega_+ \approx -i \left( V - \frac{k^2}{2m} - 2mc^2 \right), \quad \omega_- \approx -i \left( \frac{k^2}{2m} + V \right).$$

In conclusion,  $\phi^-$  is composed by two modes,  $\omega_-$  is the correct stable mode we would expect according to Eq. (3.41), while  $\omega_+$  is a second mode, whose effect consists of a uniform amplification of  $\phi^-$  and is dominated by  $2mc^2$  at long wavelengths  $\frac{k^2}{2m} \ll V$ . As previously discussed, the normalization step compensates this effect. In the sequel, we shall validate qLB for ground-state computations by comparing it against well-established methods such as Crank-Nicolson time-marching and Backward Euler Finite Difference scheme.

### 3.6 Crank-Nicolson and Backward Euler Finite Difference schemes

Let us rewrite Eq. (3.13) for a real-valued function  $\phi(\mathbf{r}, \tau)$  (since the ground state wave function is real-valued):

$$\partial_\tau \phi(\mathbf{r}, \tau) = \left( \frac{1}{2\tilde{m}} \Delta_{\mathbf{r}} - V_{ext}(\mathbf{r}) - V_{nl} |\phi(\mathbf{r}, \tau)|^2 \right) \phi(\mathbf{r}, \tau), \quad (3.48)$$



with the normalization condition

$$\int_{\mathbb{R}^d} |\phi(\mathbf{r}, \tau)|^2 d\mathbf{r} = 1. \quad (3.49)$$

Here we use the same scaling imposed by the qLB model (see Sec. 3.11 for details). The external potential is given by Eqs. (3.5) and (3.6) in one and two dimensions respectively.

In order to make a comparison and validate our results, Eq. (3.48) is solved by using the classical Crank-Nicolson (CN) and Backward Euler Finite Difference (BEFD) schemes in the same computational domain and with the same set of parameters of the qLB.

We note that to guarantee that  $\phi(\mathbf{r}, \tau)$  fulfills condition of Eq. (3.49) a normalization step is needed also for CN and BEFD schemes [10].

### 3.6.1 One dimensional CN and BEFD schemes

Let us consider a computational domain  $[z_{min}, z_{max}]$  subdivided into  $N$  subintervals of width  $h = (z_{max} - z_{min})/N$ . Furthermore, let  $k$  be the time step,  $z_i$  the nodal points and  $\tau_n$  the discrete instants of time:

$$z_i = z_{min} + ih, \quad \tau_n = nk, \quad i = 0, \dots, N, \quad n = 0, 1, 2, \dots$$

We indicate with  $\phi_i^n$  the numerical approximation of  $\phi(z_i, \tau_n)$  and with  $\tilde{\phi}_i^n$  the non-normalized  $\phi_i^n$ . With this notation, the CN scheme reads

$$\begin{aligned} \frac{\tilde{\phi}_i^{n+1} - \phi_i^n}{k} &= \frac{1}{4\tilde{m}h^2} \left( \tilde{\phi}_{i+1}^{n+1} - 2\tilde{\phi}_i^{n+1} + \tilde{\phi}_{i-1}^{n+1} + \phi_{i+1}^n - 2\phi_i^n + \phi_{i-1}^n \right) \\ &\quad - \frac{V_{ext}(z_i)}{2} \left( \tilde{\phi}_i^{n+1} + \phi_i^n \right) - \frac{V_{nl}}{2} |\phi_i^n|^2 \left( \tilde{\phi}_i^{n+1} + \phi_i^n \right), \end{aligned}$$

while the BEFD scheme is given by

$$\begin{aligned} \frac{\tilde{\phi}_i^{n+1} - \phi_i^n}{k} &= \frac{1}{2\tilde{m}h^2} \left( \tilde{\phi}_{i+1}^{n+1} - 2\tilde{\phi}_i^{n+1} + \tilde{\phi}_{i-1}^{n+1} \right) \\ &\quad - V_{ext}(z_i) \tilde{\phi}_i^{n+1} - V_{nl} |\phi_i^n|^2 \tilde{\phi}_i^{n+1}, \end{aligned}$$

for  $i = 1, \dots, N-1$  and  $n = 0, 1, 2, \dots$

Dirichlet boundary conditions are imposed for both schemes

$$\tilde{\phi}_0^{n+1} = \tilde{\phi}_N^{n+1} = 0,$$

and the normalization step is performed as follows

$$\phi_i^{n+1} = \frac{\tilde{\phi}_i^{n+1}}{\|\tilde{\phi}^{n+1}\|},$$

for  $i = 0, \dots, N$  and  $n = 0, 1, 2, \dots$

### 3.6.2 Two dimensional CN and BEFD schemes

Let us consider a squared computational domain  $[z_{min}, z_{max}] \times [y_{min}, y_{max}] \equiv [l_{min}, l_{max}] \times [l_{min}, l_{max}]$  and let us assume, for the sake of simplicity,  $h_x = h_y \equiv h$ . Hence, we subdivide  $[l_{min}, l_{max}]$  into  $N_x = N_y \equiv N$  subintervals of width  $h$ . Furthermore, let be  $k$  the time step. We indicate with  $(z_i, y_j)$  the nodal points of the lattice and with  $\tau_n$  the discrete instants of time:

$$z_i = l_{min} + ih, \quad y_j = l_{min} + jh, \quad \tau_n = nk, \quad i, j = 0, \dots, N, \quad n = 0, 1, 2, \dots$$

Let be  $\phi_{i,j}^n$  the numerical approximation of  $\phi(z_i, y_j, \tau_n)$  and  $\tilde{\phi}_{i,j}^n$  the non-normalized  $\phi_{i,j}^n$ . With this notation, the normalized CN scheme in two dimensions reads:

$$\begin{aligned} \frac{\tilde{\phi}_{i,j}^n - \phi_{i,j}^n}{k} = & \frac{1}{4\tilde{m}h^2} \left( \tilde{\phi}_{i+1,j}^{n+1} - 2\tilde{\phi}_{i,j}^{n+1} + \tilde{\phi}_{i-1,j}^{n+1} + \phi_{i+1,j}^n - 2\phi_{i,j}^n + \phi_{i-1,j}^n \right) \\ & + \frac{1}{4\tilde{m}h^2} \left( \tilde{\phi}_{i,j+1}^{n+1} - 2\tilde{\phi}_{i,j}^{n+1} + \tilde{\phi}_{i,j-1}^{n+1} + \phi_{i,j+1}^n - 2\phi_{i,j}^n + \phi_{i,j-1}^n \right) \\ & - \frac{V_{ext}(z_i, y_j)}{2} \left( \tilde{\phi}_{i,j}^{n+1} + \phi_{i,j}^n \right) - \frac{V_{nl}}{2} |\phi_{i,j}^n|^2 \left( \tilde{\phi}_{i,j}^{n+1} + \phi_{i,j}^n \right), \end{aligned}$$

while the BEFD scheme is given by

$$\begin{aligned} \frac{\tilde{\phi}_{i,j}^n - \phi_{i,j}^n}{k} = & \frac{1}{2\tilde{m}h^2} \left( \tilde{\phi}_{i+1,j}^{n+1} - 2\tilde{\phi}_{i,j}^{n+1} + \tilde{\phi}_{i-1,j}^{n+1} \right) \\ & + \frac{1}{2\tilde{m}h^2} \left( \tilde{\phi}_{i,j+1}^{n+1} - 2\tilde{\phi}_{i,j}^{n+1} + \tilde{\phi}_{i,j-1}^{n+1} \right) \\ & - V_{ext}(z_i, y_j) \tilde{\phi}_{i,j}^{n+1} - V_{nl} |\phi_{i,j}^n|^2 \tilde{\phi}_{i,j}^{n+1}, \end{aligned}$$

for  $i, j = 1, \dots, N-1$  and  $n = 0, 1, 2, \dots$ .

Dirichlet boundary conditions are imposed for both schemes

$$\tilde{\phi}_{0,j}^{n+1} = \tilde{\phi}_{i,0}^{n+1} = \tilde{\phi}_{N,j}^{n+1} = \tilde{\phi}_{i,N}^{n+1} = 0, \quad i, j = 0, \dots, N, \quad n = 0, 1, 2, \dots,$$

and the normalization step is performed as follows

$$\phi_{i,j}^{n+1} = \frac{\tilde{\phi}_{i,j}^{n+1}}{\|\tilde{\phi}^{n+1}\|},$$

for  $i, j = 0, \dots, N$  and  $n = 0, 1, 2, \dots$ .

## 3.7 Thomas–Fermi approximation

It is useful to discuss the solution of the Gross–Pitaevskii equation in the so-called Thomas–Fermi approximation, which corresponds to the strong-interaction limit in which kinetic energy contributions can be neglected [39]. This limit is reached

by setting large values of the parameter  $NU_d$ .

Consider the time-independent GPE of Eq. (3.8), by ignoring the kinetic energy term, we have

$$\mu_{TF}\phi(\mathbf{r}) = (V_{ext}(\mathbf{r}) + NU_d|\phi(\mathbf{r})|^2)\phi(\mathbf{r}),$$

where we indicate  $\mu$  with  $\mu_{TF}$  to recall that this is the Thomas–Fermi chemical potential.

In this case, the solution of the GPE is trivial and the wave function  $\phi(\mathbf{r})$  satisfies

$$|\phi(\mathbf{r})|^2 = \begin{cases} \frac{1}{NU_d}(\mu_{TF} - V_{ext}(\mathbf{r})), & \text{if } \mu > V_{ext}(\mathbf{r}), \\ 0, & \text{otherwise.} \end{cases} \quad (3.50)$$

The chemical potential given by this approximation,  $\mu_{TF}$ , can be found by imposing the normalization condition of Eq. (3.9).

### 3.7.1 Thomas–Fermi chemical potential in one dimension

We recall that, in one dimension, the harmonic external potential is given by

$$V_{ext}(z) = \frac{1}{2}m\omega_z^2(z - z_0)^2. \quad (3.51)$$

The normalization condition of Eq. (3.9) for the Thomas–Fermi wave function of Eq. (3.50) is

$$\int_{\mu_{TF} - V_{ext}(z) > 0} (\mu_{TF} - V_{ext}(z)) dz = NU_1.$$

Including the definition of  $V_{ext}(z)$  of Eq. (3.51), the condition  $\mu_{TF} - V_{ext}(z) > 0$  implies

$$z_0 - C < z < z_0 + C, \quad \text{where} \quad C = \left( \frac{2\mu_{TF}}{m\omega_z^2} \right)^{1/2}.$$

Hence, the normalization condition can be written as

$$\int_{z_0-C}^{z_0+C} \mu_{TF} dz - \frac{1}{2}m\omega_z^2 \int_{z_0-C}^{z_0+C} (z - z_0)^2 dz = NU_1.$$

Upon integrating we obtain

$$\mu_{TF} = \left( \frac{3}{4}NU_1 \right)^{2/3} \left( \frac{m\omega_z^2}{2} \right)^{1/3}.$$

Using the qLB scaling (see Sec. 3.11), we get

$$\mu_{TF} = \left( \frac{3}{4}V_{nl} \right)^{2/3} \left( \frac{\tilde{m}\omega_z^2}{2} \right)^{1/3}, \quad (3.52)$$

where each quantity is expressed in lattice units.

### 3.7.2 Thomas–Fermi chemical potential in two dimensions

Let us consider a two dimensional harmonic potential with  $\omega_z = \omega_y \equiv \omega$

$$V_{ext}(z, y) = \frac{1}{2}m\omega^2(z^2 + y^2), \quad (3.53)$$

in this case, for the sake of simplicity, we assume  $(z_0, y_0) = (0, 0)$ , a choice which does not affect the computation of  $\mu_{TF}$ .

In order to impose the normalization condition to the Thomas–Fermi wave function of Eq. (3.50), we need to solve

$$\frac{1}{2}m\omega^2(z^2 + y^2) < \mu_{TF}.$$

In polar coordinates ( $\rho = (z^2 + y^2)^{1/2}, \theta = \arctan(y/z)$ ) we have

$$\frac{1}{2}m\omega^2\rho^2 < \mu_{TF},$$

from which

$$0 < \rho < \left( \frac{2\mu_{TF}}{m\omega^2} \right)^{1/2} \equiv C.$$

The normalization condition is then given by

$$\int_0^C [\mu_{TF} - V_{ext}(\rho)] \rho d\rho = \frac{NU_2}{2\pi}.$$

Integrating we obtain

$$\mu_{TF} = \left( NU_2 \frac{m\omega^2}{\pi} \right)^{1/2}.$$

Using the qLB scaling (see Sec. 3.11), we get

$$\mu_{TF} = \left( \frac{V_{nl}\tilde{m}\omega^2}{\pi} \right)^{1/2}, \quad (3.54)$$

where each quantity is expressed in lattice units.

## 3.8 Numerical results

In this section we compare the qLB model against the numerical results obtained by the normalized CN and BEFD schemes, as well as via the Thomas–Fermi approximation.

### 3.8.1 Numerical results in one dimension

Recall that in one dimension and using the qLB scaling (see Eq. (3.13) and Sec. 3.11 for details), the potential is given by

$$V(z, \tau) = V_{ext}(z) + V_{nl}|\phi(z, \tau)|^2 = \frac{1}{2}\tilde{m}\omega_z^2(z - z_0)^2 + V_{nl}|\phi(z, \tau)|^2.$$

As initial condition, we take a Gaussian packet centered about  $z_0$  and with initial spreading  $\Delta_0$

$$\phi(z, 0) = (2\pi\Delta_0^2)^{-1/4} \exp\left(-\frac{(z - z_0)^2}{4\Delta_0^2}\right).$$

By working in lattice units (for qLB, CN and BEFD schemes), we fix a computational domain given by the interval  $[0, nz] = [0, 1024]$  and set  $z_0 = 512$ . Moreover, we set  $\Delta_0 = 16$ ,  $\omega_z = 1/128$  and  $\tilde{m} = 1/8$ . For the qLB the discretization steps are fixed at 1 and Dirichlet boundary conditions are used (i. e.  $\phi^- = 0$  on the boundary). For CN and BEFD schemes, instead, we set  $h = 0.1$  and  $k = 0.1$ . The models asymptotically tend to a stationary solution. Hence, for all models, the simulation is stopped whenever:

$$\max_{i=0,\dots,N} |\phi_i^{n+1} - \phi_i^n| < \varepsilon, \quad (3.55)$$

where  $N$  is the number of nodal points (and it is smaller for qLB than CN and BEFD) and  $\varepsilon = 10^{-8}$ .

Our results are compared at varying the parameter  $V_{nl}$ . In Tab. 3.1 the limit value of  $\mu$  is reported for qLB, CN and BEFD models. Moreover, the Thomas–Fermi chemical potential  $\mu_{TF}$  given by Eq. (3.52) is also shown. We observe that, for  $V_{nl} \geq 40$ , the qLB chemical potential becomes slightly smaller than the Thomas–Fermi chemical potential, which should always be a lower bound instead. However, by increasing the accuracy of the qLB model (i. e. halving the discretization step) the values of  $\mu_{qLB}$  becomes larger than  $\mu_{TF}$  (see Sec. 3.10 for details), as they should. In Tab. 3.2, the maximum value of  $\phi$  at the end of the simulation ( $\phi_g(z_0)$ ) is reported for all the three models.

In Fig. 3.1, we compare the ground-state wave function  $\phi_g(z)$  given by the models for some values of  $V_{nl}$ , in Fig. 3.2 the same comparison is reported for the chemical potential decay profiles. In Fig. 3.3, we compare the ground state profile given by the qLB model with the wave function of the Thomas–Fermi approximation of Eq. (3.50) for some values of  $V_{nl}$ . Finally, in Fig. 3.4, we report the ground-state profiles given by qLB varying  $V_{nl}$ .

Table 3.1: Ground state chemical potential  $\mu$  for qLB, CN and BEFD models. Numerical results are also compared with the Thomas–Fermi chemical potential (see Eq. (3.52)). The results are computed for different values of  $V_{nl}$ , the other parameters are set as  $\omega_z = 1/128$ ,  $\tilde{m} = 1/8$ ,  $\Delta_0 = 16$ ,  $nz = 1024$ .

$V_{nl}$	$\mu$ qLB	$\mu$ CN	$\mu$ BEFD	$\mu$ TF
0	0.003906	0.003906	0.003906	–
1	0.013678	0.013740	0.013740	0.012898
5	0.037978	0.038078	0.038071	0.037714
10	0.060007	0.060112	0.060112	0.059868
20	0.095084	0.095201	0.095201	0.095034
30	0.124540	0.124663	0.124663	0.124530
40	0.150843	0.150971	0.150971	0.150858
50	0.175024	0.175154	0.175154	0.175055
60	0.197637	0.197769	0.197769	0.197680
70	0.219023	0.219157	0.219157	0.219075
80	0.239412	0.239548	0.239548	0.239472

Table 3.2: Maximum value reached by the ground state profile  $\phi_g(z_0)$  for qLB, CN and BEFD models. The results are computed for different values of  $V_{nl}$ , the other parameters are set as  $\omega_z = 1/128$ ,  $\tilde{m} = 1/8$ ,  $\Delta_0 = 16$ ,  $nz = 1024$ .

$V_{nl}$	$\phi_g(z_0)$ qLB	$\phi_g(z_0)$ CN	$\phi_g(z_0)$ BEFD
0	0.1316	0.1327	0.1328
1	0.1105	0.1109	0.1109
5	0.0867	0.0868	0.0867
10	0.0773	0.0774	0.0774
20	0.0689	0.0689	0.0689
30	0.0644	0.0644	0.0644
40	0.0614	0.0614	0.0614
50	0.0591	0.0592	0.0592
60	0.0574	0.0574	0.0574
70	0.0559	0.0559	0.0559
80	0.0547	0.0547	0.0547

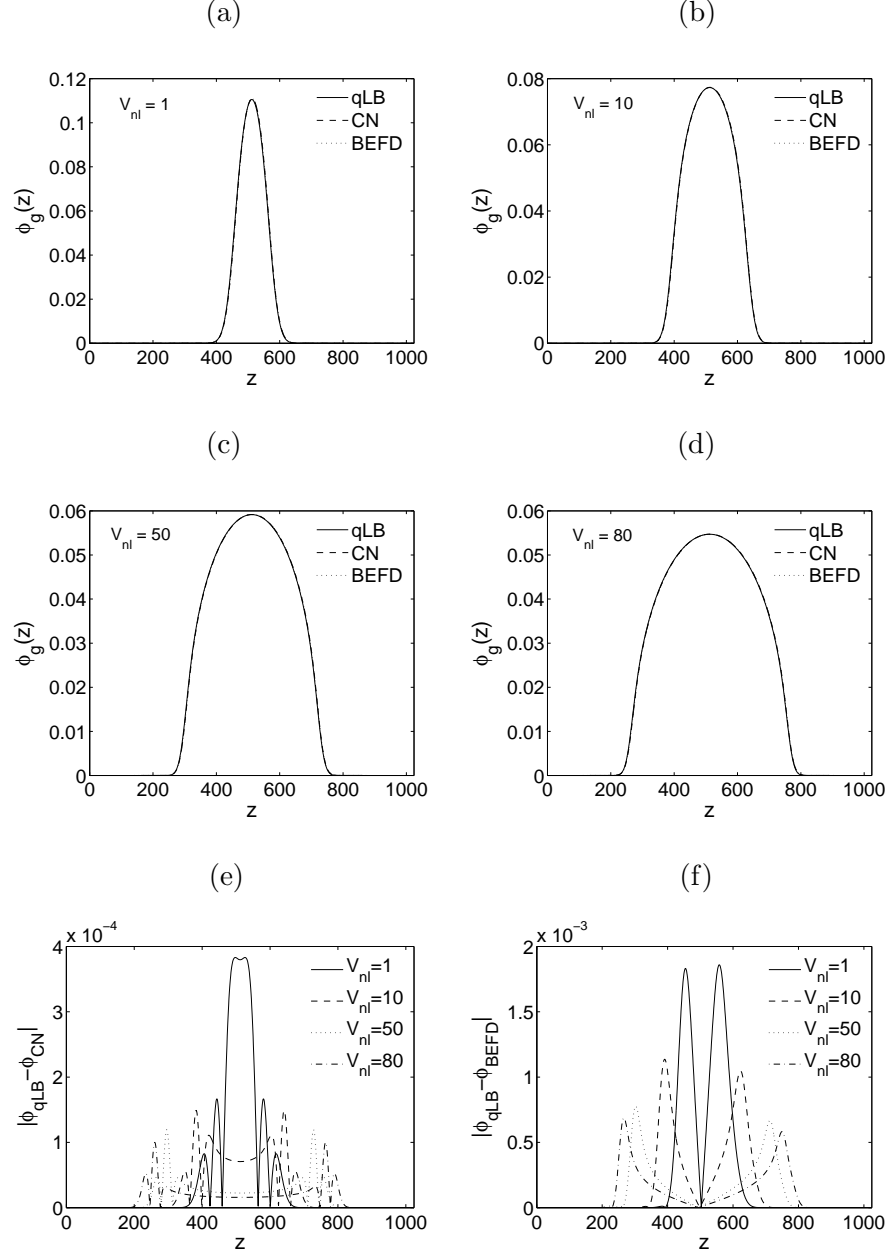


Figure 3.1: Ground state profile  $\phi_g(z)$  for different values of  $V_{nl}$ . Simulation parameters are set as:  $\tilde{m} = 1/8$ ,  $\Delta_0 = 16$ ,  $\omega_z = 1/128$ ,  $nz = 1024$ . (a)  $V_{nl} = 1$ , (b)  $V_{nl} = 10$ , (c)  $V_{nl} = 50$ , (d)  $V_{nl} = 80$ . Solid lines: qLB model; dashed lines: CN model; dotted lines: BEFD model. The deviations of qLB from CN and BEFD are not visible on this scale, hence in (e) and (f) the differences  $|(\phi_g)_{qLB} - (\phi_g)_{CN}|$  and  $|(\phi_g)_{qLB} - (\phi_g)_{BEFD}|$  computed at the qLB nodal points are plotted. Space is expressed in lattice units.

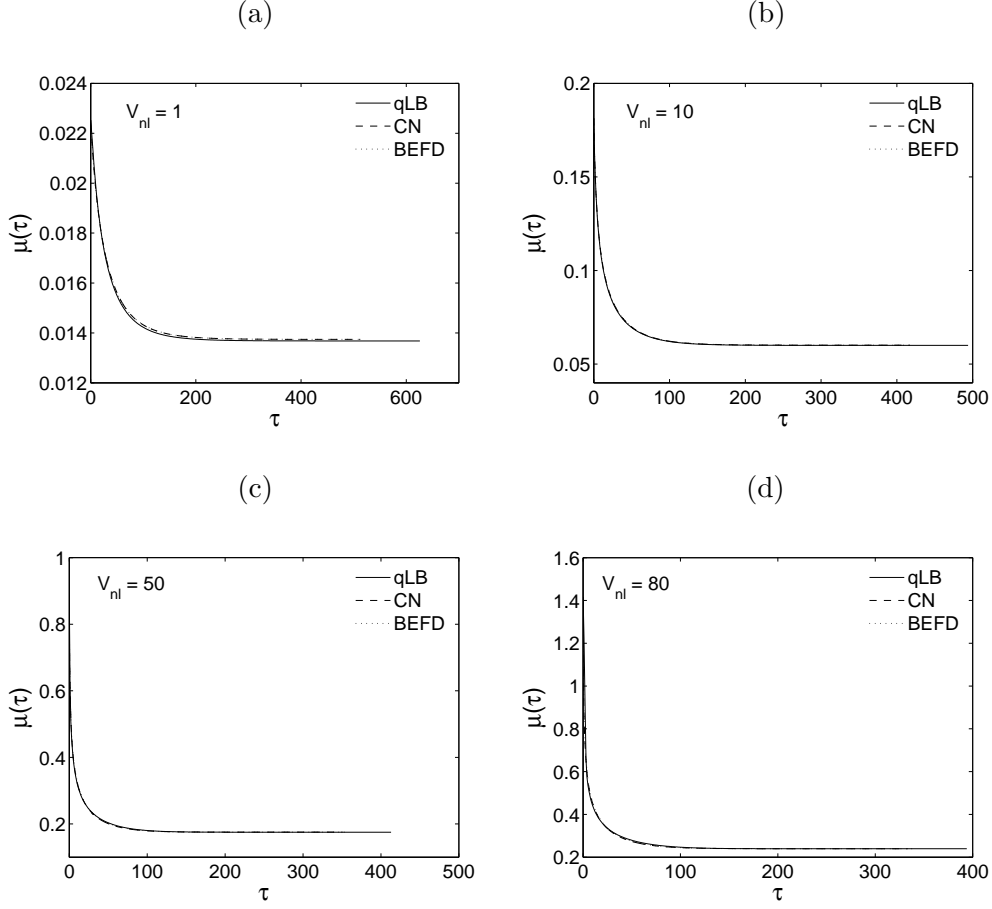


Figure 3.2: Chemical potential decay for different values of  $V_{nl}$ . Simulation parameters are set as:  $\tilde{m} = 1/8$ ,  $\Delta_0 = 16$ ,  $\omega_z = 1/128$ ,  $nz = 1024$ . (a)  $V_{nl} = 1$ , (b)  $V_{nl} = 10$ , (c)  $V_{nl} = 50$ , (d)  $V_{nl} = 80$ . Solid lines: qLB model; dashed lines: CN model; dotted lines: BEFD model. Time and chemical potential are expressed in lattice units.



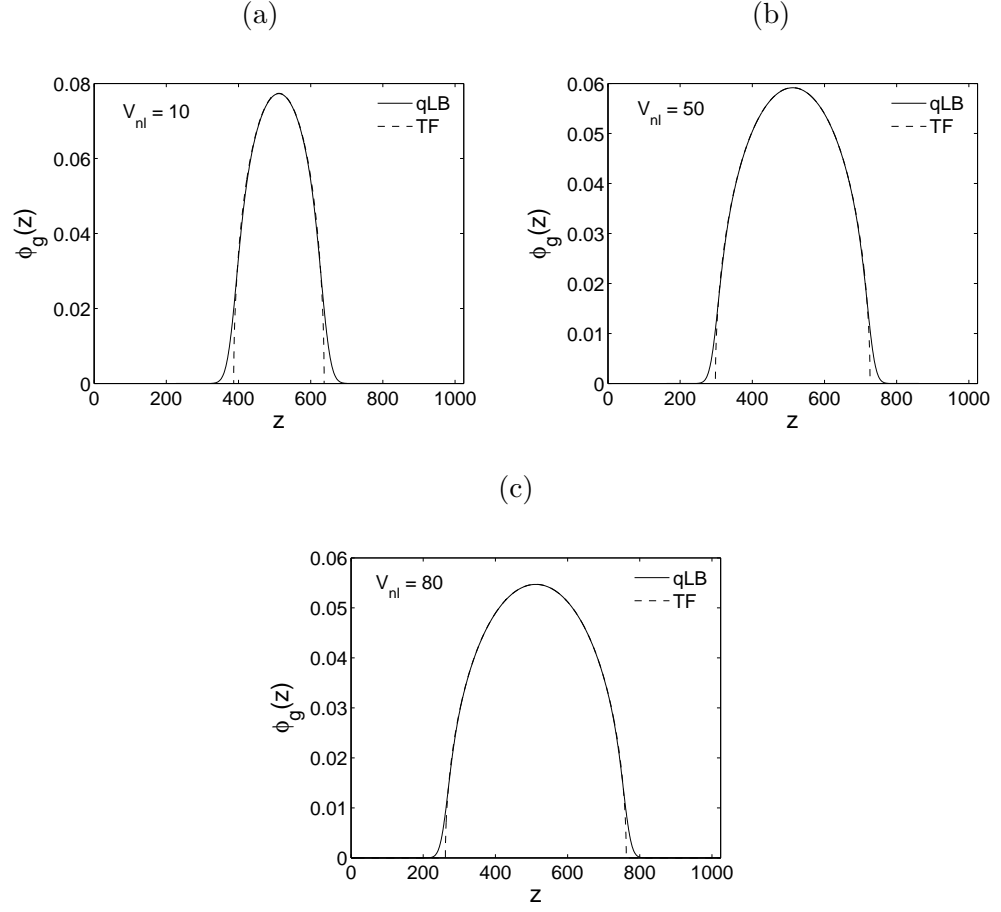


Figure 3.3: Ground state profile  $\phi_g(z)$  for different values of  $V_{nl}$ . Simulation parameters are set as:  $\tilde{m} = 1/8$ ,  $\Delta_0 = 16$ ,  $\omega_z = 1/128$ ,  $nz = 1024$ . (a)  $V_{nl} = 10$ , (b)  $V_{nl} = 50$ , (c)  $V_{nl} = 80$ . Solid lines: qLB model; dashed lines: Thomas-Fermi approximation. Space is expressed in lattice units. The tails associated with the kinetic energy contribution are well visible.

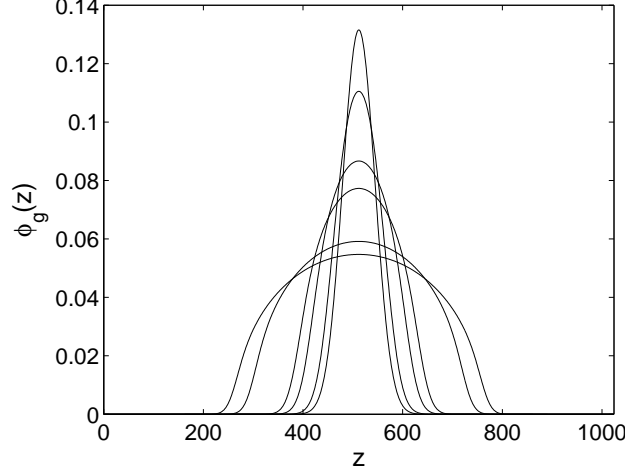


Figure 3.4: Ground state profiles given by the qLB model for different values of  $V_{nl}$ . Simulation parameters are set as:  $\tilde{m} = 1/8$ ,  $\Delta_0 = 16$ ,  $\omega_z = 1/128$ ,  $nz = 1024$ . For increasing values of  $V_{nl}$ , curves goes from the top toward the bottom.  $V_{nl}$  takes the following values: 0, 1, 5, 10, 50 and 80. Space is expressed in lattice units.

### 3.8.2 Numerical results in two dimensions

In this section we present results referring to the following two-dimensional potential:

$$\begin{aligned} V(z, y, \tau) &= V_{ext}(z, y) + V_{nl}|\phi(z, y, \tau)|^2 \\ &= \frac{1}{2}\tilde{m}[\omega_z^2(z - z_0)^2 + \omega_y^2(y - y_0)^2] + V_{nl}|\phi(z, y, \tau)|^2. \end{aligned}$$

As initial condition, we consider a Gaussian packet centered about  $(z_0, y_0)$  and with initial spreads  $\Delta_{0z}$ ,  $\Delta_{0y}$  along  $z$  and  $y$  respectively:

$$\phi(z, y, 0) = (2\pi\Delta_{0z}\Delta_{0y})^{-1/2} \exp\left(-\frac{(z - z_0)^2}{4\Delta_{0z}^2}\right) \exp\left(-\frac{(y - y_0)^2}{4\Delta_{0y}^2}\right). \quad (3.56)$$

Let  $[0, nz] \times [0, ny] = [0, 512] \times [0, 512]$  be our domain and  $(z_0, y_0) = (256, 256)$ , furthermore we fix  $\Delta_{0z} = \Delta_{0y} = 16$ ,  $\omega_z = \omega_y = 1/128$  and  $\tilde{m} = 1/8$ . Discretization steps for the qLB model are again fixed to unity, while for CN and BEFD we set  $h = 0.5$  and  $k = 0.1$ . Dirichlet boundary conditions are imposed in all qLB simulations. The stop condition for the simulation is

$$\max_{i,j=0,\dots,N} |\phi_{i,j}^{n+1} - \phi_{i,j}^n| < \varepsilon, \quad (3.57)$$

with  $\varepsilon = 10^{-9}$ .

In Tab. 3.3, the limit value of  $\mu$  is reported for the three models. Moreover, the Thomas–Fermi chemical potential  $\mu_{TF}$  given by Eq. (3.54) is also shown. In Tab. 3.4, the maximum value of  $\phi$  at the end of the simulation ( $\phi_g(z_0, y_0)$ ) computed by qLB, CN and BEFD is reported.

In Fig. 3.5, we compare the ground-state wave function  $\phi_g(z, y)$  taken at  $y = y_0$  given by the models for some values of  $V_{nl}$ , in Fig. 3.6 the same comparison is reported for the chemical potential decay profiles. In Fig. 3.7, we compare the ground state profile taken at  $y = y_0$  given by the qLB model with the wave function of the Thomas–Fermi approximation of Eq. (3.50) for some values of  $V_{nl}$ . Finally, in Fig. 3.8, we report the ground-state profiles given by qLB varying  $V_{nl}$  at the cross section  $y = y_0$ .

Table 3.3: Ground state chemical potential  $\mu$  for qLB, CN and BEFD models. Numerical results are also compared with the Thomas–Fermi chemical potential (see Eq. (3.54)). The results are computed for different values of  $V_{nl}$ , the other parameters are set as  $\omega_z = \omega_y = 1/128$ ,  $\tilde{m} = 1/8$ ,  $\Delta_{0z} = \Delta_{0y} = 16$ ,  $nz = ny = 512$ .

$V_{nl}$	$\mu$ qLB	$\mu$ CN	$\mu$ BEFD	$\mu$ TF
0	0.007816	0.007812	0.007812	–
10	0.009219	0.009250	0.009250	0.004928
100	0.017489	0.017597	0.017597	0.015584
500	0.035802	0.035949	0.035949	0.034846
1000	0.049964	0.050125	0.050125	0.049280
2000	0.070161	0.070338	0.070338	0.069692
3000	0.085721	0.085905	0.085905	0.085355
4000	0.098860	0.099050	0.099050	0.098560
5000	0.110447	0.110642	0.110642	0.110193
10000	0.155967	0.156176	0.156176	0.155837

These data witness a satisfactory agreement between qLB and the reference CN and BEFD solutions, while CN and BEFD are in excellent agreement with each other (this is due to the high resolution adopted in these reference cases).

As a second example, we consider an external potential where a Gaussian stirring term (representing, for example, a far-blue detuned laser beam [30]) is added to the harmonic trap:

$$V_{ext}(z, y) = \frac{1}{2} \tilde{m} [\omega_z^2 (z - z_0)^2 + \omega_y^2 (y - y_0)^2] + \omega_0 e^{-\delta\{[(z-z_0)-r_0]^2 + (y-y_0)^2\}}. \quad (3.58)$$

A similar example is given in [10]. As mentioned in [10], in the time-dependent

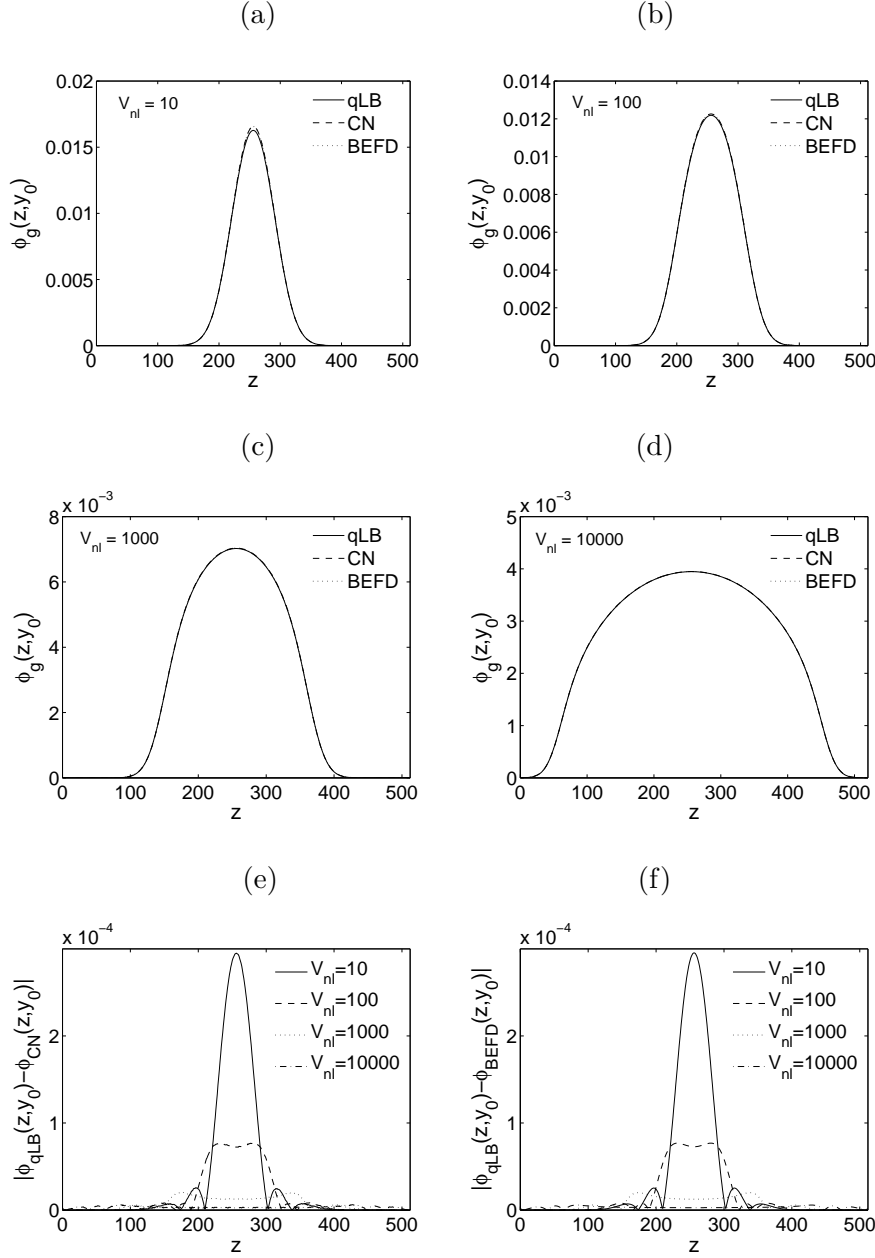


Figure 3.5: Ground state profile  $\phi_g(z, y)$  taken at  $y = y_0$  for different values of  $V_{nl}$ . Simulation parameters are set as:  $\tilde{m} = 1/8$ ,  $\Delta_{0z} = \Delta_{0y} = 16$ ,  $\omega_z = \omega_y = 1/128$ ,  $nz = ny = 512$ . (a)  $V_{nl} = 10$ , (b)  $V_{nl} = 100$ , (c)  $V_{nl} = 1000$ , (d)  $V_{nl} = 10000$ . Solid lines: qLB model; dashed lines: CN model; dotted lines: BEFD model. The deviations of qLB from CN and BEFD are not visible on this scale, hence in (e) and (f) the differences  $|(\phi_g)_{qLB}(z, y_0) - (\phi_g)_{CN}(z, y_0)|$  and  $|(\phi_g)_{qLB}(z, y_0) - (\phi_g)_{BEFD}(z, y_0)|$  computed at the qLB nodal points are plotted. Space is expressed in lattice units.

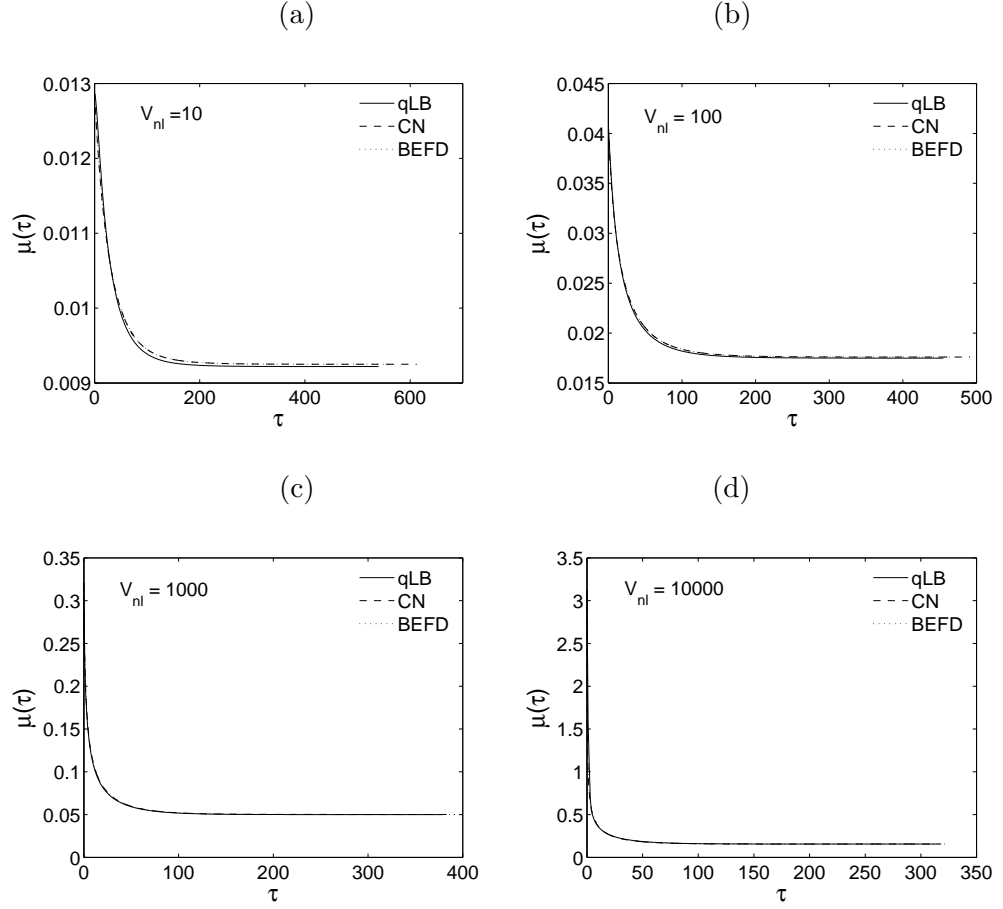


Figure 3.6: Chemical potential decay for different values of  $V_{nl}$ . Simulation parameters are set as:  $\tilde{m} = 1/8$ ,  $\Delta_{0z} = \Delta_{0y} = 16$ ,  $\omega_z = \omega_y = 1/128$ ,  $n_z = n_y = 512$ . (a)  $V_{nl} = 10$ , (b)  $V_{nl} = 100$ , (c)  $V_{nl} = 1000$ , (d)  $V_{nl} = 10000$ . Solid lines: qLB model; dashed lines: CN model; dotted lines: BEFD model. Time and chemical potential are expressed in lattice units.

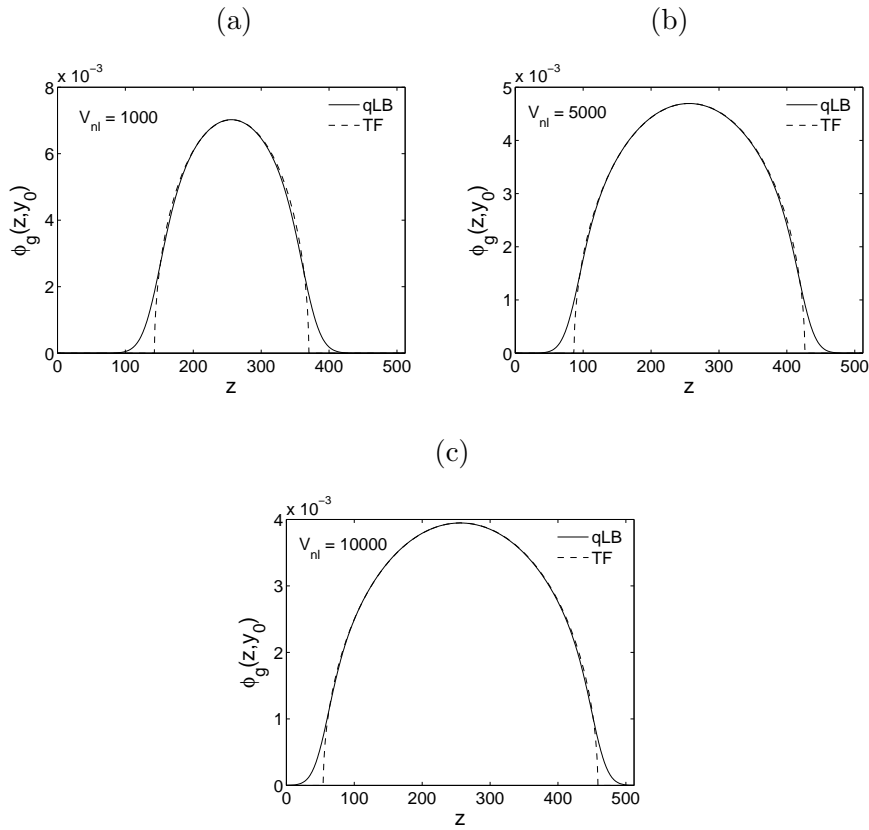


Figure 3.7: Ground state profile  $\phi_g(z, y)$  taken at  $y = y_0$  for different values of  $V_{nl}$ . Simulation parameters are set as:  $\tilde{m} = 1/8$ ,  $\Delta_{0z} = \Delta_{0y} = 16$ ,  $\omega_z = \omega_y = 1/128$ ,  $nz = ny = 512$ . (a)  $V_{nl} = 1000$ , (b)  $V_{nl} = 5000$ , (c)  $V_{nl} = 10000$ . Solid lines: qLB model; dashed lines: Thomas–Fermi approximation. Space is expressed in lattice units. The tails associated with the kinetic energy contribution are well visible.

Table 3.4: Maximum value reached by the ground state wave function  $\phi_g(z_0, y_0)$  for qLB, CN and BEFD models. The results are computed for different values of  $V_{nl}$ , the other parameters are set as  $\omega_z = \omega_y = 1/128$ ,  $\tilde{m} = 1/8$ ,  $\Delta_{0z} = \Delta_{0y} = 16$ ,  $nz = ny = 512$ .

$V_{nl}$	$\phi_g(z_0, y_0)$ qLB	$\phi_g(z_0, y_0)$ CN	$\phi_g(z_0, y_0)$ BEFD
0	0.01723	0.01763	0.01763
10	0.01627	0.01656	0.01656
100	0.01218	0.01226	0.01225
500	0.00835	0.00837	0.00836
1000	0.00702	0.00704	0.00703
2000	0.00590	0.00591	0.00591
3000	0.00533	0.00534	0.00534
4000	0.00496	0.00497	0.00496
5000	0.00469	0.00470	0.00470
10000	0.00395	0.00395	0.00395

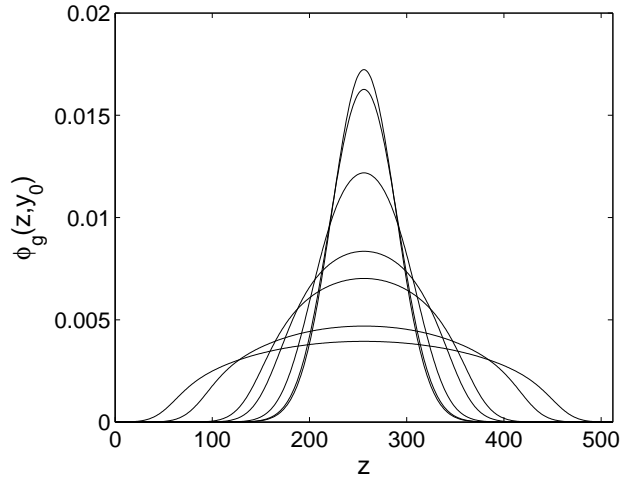


Figure 3.8: Ground state profiles given by the qLB model for different values of  $V_{nl}$ . Simulation parameters are set as:  $\tilde{m} = 1/8$ ,  $\Delta_{0z} = \Delta_{0y} = 16$ ,  $\omega_z = \omega_y = 1/128$ ,  $nz = ny = 512$ . For increasing values of  $V_{nl}$ , curves go from the top to bottom.  $V_{nl}$  takes the following values: 0, 10, 100, 500, 1000, 5000 and 10000. Space is expressed in lattice units.

GPE, such a potential (where the stirring Gaussian term is itself time-dependent through the motion of the center  $r_0(t)$ ) is used to generate vortices in BEC [30, 73]. The initial condition is still given by the Gaussian packet given in Eq. (3.56). We consider the computational domain  $[0, nz] \times [0, ny] = [0, 512] \times [0, 512]$  and  $z_0 = y_0 = 256$  and we choose  $\tilde{m} = 1/8$ ,  $\Delta_{0z} = \Delta_{0y} = 22.63$ ,  $\omega_z = \omega_y = 1/128$ ,  $V_{nl} = 1000$ ,  $\omega_0 = 8/128$ ,  $r_0 = 50$  and  $\delta = 1/512$ . For CN and BEFD schemes, we set  $h = 0.5$  and  $k = 0.1$ , while for the qLB scheme the discretization steps are set to unit value. With these parameters, the ground state chemical potentials computed by qLB, CN and BEFD schemes are as follows:

$$\mu_{qLB} = 0.052238, \quad \mu_{CN} = 0.052408, \quad \mu_{BEFD} = 0.052408.$$

In Fig. 3.9 a comparison between the chemical potential decays obtained by qLB, CN and BEFD models is reported. Finally, in Fig. 3.10, the ground state surfaces computed by qLB, CN and BEFD models are shown by plotting the isolines taken at different values of  $|\phi_g(z, y)|$ . Again, a satisfactory agreement between qLB and the reference CN and BEFD results is generally observed.

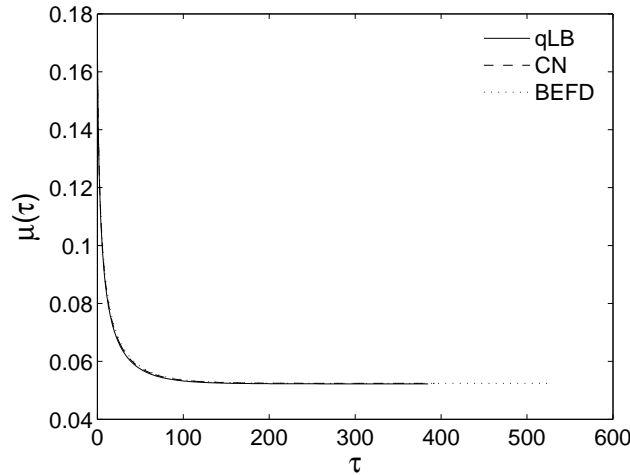


Figure 3.9: Chemical potential decay profiles given by qLB, CN and BEFD models with the external potential of Eq. (3.58). Simulation parameters are set as:  $\tilde{m} = 1/8$ ,  $\Delta_{0z} = \Delta_{0y} = 22.63$ ,  $\omega_z = \omega_y = 1/128$ ,  $nz = ny = 512$ ,  $V_{nl} = 1000$ ,  $\omega_0 = 8/128$ ,  $r_0 = 50$  and  $\delta = 1/512$ . Solid line: qLB; dashed line: CN; dotted line: BEFD. Time and chemical potential are expressed in lattice units.



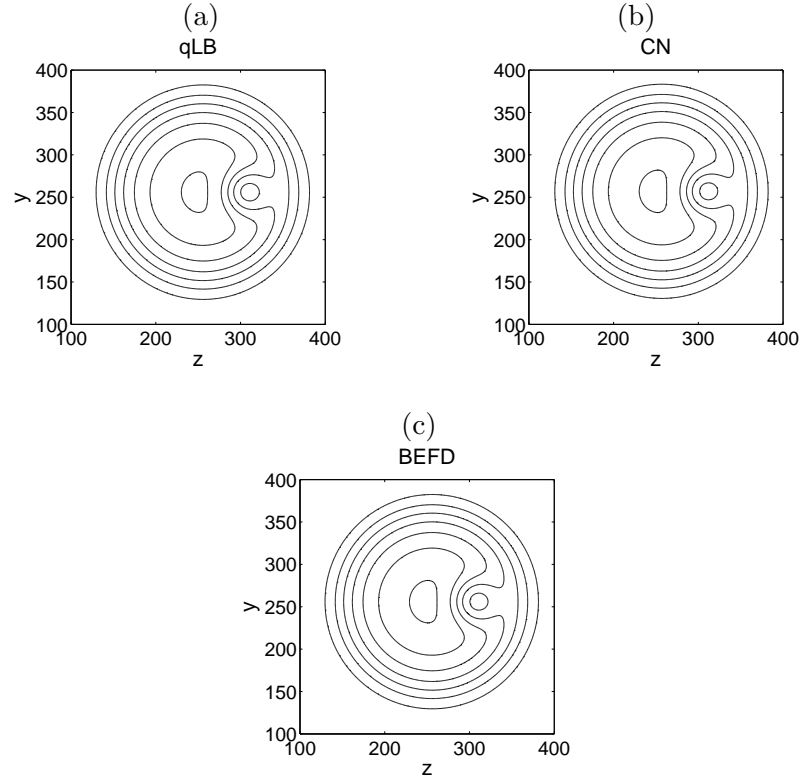


Figure 3.10: Ground state contour plots computed by qLB, CN and BEFD models with the external potential of Eq. (3.58). Simulation parameters are set as:  $\tilde{m} = 1/8$ ,  $\Delta_{0z} = \Delta_{0y} = 22.63$ ,  $\omega_z = \omega_y = 1/128$ ,  $n_z = n_y = 512$ ,  $V_{nl} = 1000$ ,  $\omega_0 = 8/128$ ,  $r_0 = 50$  and  $\delta = 1/512$ . (a) qLB model, (b) CN model, (c) BEFD model. The isolines correspond to the following values of  $\phi_g(x, y)$ : 0.001, 0.002, 0.003, 0.004, 0.005, 0.006 and 0.007 going from the outside toward the inside. Space is expressed in lattice units.

### 3.9 Computation of the first excited state

In [10], it is observed how the normalized gradient flow (and its discretization) is able to directly compute the first excited state solution. In particular, when the external potential is the harmonic oscillator potential, the first excited state solution in one dimension,  $\phi_1(z)$ , is a real odd function. In [10], it is numerically shown that, in such a case, the normalized gradient flow can be applied to compute  $\phi_1(z)$  provided that the initial data is an odd function.

Here, we apply the imaginary-time qLB method to the computation of the first excited state solution and we compare our numerical results with the ones obtained by the Crank–Nicolson scheme.

Our model shows different behaviors in one and two dimensions, respectively. In one dimension, the model reaches the first excited state solution which is then kept constant up to the required precision. In two dimensions, instead, the first excited state solution is reached and kept almost constant for a certain number of time steps. However, the chemical potential keeps decreasing below the first excited state energy and finally reaches the ground state value. It is possible to observe that larger is the ratio between the first excited state chemical potential,  $\mu_1$ , and the ground state chemical potential  $\mu_0$ , larger is the number of time steps during which the first excited state solution is kept constant by the model.

#### 3.9.1 Computation of the first excited state in one dimension

Let us consider the usual external potential

$$V(z, \tau) = \frac{1}{2} \tilde{m} \omega_z^2 (z - z_0)^2 + V_{nl} |\phi(z, \tau)|^2,$$

and the following odd function as initial condition

$$\phi(z, 0) = (2\pi\Delta_0^2)^{-1/4} \frac{(z - z_0)}{\Delta_0} \exp\left(-\frac{(z - z_0)^2}{4\Delta_0^2}\right).$$

By working in lattice units (for qLB, CN and BEFD schemes), we fix a computational domain given by the interval  $[0, nz] = [0, 2048]$  and set  $z_0 = 1024$ . Moreover, we set  $\Delta_0 = 16$ ,  $\omega_z = 1/512$  and  $\tilde{m} = 1/4$ . The stop criterion is given by Eq. (3.55) with  $\varepsilon = 10^{-8}$ . For the qLB, the discretization steps are fixed at 1 and Dirichlet boundary conditions are used, while for CN and BEFD schemes, we set  $h = 0.1$  and  $k = 0.1$ . In Tab. 3.5 the chemical potential of the first excited state  $\mu_1$  is reported for both qLB and CN models and for different values of  $V_{nl}$ . Moreover, the ground state chemical potential  $\mu_0$  computed by the qLB scheme and the ratio  $\mu_1/\mu_0$  are also shown. We observe that, for  $V_{nl} = 0$ ,  $\mu_1/\mu_0 \approx 3$  as expected (in fact, for  $V_{nl} = 0$ ,  $\mu_0 = \omega_z \hbar/2$  and  $\mu_1 = (3/2)\omega_z \hbar$ ), then, for increasing values of

$V_{nl}$ ,  $\mu_1/\mu_0$  tends to unit value. In Fig. 3.11 the first excited state profile is shown for some values of  $V_{nl}$  and for both qLB and CN models. In Fig. 3.12 the same comparison is reported for the chemical potential decay. Finally, in Fig. 3.13 the first excited state profiles given by the qLB model for some values of  $V_{nl}$  are also reported.

Table 3.5: First excited state chemical potential for qLB and CN. The ground state chemical potential given by the qLB model and the ratio  $\mu_1/\mu_0$  are also reported. The results are computed for different values of  $V_{nl}$ . Parameters are set as follows:  $\omega_z = \omega_y = 1/512$ ,  $\tilde{m} = 1/4$ ,  $\Delta_0 = 16$ .

$V_{nl}$	$\mu_1$ CN	$\mu_1$ qLB	$\mu_0$ qLB	$(\mu_1/\mu_0)$ qLB
0	0.002930	0.002929	0.000976	3.001
1	0.008038	0.008021	0.006567	1.223
5	0.020315	0.020280	0.018903	1.073
10	0.031366	0.031314	0.029963	1.045
25	0.056549	0.056461	0.055154	1.024
50	0.088928	0.088790	0.087535	1.014
65	0.105655	0.105490	0.104263	1.012
80	0.121132	0.120941	0.119740	1.010

### 3.9.2 Computation of the first excited state in two dimensions

Let us consider the two-dimensional potential given by

$$V(z, y, \tau) = \frac{1}{2} \tilde{m} [\omega_z^2 (z - z_0)^2 + \omega_y^2 (y - y_0)^2] + V_{nl} |\phi(z, y, \tau)|^2.$$

and the following wave function as initial condition

$$\begin{aligned} \phi(z, y, 0) &= (2\pi \Delta_{0z} \Delta_{0y})^{-1/2} \frac{(z - z_0)(y - y_0)}{\Delta_{0z} \Delta_{0y}} \\ &\times \exp\left(-\frac{(z - z_0)^2}{4\Delta_{0z}^2}\right) \exp\left(-\frac{(y - y_0)^2}{4\Delta_{0y}^2}\right). \end{aligned}$$

Let  $[0, nz] \times [0, ny] = [0, 256] \times [0, 256]$  be our domain and  $(z_0, y_0) = (128, 128)$ , furthermore we fix  $\Delta_{0z} = \Delta_{0y} = 16$ ,  $\omega_z = \omega_y = 1/256$  and  $\tilde{m} = 1/4$ . Discretization steps for the qLB model are again fixed to unity, while for CN and BEFD we set  $h = 0.5$  and  $k = 0.1$ . Dirichlet boundary conditions are imposed in all qLB simulations. The stop criterion is given by Eq. (3.57) with  $\varepsilon = 10^{-9}$ .

As previously mentioned, in this case the qLB model does not stop at the first

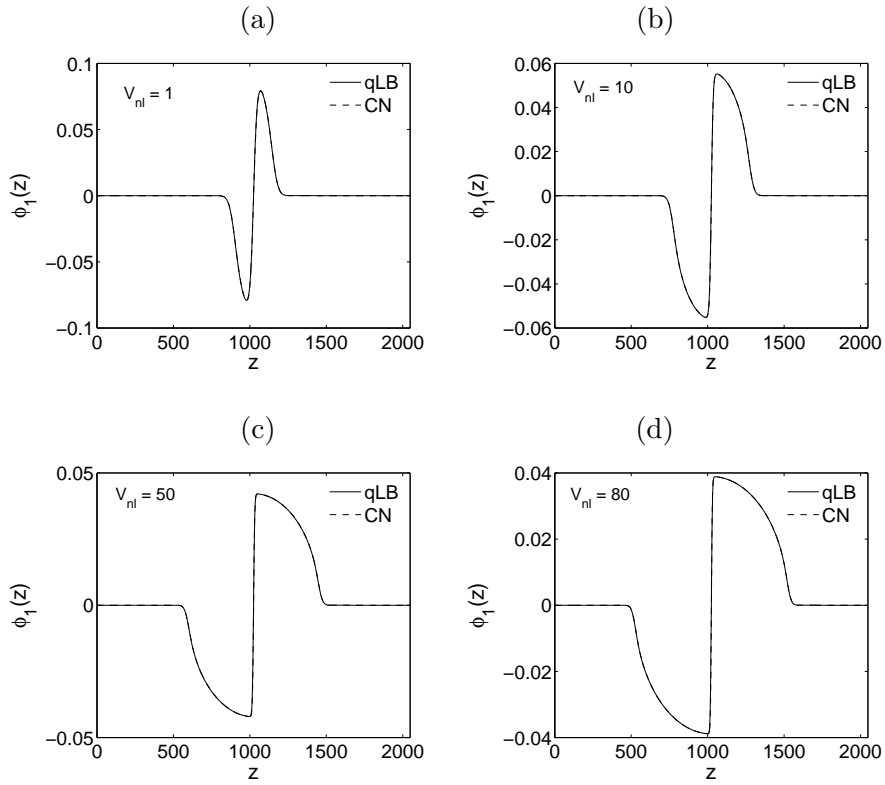


Figure 3.11: First excited state profile  $\phi_1(z)$  for different values of  $V_{nl}$ . Simulation parameters are set as:  $\tilde{m} = 1/4$ ,  $\Delta_0 = 16$ ,  $\omega_z = 1/512$ . (a)  $V_{nl} = 1$ , (b)  $V_{nl} = 10$ , (c)  $V_{nl} = 50$ , (d)  $V_{nl} = 80$ , Solid lines: qLB model; dashed lines: CN models. Space is expressed in lattice units.

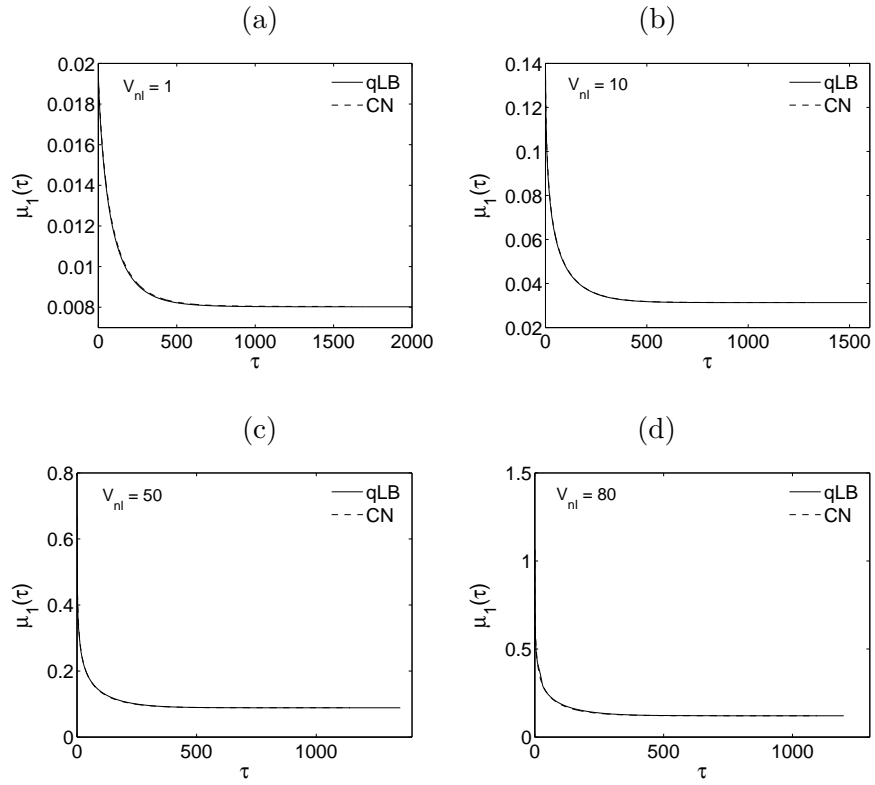


Figure 3.12: Chemical potential decay for different values of  $V_{nl}$  for the first excited state. Simulation parameters are set as:  $\tilde{m} = 1/4$ ,  $\Delta_0 = 16$ ,  $\omega_z = 1/512$ . (a)  $V_{nl} = 1$ , (b)  $V_{nl} = 10$ , (c)  $V_{nl} = 50$ , (d)  $V_{nl} = 80$ , Solid lines: qLB model; dashed lines: CN models. Time and chemical potential are expressed in lattice units.

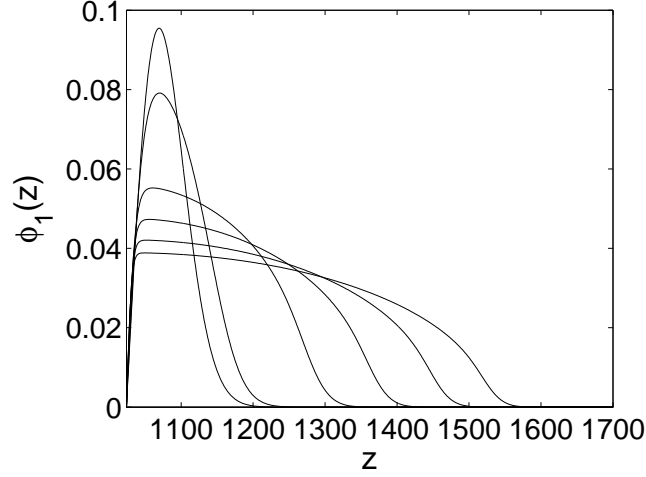


Figure 3.13: First excited state profiles given by the qLB model for different values of  $V_{nl}$ . Simulation parameters are set as:  $m = 1/4$ ,  $\Delta_0 = 16$ ,  $\omega_x = 1/512$ . For increasing values of  $V_{nl}$ , curves goes from the top toward the bottom.  $V_{nl}$  takes the following values: 0, 1, 10, 25, 50 and 80. Space is expressed in lattice units.

excited state solution. In particular, it reaches the first excited state chemical potential and then remains almost constant for a large number of time steps, but then the chemical potential starts to further decrease toward the ground state level. Hence, for the qLB model in two dimensions, we identify two relevant chemical potential values (see Fig. 3.14):  $\mu_1$  and  $\tilde{\mu}_0$ . The first one corresponds to the first excited state chemical potential, the second is the limit value reached by the model that is found to be in close agreement with the ground state chemical potential which we denote with  $\mu_0$ . In Tab. 3.6, we report  $\mu_1$ ,  $\tilde{\mu}_0$ ,  $\mu_0$  and the ratio  $\mu_1/\mu_0$  as computed by the qLB model, we also show the first excited state chemical potential given by the CN scheme.

In Fig. 3.14, the chemical potential decay for qLB and CN models and for different values of  $V_{nl}$  is reported. We can observe that the qLB chemical potential profiles show a first “plateau” which corresponds to the first excited state solutions, the plateau is larger for lower values of  $V_{nl}$  (or higher values of the ratio  $\mu_1/\mu_0$ ). In Fig. 3.15, we show the first excited state solutions given by qLB and CN models, in particular we report the the cross section taken for  $y = z$  and for  $y = N - z$ , where  $N \equiv nz = ny$ . The solutions computed by qLB are taken in correspondence with the first plateau observed in Fig. 3.14. Finally, in Fig. 3.16, we show the first excited state surfaces for  $V_{nl} = 50$  and  $V_{nl} = 300$  for both schemes.

Table 3.6: First excited state chemical potential in two dimensions for qLB and CN. For the qLB model  $\mu_1$  and  $\tilde{\mu}_0$  are reported. Moreover, the ground state chemical potential given by the qLB model  $\mu_0$  and the ratio  $\mu_1/\mu_0$  are shown. The results are computed for different values of  $V_{nl}$ , the other parameters are set as  $\tilde{m} = 1/4$ ,  $\Delta_{0z} = \Delta_{0y} = 16$  and  $\omega_z = \omega_y = 1/256$ .

$V_{nl}$	$\mu_1$ CN	$\mu_1$ qLB	$\tilde{\mu}_0$ qLB	$\mu_0$ qLB	$(\mu_1/\mu_0)$ qLB
0	0.011718	0.011711	0.003908	0.003908	3.00
10	0.012553	0.012534	0.005243	0.005243	2.39
50	0.015322	0.015265	0.008779	0.008779	1.74
100	0.018026	0.018031	0.011779	0.011774	1.53
300	0.025602	0.025739	0.019625	0.019531	1.32

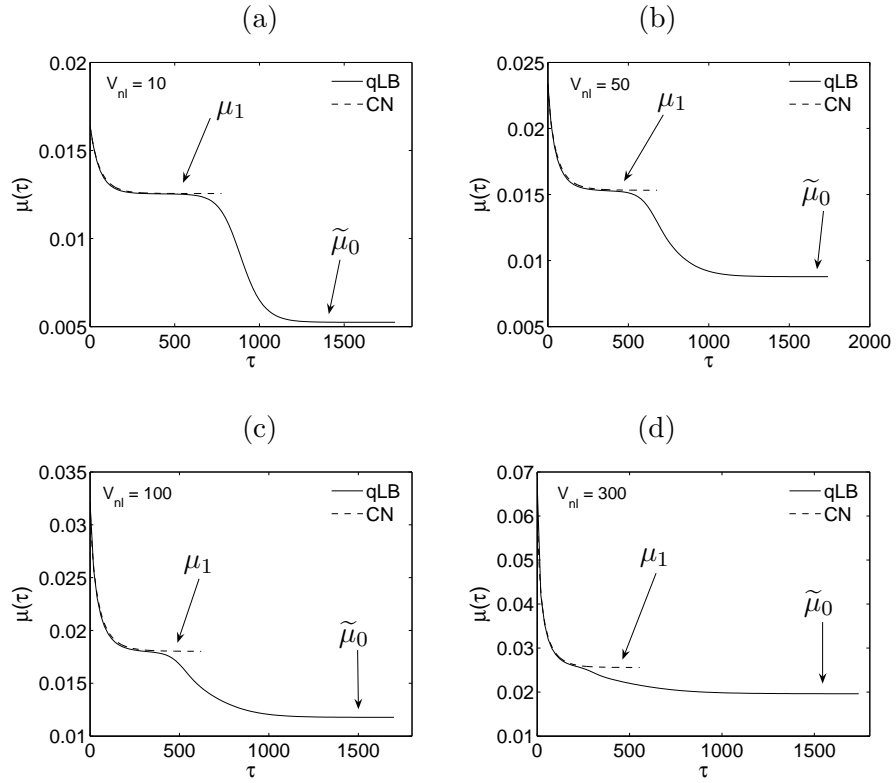


Figure 3.14: Chemical potential decay for different values of  $V_{nl}$  for the first excited state. Simulation parameters are set as:  $\tilde{m} = 1/4$ ,  $\Delta_{0z} = \Delta_{0y} = 16$  and  $\omega_z = \omega_y = 1/256$ . (a)  $V_{nl} = 10$ , (b)  $V_{nl} = 50$ , (c)  $V_{nl} = 100$ , (d)  $V_{nl} = 300$ . Solid lines: qLB model; dashed lines: CN models. Time and chemical potential are expressed in lattice units.

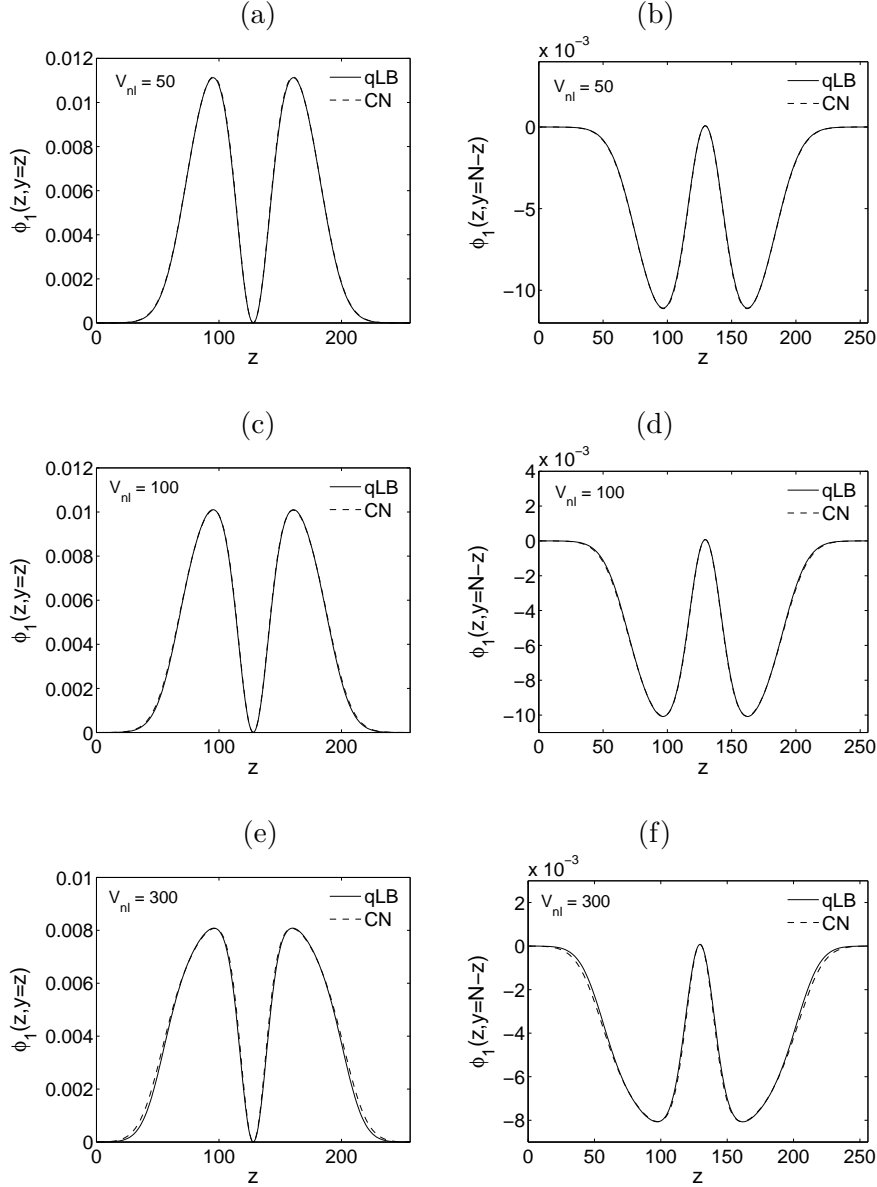


Figure 3.15: First excited state solution  $\phi_1(z, y)$  computed by qLB and CN for different values of  $V_{nl}$ , the solutions are taken at the cross sections  $y = z$  and  $y = N - z$ . Simulation parameters are set as:  $\tilde{m} = 1/4$ ,  $\Delta_{0z} = \Delta_{0y} = 16$  and  $\omega_z = \omega_y = 1/256$ . (a)  $V_{nl} = 500$ , section  $y = z$ , the qLB solution is taken at time  $\tau = 400$ ; (b)  $V_{nl} = 50$ , section  $y = N - z$ , the qLB solution is taken at time  $\tau = 400$ ; (c)  $V_{nl} = 100$ , section  $y = z$ , the qLB solution is taken at time  $\tau = 340$ ; (d)  $V_{nl} = 100$ , section  $y = N - z$ , the qLB solution is taken at time  $\tau = 340$ ; (e)  $V_{nl} = 300$ , section  $y = z$ , the qLB solution is taken at time  $\tau = 260$ ; (f)  $V_{nl} = 300$ , section  $y = N - z$ , the qLB solution is taken at time  $\tau = 260$ . Space is expressed in lattice units.



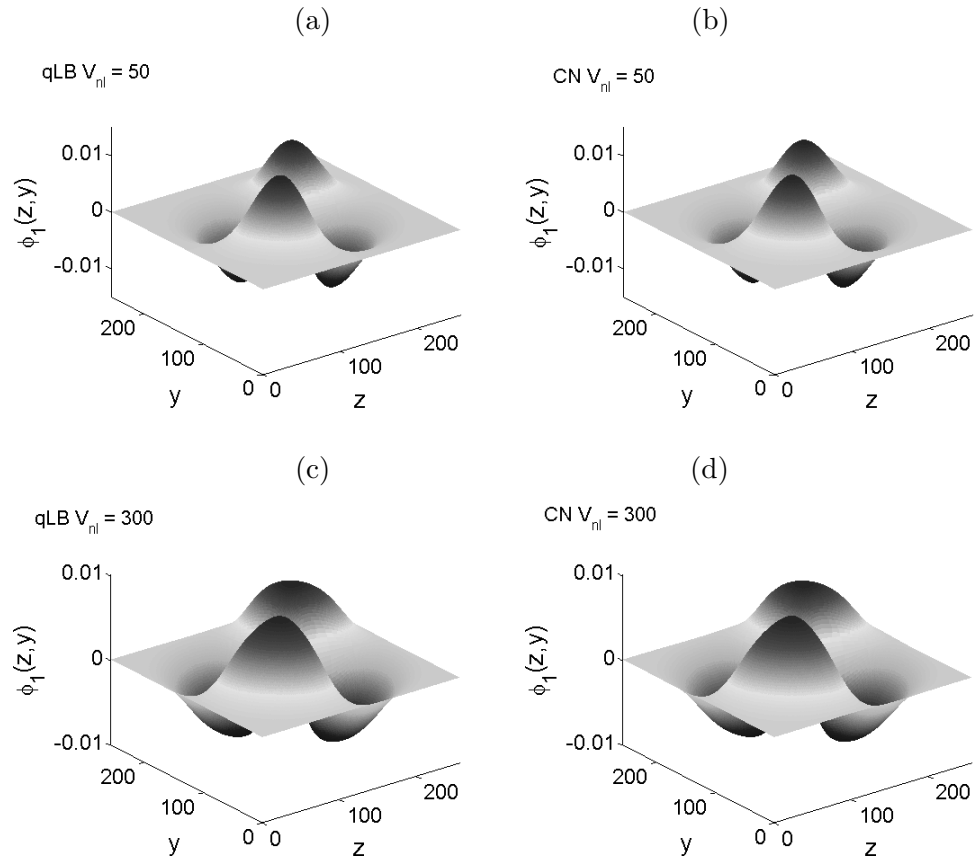


Figure 3.16: First excited state surfaces for  $V_{nl} = 50$  and  $V_{nl} = 300$  computed by qLB and CN. Simulation parameters are set as:  $\tilde{m} = 1/4$ ,  $\Delta_{0z} = \Delta_{0y} = 16$  and  $\omega_z = \omega_y = 1/256$ . (a) qLB model with  $V_{nl} = 50$ , (b) CN model with  $V_{nl} = 50$ , (c) qLB model with  $V_{nl} = 300$ , (d) CN model with  $V_{nl} = 300$ .

### 3.10 Halving the discretization step

One of the distinctive properties of qLB, as opposed to usual explicit schemes for quantum wave equations, is that the time-step scales linearly with the mesh-spacing.

In order to verify this linear dependence, we halved  $\Delta z$  (and consequently  $\Delta\tau$ ) while keeping  $\omega_c$  fixed and we checked the model still gives the same solution.

As an example, we consider the interval  $[0, 1024]$  and set  $\tilde{m} = 1/8$ ,  $\omega_z = 1/128$ ,  $\Delta_0 = 16$  and  $V_{nl} = 10$ . To make a comparison, we compute the solution with CN and BEFD schemes for  $h = 0.0625$  and  $k = 0.1$ . In Tab. 3.7 the values of  $\mu$  obtained halving  $\Delta$  are reported. The “exact” value given by CN and BEFD models with a very small spatial discretization step is  $\mu_{exact} = 0.060112$ . We can observe that, by halving  $\Delta$ , the value of  $\mu$  given by the qLB model increases towards  $\mu_{exact}$ . In Fig. 3.17  $\phi_g(z)$  is plotted for different values of  $\Delta$  and the curves are almost coinciding.

Table 3.7: Chemical potential  $\mu$  obtained halving the discretization step  $\Delta$ . Simulation parameters are set as:  $\tilde{m} = 1/8$ ,  $\omega_z = 1/128$ ,  $\Delta_0 = 16$  and  $V_{nl} = 10$ .

$\Delta$	$\mu$
1	0.060010
0.5	0.060026
0.25	0.060040
0.125	0.060059
0.0625	0.060096
$\mu_{exact}$	0.060112

Although a systematic study of the computational efficiency of the qLB method lies beyond the scope of the present work, as an indication, we just provide some representative data on the computational performance of the scheme. To this end, we consider a domain  $[0, 256] \times [0, 256]$  and set  $\tilde{m} = 1/8$ ,  $\omega_z = \omega_y = 1/128$ ,  $\Delta_{0z} = \Delta_{0y} = 16$  and  $V_{nl} = 50$ . The simulation is stopped when time  $T_{max} = 1000$  is reached. To compare qLB, CN and BEFD performances, we choose the same mesh-spacing and time step for the three models:

$$\Delta \equiv \Delta z = \Delta y = -i\Delta\tau = h = k,$$

and  $\Delta$  is initially set to unit value and then halved twice. In Tab. 3.8, the CPU times required by the models on a standard PC (Intel Pentium 4 CPU 3 GHz) are reported.

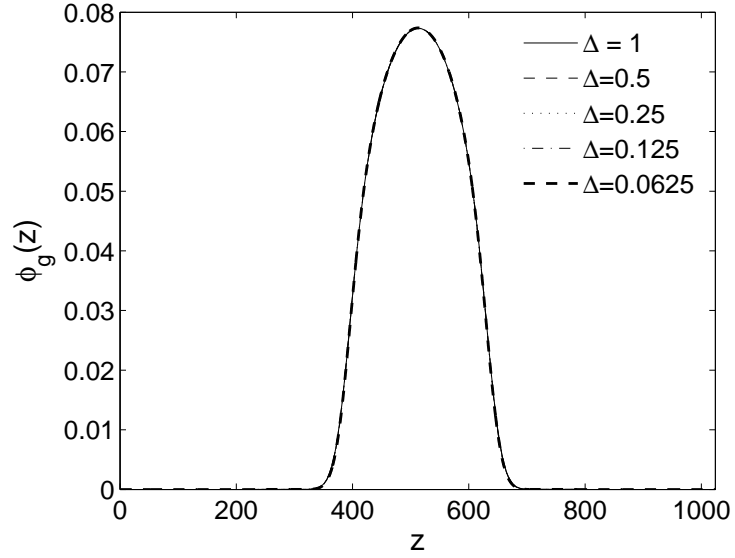


Figure 3.17: Ground state profiles for different values of  $\Delta$ . Simulation parameters are set as:  $\tilde{m} = 1/8$ ,  $\omega_z = 1/128$ ,  $\Delta_0 = 16$  e  $V_{nl} = 10$ . Space is expressed in lattice units.

Table 3.8: CPU times required by qLB, CN and BEFD models using the same mesh-spacing and time step. The discretization step  $\Delta$  is initially set to unit value and then halved twice. Simulation parameters are as follows:  $\tilde{m} = 1/8$ ,  $\omega_z = \omega_y = 1/128$ ,  $\Delta_{0z} = \Delta_{0y} = 16$ ,  $V_{nl} = 50$  and  $T_{max} = 1000$ .

$\Delta$	Mesh size	CPU time qLB (sec)	CPU time CN (sec)	CPU time BEFD (sec)
1	$256 \times 256$	95	81	114
0.5	$512 \times 512$	760	810	1014
0.25	$1024 \times 1024$	6120	9544	10672

These data indicate that qLB performs competitively with respect to CN and BEFD, especially as grid resolution is increased.

### 3.11 From qLB to physical units

Let us consider the Gross–Pitaevskii equation in three dimensions expressed in physical units:

$$i\hbar \frac{\partial \psi(\mathbf{r}, t)}{\partial t} = \left( -\frac{\hbar^2}{2m} \Delta_{\mathbf{r}} + V_{ext}(\mathbf{r}) + NU_0 |\psi(\mathbf{r}, t)|^2 \right) \psi(\mathbf{r}, t), \quad (3.59)$$

where  $\mathbf{r} = (x, y, z)^T$  and  $V_{ext}(\mathbf{r}) = (1/2)m\omega_H^2 \mathbf{r}^2$  and we are assuming, for the sake of simplicity,  $\omega_x = \omega_y = \omega_z \equiv \omega_H$  and we recall that  $U_0 = 4\pi\hbar^2 a/m$ .

The qLB scaling is given by

$$\begin{aligned} \tilde{t} &= t/\Delta t, \quad \tilde{\mathbf{r}} = \mathbf{r}/\Delta r \quad \text{where} \quad (\Delta x = \Delta y = \Delta z \equiv \Delta r), \\ \tilde{\psi}(\tilde{\mathbf{r}}, \tilde{t}) &= (\Delta r)^{3/2} \psi(\mathbf{r}, t), \quad \tilde{\omega}_H = \omega_H \Delta t, \end{aligned} \quad (3.60)$$

where  $\Delta t$  and  $\Delta r$  are the discretization steps expressed in physical units.

From  $\tilde{\omega}_H = \omega_H \Delta t$ , the time step is readily computed as  $\Delta t = \tilde{\omega}_H / \omega_H$ . Since the relation  $\Delta z = c\Delta t$  must hold, it is apparent that in order to simulate physical situations  $c$  must be taken much smaller than the physical light speed. Otherwise, we would need a very small time step to achieve a reasonable  $\Delta r$ . In particular, from the definition of the model parameter

$$\tilde{m} = \omega_c \Delta t = \frac{mc^2}{\hbar} \Delta t,$$

we obtain

$$c^2 = \frac{\tilde{m}\hbar}{m\Delta t}$$

and, consequently

$$\Delta r = c\Delta t = \left( \frac{\tilde{m}\hbar}{m\Delta t} \right)^{1/2} \Delta t \quad (3.61)$$

Applying the qLB scaling of Eq. (3.60) to Eq. (3.59), we obtain

$$i\partial_{\tilde{t}} \tilde{\psi} = -\frac{\hbar}{2m} \frac{\Delta t}{(\Delta r)^2} \Delta_{\tilde{\mathbf{r}}} \tilde{\psi} + \frac{1}{2} \frac{m\tilde{\omega}_H^2}{\hbar} \frac{(\Delta r)^2}{\Delta t} \tilde{\mathbf{r}}^2 + \frac{NU_0}{\hbar} \frac{\Delta t}{(\Delta r)^3} |\tilde{\psi}|^2 \tilde{\psi}.$$

Let us indicate each term as follows:

$$\tilde{D} = -\frac{\hbar}{2m} \frac{\Delta t}{(\Delta r)^2}, \quad (3.62)$$

$$\tilde{V}_{ext} = \frac{1}{2} \frac{m\tilde{\omega}_H^2}{\hbar} \frac{(\Delta r)^2}{\Delta t}, \quad (3.63)$$

$$\tilde{V}_{nl} = \frac{NU_0}{\hbar} \frac{\Delta t}{(\Delta r)^3}. \quad (3.64)$$

Consider now  $\tilde{D}$  (see Eq. (3.62)), from Eq. (3.61), we obtain

$$\tilde{D} = -\frac{\hbar}{2m} \frac{\Delta t}{(\Delta r)^2} = -\frac{1}{2\tilde{m}}. \quad (3.65)$$

As to  $\tilde{V}_{ext}$ , we obtain

$$\tilde{V}_{ext} = \frac{1}{2} \frac{m\tilde{\omega}_H^2}{\hbar} \frac{(\Delta r)^2}{\Delta t} = \frac{1}{2} \tilde{m}\tilde{\omega}_H^2. \quad (3.66)$$

Finally, consider the nonlinear term  $V_{nl}$

$$\tilde{V}_{nl} = \frac{NU_0}{\hbar} \frac{\Delta t}{(\Delta r)^3} = \frac{N4\pi\tilde{a}\hbar}{m} \frac{\Delta t}{(\Delta r)^2} = \frac{N4\pi\tilde{a}}{\tilde{m}}, \quad (3.67)$$

where  $\tilde{a} = a/\Delta r$  is the dimensionless s-wave scattering length.

A typical set of physical parameters, used in current experiments with  $^{87}\text{Rb}$ , reads as follows:

$$m = 1.44 \times 10^{-25} \text{ Kg}, \quad \omega_H = 20\pi 1/s, \quad a = 5.1 \times 10^{-9} m$$

and usual values for the model parameters  $\tilde{\omega}_H$  and  $\tilde{m}$  are

$$\tilde{\omega}_H = 1/128, \quad \tilde{m} = 1/8,$$

thus delivering

$$c = 6.2916 \times 10^{-4} m/s, \quad \Delta z = 1.4487 \times 10^{-7} m, \quad \Delta t = 2.3026 \times 10^{-4} s,$$

from which the number of atoms composing the simulated condensate can be computed

$$N = \frac{\tilde{V}_{nl}}{4\pi} \frac{\tilde{m}}{a} \Delta r \sim \frac{\tilde{V}_{nl}}{4\pi} 3.55.$$

From Eqs. (3.65), (3.66) and (3.67), removing all the  $\tilde{\cdot}$  (apart from  $\tilde{m}$ , in order to not confuse this scaling parameter with the particle mass), we conclude that, with the qLB scaling, the GPE given in Eq. (3.59) becomes

$$i \frac{\partial \psi(\mathbf{r}, t)}{\partial t} = \left( -\frac{1}{2\tilde{m}} \Delta_{\mathbf{r}} + \frac{1}{2} \tilde{m} \omega_H^2 \mathbf{r}^2 + V_{nl} |\psi(\mathbf{r}, t)|^2 \right) \psi(\mathbf{r}, t),$$

where each quantity is expressed in lattice units.



## Chapter 4

# Quantum LB simulation of expanding BECs in random potentials

The study of the dynamics of Bose-Einstein condensates (BEC) in the presence of a random potential is a very active topic in modern condensed matter and atomic physics research. Recently, a large number of experimental and numerical studies have been devoted to the localization properties of Bose gases [123, 93, 36, 56, 37, 101, 3, 130, 94]. It is well known that disorder can profoundly affect the behavior of quantum systems, Anderson localization being one of the most fascinating phenomena in point [8]. Back in 1958, Anderson showed that the eigenstates of single quantum particles in a weak random potential can become localized, which means that the corresponding wave functions exhibit an exponential decay at large distances [123]. Indeed, strong suppression of transport phenomena in expanding BEC's in the presence of disorder has been recently observed experimentally and confirmed by numerical simulations [36, 56, 37, 130, 101, 3]. However, this suppression of transport is not due to Anderson localization, but rather to the fragmentation of the BEC, as it gets trapped between the peaks of the random potential. In Ref. [124], a theoretical and numerical study prescribes the conditions under which a one-dimensional BEC can exhibit Anderson localization. These conditions basically amount to require that the amplitude of the random potential be sufficiently large to promote destructive interference between free-propagating plane waves, and yet significantly smaller than the condensate energy, so as to avoid disruptive fragmentation of the wave function. In addition, the correlation length of the random potential should be smaller than the healing length of the condensate (the scale below which kinetic energy is dominant), so that noise can couple to a sizeable fraction of the spectrum of kinetic-energy car-

riers.

The aim of this chapter, which is an extended version of the paper in Ref. [106], is to further investigate these conditions by means of a quantum lattice Boltzmann model (qLB). As shown in the previous chapters, qLB has been originally developed starting from a formal analogy between the Dirac equation and a Boltzmann equation for a complex distribution function [138, 135, 133]. A major feature of qLB is that unitarity/stability can be achieved with time-step scaling linearly with mesh-size rather than quadratically like most explicit schemes for quantum wave functions [84]. Moreover, a multidimensional formulation of the qLB scheme has been proposed and also extended to the case of nonlinear interactions, as described by the Gross-Pitaevskii equation (GPE) [105, 108] (see Chapter 2 and Chapter 3). In the past decade, many different numerical approaches have been applied to the solution of the time-dependent GPE: a particle-inspired scheme proposed by Chiofalo et al. [33, 34], finite difference methods proposed by Ruprecht et al. [120], Ensher et al. [54] and Wang [144] and a time-splitting spectral (TSSP) method developed by Bao and coworkers initially for the Schrödinger equation in the semi-classical regime [15, 16] and then extended to the GPE [14, 11]. In particular, the TSSP method shows good properties of accuracy and efficiency.

In the present chapter, we explore the use of qLB for the case of nonlinear interactions with random potentials. A systematic comparison with the classical Crank-Nicolson (CN) scheme is also presented, in order to validate qLB numerical results and assess the computational performances at different space-time resolutions. Finally, we investigate the mechanism by which the localized state of the BEC is modified by the residual self-interaction in the (very) long-time term evolution of the condensate.

## 4.1 Review of the quantum Lattice Boltzmann model

The quantum lattice Boltzmann (qLB) model proposed in Refs. [138, 135, 133] is based on a formal analogy between the Dirac equation and the discrete kinetic equation known as lattice Boltzmann equation (LBE). In particular, it is possible to show that the non-relativistic Schrödinger equation ensues from the relativistic Dirac equation in the adiabatic limit where antisymmetric fast modes are enslaved to the symmetric slow ones (see Chapter 1 for details).

In this section, we briefly revise the one dimensional qLB model in order to recall the most important properties of the scheme.



#### 4.1.1 The real-time qLB model

Let us recall the main ideas behind the quantum lattice Boltzmann scheme in one dimension. Consider the Dirac equation in one dimension. Using the Majorana representation [87] and projecting upon chiral eigenstates, the Dirac equation reads:

$$\begin{aligned}\partial_t u_{1,2} + c\partial_z u_{1,2} &= \omega_c d_{2,1} + igu_{1,2}, \\ \partial_t d_{1,2} - c\partial_z d_{1,2} &= -\omega_c u_{2,1} + igd_{1,2},\end{aligned}\tag{4.1}$$

where  $u_{1,2}$  and  $d_{1,2}$  are complex wave functions composing the Dirac quadrispinor  $\psi = (u_1, u_2, d_1, d_2)^T$ , and  $\omega_c = mc^2/\hbar$  is the Compton frequency,  $g = qV/\hbar$  is the space-dependent frequency coupling to the external potential  $V$  and  $q$  is the particle electric charge. Since we restrict our attention to electrostatic potentials, the spinorial indices will be dropped in the following.

As observed in Ref. [138], Eq. (4.1) is a discrete Boltzmann equation for a couple of complex wave functions  $u$  and  $d$ . In particular, the propagation step consists of streaming  $u$  and  $d$  along the  $z$ -axis with opposite speeds  $\pm c$ , while the collision step is performed according to the scattering matrix defined by the right hand side of Eq. (4.1).

Non-relativistic motion is reproduced by the model in the adiabatic (low frequency) limit:

$$|\omega - \omega_c| \ll |\omega_c + g|,\tag{4.2}$$

where  $\omega$  is the typical frequency (energy) of the solution  $\psi$ . With the additional constraint of “small” potential interaction

$$|g| \ll \omega_c,\tag{4.3}$$

it can be shown that the “slow” mode (to be defined shortly) dynamics is governed by the Schrödinger equation for a spinless particle of mass  $m$ . In particular, under the unitary transformation

$$\phi^\pm = \frac{1}{\sqrt{2}} \exp(i\omega_c t)(u \pm id),$$

from Eq. (4.1) it is easy to check that the following equations are satisfied

$$\begin{aligned}\partial_t \phi^+ + c\partial_z \phi^- &= ig\phi^+, \\ \partial_t \phi^- + c\partial_z \phi^+ &= 2i\omega_c \phi^- + ig\phi^-\end{aligned}\tag{4.4}$$

From Eq. (4.4), after adiabatic elimination of the “fast” antisymmetric mode

$$|\partial_t \phi^-| \ll |2\omega_c + g||\phi^-|,$$

we obtain

$$i\hbar\partial_t\phi^+ = -\frac{\hbar c^2}{2\omega_c}\partial_z\left(\frac{2\omega_c}{2\omega_c+g}\partial_z\phi^+\right) - qV\phi^+ \approx -\frac{\hbar^2}{2m}\partial_z^2\phi^+ - qV\phi^+, \quad (4.5)$$

where the last approximation in Eq. (4.5) is valid in the “small” potential interaction limit given by Eq. (4.3).

The qLB scheme is obtained by integrating Eq. (4.1) along the characteristics of  $u$  and  $d$  respectively and approximating the right hand side integral by using the trapezoidal rule. Assuming  $\Delta z = c\Delta t$ , the following scheme is obtained

$$\begin{aligned} \hat{u} - u &= \frac{\tilde{m}}{2}(d + \hat{d}) + \frac{i\tilde{g}}{2}(u + \hat{u}), \\ \hat{d} - d &= -\frac{\tilde{m}}{2}(u + \hat{u}) + \frac{i\tilde{g}}{2}(d + \hat{d}), \end{aligned} \quad (4.6)$$

where  $\hat{u} = u(z + \Delta z, t + \Delta t)$ ,  $\hat{d} = d(z - \Delta z, t + \Delta t)$ ,  $u = u(z, t)$ ,  $d = d(z, t)$  and  $\tilde{m} = \omega_c\Delta t$ ,  $\tilde{g} = g\Delta t$ . The linear system of Eq. (4.6) is algebraically solved for  $\hat{u}$  and  $\hat{d}$  and yields the explicit scheme:

$$\begin{aligned} \hat{u} &= au + bd, \\ \hat{d} &= ad - bu, \end{aligned} \quad (4.7)$$

where

$$a = (1 - \Omega/4)/(1 + \Omega/4 - i\tilde{g}), \quad b = \tilde{m}/(1 + \Omega/4 - i\tilde{g}),$$

with  $\Omega = \tilde{m}^2 - \tilde{g}^2$ . Here  $\tilde{m} = \omega_c\Delta t$  represents the dimensionless Compton frequency. Note that, since  $|a|^2 + |b|^2 = 1$ , the collision matrix is unitary, thus the method is norm-preserving and the stability is secured provided that  $\Delta z = c\Delta t$  for any value of  $\Delta t$ . In particular, the quantity  $\|\phi^+\|^2 + \|\phi^-\|^2$ , where  $\|\cdot\|$  indicates the  $L^2$  norm, is kept at unit value all along the evolution. It follows that  $\|\phi^+\|^2$  cannot be preserved during the evolution. Indeed, we have  $\|\phi^-\| \ll \|\phi^+\|$  with both terms oscillating in such a way that  $\|\phi^+\|^2 + \|\phi^-\|^2 = 1$ .

## 4.2 The Gross-Pitaevskii equation

Let us briefly introduce the three-dimensional Gross-Pitaevskii equation (GPE) and the procedure which leads to its reduction to one dimension for a special setting of the harmonic trap.

At zero temperature, the dynamics of a trapped Bose-Einstein condensate (BEC) is described by the time-dependent Gross-Pitaevskii equation (GPE). The

GPE for a quantum wave function  $\psi(\mathbf{r}, t)$ , with  $\mathbf{r} = (x, y, z)^T \in \mathbb{R}^3$ , reads as follows

$$i\hbar\partial_t\psi(\mathbf{r}, t) = \left(-\frac{\hbar^2}{2m}\Delta_r + V_{ext}(\mathbf{r}) + NU_0|\psi(\mathbf{r}, t)|^2\right)\psi(\mathbf{r}, t), \quad (4.8)$$

where  $m$  is the atomic mass,  $U_0 = 4\pi\hbar^2 a/m$  is the coupling strength,  $a$  is the scattering length,  $N$  is the number of particles in the condensate and  $V_{ext}(\mathbf{r})$  is the external trapping potential.

Typically, the external potential is taken in the form of an harmonic trap:

$$V_{ext}(x, y, z) = \frac{1}{2}m(\omega_x^2 x^2 + \omega_y^2 y^2 + \omega_z^2 z^2).$$

The three-dimensional GPE can be easily reduced to one dimension for a particular choice of the harmonic trap [72, 88, 12, 1, 33] (see Chapter 3). In particular, for  $\omega_x = \omega_y \equiv \omega_\perp$  and  $\omega_z \ll \omega_\perp$ , the GPE of Eq. (4.8) is transformed into

$$i\hbar\partial_t\psi(z, t) = \left(-\frac{\hbar^2}{2m} + V_{ext}(z) + NU_1|\psi(z, t)|^2\right)\psi(z, t), \quad (4.9)$$

where  $U_1 = 2a\hbar\omega_\perp$  is the one-dimensional coupling constant equivalent to the three-dimensional one and  $V_{ext}(z) = (1/2)m\omega_z^2 z^2$ .

In order to numerically solve Eq. (4.9) by using qLB and CN scheme, the so-called qLB scaling (see Sec. 3.11) is applied to Eq. (4.9). In the following subsection, we describe the scaling procedure for the one dimensional GPE in order to compute the nonlinearity coupling coefficient in lattice units.

#### 4.2.1 qLB scaling

The qLB scaling is defined by

$$\tilde{t} = \frac{t}{\Delta_t}, \quad \tilde{z} = \frac{z}{\Delta_z}, \quad \tilde{\psi}(\tilde{z}, \tilde{t}) = (\Delta_z)^{1/2}\psi(z, t), \quad \tilde{\omega}_z = \omega_z\Delta_t,$$

where  $\Delta_z$  and  $\Delta_t$  are the discretization steps in physical units. From  $\tilde{\omega}_z = \omega_z\Delta_t$ , the time step is readily computed  $\Delta_t = \tilde{\omega}_z/\omega_z$ . As observed in Ref. [108], since the relation  $\Delta_z = c\Delta_t$  must hold, it is apparent that in order to simulate physical situations  $c$  must be taken much smaller than the physical light speed. Otherwise, we would need a very small time step to achieve a reasonable  $\Delta_z$ . In particular, from the definition of the model parameter  $\tilde{m} = \omega_c\Delta_t = (mc^2/\hbar)\Delta_t$ , we have

$$c^2 = \frac{\tilde{m}\hbar}{m\Delta_t},$$

and then

$$\Delta_z = c\Delta_t = \left(\frac{\tilde{m}\hbar}{m\Delta_t}\right)^{1/2} \Delta_t.$$

By applying this scaling to Eq. (4.9) and removing all the  $\tilde{\cdot}$ , we obtain

$$i\partial_t\psi(z,t) = \left( -\frac{1}{2\tilde{m}}\partial_z^2 + \frac{1}{2}\tilde{m}\omega_z^2 z^2 + \beta_{qLB}|\psi(z,t)|^2 \right) \psi(z,t),$$

where the nonlinearity coupling constant  $\beta_{qLB}$  is given by

$$\beta_{qLB} = \frac{2a_z^2 a \omega_z N}{\Delta_z a_\perp^2},$$

with  $a_z = \sqrt{\hbar/(m\omega_z)}$  and  $a_\perp = \sqrt{\hbar/(m\omega_\perp)}$ . From the above expression, it is clear that the adiabatic assumption underlying the qLB theory, sets a limit on the strength of the non linear interactions, i.e. on the number of bosons,  $N$ . More precisely, the high-energy components of the wave functions, evolve accordingly to a second-order hyperbolic (Klein-Gordon) equation, rather than to the first-order parabolic (Schrödinger) diffusive dynamics.

### 4.3 Numerical construction of the random speckle potential

In this section, we describe how the random speckle distribution is numerically constructed. For the sake of simplicity, here we use arbitrary, dimensionless units (i. e., lengths are expressed in units of an arbitrary scale whose actual value is irrelevant here).

For this discussion we follow closely the work of Modugno [101] which describes a one-dimensional version of an algorithm presented in Ref. [71]. A mathematical analysis of the statistical properties of the speckle distribution can be found in Ref. [60].

The speckle distribution is constructed by starting from a random complex field  $\phi(z)$  whose real and imaginary part are obtained from two independent Gaussian random distribution  $\eta(z)$  with zero mean,  $\langle\eta(z)\rangle = 0$ , unit standard deviation and correlation function  $\langle\eta(x)\eta(y)\rangle = 0$ . The speckle intensity field is then defined as

$$I(z) = |\mathcal{F}^{-1} [W(k)\mathcal{F}[\phi(z)]]|^2, \quad (4.10)$$

where the operator  $\mathcal{F}$  indicates the Fourier transform operator and  $W(k)$  is the following frequency filter

$$W(k) = \begin{cases} 1 & \text{if } |k| < D/2, \\ 0 & \text{elsewhere.} \end{cases}$$

The resulting distribution probability of the speckle intensities is

$$P(I) = \frac{e^{-I/\langle I \rangle}}{\langle I \rangle}. \quad (4.11)$$

The spatial autocorrelation function is

$$C(z) = \langle I(z')I(z' + z) \rangle = 1 + \left( \frac{\sin(\pi Dz)}{(\pi Dz)} \right)^2, \quad (4.12)$$

where  $\langle \cdot \rangle$  stands for an integration over  $z'$  and an average over many realizations.

The distribution of Eq. (4.10) can be easily transformed so to have zero mean and unit standard deviation, let us define the normalized speckle distribution:

$$v_n(z) = \frac{I(z) - \langle I \rangle}{(\langle I^2 \rangle - \langle I \rangle^2)^{1/2}}, \quad (4.13)$$

the corresponding distribution probability of the intensities is

$$P(v_n) = \exp(-[v_n + 1])\Theta(v_n + 1), \quad (4.14)$$

where  $\Theta$  is the Heaviside step function.

The autocorrelation function then becomes

$$C_n(z) = \langle v_n(z')v_n(z' + z) \rangle = \left( \frac{\sin(\pi Dz)}{(\pi Dz)} \right)^2. \quad (4.15)$$

In particular, in order to obtain a fixed value of the correlation length,  $\sigma$ , we set

$$D = \frac{1}{\pi\sigma},$$

so that

$$C_n(z) = \langle v_n(z')v_n(z' + z) \rangle = \text{sinc}^2(z/\sigma), \quad \text{where} \quad \text{sinc}(x) := \sin^2(x)/x^2.$$

In Fig. 4.1, autocorrelation function of the normalized speckle distribution,  $v_n(z)$ , obtained by averaging over 500 realizations of the speckle potential is compared with  $C(z)$  of Eq. (4.15). For this test we set  $D = 0.1$  and we used a lattice of 8192 nodal points. In Fig. 4.2 the intensity distribution,  $P(v_n)$ , is compared with the expected exponential curve given by Eq. (4.14).

## 4.4 Anderson localization of expanding BEC in speckle potential

The aim of this chapter is to apply the qLB scheme to the study of an expanding BEC in the presence of disorder. As it is well known, quantum systems can be highly affected by disorder, one of the most famous phenomena which may occur being Anderson localization (AL) [8], whereby the eigenstates of single quantum

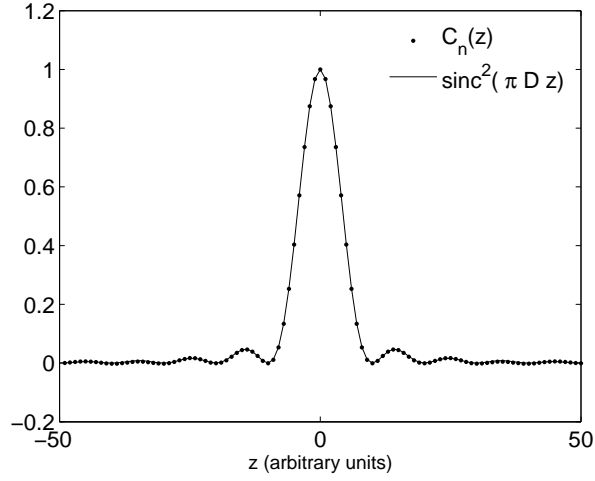


Figure 4.1: Autocorrelation function for the normalized speckle potential obtained by averaging over 500 realizations. The autocorrelation function is compared with the expected analytical curve of Eq. (4.15). The filter aperture is set as  $D = 0.1$ .

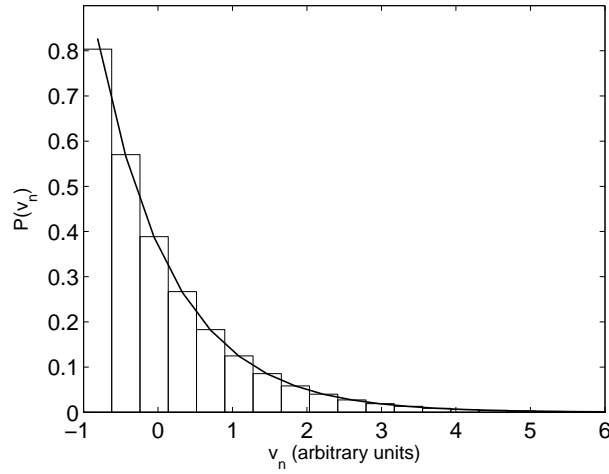


Figure 4.2: Intensity distribution for the normalized speckle potential obtained by averaging over 500 realizations. The intensity distribution is compared with the expected analytical curve of Eq. (4.14). The filter aperture is set as  $D = 0.1$ .

particles in weak random potential can become localized, i. e. the eigenstates exhibit an exponential decay at large distances [123]. In one spatial dimension, the entire wave function is localized, i. e. all eigenstates are localized. Recently, both experimental and numerical studies have been devoted to localization of Bose gases [123, 93, 36, 56, 37, 101, 3] in order to fully understand the interplay between nonlinear interactions and disorder. The strength of the interaction is characterized by the inverse ratio of the initial healing length  $\xi_h = \hbar/\sqrt{4m\mu}$ , to the Thomas-Fermi half length  $L_{TF} = \sqrt{2\mu/m\omega_z^2}$ , where  $\mu$  is the chemical potential,  $m$  the boson mass and  $\omega_z$  the longitudinal frequency of the optical trap [123]. The properties of random potential are summarized by its intensity  $V_R$  and correlation length  $\sigma_R$ .

As shown in Ref. [124], for  $\sigma_R < \xi_h$  and for a weak disorder  $V_R/\mu < 1$ , a one-dimensional BEC can exhibit Anderson localization.

As observed in Ref. [124], localization of BEC in a random potential has been already reported in Refs. [36, 56, 37]. However, in this case, suppression of transport was not due to Anderson localization, but rather to the fragmentation of the BEC, as a result of trapping between the peaks of the potential.

Following the model proposed in Ref. [124], we consider a one-dimensional Bose-Einstein condensate trapped in an harmonic potential in the presence of a random potential  $V(z)$ . The corresponding Gross-Pitaevskii equation reads as follows:

$$i\hbar\partial_t\psi(z,t) = \left(-\frac{\hbar^2}{2m}\partial_z^2 + \frac{1}{2}m\omega_z^2 z^2 + V(z) + NU_1|\psi(z,t)|^2 - \mu\right)\psi(z,t), \quad (4.16)$$

where  $U_1$  is the coupling constant and  $\mu$  is the chemical potential. The random potential  $V(z)$  is taken in the form of a one dimensional speckle potential [60, 71, 70, 101], with a truncated negative exponential single-point distribution:

$$P(V) = \frac{\exp(-[V + V_R]/V_R)}{V_R} \Theta\left(\frac{V}{V_R} + 1\right), \quad (4.17)$$

where  $\Theta$  is the Heaviside step function. This particular form of the speckle potential is obtained by multiplying the normalized speckle potential  $v_n(z)$  of Eq. (4.13), which has zero average and unit standard deviation, by  $V_R$ , hence  $V(z) = V_R v_n(z)$ . The average of  $V$  over the disorder vanishes, while  $\langle V^2 \rangle = V_R$ . The correlation function  $C(z) = \langle V(z')V(z'+z) \rangle$  can be written as a function of the correlation length of the potential,  $\sigma_R$ , in particular it reads as follows [60, 37]:

$$C(z) = \langle V(z')V(z'+z) \rangle = V_R^2 \text{sinc}^2(z/\sigma_R), \quad \text{where} \quad \text{sinc}(x) := \sin(x)/x, \quad (4.18)$$

where  $\langle \cdot \rangle$  stands for integration over  $z'$  and average over many realizations. The Fourier transform of  $C(z)$  is given by

$$\begin{aligned}\widehat{C}(k) &= V_R^2 \sigma_R \widehat{c}(k\sigma_R), \quad \text{where} \\ \widehat{c}(\kappa) &= \sqrt{\frac{\pi}{2}} \left(1 - \frac{|\kappa|}{2}\right) \Theta\left(1 - \frac{|\kappa|}{2}\right),\end{aligned}\tag{4.19}$$

so that  $\widehat{C}(k) = 0$  for  $|k| > 2/\sigma_R$ . This form of the Fourier transform of  $C(z)$  (and, in particular, its finite support), are crucial for the quantitative estimation of the localization length.

Let us summarize the procedure outlined in Ref. [124] in order to derive a large-distance asymptotic behavior of the wave function density  $n(z)$ . Initially, the BEC is assumed to be at equilibrium in the harmonic trap and in the absence of disorder. In the Thomas-Fermi regime (TF) where  $\mu \gg \hbar\omega$ , the initial BEC density is an inverted parabola  $n(z) = (\mu/g)(1 - z^2/L_{TF}^2)\Theta(1 - |z|/L_{TF})$ . The expansion is induced by switching off the confining trap at time  $t = 0$  still in absence of disorder. Repulsive atom-atom interaction are significant in the short-time ( $t \leq 1/\omega$ ) expansion, while at larger times ( $t \gg 1/\omega$ ) the interactions are no longer important and the expansion becomes free. Hence, the expanding BEC density profile is rescaled but remain an inverted parabola [75, 32]:

$$\psi(z, t) = \left(\psi(z/b(t), 0)/\sqrt{b(t)}\right) \exp(imz^2\dot{b}(t)/2\hbar b(t)),\tag{4.20}$$

where  $b(t) = 1$  for  $t = 0$  and  $b(t) \sim \sqrt{2}\omega t$  for  $t \gg 1/\omega$  [36]. Then the random potential is switched on at time  $t_0 \gg 1/\omega$ . Since the atom-atom interactions are no longer important, the BEC may be represented as a superposition of almost independent plane waves:

$$\psi(z, t) = \int \frac{dk}{\sqrt{2\pi}} \widehat{\psi}(k, t) \exp(ikz).\tag{4.21}$$

The momentum distribution  $\mathcal{D}(k)$  follows from Eq. (4.20). For  $t \gg 1/\omega$  it is stationary and has a high-momentum cutoff at  $1/\xi_h$ :

$$\mathcal{D}(k) = |\widehat{\psi}(k, t)|^2 \sim \frac{3\xi_h}{4} (1 - k^2\xi_h^2) \Theta(1 - k\xi_h),\tag{4.22}$$

with the normalization condition  $\int_{-\infty}^{+\infty} \mathcal{D}(k) dk = 1$ .

According to Anderson localization theory,  $k$  waves will exponentially localize as a result of multiple scattering from the random potential. Thus components  $\exp(ikz)$  in Eq. (4.21) will become localized function  $\phi_k(z)$ . At long distances,  $\phi_k(z)$  decay exponentially such that  $\ln|\phi_k(z)| \sim -\gamma(k)|z|$ , where  $\gamma(k)$  is the so



called Lyapunov exponent. Assuming that the phases of the functions  $\phi_k(z)$  are random uncorrelated functions for different momenta, the BEC density is given by

$$n_0(z) = \langle |\psi(z)|^2 \rangle = 2 \int_0^\infty dk \mathcal{D}(k) \langle |\psi_k(k)|^2 \rangle, \quad (4.23)$$

where we have taken into account that  $\mathcal{D}(k) = \mathcal{D}(-k)$  and  $\langle |\phi_k(z)|^2 \rangle = \langle |\phi_{-k}(z)|^2 \rangle$ . In Ref. [124], an approximation for the Lyapunov exponent  $\gamma(k)$  is computed and is given by

$$\gamma(k) = \frac{\sqrt{2\pi}}{8\sigma_R} \left( \frac{V_R}{E} \right)^2 (k\sigma_R)^2 \hat{c}(2k\sigma_R), \quad (4.24)$$

where  $E = \hbar^2 k^2 / (2m)$ . The approximation of Eq. (4.24) is valid assuming that the following inequalities holds

$$V_R \sigma_R \ll \left( \frac{\hbar k}{m} (k\sigma_R)^{1/2} \right). \quad (4.25)$$

Deviations from a pure exponential decay of  $\phi_k$  can be computed and, at large distances ( $\gamma(k)|z| \gg 1$ ), one obtains

$$\langle |\phi_k(z)|^2 \rangle \approx \frac{\pi^{7/2}}{64\sqrt{2\gamma(k)}} |z|^{-3/2} \exp(-2\gamma(k)|z|). \quad (4.26)$$

From Eq. (4.24), we observe that the localization effect is closely related to the properties of the correlation function. For the speckle potential of Eq. (4.17), substituting Eq. (4.19) into Eq. (4.24), we obtain

$$\gamma(k) \sim \gamma_0(k)(1 - |k|\sigma_R)\Theta(1 - |k|\sigma_R), \quad \gamma_0(k) = \frac{\pi m^2 V_R^2 \sigma_R}{2\hbar^4 k^2}, \quad (4.27)$$

so that  $\gamma(k) > 0$  only for  $k\sigma_R < 1$ .

We now use Eqs. (4.22), (4.26) and (4.27) to calculate the density profile of the localized BEC at large distances from Eq. (4.23).

In particular, since the high-momentum cutoff for  $\mathcal{D}(k)$  is  $1/\xi_h$  (see Eq. (4.22)), while for  $\gamma(k)$  the cutoff is given by  $1/\sigma_R$ , the upperbound for the integration of Eq. (4.23) is

$$k_c = \min\{1/\xi_h, 1/\sigma_R\}.$$

Since the density profile is a sum of functions  $\langle |\phi_k(z)|^2 \rangle$  which decay exponentially with a rate  $2\gamma(k)$ , the long tail behavior is mainly determined by the components with the smallest  $k$ , i. e. those with  $k$  close to  $k_c$ .

For  $\xi_h > \sigma_R$ , the high-momentum cutoff in Eq. (4.23) is set by the momentum distribution  $\mathcal{D}(k)$  and is equal to  $\xi_h$ . In this case, all functions  $\langle |\phi_k(z)|^2 \rangle$  have a finite Lyapunov exponent,  $\gamma(k) > \gamma(1/\xi_h)$ , and the whole BEC wave function is

exponentially localized.

For the long-tail behavior, from Eqs. (4.22), (4.23) and (4.26), we obtain

$$n(z) \propto |z|^{-3/2} \exp(-2\gamma(1/\xi_h)|z|). \quad (4.28)$$

Moreover, according to Eq. (4.25), since the typical momentum of the expanding BEC is  $1/\xi_h$ , this approach is valid for

$$V_R \ll \mu(\xi_h/\sigma_R)^{1/2}. \quad (4.29)$$

As shown in Ref. [124], for  $\xi_h < \sigma_R$ ,  $k_c$  is provided by the Lyapunov exponents of  $\langle |\phi_k(z)|^2 \rangle$  and in this case the localization becomes algebraic and it is only partial since the part of the BEC wave function corresponding to the waves with momenta in the range  $1/\sigma_R < |k| < 1/\xi_h$  continues to expand.

Here, we consider a parameter setting such that  $\sigma_R < \xi_h$  and the condition of Eq. (4.29) is fulfilled so that the expanding condensate can exhibit Anderson localization.

## 4.5 Numerical results

The time evolution of the BEC wave function is traced by solving Eq. (4.16) by means of qLB and CN schemes. We observe that qLB is designed so as to solve Eq. (4.16) in the qLB scaling, whereby  $c\Delta t/\Delta z = 1$ , so that  $\Delta z$  and  $\Delta t$  scale linearly with each other. The unitarity of the collision matrix implies that the scheme is stable and norm-preserving for any value of  $\Delta z = c\Delta t$ . The CN is an implicit scheme, hence unconditionally stable, although its accuracy depends on the diffusion Courant-Friedrichs-Lewy (CFL) coefficient  $C_D = \frac{D\Delta t}{(\Delta z)^2}$ , where  $D = \hbar/(2m)$  and the potential CFL coefficient  $C_V = \frac{V\Delta t}{\hbar}$ , where  $V = V_R + NU_1 \max_z(|\psi(z)|^2)$ .

We solve Eq. (4.16) with the qLB scaling by using both qLB and CN and we increase time and space resolution while keeping  $\Delta z = \Delta t$  ( $c = 1$  in atomic units) as required by qLB.

As observed in Sec. 4.1, the real-time qLB scheme solves GPE in the limit of “small” potential interaction. Hence, large values for the coupling constant  $\beta_{qLB}$  violate the adiabatic assumption. This implies limitations to the ratio between  $L_{TF}$  and  $\xi_h$ , where  $L_{TF} = \sqrt{2\mu/m\omega_z^2}$  is the Thomas-Fermi half length. In practice, qLB is constrained to  $\lambda \equiv L_{TF}/\xi_h \sim 10$ .

In particular, for the present simulations, parameters are set as follows:

$$\omega_z = 5 \times 10^{-3}, \quad \beta_{qLB} = 2, \quad \tilde{m} = 1/4,$$

This set-up delivers  $\mu = 0.01943$ ,  $L_{TF} = 78.85$  and  $\xi_h = 7.17$ . The domain length is set to  $L = 32000 \sim 400L_{TF}$  and the simulation span at  $T = 150/\omega_z = 30000$ .

As a result,  $\lambda = 10.997$  and we set  $V_R = 0.2\mu$  and  $\sigma_R = 0.5\xi_h$ , so that  $\sigma_R < \xi_h$  and condition of Eq. (4.29) are fulfilled.

As previously mentioned, localization of expanding BEC in random potentials has been experimentally observed in Refs. [36, 56, 130, 37, 94]. However, in those experiments, the parameter setting does not fulfill the condition  $\sigma_R < \xi_h$  and the constraint of Eq. (4.29), which are crucial in order to detect the Anderson localization phenomena [124]. Nonetheless, the parameter setting proposed in Ref. [124] and used here is definitely accessible in current experiments. Indeed, recent experiments reported in Ref. [21] have investigated this range of parameters and reported clear evidence of Anderson localization, in good agreement with theoretical predictions of Refs. [124, 92]. In particular, in the experiment of Ref. [21], the authors consider a BEC composed of  $N = 1.7 \times 10^4$  atoms of  $^{87}\text{Rb}$  with an initial chemical potential  $\mu/(2\pi\hbar) = 219$  Hz. The BEC is initially trapped by an elongated harmonic potential with a transverse frequency  $\omega_\perp/(2\pi) = 70$  Hz and a longitudinal frequency  $\omega_z/(2\pi) = 5.4$  Hz. This implies a Thomas-Fermi half length  $L_{TF} = 41.75 \mu\text{m}$  and an initial healing length  $\xi_h = 0.364 \mu\text{m}$ , thus yielding a separation scale  $\lambda = 114$ . The speckle potential can be accurately controlled in order to attain specific values for the mean intensity  $V_R$  and correlation length  $\sigma_R$ . In Ref. [21], the mean intensity is tuned so that  $V_R/\mu$  varies in the range  $0.07 - 0.34$ , while the correlation length is set at  $\sigma_R = 0.26 \mu\text{m}$ , thus satisfying the condition  $\sigma_R < \xi_h$  and the constraint of Eq. (4.29).

With this setting, the exponential localization is clearly observed and the localization length  $L_{loc}$  is found to vary from about 2 mm to 0.25 mm, while increasing the mean intensity of the speckle potential  $V_R$ .

In our simulations, we are considering a weaker interacting BEC, which could be experimentally achieved by decreasing the inter-atomic interaction either by density control (i. e. lower number of atoms) or by Feshbach resonances [21]. In particular, by leaving all the other parameters unchanged, we are simulating a BEC with  $\mu/(2\pi\hbar) = 21$  Hz, which delivers  $L_{TF} = 13 \mu\text{m}$  and  $\xi_h = 1.18 \mu\text{m}$ , thus yielding  $\lambda \sim 11$ . As we shall see below, with this setting we obtain a localization length  $L_{loc} = 1.19$  mm for  $V_R/\mu = 0.2$ .

In conclusion, our set of parameters is representative of current BEC experiments, although with possibly a weaker nonlinearity, i. e. narrower separation between the outer and inner length-scales,  $L_{TF}$  and  $\xi_h$ , respectively.

As we shall demonstrate, a scale separation  $\lambda \sim 10$  is nonetheless sufficient to yield clear evidence of Anderson localization.

In Fig. 4.3, we present the averaged wave function for five different values of the separation parameter  $\lambda$ .

From this figure, a clear delocalization trend with decreasing values of  $\lambda$  is observed.

The separation parameter  $\lambda$  is changed by tuning the coupling constant  $\beta_{qLB}$ . By changing  $\beta_{qLB}$ , the chemical potential  $\mu$  also changes and, consequently,  $L_{TF}$  and  $\xi_h$  are modified. Parameters are chosen in such a way that the ratios  $V_R/\mu$  and  $\sigma_R/\xi_h$  are kept at 0.2 and 0.5, respectively. Discretization steps are chosen so that a sufficient resolution is achieved. In particular, numerical experiments show that satisfactory results are obtained for  $R > 5$ , where  $R \equiv \xi_h/\Delta z$  is the resolution parameter. This has been set to the following values:

$$\begin{aligned} \lambda = 1 : R = 23.78(\Delta z = 1), \quad \lambda = 5 : R = 10.63(\Delta z = 1), \\ \lambda = 10 : R = 7.16(\Delta z = 1), \quad \lambda = 20 : R = 10.62(\Delta z = 0.5), \\ \lambda = 50 : R = 6.72(\Delta z = 0.5). \end{aligned}$$

For  $\lambda > 10$ , an unphysical pile-up on the tails of the wave function is observed, which is due to the lack of adiabaticity of the fast (high-frequency) modes. As we shall see, this problem also arises for  $\lambda \sim 10$ , when the grid resolution is not sufficient, i.e whenever the wavelength of the highest frequencies becomes comparable with the lattice spacing.

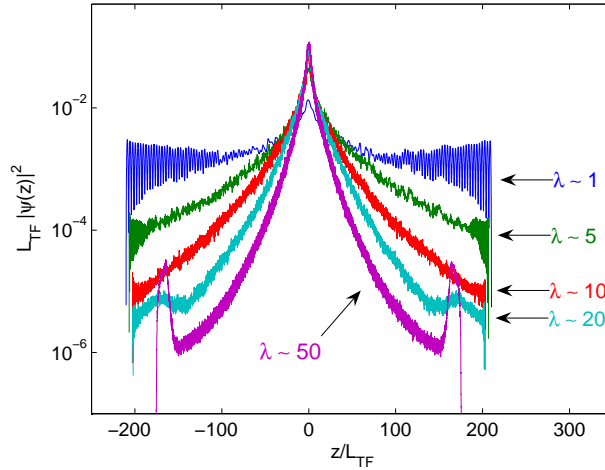


Figure 4.3: Averaged wave function densities computed by qLB for five different values of the ratio  $\lambda \equiv L_{TF}/\xi_h = 1, 5, 10, 20, 50$  (top-down). Parameters are set as follows:  $\omega_z = 5 \times 10^{-3}$ ,  $\tilde{m} = 1/4$ ,  $V_R = 0.2\mu$ ,  $\sigma_R = 0.5\xi_h$ ,  $T = 150/\omega_z$ . The delocalization trend at decreasing values of  $\lambda$  is well visible.

It is instructive to investigate the effects of spatial resolution, as measured by the parameter  $R$ , representing the number of nodal points covering the initial

healing length. We start with an under-resolved situation,  $R = 0.448$  (corresponding to  $N_g = 2000$  nodal points), and subsequently increase the resolution up to  $R = 28.68$  ( $N_g = 128000$ ). While increasing the spatial resolution, we also increase the time resolution by keeping  $\Delta t = \Delta z$ . The elapsed time spent by qLB and CN are pretty similar at all resolutions, with a mild tendency of qLB to outperform CN at high-resolutions (5058 versus 6242 CPU seconds for  $N_g = 128000$  on a standard PC Intel Pentium 4, 3 GHz).

The wave function density is computed by averaging over the solutions obtained with 100 realizations of the speckle potential. In Fig. 4.4 and Fig. 4.5, the averaged wave function densities computed by qLB and CN respectively at the four spatial resolutions ( $N_g = 2000, 8000, 32000, 128000$ ) are shown and compared with the asymptotic behavior given by Eq. (4.28). In qLB simulations, pile-up at high-frequencies/large distances is observed (see Fig. 4.4), which is due to the lack of the adiabaticity assumption at high energies. The CN solution, on the other hand, shows a very different behavior at low-resolution, namely an over-localization of the wave-function (see Fig. 4.5 for  $N_g = 2000$ ). This signals the potential 'danger' that under-resolved CN simulations may *over-estimate* Anderson localization.

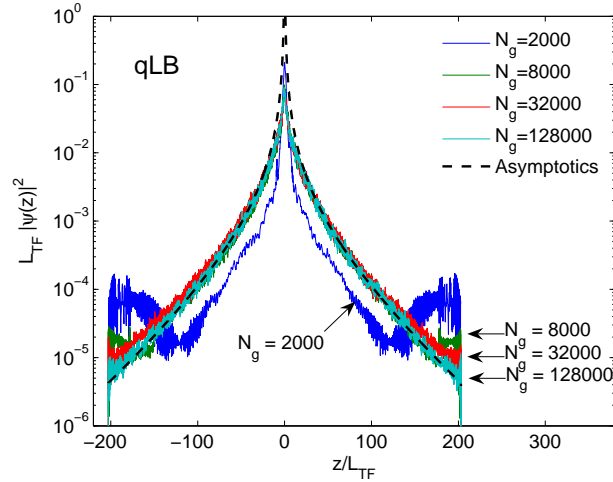


Figure 4.4: Averaged wave function density computed by qLB at four different resolutions. The numerical results are compared with the long-tail asymptotic behavior given by Eq. (4.28). Parameters are set as follows:  $\omega_z = 5 \times 10^{-3}$ ,  $\beta_{qLB} = 2$ ,  $\tilde{m} = 1/4$ ,  $V_R = 0.2\mu$ ,  $\sigma_R = 0.5\xi_h$ ,  $\lambda = 10.997$ ,  $T = 150/\omega_z$ .

In Fig. 4.6, the averaged wave-function densities, computed at the four different resolutions by qLB and CN respectively, are compared. We observe that for  $N_g \geq 32000$  the two methods are in good agreement with each other, as well as with the predicted asymptotic behavior.

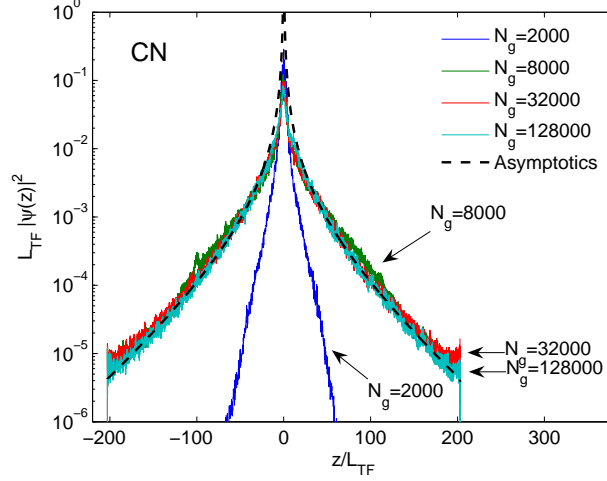


Figure 4.5: Averaged wave function density computed by CN using the qLB scaling at four different resolutions. The numerical results are compared with the long-tail asymptotic behavior described by Eq. (4.28). Parameters are set as follows:  $\omega_z = 5 \times 10^{-3}$ ,  $\beta_{qLB} = 2$ ,  $\tilde{m} = 1/4$ ,  $V_R = 0.2\mu$ ,  $\sigma_R = 0.5\xi_h$ ,  $\lambda = 10.997$ ,  $T = 150/\omega_z$

## 4.6 Long-time depletion

In Ref. [124], it is argued that the expanding and then localized BEC might be a long-lived metastable state rather than a true ground-state solution. If so, the residual self-interaction should cause a long-term depletion of the BEC. The question arises as to whether such long-term depletion really occurs, and, if so, on which time-scale. In order to explore this question, we have performed very-long time simulations up to time  $t = 15000/\omega_z$ , one hundred times longer than in the previous literature. As previously mentioned, the qLB scheme is norm-preserving due to the unitarity of the collision matrix, a property which has been verified also for such long simulations. The global norm  $\|\phi^+\|^2 + \|\phi^-\|^2$  is observed to remain at a unit value up to the sixth digit at the end of our longest simulation ( $3 \times 10^6$  time steps); in particular the mean value is  $\langle \|\phi^+\|^2 + \|\phi^-\|^2 \rangle = 1.00000019$  with a standard deviation of  $1.47 \times 10^{-7}$  to be compared with the value  $3.72 \times 10^{-8}$  after  $3 \times 10^5$  time steps. These values indicate that the qLB solver does not seem to suffer of any significant degradation in the course of the very-long time simulations.

The averaged wave function densities at times  $t = 1500/\omega_z$  and  $t = 15000/\omega_z$

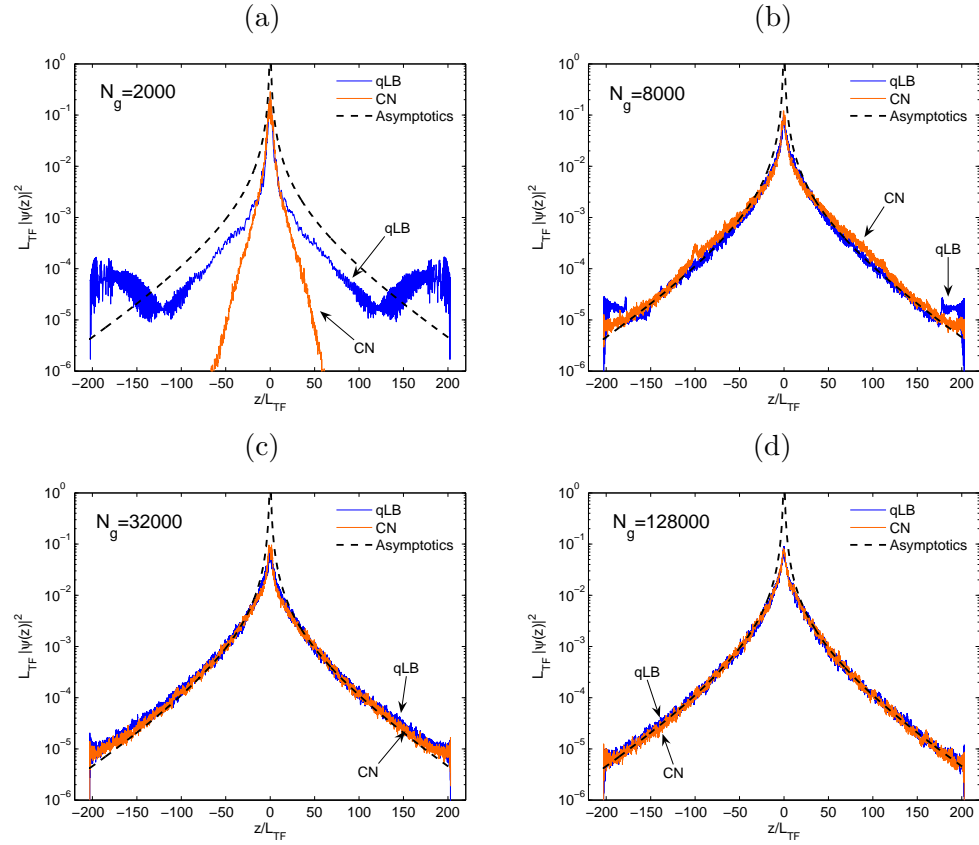


Figure 4.6: Comparison between the averaged wave function densities computed by qLB and CN at four different resolutions. The numerical results are compared with the long-tail asymptotic behavior described by Eq. (4.28). Parameters are set as follows:  $\omega_z = 5 \times 10^{-3}$ ,  $\beta_{qLB} = 2$ ,  $\tilde{m} = 1/4$ ,  $V_R = 0.2\mu$ ,  $\sigma_R = 0.5\xi_h$ ,  $\lambda = 10.997$ ,  $T = 150/\omega_z$ . (a)  $N_g = 2000$ , (b)  $N_g = 8000$ , (c)  $N_g = 32000$ , (d)  $N_g = 128000$ .

are compared with the one obtained at time  $t = 150/\omega_z$ , as shown in Fig. 4.7. The BEC is still well localized, but clearly on the way of losing its localization. In particular, by fitting the numerical wave function densities with the analytical curve  $n(z) \propto |z|^{-3/2} \exp(-2\gamma|z|)$ , the following time-decay law for  $\gamma$  is found (see Fig. 4.8):

$$L_{TF}\gamma(t) = \frac{0.055}{(\omega_z t)^{1/3}}. \quad (4.30)$$

In Fig. 4.7, the analytical curves obtained with the values of  $\gamma$  given by Eq. (4.30) for  $t\omega_z = 150, 1500$  and  $15000$  are also shown. In Fig. 4.8, numerical results for  $L_{TF}\gamma$  as a function of  $\omega_z t$  are reported and compared with the scaling law, Eq. (4.30). For this numerical test, we used the qLB scheme with  $N = 32000$  nodal points, while other parameters are set as before.

Although a direct comparison with experimental results reported in Ref. [21] is not possible, since we are simulating a BEC with a weaker nonlinearity ( $\lambda \sim 11$  instead of  $\lambda \sim 114$ ) and with a different value for the ratio  $\sigma_R/\xi_h$ , in Fig. 4.8 we report the experimental value obtained in Ref. [21] for  $\lambda = 114$ ,  $\sigma_R/\xi_h \sim 0.7$  and  $V_R/\mu = 0.2$ . This last parameter is the same as in our simulations. The experimental result corresponds to a localization length of about  $L_{loc} = 0.5$  mm, while in our simulation, we obtain  $L_{loc} = 1.19$  mm.

The pictures show a clear delocalization trend in the very-long term evolution of

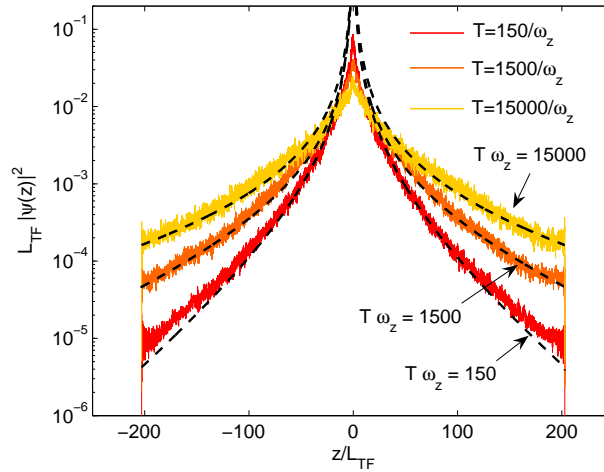


Figure 4.7: Averaged wave function densities computed by qLB with  $N = 32000$  discretization points up to times  $T = 150/\omega_z$ ,  $T = 1500/\omega_z$  and  $T = 15000/\omega_z$ . Parameters are set as follows:  $\omega_z = 5 \times 10^{-3}$ ,  $\beta_{qLB} = 2$ ,  $\tilde{m} = 1/4$ ,  $V_R = 0.2\mu$ ,  $\sigma_R = 0.5\xi_h$ ,  $\lambda = 10.997$ .



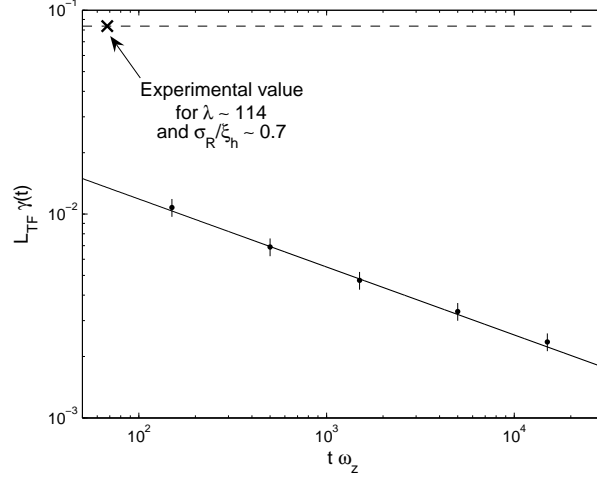


Figure 4.8: Numerical values of  $L_{TF}\gamma$  at different times compared with the decaying law of Eq. (4.30). Parameters are set as follows:  $\omega_z = 5 \times 10^{-3}$ ,  $\beta_{qLB} = 2$ ,  $\tilde{m} = 1/4$ ,  $V_R = 0.2\mu$ ,  $\sigma_R = 0.5\xi_h$ ,  $\lambda = 10.997$ . Error bars indicate the min-max values over the ensemble of realizations. The 'X' point indicates the experimental result obtained in Ref. [21] for  $V_R/\mu = 0.2$ , as in our simulation, but for a different setting of  $\lambda$  and  $\sigma_R/\xi_h$ , which take the values 114 and 0.7, respectively.

the condensate, thereby supporting the conjecture that Anderson localization is a long-lived *metastable* state of the expanding condensate.



## Chapter 5

# Ground state computation of the GPE-Newton equations

Inspired by a work of Moroz, Penrose and Tod [102], we considered a particular nonlinear quantum wave equation, namely the so-called Schrödinger-Newton equation (SNE) proposed by Penrose [115] within a theory which explains the quantum state reduction as a gravitational effect.

Due to the similar mathematical structure of the GPE with attractive interactions and the SNE, we applied the approach presented in Ref. [102] to the GPE equation in order to compare the eigenstates of these two systems. Moreover, we combined the GPE with a “gravitational”-like interaction in order to study the effects of such a potential in the ground state solutions.

In the following we first introduce the SNE, then we present the GPE with attractive interactions and finally we combine the two equations and we inspect the perturbation in the GPE solution due to the “gravitational” potential.

In this chapter, we present a work which deviates from the main stream of this thesis because we decided to not use the quantum lattice Boltzmann scheme. This choice was induced by several considerations which are briefly summarized in the following.

As we shall explain in more detail below, the SNE is a Schrödinger equation coupled with a Newtonian gravitational potential

$$\begin{aligned} i\hbar\partial_t\psi &= -\frac{\hbar^2}{2m}\Delta\psi + U\psi, \\ \Delta U &= 4\pi Gm^2|\psi|^2, \end{aligned} \tag{5.1}$$

where  $G$  is the gravitational constant and  $m$  is the mass of the particle. Moreover, the normalization condition  $\int |\psi|^2 = 1$  is imposed. Initially, we intended to apply

the imaginary-time qLB scheme to Eq. (5.1), however, the qLB scheme implies a particular scaling to the target equation. To be more precise, let us consider the qLB scaling (see Sec. 3.11):

$$\begin{aligned}\tilde{t} &= t/\Delta t, \quad \tilde{\mathbf{r}} = \mathbf{r}/\Delta r \quad \text{where} \quad (\Delta x = \Delta y = \Delta z \equiv \Delta r), \\ \tilde{\psi}(\tilde{\mathbf{r}}, \tilde{t}) &= (\Delta r)^{3/2} \psi(\mathbf{r}, t),\end{aligned}$$

where  $\Delta t$  and  $\Delta r$  are the discretization steps expressed in physical units. We recall that, from the definition of the model parameter

$$\tilde{m} = \omega_c \Delta t = \frac{mc^2}{\hbar} \Delta t,$$

we obtain

$$c^2 = \frac{\tilde{m}\hbar}{m\Delta t}$$

and, consequently

$$\Delta r = c\Delta t = \left( \frac{\tilde{m}\hbar}{m\Delta t} \right)^{1/2} \Delta t.$$

Applying this scaling to the time-dependent version of Eq. (5.1), we obtain

$$\begin{aligned}i\partial_{\tilde{t}}\tilde{\psi} &= -\frac{1}{2\tilde{m}}\tilde{\Delta}\tilde{\psi} + \tilde{U}\tilde{\psi}, \\ \tilde{\Delta}\tilde{U} &= \frac{4\pi Gm^3\Delta r}{\tilde{m}^2\hbar^2}|\tilde{\psi}|^2,\end{aligned}$$

where  $\tilde{U} = U/(\omega_c\hbar)$ . For a typical set of parameters we have  $m \sim 10^{-27}$  and  $\tilde{m} \sim 0.1$ , thus delivering  $4\pi Gm^3/(\tilde{m}^2\hbar^2) \sim 10^{-21}$ , forcing  $\Delta r$  to be of order  $10^{20}$  in order to have reasonable numerical coefficients.

From Ref. [102], we can observe that, for a single particle, this is indeed the case, since the length scale of the wave function is of order  $10^{22}$ . However, our intention is to compare this kind of attractive gravitational interaction with the nonlinear interactions of an attractive BEC and, possibly, to couple these systems.

As we shall point out in the following, it turns out that SNE and attractive GPE are characterized by parameters separated by several orders of magnitude.

In addition, for this kind of problems, the dimensionality is very important, indeed these systems can show a significantly different behavior in one, two or three spatial dimensions. In Ref. [115], the authors consider a three-dimensional system with the assumption of spherical symmetry. This assumption allows to transform the system of three-dimensional partial differential equations of Eq. (5.1) into a system of two ordinary differential equations, thus highly simplifying the computations. Unfortunately, the qLB is designed for Cartesian geometries and it is not yet suitable for spherical coordinates.

For all of these reasons, in this case, it seemed more convenient to extend the scheme proposed in Ref. [102] for the SNE to the GPE with attractive interactions, rather than using the qLB scheme.

## 5.1 Quantum state reduction as a gravitational effect

The collapse of the wave function is a highly debated issue in quantum mechanics, the main question being how to explain the collapse of the wave function when a measurement is performed. A measurement consists of the isolated quantum system becoming entangled with the physical apparatus with this entanglement leading to the reduction of the state vector.

An interesting approach to this problem is to argue that present-day quantum mechanics is a limiting case of a more general, unified theory, such that both the reduction operator and the evolution operator (described by the linear Schrödinger equation) should be viewed as approximations to a more general theory of physical reality [115]. Inspired by this idea, many schemes of reality have been proposed [20, 59, 145, 111] and, over the years, several arguments have been presented to support the idea that the deviation from standard quantum evolution, which leads to the collapse of the wave function, is due to some gravitational effect [77, 78, 79, 42, 43, 58, 113, 114, 115, 116].

In 1996, Penrose proposed a model of this type [115] according to which a macroscopic quantum superposition of two different mass distributions is *unstable* and would decay to one of the two states after a characteristic time  $T$ . Starting from this idea, Moroz, Penrose and Tod in [102] have shown that this decorrelation time would be of order  $10^{53}$  seconds. for a single particle, but it would become of order 1 second for  $10^{11}$  nucleons. This is in agreement with observations, since it means that a single particle will not self-reduce on a time scale of relevance to any actual experiment, while, for a larger system, the reduction effect can become measurable.

The closest easily available approximation to such a system is given by Bose-Einstein condensate with attractive interactions [38] (an hypothetical experimental test with up to  $10^{14}$  atoms has been discussed in [96]).

In this chapter, we apply the same analysis performed in [102] for the Schrödinger-Newton equations (SNE) to the attractive BEC. Indeed, the Gross-Pitaevskii equation (GPE) describing a BEC is mathematically similar to the SNE, yet with an important difference on the scaling of the potential energy, as we shall see in the following. As it is known, a BEC with attractive interactions is more unstable than a repulsive condensate, and indeed it can exhibit a stable stationary state only up to a limited number of particles. Theoretical studies on the stationary and dynamical behavior of an attractive BEC have been performed by several authors

[131, 74, 118, 120, 17, 80, 25] and the problem of the collapse of the wave function for attractive interactions in the absence of the confining potential has also been investigated by using a variational approach [147, 121, 142, 85, 80]. However, to the best of our knowledge, none of these papers include the study of the coupling between the GPE and a Newton equation.

Here, the ground state solution for a three-dimensional spherically symmetric, attractive condensate is numerically computed by using a Runge-Kutta based method similar to the one proposed in [53]. The time-independent GPE has been numerically solved by using several approaches: Runge-Kutta methods [53, 1], explicit imaginary-time algorithms [33, 35, 10, 13, 133, 105, 108] and direct minimization of the energy functional [12].

Moreover, we have also explored the coupling between GPE and SNE comparing this system of equations with the SNE proposed by Penrose. Indeed, these two systems of equations show a similar structure even though there is a fundamental difference which we clarify in the following.

Finally, we have found that the effects of ordinary gravity are totally negligible since the BEC's attractive potential is much stronger than the gravitational attraction. Indeed, in order to observe an effect due to the "gravitational" interaction, this must be amplified of several orders of magnitude.

## 5.2 The Schrödinger-Newton model

As previously mentioned, in 1996, Penrose [115] proposed an interpretation of the wave function collapse due to measurement. In particular, he argued that a superposition of two quantum states, each of which would be stationary on its own, but characterized by two different mass distributions, is unstable due to the gravitational interaction. Consequently, this superposed state would decay, after a characteristic lifetime  $T$ , into one of the two states. According to this proposal, the decorrelation time can be calculated as the reciprocal of the gravitational self-energy  $E$  of the difference between the mass distributions of the two states, namely  $T = \hbar/E$ . However, the major difficulty with such a proposal is to determine the basic, stationary states into which a superposition of such states is supposed to decay. The approach proposed by Penrose in [115] is to regard these basic stationary states as the solutions of the Schrödinger equation with the addition of a term including the effect of a gravitational potential. The proper form of this gravitational potential term would depend on the gravitational theory considered, and in [102, 115] it is assumed that it is sufficient to consider Newtonian gravity.

This assumption gives rise to the so-called Schrödinger-Newton equations (SNE):

$$\begin{aligned} -\frac{\hbar^2}{2m}\Delta\psi + U\psi &= \mu\psi, \\ \Delta U &= 4\pi Gm^2|\psi|^2 \end{aligned} \quad (5.2)$$

where  $G$  is the gravitational constant,  $\mu$  is the energy eigenvalue, and the normalization condition  $\int |\psi|^2 = 1$  is also imposed. By multiplying the first of Eq. (5.2) by  $\psi^*$  and integrating, we obtain  $\mu$  as a function of the eigenstate  $\psi$

$$\mu[\psi] = \int_{\mathbb{R}^3} \left( \frac{\hbar^2}{2m} |\nabla\psi(\mathbf{r})|^2 + U(\mathbf{r})|\psi(\mathbf{r})|^2 \right) d\mathbf{r},$$

where  $U$  is given by the Poisson equation in Eq. (5.2).

The energy functional is defined as

$$E[\psi] = \int_{\mathbb{R}^3} \left( \frac{\hbar^2}{2m} |\nabla\psi(\mathbf{r})|^2 + \frac{U(\mathbf{r})}{2} |\psi(\mathbf{r})|^2 \right) d\mathbf{r}. \quad (5.3)$$

In [102], a family of solutions is found, the so-called “bound-state” solutions, labelled by the non negative integers. The wave function of the  $n$ -th solution has  $n$  zeros and the wave functions are normalizable. The corresponding energy eigenvalues are negative, converging monotonically to zero as  $n$  is increased [102]. In particular, the energy eigenvalues associated to each eigenstate reads as follows

$$\mu = 2 \left( \frac{m}{m_p} \right)^5 E_p \phi_n, \quad (5.4)$$

where  $m_p = (\hbar c/G)^{1/2}$  is the Planck mass,  $E_p = m_p c^2$  is the Planck energy and  $\phi_n$  is a dimensionless factor describing the sequence of excited eigenstates (i. e. it takes different values for the ground state ( $n = 0$ ), the first excited state ( $n = 1$ ), and so on).

Summarizing, in [102] it is argued that the eigenstate of Eq. (5.2) are the basic states to which any other quantum state reduces in a time which is proportional to  $\hbar/\mu$ . By directly computing  $\mu$ , for example for the ground state, it turns out that the reduction time is of the order of  $10^{53}$  seconds for the the mass of a single nucleon and of order 1 second for  $10^{11}$  nucleon masses.

In [102], the computation of the eigenstates of Eq. (5.2) is performed by properly transforming the variables  $\psi$  and  $U$  and restricting to spherically-symmetric solutions, so that Eq. (5.2) is transformed into a system of two ODEs which can be analytically studied [140] and then numerically integrated.

Now, let us rewrite Eq. (5.2) in dimensionless form by rescaling the variables as follows:  $\tilde{r} = r/l_c$ ,  $\tilde{\psi}(\tilde{r}) = (l_c)^{3/2}\psi(r)$  and  $\tilde{\mu} = \mu/E_c$  where  $l_c = \hbar/(mc)$  is the

Compton length and  $E_c = mc^2/2$  is the Compton energy. Using this scaling, Eq. (5.2) is transformed into

$$-\tilde{\Delta}\tilde{\psi} + \gamma_{SN} \left( \tilde{\Delta}^{-1} |\tilde{\psi}|^2 \right) \tilde{\psi} = \tilde{\mu}\tilde{\psi}, \quad (5.5)$$

where  $\gamma_{SN} = 8\pi(l_p/l_c)^2$ , with  $l_p = (\hbar G/c^3)^{1/2}$  being the Planck length.

A simple dimensional analysis of Eq. (5.5) shows that the energy functional always has a minimum. Indeed, assuming that  $\sigma$  is the characteristic width of the wave function, then the kinetic energy is  $O(\sigma^{-2})$ , while the interaction term is  $O(\sigma^{-1})$ , thus always allowing stable solutions. A direct insight into the behavior of the energy functional can be obtained by means of a variational approach based on Gaussian functions [17]. On the assumption of spherical symmetry, one can substitute the following ansatz

$$\tilde{\psi}(\tilde{r}) = \left( \frac{1}{\sigma^3 \pi^{3/2}} \right)^{1/2} \exp \left( -\frac{\tilde{r}^2}{2\sigma^2} \right), \quad (5.6)$$

into the energy functional of Eq. (5.3). This yields

$$\tilde{E}[\sigma] = \frac{3}{2}\sigma^{-2} - \frac{\gamma_{SN}}{2}(2\pi)^{-3/2}\sigma^{-1},$$

which always has a minimum at  $\sigma_{min} = 6(2\pi)^{3/2}/\gamma_{SN}$ .

The solution of Eq. (5.5) corresponding to this minimum is the ground state solution. From Eq. (5.4), since  $\phi_0 = 0.081385$ , the decorrelation time corresponding to the the ground state energy goes from  $10^{53}$  seconds for  $N = 1$  to the order of one second for  $N = 10^{11}$  nucleon masses.

### 5.3 The attractive Bose-Einstein condensate

In order to experimentally reproduce the situation described in the previous section, one should keep together  $10^{11}$  nucleons in a quantum macroscopic state. Since this is not feasible yet, we consider an “approximation” to this system as provided by attractive BEC.

As it is well known, at zero temperature the dynamics of a trapped BEC is described by the time-dependent Gross-Pitaevskii equation (GPE). Since we are interested to stationary solutions of the GPE, we consider its time-independent version, namely:

$$\left( -\frac{\hbar^2}{2m}\Delta + V(\mathbf{r}) + NU_0|\psi|^2 \right) \psi = \mu\psi, \quad (5.7)$$

where  $\mathbf{r} = (x, y, z)^T$ ,  $m$  is the atomic mass,  $U_0 = 4\pi\hbar^2 a/m$  is the coupling strength,  $a$  is the  $s$ -wave scattering length,  $N$  is the number of particles in the condensate



and  $\mu$  is the chemical potential. The external trap  $V(\mathbf{r})$  is usually taken in the form of an harmonic potential and here we consider an isotropic harmonic trap  $V(\mathbf{r}) = m\omega^2 \mathbf{r}^2/2$ . Furthermore, the wave function  $\psi$  satisfies the normalization condition

$$\int |\psi(\mathbf{r})|^2 d\mathbf{r} = 1. \quad (5.8)$$

Multiplying Eq. (5.7) by  $\psi^*$  and integrating we obtain  $\mu$  as a function of the eigenstate  $\psi$

$$\mu[\psi] = \int_{\mathbb{R}^3} \left( \frac{\hbar^2}{2m} |\nabla \psi(\mathbf{r})|^2 + V(\mathbf{r}) |\psi(\mathbf{r})|^2 + NU_0 |\psi(\mathbf{r})|^4 \right) d\mathbf{r},$$

while the energy functional associated to Eq. (5.7) is given by

$$E[\psi] = \int_{\mathbb{R}^3} \left( \frac{\hbar^2}{2m} |\nabla \psi(\mathbf{r})|^2 + V(\mathbf{r}) |\psi(\mathbf{r})|^2 + \frac{NU_0}{2} |\psi(\mathbf{r})|^4 \right) d\mathbf{r}. \quad (5.9)$$

Depending on the type of atoms in the condensate, the  $s$ -wave scattering length can be positive or negative, denoting repulsive or attractive interactions between the particles of the condensate, respectively. Here, we restrict to the attractive interaction case, since this is the situation in which GPE presents direct similarities with the SNE.

As previously mentioned, the case of attractive interaction is more critical than the repulsive one. This is due to the fact that, for attractive forces, the condensate tends to increase its density in the center of the trap in order to lower the interaction energy. This tendency is contrasted by the kinetic energy which eventually manages to stabilize the system. However, as the central density keeps growing, the kinetic energy is no longer able to prevent the collapse of the condensate [38]. In practice, it is possible to obtain a stable state only up to a limited number of particles [131, 74, 118, 25].

Let us write Eq. (5.7) in dimensionless form by expressing the variables in Compton units, this reads

$$-\tilde{\Delta} \tilde{\psi} + \left( \frac{\omega l_c}{c} \right)^2 \tilde{\mathbf{r}}^2 \tilde{\psi} - \gamma_{BEC} |\tilde{\psi}|^2 \tilde{\psi} = \tilde{\mu} \tilde{\psi}, \quad (5.10)$$

where  $\gamma_{BEC} = 8\pi|a|N/l_c$ . The GPE of Eq. (5.10) is mathematically similar to the SNE of Eq. (5.5), yet with the important distinction on the scaling of the potential energy due to the Laplace operator. Indeed, by using the same variational approach [17] described above for the SNE, we substitute the Gaussian ansatz of Eq. (5.6) into the energy functional of Eq. (5.9) associated to Eq. (5.10) to obtain:

$$\tilde{E}[\sigma] = \frac{3}{2} \sigma^{-2} + \frac{3}{2} \left( \frac{\omega l_c}{c} \right)^2 \sigma^2 - \frac{\gamma_{BEC}}{2} (2\pi)^{-3/2} \sigma^{-3}. \quad (5.11)$$

This functional has a minimum only for sufficiently small values of the coupling constant  $\gamma_{BEC}$  (i. e. a small number of atoms in the condensate). Note that, in the absence of the harmonic potential, the energy functional never has a minimum, which is why we need to add the external trap in order for a ground state to exist. The critical number of atoms has been exactly computed for a spherically symmetric trap [120] and it turns out to satisfy the following relation

$$N < N_{cr} = 0.575 \frac{a_0}{|a|}, \quad (5.12)$$

where  $a_0 = \sqrt{\hbar/(m\omega)}$  is the harmonic unit length. For a typical experimental setting [28, 27, 122] where the BEC is composed of  $^7\text{Li}$  atoms, the trap frequency is  $\omega = 147 \text{ Hz}$ ,  $a = -1.44 \times 10^{-9} \text{ m}$ , expression of Eq. (5.12) yields  $N_{cr} \sim 3137$ . Attractive BECs composed of  $N \sim 1500$  atoms are typically accessible to current experiments [27], so that the above inequality is indeed fulfilled.

We now turn to the numerical solution of Eq. (5.7) by means of a Runge-Kutta scheme similar to the one proposed in [102] for the SNE. In order to have reasonable numerical coefficients, it is necessary to write Eq. (5.7) in dimensionless form using the harmonic scaling:  $\hat{\mathbf{r}} = \mathbf{r}/a_0$ ,  $\hat{\psi}(\hat{\mathbf{r}}) = (a_0)^{3/2}\psi(\mathbf{r})$ ,  $\hat{\mu} = \mu/(\hbar\omega)$ . We apply this scaling and then remove all the  $\hat{\cdot}$  apart from the one on the nonlinearity coefficient, not to confuse it with  $\gamma_{BEC}$  expressed in Compton units. This yields

$$\left( -\frac{1}{2}\Delta + \frac{1}{2}r^2 - \hat{\gamma}_{BEC}|\psi|^2 \right) \psi = \mu\psi, \quad (5.13)$$

where  $\hat{\gamma}_{BEC} = 4\pi|a|N/a_0$ .

Since we are assuming that the solution is spherically symmetric, the wave function depends only on  $r = |\mathbf{r}|$  and the normalization condition of Eq. (5.8) becomes

$$4\pi \int_0^{+\infty} r^2 |\psi(r)|^2 dr = 1. \quad (5.14)$$

Moreover, Eq. (5.13) reduces to an ordinary differential equation which can be solved by using a Runge-Kutta method. In particular, we set  $\psi(0) = 1$  and  $\psi'(0) = 0$  (this latter position is necessary in order to have smooth solutions in  $r = 0$ ) and we solve the following ODE

$$\mu\psi = -\frac{1}{2r} \frac{d^2}{dr^2}(r\psi(r)) + \frac{1}{2}r^2\psi - A|\psi|^2\psi, \quad (5.15)$$

for a given value,  $A$ , of the nonlinearity coefficient. Let  $\psi_A(r)$  be a solution of Eq. (5.15) satisfying the proper boundary condition ( $\psi_A(r) \rightarrow 0$  for  $r \rightarrow +\infty$  so that  $\int r^2 |\psi_A|^2 < \infty$ ) and having no zero, this solution corresponds to the ground

state. However, in general,  $\psi_A(r)$  does not satisfy the normalization condition of Eq. (5.14), i. e.

$$4\pi \int_0^{+\infty} r^2 |\psi_A(r)|^2 dr = I_A \neq 1.$$

From  $\psi_A(r)$ , we derive the wave function  $\psi(r)$  satisfying the correct normalization condition which solves Eq. (5.15) for a value of the nonlinearity coefficient different from  $A$ . In particular, by defining

$$\psi(r) = \frac{\psi_A(r)}{\sqrt{I_A}},$$

then  $\psi(r)$  is the ground state solution of Eq. (5.13) with  $\hat{\gamma}_{BEC} = AI_A$  and satisfying the normalization condition of Eq. (5.14). From the relation  $\hat{\gamma}_{BEC} = AI_A$ , we easily compute the number of atoms composing the BEC:

$$N = \frac{AI_A a_0}{4\pi|a|}.$$

Recalling that, in three dimensions, the attractive BEC is unstable if the number of atoms is larger than a critical value, from Eq. (5.12), we can compute the threshold value for the nonlinearity coefficient

$$\hat{\gamma}_{cr} = \frac{4\pi|a|N_{cr}}{a_0} = 7.2256.$$

As it is known, the attractive self-interaction of the condensate destabilizes the harmonic oscillator ground state and gives rise to new ones with lower energy eigenvalues. As a result, the decorrelation time induced by the attractive interactions can be estimated as the time required for the wave packet to switch from the harmonic oscillator ground state (corresponding to  $\hat{\gamma}_{BEC} = 0$ ) to the GPE ones ( $\hat{\gamma}_{BEC} \neq 0$ ), namely,  $T \sim \hbar/(\mu(0) - \mu(\gamma_{BEC}))$ . In Tab. 5.1 we report the numerical results for an increasing value of the nonlinearity coefficient  $\hat{\gamma}_{BEC}$  up to the critical value. In the table we report the ground state chemical potential, the maximum value of  $\psi$ ,  $\psi(0)$ , and the decorrelation time associated to these ground state solutions. Note that these decorrelation times are of order  $10^{-3}$  and  $10^{-2}$ , hence they should be observable on a macroscopic scale.

Finally, in Fig. 5.1, we show the ground state wave function for different values of  $\hat{\gamma}_{BEC}$ , and note that for increasing values of  $\hat{\gamma}_{BEC}$  the eigenfunction is more and more localized and its energy eigenvalue decreases. In Fig. 5.2, the total potential,  $V_{tot} = (1/2)r^2 - \hat{\gamma}_{BEC}|\psi|^2$ , corresponding to the ground state wave functions of Fig. 5.1 is also shown.

Table 5.1: GPE only. Ground state chemical potential  $\tilde{\mu}$  and maximum value of  $\psi$ ,  $\psi(0)$  computed for different values of the nonlinearity coefficient  $\hat{\gamma}_{BEC}$ . In the table, the chemical potential gap  $\mu(0) - \mu(\gamma_{BEC})$  is given in harmonic units and indicated as  $\Delta\hat{\mu}$ . Finally, the nonlinearity coefficient  $A$ , imposed while solving Eq. (5.15) to compute  $\psi_A$  is also reported.

$\hat{\gamma}_{BEC}$	$\hat{\mu}$	$\psi(0)$	$\Delta\hat{\mu}$	$A$
0	1.5	0.423778	0	0
2.2952	1.336852	0.466740	0.163148	0.5
3.8508	1.196837	0.509596	0.303163	1
5.6661	0.966978	0.594116	0.533022	2
6.5546	0.782733	0.676529	0.717267	3
6.9846	0.628297	0.756759	0.871703	4
7.1721	0.494329	0.834951	1.005671	5
7.2255	0.375029	0.911251	1.124971	6

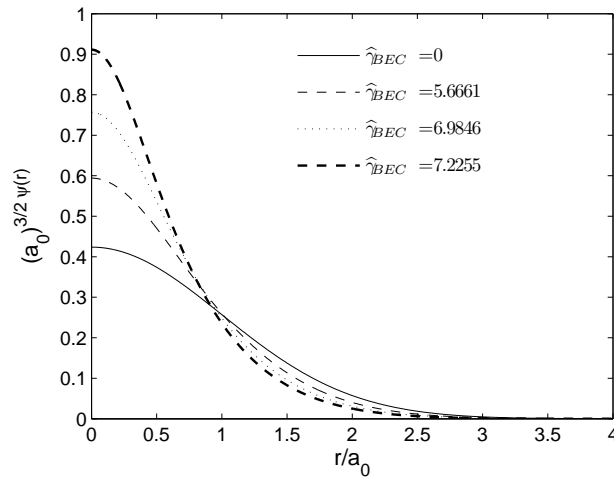


Figure 5.1: Ground state wave function for different values of the coupling constant  $\hat{\gamma}_{BEC}$ .

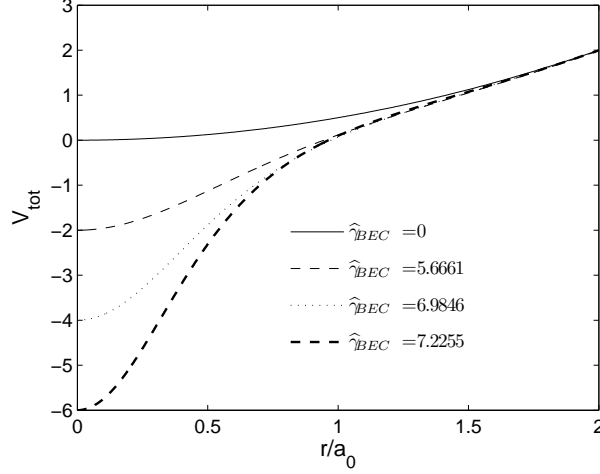


Figure 5.2: Total potential,  $V_{tot} = (1/2)r^2 - \hat{\gamma}_{BEC}|\psi|^2$ , corresponding to the ground state wave functions of Fig. 5.1.

## 5.4 Adding a “gravitational” term to the attractive BEC

In this section we combine the two models presented in the above sections: the Schrödinger-Newton equations and the GPE for an attractive BEC. We assume the GPE system as a reference case (macroscopic quantum system) and study the perturbation of its energy levels due to “gravitational” interactions.

As we shall illustrate in the following, by taking the physical values for the parameters, the coupling constant of the gravitational term turns out to be much smaller than the attractive interaction between the atoms due to the BEC self-interaction term. Therefore, we expect gravity to be totally negligible, and in this section we provide numerical evidence that this is indeed the case.

However, we study the perturbation in the solution due to a “gravitational”-like potential in order to inspect the mathematical effect of such an interaction.

Let us consider the following GPE with the addition of a gravitational potential term as in Eq. (5.2)

$$\left( -\frac{\hbar^2}{2m}\Delta + \frac{1}{2}m\omega^2\mathbf{r}^2 + NU_0|\psi|^2 + NU \right) \psi = \mu\psi, \quad (5.16)$$

$$\Delta U = 4\pi Gm^2|\psi|^2.$$

In order to compare the magnitude of the attractive and gravitational terms, we rescale Eq. (5.16) by writing it in Compton units. In particular, the scaling reads

as follows:  $\tilde{\mathbf{r}} = \mathbf{r}/l_c$ ,  $\tilde{\psi}(\tilde{\mathbf{r}}) = (l_c)^{3/2}\psi(\mathbf{r})$  and  $\tilde{\mu} = \mu/E_c$ , where  $l_c = \hbar/mc$  is the Compton length and  $E_c = mc^2/2$  is the Compton energy.

With this scaling Eq. (5.16) becomes

$$\begin{aligned} \left( -\frac{\hbar^2}{2m}\tilde{\Delta} + \left( \frac{\omega l_c}{c} \right)^2 \tilde{\mathbf{r}}^2 - \gamma_{BEC}|\tilde{\psi}|^2 + \gamma_{SN}\tilde{U} \right) \tilde{\psi} &= \tilde{\mu}\tilde{\psi}, \\ \Delta\tilde{U} &= |\tilde{\psi}|^2, \end{aligned} \quad (5.17)$$

where we recall that  $\gamma_{BEC} = 8\pi|a|N/l_c$ , while  $\gamma_{SN} = 8\pi N(l_p/l_c)^2$  with  $l_p$  being the Planck length.

In order to compare the energy associated to each of the two potential terms, let us define the following dimensionless quantities:

- $E_{SN}/E_c$ , is the gravitational potential energy in Compton units;
- $E_{BEC}/E_c$ , is the attractive interaction energy.

From Eq. (5.17), we have that

$$\begin{aligned} E_{SN}/E_c &\approx 8\pi N \left( \frac{l_p}{l_c} \right)^2 \tilde{\Delta}^{-1}(|\tilde{\psi}|^2) \approx \frac{8\pi N l_p^2}{l_c} \frac{1}{l}, \\ E_{BEC}/E_c &\approx \frac{8\pi|a|N}{l_c} |\tilde{\psi}|^2 \approx \frac{8\pi|a|N l_c^2}{l^3}, \end{aligned}$$

where  $|\tilde{\psi}|^2 \sim (l_c/l)^3$ ,  $\tilde{\Delta} \sim (l_c/l)^2$  and  $l$  is the physical length which characterize the system, i. e. the typical length scale of an attractive BEC.

For a fixed value of the physical length parameter  $l$ , the ratio between the attractive interaction energy and the gravitational potential energy is given by

$$\gamma(l) = \frac{E_{BEC}(l)}{E_{SN}(l)} \approx \frac{|a|l_c^3}{l_p^2} \frac{1}{l^2}.$$

For a typical attractive BEC the parameters are as follows:  $|a| \sim 10^{-9}$  m,  $l_c \sim 10^{-17}$  m and  $l \sim 10^{-5}$  m, while  $l_p \sim 10^{-35}$  m, thus  $\gamma(l) \sim 10^{20}$ .

From this observation, we conclude that in the presence of an attractive potential, the gravitational effect is totally negligible.

Therefore, in order to appreciate the qualitative effect of such a term, let us artificially magnify the gravitational term and consider the following equation

$$\begin{aligned} \left( -\frac{\hbar^2}{2m}\Delta + \frac{1}{2}m\omega^2\mathbf{r}^2 + NU_0|\psi|^2 + NU \right) \psi &= \mu\psi, \\ \Delta U &= \eta_{SN}|\psi|^2, \end{aligned} \quad (5.18)$$

where  $\eta_{SN}$  is an amplified “gravitational” parameter which is varied in order to study the effect of this additional term into the attractive GPE.

As in the previous section, in order to have reasonable numerical coefficients, it is useful to write Eq. (5.18) in harmonic units:  $\hat{\mathbf{r}} = \mathbf{r}/a_0$ ,  $\hat{\psi}(\hat{\mathbf{r}}) = (a_0)^{3/2}\psi(\mathbf{r})$  and  $\hat{\mu} = \mu/(\hbar\omega)$ . With this scaling, Eq. (5.18) becomes

$$\begin{aligned} \left( -\frac{1}{2}\hat{\Delta} + \frac{1}{2}\hat{\mathbf{r}}^2 - \hat{\gamma}_{BEC}|\hat{\psi}|^2 + \hat{\eta}_{SN}\hat{U} \right) \hat{\psi} &= \hat{\mu}\hat{\psi}, \\ \Delta\hat{U} &= |\hat{\psi}|^2, \end{aligned} \quad (5.19)$$

where  $\hat{\gamma}_{BEC} = 4\pi|a|N/a_0$  and  $\hat{\eta}_{SN} = N\eta_{SN}/(a_0\hbar\omega)$ . Note that, the physical value of  $\hat{\eta}_{SN}$  for the true gravitational potential is of order  $10^{-22}$ .

We note that, the addition of the gravitational term is not sufficient to stabilize the system which remains stable only up to a limited number of atoms. By using the same variational approach described above, we substitute the Gaussian ansatz

$$\hat{\psi}(\hat{\mathbf{r}}) = \left( \frac{1}{\sigma^3\pi^{3/2}} \right)^{1/2} \exp\left( -\frac{\hat{\mathbf{r}}^2}{2\sigma^2} \right),$$

into the energy functional associated to Eq. (5.19) and we obtain

$$\hat{E}(\sigma) = \frac{3}{4}(\sigma^{-2} + \sigma^2) - (2\pi)^{-1/2} \frac{N|a|}{a_0} \sigma^{-3} - \frac{\hat{\eta}_{SN}}{2} (2\pi)^{-3/2} \sigma^{-1}. \quad (5.20)$$

This functional has a minimum only for  $N|a|/a_0$  smaller than a critical value and, for each value of  $N|a|/a_0$ , the minimum exists only up to a critical value of  $\hat{\eta}_{SN}$ . In particular, by requiring that both the first and second derivatives of  $\hat{E}(\sigma)$  vanish at the critical point  $\sigma = \sigma_{cr}$  and  $\hat{\eta}_{SN} = \hat{\eta}_{cr}$ , for each fixed value of  $N|a|/a_0$  one can compute the corresponding  $\hat{\eta}_{cr}$ . The resulting relation between  $N|a|/a_0$  and  $\hat{\eta}_{cr}$  is shown in Fig. 5.3. We observe that for  $N|a|/a_0 \rightarrow 0$ ,  $\hat{\eta}_{cr} \rightarrow \infty$  as expected, since when the attractive potential vanishes we obtain the SNE whose energy functional always has a minimum. On the other hand, for  $N|a|/a_0$  which tends toward its critical value (in the Gaussian approximation the critical value for  $N|a|/a_0$  is 0.671 [38]),  $\hat{\eta}_{cr} \rightarrow 0$ .

A qualitative understanding of the behavior of the energy functional is obtained by plotting the energy functional of Eq. (5.20) for a fixed value of  $N|a|/a_0$  and varying  $\hat{\eta}_{SN}$ . In Fig. 5.4, we show the energy functional of Eq. (5.20) computed for  $N|a|/a_0 = 0.3064$  and for some values of  $\hat{\eta}_{SN}$ .

From Fig. 5.4, we observe that, as expected, gravitational interactions destabilize the GPE ground state and give rise to new ones with lower energy (the top curve indicates the reference case without gravity,  $E_{min}(0) \equiv E_{GPE}$ ). The data in Fig. 5.4 indicate that the energy gap between the minimum of the GPE with the gravitational term and the reference minimum of the pure GPE curve are of the same order of magnitude as  $E_{GPE}$ . The actual numerical values for the case shown in Fig. 5.4 are reported in Tab. 5.2. In order to compare these results obtained

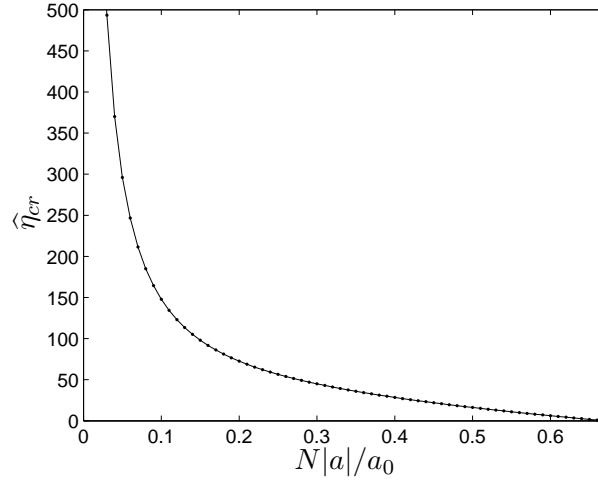


Figure 5.3: Critical value for  $\hat{\eta}_{SN}$  computed as a function of the attractive potential coupling constant  $N|a|/a_0$ . The solid line is just for eye-guiding purposes.

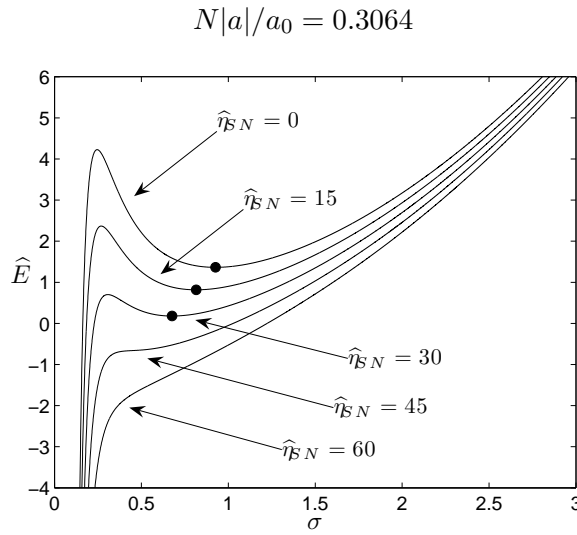


Figure 5.4: Energy functional of Eq. (5.20) given by the Gaussian ansatz and computed for a fixed value of the attractive interaction coefficient  $N|a|/a_0 = 0.3064$  and varying the “gravitational” coupling constant  $\hat{\eta}_{SN}$ . The full circles denote the point of minimum (where it exists).



Table 5.2: GPE coupled with SNE (Gaussian approximation). The computation is performed for a fixed value of  $N|a|/a_0 = 0.3064$  and varying  $\hat{\eta}_{SN}$ . For comparison with the results computed below by the numerical scheme we also report the approximated chemical potentials  $\mu(\eta_{SN})$ . The energy gap  $E_{min}(0) - E_{min}(\eta_{SN})$  expressed in harmonic units is indicated as  $\Delta\hat{E}$ , while the chemical potential difference  $\mu(0) - \mu(\eta_{SN})$  in harmonic units is denoted as  $\Delta\hat{\mu}$ .

$\hat{\eta}_{SN}$	$\hat{E}_{min}$	$\Delta\hat{E}$	$\hat{\mu}$	$\Delta\hat{\mu}$
$N a /a_0 = 0.3064$				
0	1.3638	0	1.21	0
5	1.1892	0.1746	0.8385	0.3715
15	0.8172	0.5466	0.0071	1.2029
20	0.6173	0.7465	-0.4693	1.6793
30	0.1793	1.1845	-1.6243	2.8343
40	-0.3374	1.7012	-3.4001	4.6101

from the Gaussian approximation with the ones given below by the numerical scheme, we also report in Tab. 5.2 the approximated chemical potentials  $\mu(\eta_{SN})$ .

To be noted that in the transition between the various gravitational ground-states, the wave packet undergoes a progressive shrinking, as also explicitly shown in Fig. 5.5 and Fig. 5.7. Beyond a critical threshold of the gravitational coupling, the kinetic energy is no longer capable of balancing the GPE attraction and the wave function collapse cannot be escaped (no energy minimum can exist any longer).

We now turn to the numerical solution of Eq. (5.19) by means of a Runge-Kutta scheme similar to the one already described for the attractive BEC. To this end, let us rewrite Eq. (5.19) by removing all the  $\hat{\cdot}$  apart from the ones on  $\hat{\gamma}_{BEC}$  and  $\hat{\eta}_{SN}$  and define

$$V = \hat{\mu} - \hat{U}.$$

Hence, Eq. (5.19) becomes

$$\left( -\frac{1}{2}\Delta + \frac{1}{2}\mathbf{r}^2 - \hat{\gamma}_{BEC}|\psi|^2 \right) \psi = V\psi, \quad (5.21)$$

$$\Delta V = -\hat{\eta}_{SN}|\psi|^2.$$

In analogy with the numerical treatment of [102], the energy eigenvalue of Eq. (5.21),  $\mu$ , is obtained for  $r \rightarrow +\infty$  as  $V(\infty)$ .

We assume once again that the solution is spherically symmetric, so that the wave

function depends only on  $r = |\mathbf{r}|$  and the normalization condition is given by Eq. (5.14). Moreover, Eq. (5.21) reduces to a system of two ordinary differential equations which can be solved by using a Runge-Kutta method.

In particular, we set  $\psi(0) = 1$ , while  $V(0)$  is varied until the solution meets the proper boundary condition for  $r \rightarrow +\infty$ . We then set  $\psi'(0) = 0$  and  $V'(0) = 0$  in order to have smooth solutions in  $r = 0$  and we solve the following set of ODEs

$$\begin{aligned} V\psi &= -\frac{1}{2r} \frac{d^2}{dr^2}(r\psi(r)) + \frac{1}{2}r^2\psi - A|\psi|^2\psi, \\ \frac{1}{r} \frac{d^2}{dr^2}(rV(r)) &= -B|\psi|^2, \end{aligned} \quad (5.22)$$

for two given values of the two parameters  $A$  and  $B$ . As already seen for the attractive BEC, let  $\psi_{AB}(r)$  be a solution of Eq. (5.22) satisfying the proper boundary condition ( $\psi_{AB}(r) \rightarrow 0$  for  $r \rightarrow +\infty$  so that  $\int r^2|\psi_{AB}|^2 < \infty$ ) and having no zero, this solution corresponds to the ground state. However, in general,  $\psi_{AB}(r)$  does not satisfy the normalization condition of Eq. (5.14), but it rather verifies

$$4\pi \int_0^{+\infty} r^2 |\psi_{AB}(r)|^2 dr = I_{AB} \neq 1.$$

From  $\psi_{AB}$  we define

$$\psi(r) = \frac{\psi_{AB}(r)}{\sqrt{I_{AB}}},$$

which is the ground state solution of Eq. (5.22) with

$$\hat{\gamma}_{BEC} = AI_{AB} \quad \text{and} \quad \hat{\eta}_{SN} = BI_{AB}.$$

In this section, we explore the effect of the gravitational term, hence we fix the attractive potential constant  $\hat{\gamma}_{BEC}$ , while varying the gravitational constant  $\hat{\eta}_{SN}$ . In Fig. 5.5, we show the ground state solutions for  $\hat{\gamma}_{BEC} = 3.8508$  (corresponding to  $N|a|/a_0 = 0.3064$ , that is case considered above for the Gaussian approximation). In Fig. 5.6, the total potential,  $V_{tot} = (1/2)r^2 - \hat{\gamma}_{BEC}|\psi|^2 + \hat{\eta}_{SN}U$ , is also shown for each one of the ground state wave functions plotted in Fig. 5.5. In Fig. 5.7 and Fig. 5.8, the same simulation is performed for  $\hat{\gamma}_{BEC} = 6.5546$ .

The chemical potential eigenvalues associated to this numerical tests are reported in Tab. 5.3 for  $\hat{\gamma}_{BEC} = 3.8508$  and  $\hat{\gamma}_{BEC} = 6.5546$ .

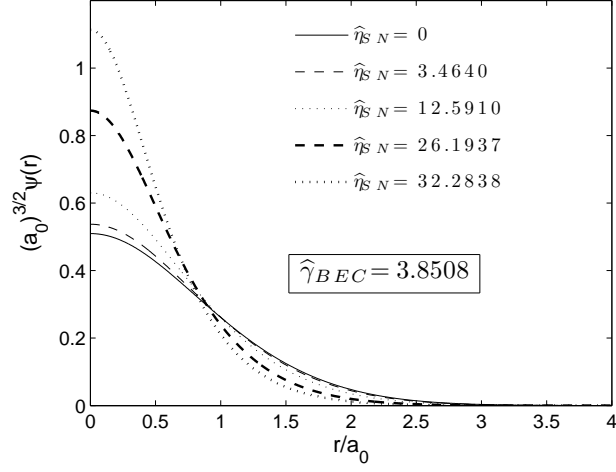


Figure 5.5: Ground state wave function for a fixed value of the coupling constant  $\hat{\gamma}_{BEC} = 3.8508$  and varying the “gravitational” constant  $\hat{\eta}_{SN}$ .

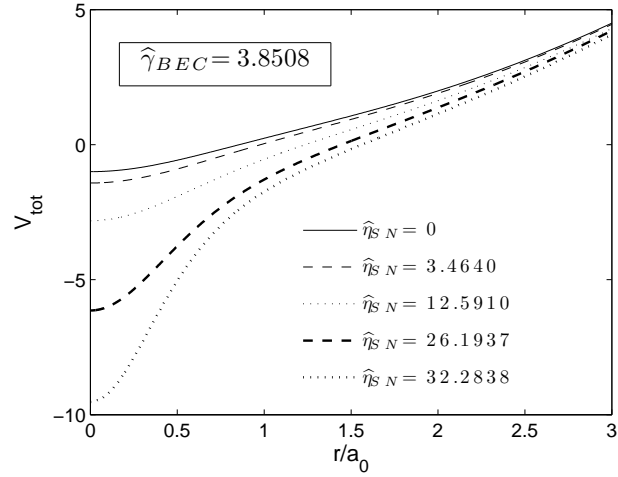


Figure 5.6: Total potential,  $V_{tot} = (1/2)r^2 - \hat{\gamma}_{BEC}|\psi|^2 + \hat{\eta}_{SN}U$ , corresponding to the ground state wave functions of Fig. 5.5. Results are computed for a fixed value of the coupling constant  $\hat{\gamma}_{BEC} = 3.8508$  and varying the “gravitational” constant  $\hat{\eta}_{SN}$ .

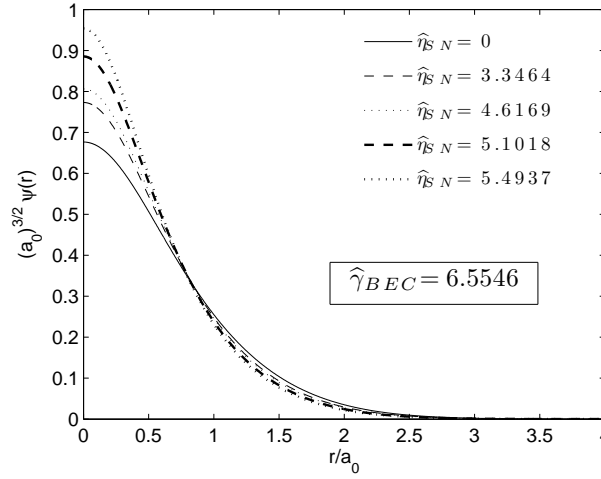


Figure 5.7: Ground state wave function for a fixed value of the coupling constant  $\hat{\gamma}_{BEC} = 6.5546$  and varying the “gravitational” constant  $\hat{\eta}_{SN}$ .

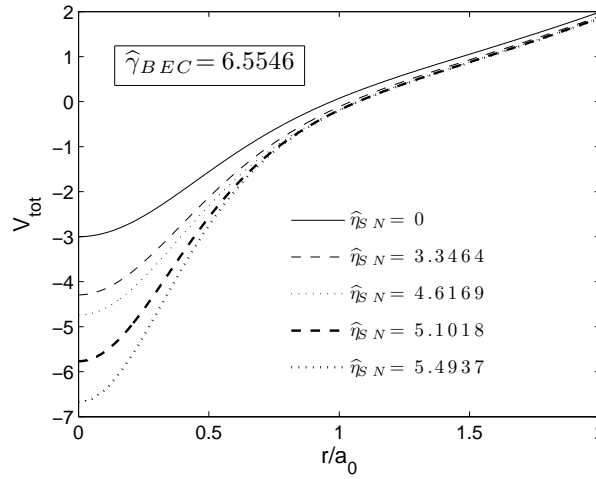


Figure 5.8: Total potential,  $V_{tot} = (1/2)r^2 - \hat{\gamma}_{BEC}|\psi|^2 + \hat{\eta}_{SN}U$ , corresponding to the ground state wave functions of Fig. 5.7. Results are computed for a fixed value of the coupling constant  $\hat{\gamma}_{BEC} = 6.5546$  and varying the “gravitational” constant  $\hat{\eta}_{SN}$ .

Table 5.3: GPE coupled with SNE (numerical solution). Ground state chemical potential  $\hat{\mu}$  and maximum value of  $\psi$ ,  $\psi(0)$  computed for two fixed values of the nonlinearity coefficient  $\hat{\gamma}_{BEC} = 3.8508$  and  $\hat{\gamma}_{BEC} = 6.5546$  and varying  $\hat{\eta}_{SN}$ . In the table, the chemical potential gap  $\mu(0) - \mu(\eta_{SN})$  is expressed in harmonic units and indicated as  $\Delta\hat{\mu}$ . Finally, the coefficients  $A$  and  $B$ , imposed while solving Eq. (5.22) to compute  $\psi_{AB}$  are also reported.

$\hat{\gamma}_{BEC} = 3.8508$					
$\hat{\eta}_{SN}$	$\hat{\mu}$	$\psi(0)$	$\Delta\hat{\mu}$	$A$	$B$
0	1.1968	0.5096	0	1	0
3.4640	0.9813	0.5373	0.2155	1.111	1
12.5910	0.3009	0.6302	0.8959	1.5291	5
26.1937	-0.9338	0.8738	2.1306	2.9375	20
32.284	-1.9931	1.1131	3.1899	4.77	40
$\hat{\gamma}_{BEC} = 6.5546$					
$\hat{\eta}_{SN}$	$\hat{\mu}$	$\psi(0)$	$\Delta\hat{\mu}$	$A$	$B$
0	0.7827	0.6765	0	3	0
3.3464	0.4275	0.7731	0.3502	3.9091	2
4.6169	0.2988	0.8061	0.4839	4.2	3
5.1018	0.1388	0.8855	0.6439	5.1388	4
5.4937	0.0008	0.9540	0.7819	5.965	5



## Chapter 6

# Future research

To date, the popularity and, consequently, the success of the qLB scheme is not comparable with that of the classical LB model for hydrodynamics. This is because, while the LB model solves the Navier-Stokes equations (NSEs) in the macroscopic limit, the qLB solves the linear and nonlinear Schrödinger equation in the adiabatic limit. The NSEs represent a much more complex systems to solve with respect to the single Schrödinger equation, thus a simple and fast method capable to solve NSEs should be welcome and widely used.

However, even relatively simple problems may become extremely difficult to cope with, when arbitrary geometries are involved and/or the computational domain becomes “large”. In such situations, the qLB scheme could be an excellent candidate since, similarly to the LB algorithm for fluid dynamics, it could be extended to complex geometries, while parallel implementation of the model is also straightforward.

In addition, as suggested in Ref. [137], the qLB model could be further extended in order to solve a set of coupled eigenvalue equations, known as Khon - Sham equations, within the density functional theory (DFT) developed in the 60’s by Hohenberg-Kohn and Khon-Sham [69, 83].

Hence, some directions for future research which should be pursued are:

- extension of the qLB model to complex geometries;
- parallel implementation of the qLB model;
- application to the solution of the Kohn-Sham equations.

Let discuss briefly each of such points.

## 6.1 Complex geometries

The lattice Boltzmann equation (LBE), both in its classical and quantum version, is not suitable for simulation in realistic complex geometries [134]. This is basically due to the constraint of discretizing the space-time under the light-cone rule ( $\Delta z = c\Delta t$ ). A similar limitation was already pointed out for the LBE for hydrodynamics, and several methods have been proposed to overcome such a difficulty [82, 103, 29, 65]. The basic strategy, common to these efforts is to gain geometrical freedom by coupling the LB model with well established techniques which can afford it, e. g., finite volumes (FV) or finite differences (FD).

Here, we intend merely put forth some ideas on how this merging is possible and to point out that, since the qLB model is essentially a complex-valued LB model, it seems a promising approach to extend these techniques to the quantum lattice Boltzmann equation.

The coupling of the classical LBE with FV or FD can be presented within the more general framework of coarse-graining. The idea is to gain geometrical flexibility by coarse graining the information carried by the differential form of LBE and define macroscopic observables on a coarse grid of virtually arbitrary shape. The crucial idea is that the coarse grid need not to be tied down to the symmetries of the underlying fine grid [134].

The starting point of the coarse-graining process is the differential form of LBE

$$\partial_t f_i + c_{ia} \partial_a f_i = C_i, \quad i = 1, \dots, b, \quad a = x, y, z, \quad (6.1)$$

where  $f_i$  are the discrete distribution functions,  $b$  is the number of the lattice speeds,  $c_i$ , and the  $C_i$ 's are suitable collision operators acting on the  $f_i$ 's.

Note that the corresponding differential form of the quantum LBE is the Dirac equation

$$\partial_t \psi_l + c \alpha_{lj}^a \partial_a \psi_j = i \frac{mc^2}{\hbar} \beta_{lj} \psi_j, \quad l, j = 1, \dots, 4, \quad a = x, y, z, \quad (6.2)$$

where  $\psi = (\psi_1, \psi_2, \psi_3, \psi_4)$  is the Dirac quadrispinor,  $\alpha^a$  and  $\beta$  are the standard Dirac matrices and  $c$  is the speed of light. Eqs. (6.1) and (6.2) are formally similar, both of them consist of a set of respectively  $b$  and 4 hyperbolic partial differential equations which are amenable to standard FV or FD discretization. In general, the result of such a discretization on Eq. (6.1) is a set of  $bN$  ordinary differential equations (ODEs) for the generic distribution function  $f_i^l$  representing the  $i$ -th population attached to the spatial node/cell labeled  $l$ . Similarly, for Eq. (6.2), we would obtain a set of  $4N$  ODEs for the generic wave function  $\psi_i^l$  representing the



$i$ -th component of the Dirac quadrispinor attached to the node/cell labeled by  $l$ .

Here, we will not further describe the methods which can be obtained by realizing the merging between LBE and FV or FD schemes. However, the FV approach has proven to be successful and lead to the so called Finite Volume-LBE (FVLBE) scheme [104, 4, 5, 149, 112, 150]. The Finite Difference-LBE schemes developed by Chen and co-workers [29] achieve second-order accuracy in both space and time and have been demonstrated to be effective for various flow in bounded domains.

## 6.2 Parallel computing

One of the main features of LB methods, either classical or quantum, is their amenability to parallel processing. This is due to the intrinsic local nature of the method, indeed the collision step is completely local, and all such steps are performed at each node simultaneously, while the streaming step involves only interactions with neighboring nodes of each lattice element. On the other hand, depending on the dimension of the problems, LB schemes can become computationally very expensive in terms of both, the number of operations and the storage requirements. Hence, a parallel implementation is sometimes mandatory in order to be able to accurately simulate certain systems (especially in three dimensions). For classical LB methods a number of parallel implementations have been proposed [125, 9, 109, 52, 41, 76] and a detailed analysis of their performance is available [109, 119, 31].

In general, due to the uniformity of the amount of computations per lattice site and to the locality of LB models, a regular domain decomposition may be the most suitable decomposition strategy [41], in this approach the computational domain is geometrically decomposed in equal subsets, whose task is then assigned to separate processors. A regular domain decomposition can be implemented using one of three standard approaches: a one-dimensional slice decomposition, a two-dimensional shaft decomposition, or a three dimensional cubic decomposition [109].

A more efficient way to distribute data among parallel processors is to use block partitioning [51, 86]. A block partitioning parallel algorithm for LB model is presented in Ref. [125] and it indeed shows a higher performance with respect to a simpler slice decomposition.

For both data decomposition approaches, the implementation of the paral-

lel code for a Distribute Memory System would be performed by using a Single Program Multiple Data parallel programming model, which means that the same program is executed on each processor operating over distinct data regions [125]. In order to assure portability, we would perform the parallel implementation by using the Message Passing Interface (MPI) library which is now the main standard for parallel computing [62, 132]. MPI provides primitives and data-structure for point-to-point and collective communications and it also allows the definition of derived data-types and operations.

The general structure of a parallel code for LB models (either classical or quantum) is as follows:

1. the computational domain is divided among the processes so that each process only stores its local sub-lattice;
2. each process exchanges information about communication sizes and locations with its neighboring processes;
3. each process properly initialize its sub-lattice;
4. the classical LB time iterations proceed by performing the following steps:
  - a) the collision step is locally performed by each process in its local sub-lattice;
  - b) the streaming step is performed by each process; this phase require communications between neighboring processes, they need to exchange information about the nodes at the boundary of each sub-lattice.

For the quantum LB scheme, the collision-streaming structure of the model is augmented with a rotation step in order to align the system along each spatial direction. The rotation step is completely local and can be performed by each process in its sub-lattice with no need to exchange data. However, the global structure of the qLB algorithm for a three-dimensional simulation is slightly more complicated than the one for classical LB models. In addition, it requires exchanging more data among neighboring processes since the streaming step is performed  $D$  times (where  $D = 1, 2$ , or  $3$  is the space dimension), once for each space dimension. Summarizing, the quantum parallel time iteration, for a three-dimensional system, is as follows:

- a) collision along  $x$  (completely local operation performed by each processor on its sub-lattice with no data exchange);
- b) streaming along  $x$  (with data exchange between neighboring processes);

- c) rotation of the system so that it becomes aligned along  $y$ ;
- d) collision along  $y$  (no data exchange);
- e) streaming along  $y$  (data exchange between neighboring processes);
- f) rotation of the system so that it becomes aligned along  $z$ ;
- g) collision along  $z$  (no data exchange);
- h) streaming along  $z$  (data exchange between neighboring processes);
- i) transformation back of the quadrispinor components,  $\psi_j$ .

Besides these more classical approaches to parallel computing, in these last few years, the programmable Graphics Processor Unit (GPU) has evolved into a very powerful computing tool. With multiple cores driven by very high memory bandwidth, today's GPUs offer incredible resources for both graphics and non-graphics processing. The lattice Boltzmann model is particularly well suited for being computed on such a device, this is due to the simplicity of the required operation. Indeed, there are already some implementations of three-dimensional lattice Boltzmann scheme on GPU developed by using the Compute Unified Device Architecture (CUDA) interface developed by nVIDIA. They show an efficiency gain of up to two orders of magnitude with respect to the computational performance of a PC (see e. g. Ref. [141] and references therein).

An implementation of the qLB scheme on GPUs is now under development.

### 6.3 Application of the qLB scheme to the Khon-Sham equations

The Khon-Sham equations are a set of eigenvalue equations within the density functional theory (DFT). DFT is a quantum mechanical theory used in physics and chemistry to investigate the eigenstate structure (mainly the ground state) of many-body systems, in particular atoms, molecules, and condensed phases. A stationary state of many-body quantum system is described by a wave function,  $\psi(\mathbf{r}_1, \dots, \mathbf{r}_N)$ , satisfying the many-body Schrödinger equation

$$H\psi := \left[ -\frac{\hbar^2}{2m} \sum_i \Delta_i + \sum_i V(\mathbf{r}_i) + \sum_{i<j} U(\mathbf{r}_i, \mathbf{r}_j) \right] \psi = E\psi, \quad (6.3)$$

where  $H$  is the total Hamiltonian of the system,  $N$  is the number of the particles,  $U$  is the particle-particle interaction potential, and  $V$  is a static external potential. From Eq. (6.3), we can see that the difference between a single particle problem and a many-body system arises from the interaction term  $U$ . The computational cost to solve Eq. (6.3) is huge, in terms of computational complexity as well as of

computer storage, for realistic values of  $N$ , hence the problem becomes intractable for conventional electronic computers when more than a few hundreds particles [137] are considered.

DFT provides an appealing alternative mapping the  $N$ -body problem (where  $U$  is present) onto a single-body problem (without  $U$ ). In particular, DFT basically claims that the ground state of a many-body wave function is uniquely determined by the electronic density

$$n(\mathbf{r}) = \sum_{j=1}^N |\phi_j(\mathbf{r})|^2,$$

where the  $\phi_j$ 's are one-particle orbitals. The ground state energy can then be obtained by summing up the single-particle orbital energies obtained by solving the Khon-Sham equations:

$$H_{KS}\phi_j = E\phi_j,$$

where the Khon-Sham Hamiltonian is

$$H_{KS} := -\frac{\hbar^2}{2m}\Delta_j + V(\mathbf{r}) + e^2 \int \frac{n(\mathbf{p})}{|\mathbf{p} - \mathbf{r}|} d\mathbf{p} + V_{ex}[n].$$

Here the first two terms are the usual kinetic and external potential operators, the third one relates to the Hartree-Fock potential and the fourth one is an effective “exchange-correlation” energy functional, including the effects of the  $N$ -body interactions.

The basic idea is that an effective functional of the electron density exists such that the ground state energy of a fictitious system of independent particles moving in such a potential is exactly the same ground state energy of the  $N$ -body interaction system.

In conclusion, a very interesting subject to investigate would be the extension of the qLB scheme for both time-dependent and time-independent (nonlinear) Schrödinger equation so to handle the Khon-Sham potential in order to solve a Khon-Sham set of equations like:

$$H_{KS}\phi_j = E_j\phi_j, \quad \text{or} \quad i\hbar\partial_t\phi_j = H_{KS}\phi_j.$$

In this respect, the possibility of using a parallel implementation of the code would be mandatory, to be able to solve systems of practical interest.

# Conclusions

In this work we have mainly analyzed the quantum lattice Boltzmann model which was first presented by Succi and Benzi in 1993 [138] as a numerical scheme to solve the Schrödinger quantum wave equation.

In particular, the qLB (quantum lattice Boltzmann) models represent one of the first attempts to extend the lattice Boltzmann concepts to quantum mechanics.

The lattice Boltzmann model is nowadays a consolidated tool for simulating fluid flows in a variety of complex settings. The idea to export the lattice kinetic approach to quantum mechanics was initially inspired by the known analogies between fluid dynamics and quantum mechanics. In particular, as we briefly illustrate in Chapter 1, quantum mechanics can be formulated in a fluid dynamic language.

Indeed, the qLB model is based on a formal analogy between the lattice Boltzmann equation (LBE) and the Dirac equation. It can be shown that the Schrödinger equation can be formally derived from the Dirac equation under an adiabatic condition which is formally equivalent to the one which takes us from the LBE to the Navier-Stokes equations.

From this analogy, a numerical scheme can be obtained basically associating the wave functions which together form the Dirac quadrispinor with the discrete distribution functions of the LBE.

The resulting model is the qLB and, as we discussed in detail in Chapter 1, the one-dimensional version of the qLB model derives naturally from the formal analogy between Dirac equation and LBE. However, in multi-dimensional formulations, the analogy is no longer straightforward. This is due to the quantum mechanical nature of the Dirac equation, in particular to the fact that, unlike classical particles, quantum particles of different types mix up – somehow –, while propagating. From a mathematical point of view, this means that the Dirac streaming matrices cannot be simultaneously diagonalized. To solve this problem, a new step has to be added besides the classical collision and streaming steps, a so-called “rotation” step, which consists of transforming the system in such a way to secure alignment between momentum and spin degrees of freedom along each direction of propagation.

Indeed, the first result of this work is the numerical validation of the multi-dimensional version of the qLB scheme. In Chapter 2, we illustrate in full detail how to extend the model to two and three space dimensions resorting to an operator splitting approach.

In addition, we present numerical results which explicitly demonstrate the applicability of the qLB scheme for the numerical simulation of the Schrödinger equation in the multidimensional case. However, most of the numerical results presented in Chapter 2 were obtained with the two-dimensional model. A detailed numerical study of the three-dimensional algorithm would necessarily require a parallel implementation. This is due to the fact that, since the distribution functions are complex valued, qLB is computationally expensive in terms of storage requirements. A systematic analysis of the numerical results given by the three dimensional model is now under development resorting to a parallel implementation of the qLB scheme on GPUs (Graphics Processing Units), see Sec. 6.2.

As a numerical scheme for quantum wave equations, the qLB model presents the usual attractive features of LB models: simplicity, computational speed and straightforward parallel implementation. Moreover it is norm-preserving and stable for any value of the time step provided that the light-cone rule is satisfied (i. e.  $\Delta t = c\Delta z$ ). Its accuracy, however, is subject to the condition  $\omega_c\Delta t = \Delta z/\lambda_B \leq 1$ ,  $\lambda_B = c/\omega_c$  being the De Broglie wavelength of the particle. Since the time-step scales linearly with the mesh-spacing (a result of the relativistic formulation), qLB can be taken down to very refined grids without suffering the time-step collapse typical of non-relativistic stability conditions,  $\Delta t < \frac{2m}{\hbar}\Delta z^2$ , thus compensating for its low-order accuracy. However, care must be taken to ensure that errors “due to lack of adiabaticity” remain under control when  $\omega_c\Delta t$  is sent to zero.

The second objective reached by this work is the extension of the qLB model to the case of non linear quantum wave equations, most notably the Gross-Pitaevskii equation (GPE) describing the dynamics of zero-temperature Bose-Einstein condensates.

As discussed in Chapter 3, we formulated an imaginary-time version of the qLB model by applying the so-called Wick rotation to the real-time qLB scheme.

The imaginary-time qLB model has been used to compute the ground state of the GPE in one and two-dimensions, and its viability demonstrated through systematic comparison with numerical solutions obtained via standard implicit methods, as well as with analytical results based on the Thomas-Fermi approximation.

We then investigated the use of the qLB model for the case of nonlinear inter-

actions with random potentials.

In particular, we simulated the phenomenon of Anderson localization within expanding Bose-Einstein condensates, solving numerically the GPE equation with a random speckle potential.

In Chapter 4, we present this application observing that qLB simulations show evidence of Anderson localization even for relatively low-energy condensates. In addition, very-long time simulations, hundred times longer than in the previous literature, show evidence of a progressive, though very slow ( $t^{-1/3}$ ), delocalization of the condensate.

Finally, in Chapter 5, starting from a work by Moroz, Penrose and Tod [102], we investigate a special non linear quantum wave equation proposed by Penrose within his theory of quantum state reduction viewed as a gravitational effect, namely the Schrödinger-Newton equation (SNE).

In particular, we extended the procedure outlined in Ref. [102] for the computation of the eigenstates of the SNE to the GPE with attractive interactions.

This last part of the work deviates, in some sense, from the main stream of this thesis because we decided to not use the qLB model for numerical computations since it seemed more convenient to apply directly the approach presented in Ref. [102] to the GPE as explained in Chapter 5.

The mathematical structures of the SNE and GPE are compared and, despite their similar behavior, there is an important difference due to the presence of the Laplacian operator in the potential energy term of the SNE. The presence of the Laplacian operator guarantees the existence of a minimum for the energy functional associated to the SNE, while the same is not true for the GPE.

Eigenfunctions of the attractive GPE are numerically computed by using a Runge-Kutta scheme under the assumption of spherical symmetry. The coupled system composed of the GPE and the SNE has also been investigated. Consistently with the theoretical expectations, the effects of ordinary gravity are found to be totally negligible with respect to the attractive force between the atoms due to the self-interaction potential of the GPE.





# Bibliography

- [1] ADHIKARI S. K. Numerical study of the spherically symmetric Gross-Pitaevskii equation in two space dimensions. *Phys. Rev. E* 62 (2000), 2937.
- [2] AFTALION A. AND DU Q. Vortices in a rotating Bose-Einstein condensate: Critical angular velocities and energy diagrams in the Thomas-Fermi regime. *Phys. Rev. A* 64 (2001), 063603.
- [3] AKKERMANS E., GHOSH S. AND MUSSLIMANI Z. Numerical study of one-dimensional and interacting Bose-Einstein condensates in a random potential. *J. Phys. B: At. Mol. Opt. Phys.* 41 (2008), 045302.
- [4] AMATI G., SUCCI S. AND BENZI R. Turbulent channel flow simulations with a coarse-grained extension of the lattice Boltzmann method. *Fluid Dyn. Res.* 19 (1997), 289–302.
- [5] AMATI G., SUCCI S. AND PIVA R. Massively Parallel Lattice-Boltzmann Simulation of Turbulent Channel Flow. *Int. J. Mod. Phys C* 8 (1997), 869–877.
- [6] ANDERSON C. D. The apparent existence of easily deflectable positives. *Science* 76 (1932), 238.
- [7] ANDERSON C. D. The Positive Electron. *Phys. Rev.* 43 (1932), 491.
- [8] ANDERSON P. W. Absence of Diffusion in Certain Random Lattices. *Phys. Rev.* 109 (1958), 1492.
- [9] ARTOLI A., HOEKSTRA A. AND SLOOT P. Optimizing Lattice Boltzmann Simulations for Unsteady Flows. *Computers & Fluids* 35 (2005), 227–240.
- [10] BAO W. AND DU Q. Computing the ground state solution of Bose-Einstein condensates by a normalized gradient flow. *SIAM J. Sci. Comput.* 25 (2004), 1674.

- [11] BAO W. AND SHEN J. A Fourth-order time-splitting Laguerre-Hermite pseudo-spectral method for Bose-Einstein condensates. *SIAM J. Sci. Comput.* 26 (2005), 2010.
- [12] BAO W. AND TANG W. Ground-state solution of Bose-Einstein condensate by directly minimizing the energy functional. *J. Comput. Phys.* 187 (2003), 230.
- [13] BAO W., CHERN I. AND LIM F. Y. Efficient and Spectrally Accurate Numerical Methods for Computing Ground and First Excited States in Bose-Einstein Condensates. *J. Comput. Phys.* 219 (2006), 836.
- [14] BAO W., JAKSCH D. AND MARKOWICH P. A. Numerical solution of the Gross-Pitaevskii Equation for Bose-Einstein condensation. *J. Comput. Phys.* 187 (2003), 318.
- [15] BAO W., JIN S. AND MARKOWICH P. A. On time-splitting spectral approximation for the Schrödinger equation in the semiclassical regime. *J. Comput. Phys.* 175 (2002), 487.
- [16] BAO W., JIN S. AND MARKOWICH P. A. Numerical study of time-splitting spectral discretizations of nonlinear Schrödinger equations in the semi-classical regimes. *SIAM J. Sci. Comput.* 25 (2003), 27.
- [17] BAYM G. AND PETHICK C. J. Ground-State Properties of Magnetically Trapped Bose-Condensed Rubidium Gas. *Phys. Rev. Lett.* 76 (1996), 6.
- [18] BENZI R., SUCCI S. AND VERGASSOLA M. The lattice Boltzmann equation: theory and applications. *Phys. Reports* 145 (1992), 222.
- [19] BIALYNICKI-BIRULA I. Weyl, Dirac and Maxwell equations on a lattice as unitary cellular automata. *Phys. Rev. D* 49 (1994), 6920.
- [20] BIALYNICKI-BIRULA I. AND MYCIELSKI J. Nonlinear wave mechanics. *Annals of Physics* 100 (1976), 62.
- [21] BILLY J., JOSSE V., ZUO Z., BERNARD A., HAMBRECHT B., LUGAN P., CLÉMENT D., SANCHEZ-PALENCIA L., BOUYER P. AND ASPECT A. Direct observation of Anderson localization of matter waves in a controlled disorder. *Nature* 453 (2008), 891.
- [22] BOGHOSIAN B. M. AND TAYLOR W. Quantum lattice-gas models for the many-body Schrödinger equation. *Internat. J. Mod. Phys. C* 8 (1997), 705.

- [23] BOGHOSIAN B. M. AND TAYLOR W. Quantum lattice-gas model for the many-particle Schrödinger equation in  $d$  dimensions. *Phys. Rev. E* 57 (1998), 54.
- [24] BOGHOSIAN B. M. AND TAYLOR W. Simulating quantum mechanics on a quantum computer. *Physica D* 120 (1998), 30.
- [25] BOHN J. L., ESRY B. D. AND GREENE C. H. Effective potentials for dilute Bose-Einstein condensates. *Phys. Rev. A* 58 (1998), 584.
- [26] BORN M., HEISENBERG W AND JORDAN P. Zur Quantenmechanik. II. *Z. f. Phys.* 35 (1925), 557.
- [27] BRADLEY C. C., SACKETT C. A. AND HULET R. G. Bose-Einstein Condensation of Lithium: Observation of Limited Condensate Number. *Phys. Rev. Lett.* 78 (1997), 985.
- [28] BRADLEY C. C., SACKETT C. A., TOLLETT J. J. AND HULET R. G. Evidence of Bose-Einstein Condensation in an Atomic Gas with Attractive Interactions. *Phys. Rev. Lett.* 75 (1995), 1687.
- [29] CAO N., CHEN S. AND JIN S. Physical symmetry and lattice symmetry in the lattice Boltzmann method. *Phys. Rev. E* 55 (1997), R21–R24.
- [30] CARADOC-DAVIES B. M., BALLAGH R. J. AND BURNETT K. Coherent Dynamics of Vortex Formation in Trapped Bose-Einstein Condensates. *Phys. Rev. Lett.* 83 (1999), 895.
- [31] CARTER J. AND OLIKER L. Performance evaluation of Lattice-Boltzmann Magnetohydrodynamics Simulations on Modern Parallel Vector Systems. *Lawrence Berkeley National Laboratory-Paper LBNL 59340* (2006).
- [32] CASTIN Y. AND DUM R. Bose-Einstein Condensates in Time Dependent Traps. *Phys. Rev. Lett.* 77 (1996), 5315.
- [33] CERIMELE M. M., CHIOFALO M. L., PISTELLA F., SUCCI S. AND TOSI M. P. Numerical solution of the Gross-Pitaevskii equation using an explicit finite-difference scheme: An application to trapped Bose-Einstein condensates. *Phys. Rev. E* 62 (2000), 1382.
- [34] CERIMELE M. M., PISTELLA F. AND SUCCI S. Particle-inspired scheme for the Gross-Pitaevski equation: An application to Bose-Einstein condensation. *Comput. Phys. Commun.* 129 (2000), 82.

- [35] CHIOFALO M. L., SUCCI S. AND TOSI M. P. Ground state of trapped interacting Bose-Einstein condensates by an explicit imaginary-time algorithm. *Phys. Rev. E* 62 (2000), 7438.
- [36] CLÉMENT C., VARÓN A. F., HUGBART M., RETTER J. A. BOUYER P., SANCHEZ-PALENCIA L., GANGARDT D. M., SHLYAPNIKOV G. V. AND ASPECT A. Suppression of Transport of an Interacting Elongated Bose-Einstein Condensate in a Random Potential. *Phys. Rev. Lett.* 95 (2005), 170409.
- [37] CLÉMENT D., VARÓN A. F., RETTER J. A., SANCHEZ-PALENCIA L., ASPECT A. AND BOUYER P. Experimental study of the transport of coherent interacting matter-waves in a 1D random potential induced by laser speckle. *New J. Phys.* 8 (2006), 165.
- [38] DALFOVO F., GIORGINI S., PITAEVSKII L. P. AND STRINGARI S. Theory of Bose-Einstein condensation in trapped gas. *Rev. Mod. Phys.* 71 (1999), 463.
- [39] DALFOVO F., PITAEVSKII L. AND STRINGARI S. The Condensate Wave Function of a Trapped Atomic Gas. *J. Res. Natl. Inst. Stand. Technol.* 101 (1996), 537.
- [40] DE BROGLIE L. Waves and Quanta. *Nature* 112 (1923), 540.
- [41] DESPLAT J. C., PAGONABARRAGA I. AND BLADON P. A parallel Lattice-Boltzmann code for complex fluids. *Computer Physics Communications* 134 (2001), 273–290.
- [42] DIÓSI L. A universal master equation for the gravitational violation of quantum mechanics. *Phys. Lett. A* (1987), 377.
- [43] DIÓSI L. Models for universal reduction of macroscopic quantum fluctuations. *Phys. Rev. A* 40 (1989), 1165.
- [44] DIRAC P. A. M. The Fundamentale Equations of Quantum Mechanics. *Proc. Roy. Soc. A* 109 (1925), 642.
- [45] DIRAC P. A. M. The Quantum Theory of the Electron. *Proc. Roy. Soc. A* 117 (1928), 610.
- [46] DIRAC P. A. M. The Quantum Theory of the Electron. Part II. *Proc. Roy. Soc. A* 118 (1928), 351.
- [47] DIRAC P. A. M. A Theory of Electrons and Protons. *Proc. Roy. Soc. A* 126 (1930), 360.

- [48] DIRAC P. A. M. Quantised Singularities in the Electromagnetic Field. *Proc. Roy. Soc. A* 133 (1931), 60.
- [49] DIRAC P. A. M. *The Principles of Quantum Mechanics*, 4th edition. Oxford University Press, 1958.
- [50] DiVINCENZO D. P. Quantum Computation. *Science* 270 (1995), 255.
- [51] DONGARRA J., FOSTER I., FOX G., GROPP W., KENNEDY K., TORCZON L. AND WHITE A., Ed. *The Sourcebook of Parallel Computing. The Morgan Kaufmann Series in Computer Architecture and Design*. Elsevier, 2002.
- [52] DUPUIS A. *From a lattice Boltzmann model to a parallel and reusable implementation of a virtual river*. PhD thesis, University of Geneva, CUI Computer Science Departement, 2002.
- [53] EDWARDS M. AND BURNETT K. Numerical solution of the nonlinear Schrödinger equation for small samples of trapped neutral atoms. *Phys. Rev. A* 51 (1995), 1382.
- [54] ENSHER J. R., JIN D. S., MATTHEWS M. R., WIEMAN C. E. AND CORNELL E. A. Bose-Einstein Condensation in a Dilute Gas: Measurement of Energy and Ground-State Occupation. *Phys. Rev. Lett.* 77 (1996), 4984.
- [55] FEYNMAN R. P. Simulating Physics with Computers. *International Journal of Theoretical Physics* 21 (1982), 467.
- [56] FORT C., FALLANI L., GUARRERA V., LYE J. L., MODUGNO M., WIERSMA D. S. AND INGUSCIO M. Effect of Optical Disorder and Single Defects on the Expansion of a Bose-Einstein Condensate in a One-Dimensional Waveguide. *Phys. Rev. Lett.* 95 (2005), 170410.
- [57] FRISCH U., HASSLACHER B. AND POMEAU Y. Lattice gas automata for the Navier–Stokes equations. *Phys. Rev. Lett.* 56 (1986), 1505.
- [58] GHIRARDI G. C., GRASSI R. AND RIMINI A. Continuous-spontaneous-reduction model involving gravity. *Phys. Rev. A* 42 (1990), 1057.
- [59] GHIRARDI G. C., RIMINI A. AND WEBER T. Unified dynamics for microscopic and macroscopic systems. *Physical Review D* 34 (1986), 470.
- [60] GOODMAN J. W. *in Laser Speckle and Related Phenomena*. Springer-Verlag, Berlin, 1975, ch. Statistical Properties of Laser Speckle Patterns.
- [61] GORDON W. *Z. f. Phys.* 40 (1926), 117.

- 
- [62] GROPP W., LUSK E. AND SKJELLUM A. *Using MPI: Portable Parallel Programming with the Message Passing Interface*. MIT Press, Cambridge, Massachusetts, USA, 1994.
- [63] GROSS E. P. Structure of a quantized vortex in boson systems. *Nuovo Cimento* 20 (1961), 454.
- [64] HE X., CHEN S. AND DOOLEN G. D. A Novel Thermal Model for the Lattice Boltzmann Method in Incompressible Limit. *J. Comput. Phys.* 146 (1998), 282.
- [65] HE X., LUO L. S. DEMBO M. Some Progress in Lattice Boltzmann Method. Part I. Nonuniform Mesh Grids. *J. Comp. Phys.* 129 (1996), 357–363.
- [66] HEISENBERG W. Über quantentheoretische Umdeutung kinematischer und mechanischer Beziehung. *Z. f. Phys.* 33 (1925), 879.
- [67] HIGUERA F. AND JIMÉNEZ J. Boltzmann approach to lattice gas simulations. *Europhys. Lett.* 9 (1989), 663.
- [68] HIGUERA F., SUCCI S. AND BENZI R. Lattice gas dynamics with enhanced collisions. *Europhys. Lett.* 9 (1989), 345.
- [69] HOHENBERG P. AND KOHN W. Inhomogeneous Electron Gas. *Phys. Rev.* 136 (1964), B864.
- [70] HORAK P., COURTOIS J. Y. AND GRYNBERG G. Atom cooling and trapping by disorder. *Phys. Rev. A* 58 (1998), 3953.
- [71] HUNTLEY J. M. Speckle photography fringe analysis: assessment of current algorithms. *Appl. Opt.* 28 (1989), 4316.
- [72] JACKSON A. D., KAVOULAKIS G. M. AND PETHICK C. J. Solitary waves in clouds of Bose-Einstein condensed atoms. *Phys. Rev. A* 58 (1998), 2417.
- [73] JACKSON B., MCCANN J. F. AND ADAMS C. S. Vortex Formation in Dilute Inhomogeneous Bose-Einstein Condensates. *Phys. Rev. Lett.* 80 (1998), 3903.
- [74] KAGAN Y., SHLYAPNIKOV G. V. AND WALRAVEN J. T. M. Bose-Einstein Condensation in Trapped Atomic Gases. *Phys. Rev. Lett.* 76 (1996), 2670.
- [75] KAGAN Y., SURKOV L. AND SHLYAPNIKOV G. V. Evolution of a Bose-condensed gas under variations of the confining potential. *Phys. Rev. A* 54 (1996), R1753.

- [76] KANDHAI D., KOPONEN A., HOEKSTRA A. G., KATAJA M., TIMONEN J. AND SLOOT P. M. A. Lattice-Boltzmann hydrodynamics on parallel systems. *Computer Physics Communications* 111 (1998), 14–26.
- [77] KÁROLYHÁZY F. *Nuovo Cimento A* 42 (1966), 390.
- [78] KÁROLYHÁZY F. Gravitation and quantum mechanics of macroscopic bodies. *Magyar Fiz. Poly.* 12 (1974), 24.
- [79] KÁROLYHÁZY F., FRENKEL A. AND LUKÁCS B. *On the possible role of gravity on the reduction of the wave function.* Oxford University Press, 1986.
- [80] KIM Y. E. AND ZUBAREV A. L. Equivalent linear two-body method for many-body problems. *J. Phys. B* 33 (2000), 55.
- [81] KLEIN O. *Z. f. Phys.* 37 (1926), 895.
- [82] KOELMAN J. A Simple Lattice Boltzmann Scheme for Navier-Stokes Fluid Flow. *Europhys. Lett.* 15 (1991), 603–608.
- [83] KOHN W. AND SHAM L. Self-Consistent Equations Including Exchange and Correlation Effects. *Phys. Rev.* 140 (1965), A1133.
- [84] KULANDER K. C., Ed. *Time Dependent Methods for Quantum Dynamics.* North-Holland, Amsterdam, 1991.
- [85] KUZNETSOV E. A., RASMUSSEN J. J., RYPDAL K. AND TURITSYN S. K. Sharper criteria for the wave collapse. *Physica D* 87 (1995), 273.
- [86] LAM M. D., ROTHBERG E. E. AND WOLF M. E. The cache performance and optimizations of blocked algorithms. In *ASPLOS-IV: Proceedings of the fourth international conference on Architectural support for programming languages and operating systems* (1991).
- [87] LANDAU L. AND LIFSHITZ E. *Relativistic Quantum Field Theory.* Pergamon, Oxford, 1960.
- [88] LEBOEUF P. AND PAVLOFF N. Bose-Einstein beams: Coherent propagation through a guide. *Phys. Rev. A* 64 (2001), 033602.
- [89] LEBOWITZ J. L., ORSZAG S. AND QIAN Y. (EDS.). Special issue on Lattice models. *J. Stat. Phys.* (1995).
- [90] LEGGET A. J. Bose-Einstein condensation in the alkali gases: Some fundamental concepts. *Rev. Mod. Phys.* 73 (2001), 307.

- [91] LOVE P. AND BOGHOSIAN B. Type II quantum algorithms. *Physica A* 362 (2006), 210.
- [92] LUGAN P., CLÉMENT D., BOUYER P., ASPECT A. AND SANCHEZ-PALENCIA L. Anderson Localization of Bogolyubov Quasiparticles in Interacting Bose-Einstein Condensates. *Phys. Rev. Lett.* 99 (2007), 180402.
- [93] LUGAN P., CLÉMENT D., BOUYER P., ASPECT A., LEWENSTEIN M. AND SANCHEZ-PALENCIA L. Ultracold Bose Gases in 1D Disorder: From Lifshits Glass to Bose-Einstein Condensate. *Phys. Rev. Lett.* 98 (2007), 170403.
- [94] LYE J. E., FALLANI L., MODUGNO M., WIERSMA D. S., FORT C. AND INGUSCIO M. Bose-Einstein Condensate in a Random Potential. *Phys. Rev. Lett.* 95 (2005), 070401.
- [95] MADELUNG E. Quantum theory in hydrodynamical form. *Z. f. Phys.* 40 (1926), 332.
- [96] MARSHALL W., SIMON C., PENROSE R. AND BOUWMEESTERS D. Towards Quantum Superpositions of a Mirror. *Phys. Rev. Lett.* 91 (2003), 130401.
- [97] MCNAMARA G. R. AND ZANETTI G. Use of the Boltzmann equation to simulate lattice gas automata. *Phys. Rev. Lett.* 61 (1988), 2332.
- [98] MEYER D. A. From quantum cellular automata to quantum lattice gases. *J. Stat. Phys.* 85 (1996), 551.
- [99] MEYER D. A. Quantum Lattice Gases and Their Invariants. *Int. J. Mod. Phys. C* 8 (1997), 717.
- [100] MINGUZZI A., SUCCI S., TOSCHI F., TOSI M. P. AND VIGNOLO P. Numerical methods for atomic quantum gases with applications to Bose-Einstein condensates and to ultracold fermions. *Phys. Rep.* 395 (2004), 223.
- [101] MODUGNO M. Collective dynamics and expansion of a Bose-Einstein condensate in a random potential. *Phys. Rev. A* 73 (2006), 013606.
- [102] MOROZ I. M., PENROSE R. AND TOD P. Spherically-symmetric solutions of the Schrödinger-Newton equations. *Class. Quantum Grav.* 15 (1998), 2733.
- [103] NANNELLI F. AND SUCCI S. The lattice Boltzmann equation on irregular lattices. *J. Stat. Phys.* 68 (1992), 401–407.
- [104] NANNELLI F. AND SUCCI S. The finite-volume formulation of the Lattice-Boltzmann equation. *Transp. Theory and Stat. Phys.* 23 (1994), 163–171.



- [105] PALPACELLI S. AND SUCCI S. Numerical validation of the quantum lattice Boltzmann scheme in two and three dimensions. *Phys. Rev. E* 75 (2007), 066704.
- [106] PALPACELLI S. AND SUCCI S. Quantum lattice Boltzmann simulation of expanding Bose-Einstein condensates in random potentials. *Phys. Rev. E* 77 (2008), 066708.
- [107] PALPACELLI S. AND SUCCI S. The Quantum Lattice Boltzmann Equation: Recent Developments. *Commun. Comput. Phys.* 4 (2008), 980.
- [108] PALPACELLI S., SUCCI S. AND SPIGLER R. Ground-state computation of Bose-Einstein condensates by an imaginary-time quantum lattice Boltzmann scheme. *Phys. Rev. E* 76 (2007), 036712.
- [109] PAN C., PRINS J. F. AND MILLER C. T. A high-performance lattice Boltzmann implementation to model flow in porous media. *Computer Physics Communications* 158 (2005), 89–105.
- [110] PAULI W. Zur Quantenmechanik des magnetischen Elektrons. *Z. f. Phys.* 43 (1927), 601.
- [111] PEARLE P. Combining stochastic dynamical state-vector reduction with spontaneous localization. *Phys. Rev. A* 39 (1989), 2277.
- [112] PENG G., XI H. AND DUNCAN C. Lattice Boltzmann method on irregular meshes. *Phys. Rev. E* 58 (1998), R4124–R4127.
- [113] PENROSE R. *Non-locality and objectivity in Quantum State Reduction in Fundamental Aspects of Quantum Theory*. Singapore, World Scientific, 1994.
- [114] PENROSE R. *Shadows of the Mind: An Approach to the Missing Science of Consciousness*. Oxford University Press, 1994.
- [115] PENROSE R. On Gravity’s role in Quantum State Reduction. *Gen. Rel. Grav.* 28 (1996), 581.
- [116] PENROSE R. Quantum computation, entanglement and state reduction. *Phil. Trans. R. Soc.* 356 (1998), 1927.
- [117] PITAEVSKII L. P. Concerning disturbances produced by a body moving in a plasma. *Sov. Phys. JEPT* 13 (1961), 185.
- [118] PITAEVSKII L. P. Dynamics of collapse of a confined Bose gas. *Phys. Lett. A* 221 (1996), 14.

- [119] POHL T., THÜREY N., DESERNO F., RÜDE U., LAMMERS P., WELLEIN G. AND ZEISER T. Performance Evaluation of Parallel Large-Scale Lattice Boltzmann Applications on Three Supercomputing Architectures. In *Supercomputing* (2004).
- [120] RUPRECHT P. A., HOLLAND M. J., BURNETT K. AND EDWARDS M. Time-dependent solution of the nonlinear Schrödinger equation for Bose-condensed trapped neutral atoms. *Phys. Rev. A* 51 (1995), 4704.
- [121] RYPDAL K., RASMUSSEN J. J. AND THOMSEN K. Similarity structure of wave-collapse. *Physica D* 16 (1985), 339.
- [122] SACKETT C. A., BRADLEY C. C., WELLING M. AND HULET R. G. Bose-Einstein condensation of lithium. *Appl. Phys. B: Lasers Opt.* 65 (1997), 433.
- [123] SANCHEZ-PALENCIA L. Smoothing effect and delocalization of interacting Bose-Einstein condensates in random potentials. *Phys. Rev. A* 74 (2006), 053625.
- [124] SANCHEZ-PALENCIA L., CLÉMENT D., LUGAN P., BOUYER P., SHLYAPNIKOV G. V. AND ASPECT A. Anderson Localization of Expanding Bose-Einstein Condensates in Random Potentials. *Phys. Rev. Lett.* 98 (2007), 210401.
- [125] SCHEPKE C. AND MAILLARD N. Performance Improvement of the Parallel Lattice Boltzmann Method Through Blocked Data Distributions. In *19th International Symposium on Computer Architecture and High Performance Computing* (2007).
- [126] SCHIFF L. I. *Quantum Mechanics, 3rd edition*. McGraw-Hill, New York, 1968.
- [127] SCHRÖDINGER E. Quantisierung als Eigenwertproblem (Dritte Mitteilung: Störungstheorie, mit Anwendung auf den Starkeffekt der Balmerlinien). *Ann. Physik* 80 (1926), 437.
- [128] SCHRÖDINGER E. Quantisierung als Eigenwertproblem (Erste Mitteilung). *Ann. Physik* 79 (1926), 361.
- [129] SCHRÖDINGER E. Quantisierung als Eigenwertproblem (Vierte Mitteilung). *Ann. Physik* 81 (1926), 109.
- [130] SCHULTE T., DRENKELFORTH S., KRUSE J., ERTMER W., ARLT J., SACHA K., ZAKRZEWSKI J. AND LEWENSTEIN M. Routes Towards

- Anderson-Like Localization of Bose-Einstein Condensates in Disordered Optical Lattices. *Phys. Rev. Lett.* 95 (2005), 170411.
- [131] SHURYAK E. V. Metastable Bose condensate made of atoms with attractive interaction. *Phys. Rev. A* 54 (1996), 3151.
- [132] SNIR M., OTTO S., HUSS-LEDERMAN S., WALKER D. AND DONGARRA J. *MPI: the Complete Reference vol. 1 and 2*. MIT Press, Cambridge, Massachusetts, USA, 1998.
- [133] SUCCI S. Numerical solution of the Schrödinger equation using discrete kinetic theory. *Phys. Rev. E* 53 (1996), 1969.
- [134] SUCCI S. *The Lattice Boltzmann Equation For Fluid Dynamics and Beyond*. Claredon Press, Oxford, 2001.
- [135] SUCCI S. Kinetic Approach to Lattice Quantum Mechanics. *Lecture Notes in Computer Science* 2493 (2002), 114.
- [136] SUCCI S. Lattice Boltzmann equation for relativistic quantum mechanics. *Phil. Trans. R. Soc. Lond. A* 360 (2002), 429.
- [137] SUCCI S. Lattice Boltzmann schemes for quantum applications. *Comput. Phys. Commun.* 146 (2002), 317.
- [138] SUCCI S. AND BENZI R. Lattice Boltzmann equation for quantum mechanics. *Physica D* 69 (1993), 327.
- [139] SUCCI S. AND VERGARI P. A Lattice Boltzmann scheme for Semiconductor Dynamics. *VLSI Design* 6 (1998), 137.
- [140] TOD P. AND MOROZ I. M. An analytical approach to the Schrödinger-Newton equations. *Nonlinearity* 12 (1999), 201.
- [141] TÖLKE J. AND KRAFCZYK. Towards three-dimensional teraflops CFD computing on a desktop PC using graphic hardware. *International Journal of Computational Fluid Dynamics* 22 (2008), 443.
- [142] TURITSYN S. K. Nonstable solitons and sharp criteria for wave collapse. *Phys. Rev. E* 47 (1993), R13.
- [143] VAHALA G., VAHALA L. AND YEPEZ J. Quantum lattice gas representation of some classical solitons. *Phys. Lett. A* 310 (2003), 187.
- [144] WANG H. Numerical studies on the split-step finite difference method for nonlinear Schrödinger equations. *Appl. Math. Comput.* 170 (2005), 17.

- 
- [145] WEINBERG S. Precision Tests of Quantum Mechanics. *Phys. Rev. Lett.* 62 (1989), 485.
  - [146] WEINBERG S. *The Quantum Theory of Fields. Volume I Foundations*. Cambridge University Press, 1995.
  - [147] WEINSTEIN M. I. Nonlinear Schrödinger equations and sharp interpolation estimates. *Commun. Math. Phys.* 87 (1983), 567.
  - [148] WOLF-GLADROW D. *Lattice gas cellular automata and lattice Boltzmann models: an introduction*. Springer, 2000.
  - [149] WOODWORD P. AND COLELLA P. The numerical simulation of two-dimensional fluid flow with strong shocks. *J. Comp. Phys.* 54 (1984), 115–173.
  - [150] XI H., PENG G. AND CHOU S. H. Finite-volume lattice Boltzmann schemes in two and three dimensions. *Phys. Rev. E* 60 (1999), 3380–3388.
  - [151] YEPEZ J. Quantum computation for physical modeling. *Comput. Phys. Commun.* 146 (2002), 277.
  - [152] YEPEZ J. AND BOGHOSIAN B. M. An efficient and accurate quantum lattice-gas model for the many-body Schrödinger wave equation. *Comput. Phys. Commun.* 146 (2002), 280.